

# **Properties and Processing Applications of Photorefractive BSO**

**Nicholas James Cook**

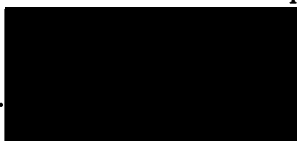
A thesis submitted in partial fulfilment of the requirements  
for the degree of Doctor of Philosophy

Sponsoring Establishment: University of Abertay Dundee

Submitted: 16<sup>th</sup> March 1998

I certify that this thesis is the true and accurate version of  
the thesis approved by the examiners.

Signed..

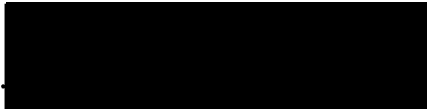


..... (Director of Studies)

Date...19/6/98

## Declaration

I hereby declare that while registered as a candidate for the degree for which this thesis is presented I have not been a candidate for any other award. I further declare that, except where stated, the work in this thesis is original and was performed by myself.

Signed.  (Nicholas James Cook) Date.....*18-6-98*

## **Acknowledgements**

I would like to thank my supervisors, Dr Colin Cartwright and Prof Allan Gillespie for their assistance and patience during my studies. I owe many other academic members of staff thanks for their advice, in particular Steve Reynolds and Charlie Main. Prof Wang Zhaoqi's help during his time as a student here is also greatly appreciated.

The technical staff of the Division of Applied Physics and Materials have been very helpful with all aspects of life as a postgraduate.

I would also like to thank my fellow students for their encouragement and support throughout my time at the University of Abertay Dundee.

# **Properties and Processing Applications of Photorefractive BSO**

**Nicholas James Cook**

## **Abstract**

A joint transform correlator (JTC) using photorefractive Bismuth Silicon Oxide (BSO) as a nonlinear recording medium, and a liquid crystal television (LCTV) as a spatial light modulator (SLM) is implemented. The physical basis of the processes involved in the photorefractive recording is studied, and the moving grating enhancement technique is investigated.

Photorefractive BSO is investigated for use as the holographic recording medium in information processing systems. The moving grating technique is investigated as a means of enhancing the photorefractive effect and therefore improving correlation performance. The nonlinear effects of moving gratings at high fringe modulations for two-wave mixing experiments are investigated and compared with numerical predictions. The effect of moving gratings on phase conjugate reflectivity via four-wave mixing is also studied experimentally.

The photorefractive joint transform correlator makes use of an LCTV as an SLM. The operation of an inexpensive LCTV is studied, and the optimum working conditions for the present application are determined.

The principles behind optical correlation are developed and the consequences of using photorefractive BSO as the recording medium are discussed. A technique for encoding information in the object plane to yield phase-only information in the Fourier plane is presented. This technique is applied to the photorefractive joint transform correlator and the performance is studied. Computational models of the correlator are presented, and the theoretical performance is compared with experimental results.

# List of Symbols

## Roman Letters:

$e$	Charge of an electron
$\mathbf{E}$	Total Electric field
$E_i$	Electric field perturbation
$E_0$	Constant part of electric field
$E_A$	Applied electric field
$E_D$	Diffusion field
$E_M$	Characteristic field
$E_q$	Saturation field
$E_w$	Normalised space charge field
$f$	Focal length
$g$	Electron generation rate
$\mathbf{H}$	Magnetic field
$I_i$	Intensity of $i$ th beam
$I_0$	Total Intensity
$\hbar$	Planck's constant divided by $2\pi$
$\mathbf{J}$	Current density
$k_B$	Boltzmann's constant
$\mathbf{k}_i$	Wave vector of $i$ th beam ( $k$ , the optical spatial frequency, is the magnitude of $\mathbf{k}$ )
$\mathbf{K}$	Grating vector ( $K$ , the grating spatial frequency, is the magnitude of $\mathbf{K}$ )
$L$	Crystal thickness
$m$	Intensity modulation
$N_A^-$	Acceptor density
$N_D$	Total donor density
$N_D^+$	Ionised donor density
$n_e$	Density of electrons

$n_0$	Unperturbed index of refraction
$\Delta n$	Change in refractive index
P	Polarisation
$r_{ij}$	Electro-optic constant
$r$	Pump beam ratio
$s$	Photoionisation cross-section
t	Time
$t_n$	Normalised time
T	Absolute temperature

### **Greek Letters:**

$\alpha$	Absorption constant
$\beta$	Probe beam ratio
$\chi$	Electronic susceptibility
$\mathcal{E}$	Optical Electric Field
$\varepsilon$	Optical dielectric constant ( $= \varepsilon_r \varepsilon_0$ )
$\varepsilon_0$	Free space permittivity
$\varepsilon_r$	Relative dielectric constant
$\varepsilon_s$	Static dielectric constant
$\phi_0$	Phase shift of intensity interference pattern
$\Phi$	Space charge grating phase shift
$\Gamma$	Two-wave coupling constant
$\gamma_R$	Recombination constant
$\eta$	Intensity diffraction efficiency
$\eta'$	Amplitude diffraction efficiency
$\eta_e$	Experimental diffraction efficiency
$\eta_q$	Quantum efficiency
$\kappa$	Coupling constant
$\Lambda$	Grating spacing
$\lambda$	Optical wavelength

$\mu$	Free electron mobility
$\mu_0$	Free space permeability
$\omega$	Angular optical frequency
$\theta$	Incident angle of writing beams
$\rho_0$	Optical activity
$\tau_D$	Dielectric relaxation time
$\tau_{nr}$	Normalised rise time

# Contents

	Page
<b>Chapter 1. Introduction</b>	1
1.1 The Photorefractive Effect	1
1.2 Processing Architectures	2
1.3 Image processing	2
1.4 The Photorefractive Joint Transform Correlator	3
<b>Chapter 2. The Photorefractive Effect</b>	5
2.1 Formation of the Refractive Index Grating	5
2.2 The Band Transport Model	9
2.3 The Steady State Solution	17
2.4 Refractive Index Changes	20
2.5 Static Dielectric Gratings	24
2.6 High Modulation Effects	28
<b>Chapter 3. Mixing and Enhancement</b>	38
3.1 Derivation of the Coupled Wave Equations	38
3.2 Moving Gratings	46
3.3 Moving Gratings at High Modulations	52
3.4 Four-Wave Mixing	62
3.5 Four-Wave Mixing with Moving Gratings	67
<b>Chapter 4. Image Processing</b>	80
4.1 Linear Space Invariant Systems	80
4.2 The Fourier Transform	84
4.3 Pattern Recognition	89
4.4 Unconventional Correlators	92
4.5 Performance Measures	98



<b>Chapter 5.</b>	<b>Characterisation of the Liquid Crystal Television</b>	106
	5.1 Liquid Crystal Displays	106
	5.2 The Epson Liquid Crystal Television	108
	5.3 Pixel Registration	116
<b>Chapter 6.</b>	<b>The Joint Transform Correlator</b>	121
	6.1 The Linear Joint Transform Correlator	121
	6.2 The Binary Joint Transform Correlator	124
	6.3 The Photorefractive Joint Transform Correlator	127
	6.4 Object-Plane Phase-Only Filters	130
	6.5 Processing requirements of binary and photorefractive JTC's	134
<b>Chapter 7.</b>	<b>The Phase-Only Photorefractive Joint Transform Correlator</b>	138
	7.1 Experimental Realisation of the POPJTC	138
	7.2 Theoretical Models and Results	141
	7.3 Experimental Results	160
<b>Chapter 8.</b>	<b>Summary and Conclusions</b>	168
<b>Appendices:</b>	<b>Computer Program Listings</b>	172
Appendix A:	Matched and phase-only correlations are performed and performance measures calculated, as described in Sections 4.4 and 4.5.	
Appendix B:	The object-plane filters described in Section 6.4 are calculated and the encoding procedure performed to yield the target filter data.	
Appendix C:	A number of correlations with added noise are calculated, as described in Section 7.1. Further noise arrays are generated until one giving results close to the average is found and used to calculate filters.	
Appendix D	Publications.	

# Chapter 1.

# Introduction

## 1.1 The Photorefractive Effect

The photorefractive effect was first encountered during frequency doubling experiments in the late 60's (Ashkin, 1966). It was noticed that electro-optic crystals, such as  $\text{LiNbO}_3$  and  $\text{LiTaO}_3$ , suffered a refractive index change when illuminated by laser radiation. The effect was a hindrance to these experiments and was initially known as 'optical damage'. In the following years it was discovered that the refractive index change was reversible and applications in holography, information processing and solid state physics were proposed.

Optical information processing makes use of the high degree of parallelism of coherent optics, and permits information to be transmitted at very high rates. The practical implementation of such processing tasks requires a material allowing efficient and high speed interaction between light beams containing information. Therefore photorefractive crystals which exhibit this reversible refractive index change under low power laser illumination have attracted a great deal of interest in the field of optical processing. The response time of a photorefractive crystal in such a system is therefore of great importance. Unfortunately, due to the nature of the effect there must be a compromise between the speed of response and the magnitude of the response, which relies on the electro-optic coefficient. For example Bismuth Silicon Oxide ( $\text{Bi}_{12}\text{SiO}_{20}$ ) is known to be a fast and sensitive material with a relatively small electro-optic coefficient, while crystals such as Barium Titanate ( $\text{BaTiO}_3$ ) have a large electro-optic coefficient but respond rather slowly. The recent introduction of organic photorefractive polymers, which are cheaper and easier to manufacture than crystals, has also provoked much interest, (Kippeln, 1997). Many applications of photorefractive crystals have been demonstrated, including coherent amplification of weak information carrying beams, phase conjugation permitting restoration of phase-distorted wavefronts, high density media storage, and real-time pattern recognition.

The physical processes involved in the photorefractive effect are most often discussed in terms of the Khukhtarev band transport model (Kukhtarev, 1976, 1979). This model is discussed in Chapter 2, and the material equations derived from it are used to describe applications throughout the thesis.

## **1.2 Processing Architectures**

The processing of information by use of photorefractive materials relies on information bearing light beams influencing the material properties of the crystal, and these physical changes in turn modulating the original or other incident light beams. The architectures used are therefore referred to in terms of the number of waves mixing inside the material. Chapter 3 looks at two distinct processing architectures, two-wave and four-wave mixing.

There has been much effort devoted to investigating methods of enhancing the magnitude of the photorefractive effect whilst retaining fast response times. One of these methods, the moving grating technique, is described and investigated for the two processing architectures. A BSO crystal was used as the photorefractive material for these and all other experiments described in this work.

## **1.3 Image Processing**

The physical optics involved in image processing is discussed in Chapter 4, and the mathematical analysis used to describe it is developed. In particular the Fourier transform, an important mathematical tool, is introduced and related to the transformation performed by a thin lens. The concept of optical pattern recognition, or correlation, is introduced and examples of filtering techniques are demonstrated.

One of the most important pieces of hardware used in optical information processing applications is the spatial light modulator (SLM), by means of which, information may be transferred to a light beam. The SLM to be used in the

experiments of Chapter 7 is a liquid crystal television (LCTV). This particular LCTV was obtained from a video projection system and is characterised in Chapter 5 to ensure correct operation as an SLM. The properties of the light transmitted by the LCTV are studied and an operating system is developed, as part of this work. This system guarantees that pixel registration is reliable, phase modulation is minimised and amplitude modulation is maximised.

## **1.4 The Photorefractive Joint Transform Correlator**

Chapter 6 introduces a particular pattern recognition system, the joint transform correlator (JTC), (Weaver, 1966). This correlator has been shown to be a robust and relatively easily implemented system, with great scope for modification to improve performance. The photorefractive JTC makes use of the two-wave mixing architecture and its performance could benefit from the moving grating technique mentioned earlier. A new method for improving the performance of the photorefractive JTC was developed as part of this work, and is presented. This method relies on the preprocessing of input information to achieve greater benefit from the recording characteristics of the BSO crystal.

Computer models of the correlation process are presented in Chapter 7 using expressions discussed in Chapter 2 to describe the photorefractive effect. These models, and other shorter programs in this work, were written by the author with the aid of IDL software, an array based package for image analysis and processing. Results from these models are compared with experimental results studying the performance of the photorefractive JTC. In the computer simulations and experiments the performance of these preprocessed filters is compared to that of the established matched filter, (VanderLugt, 1992).

## Chapter 1: References

- Ashkin, A. Boyd, G.D. Dziedzic, J.M. Smith, R.G. Ballman, A.A. LeVistein, J.J. Nassau, K. 1966, 'Optically induced refractive index inhomogeneities in LiNbO and LiTaO', *App. Phys. Lett.* **9**, No.1, pp72-74
- Kippeln, B. Sandolphon Volodin, B.L. Peyghambarian, N. 1997, 'Organic polymers for photorefractive applications', *ACS Symp. Ser.* **672**, pp218-235
- Khuktarev, N.V. 1976, 'Kinetics of hologram recording and erasure in electrooptic crystals', *Sov. Tech. Phys. Lett.* **2**, No12, pp438-441
- Kukhtarev, N.V. Markov, V.B. Odulov, S.G. Soskin, M.S. Vinetskii, V.L. 1979 'Holographic storage in electrooptic crystals. I. Steady state', *Ferroelectrics*, **22**, pp949-960
- VanderLugt, A. 1992, *Optical Signal Processing*, New York, Wiley-Interscience, Chs.3,5.
- Weaver, C.S. Goodman, J.W. 1966, 'A Technique for optically convolving two functions', *Appl. Opt.* **5**, pp1248-1249

## Chapter 2. The Photorefractive Effect

This chapter investigates the underlying physical processes which are involved in the photorefractive effect. The simplest two-wave architecture, often used in correlation experiments, is used to derive a simple expression for the space charge field. The resultant refractive index changes are described with reference to crystal orientation, and nonlinear effects at high intensity modulations are discussed.

### 2.1 Formation of the Refractive Index Grating

This section will give an explanation of the physical phenomena involved in the formation of refractive index gratings in photorefractive crystals, (Hall, 1985; Yeh, 1993; Solymar, 1996). Photorefractive crystals can be described as electro-optic crystals which are also photoconductive. Under certain conditions light incident on these crystals can therefore cause a change in the crystal's refractive index. In the simple model assumed here the crystal is regarded as having one type of mobile carrier, electrons ( $e^-$ ), and two types of impurities, donors ( $N_D$ ) and acceptors ( $N_A^-$ ) which reside somewhere deep in the band gap, as shown in Fig. 2.1. Electrons can be excited to the conduction band by photons of energy  $\hbar\omega$ , ionising a donor atom in the process. The conduction band electrons may undergo transport by drift and diffusion and then recombine with ionised donors. Some of the donor atoms and all the acceptor atoms are assumed to be ionised, and the acceptor ions play no active part in the excitation and recombination process but are present to ensure that a large number of donors are ionised in the dark. Hence the variables of the model are  $n_e$ , the density of electrons,  $N_D$  the density of donors,  $N_D^+$  the density of ionised donors, and  $N_A^-$  the density of ionised acceptors.

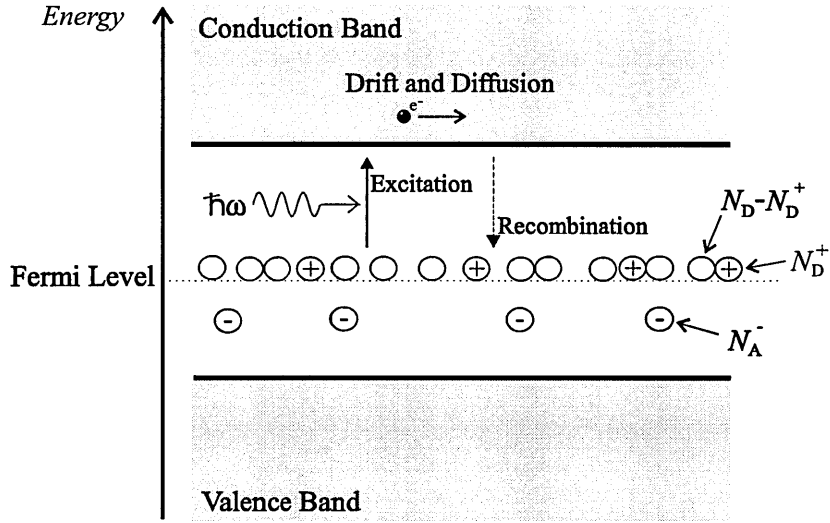


**Fig.2.1** Band Transport Model of Photorefractivity.

The model describing the formation of the grating is best described by considering the simplest experimental situation of two plane waves incident symmetrically on the crystal at angles  $\pm\theta$ . The photorefractive process is driven by the intensity distribution caused by the interference of these two beams, of intensity  $I_1$  and  $I_2$ .

This intensity distribution can be written as

$$I = I_0(1 + m\cos(Kz + \phi_0)), \quad (2.1)$$

where  $I_0 = I_1 + I_2$ , is a constant intensity,  $m$  is the modulation of the interference pattern, given by

$$m = \frac{2\sqrt{I_1 I_2}}{I_0}. \quad (2.2)$$

$K$  is the grating vector, given by

$$K = \frac{2\pi}{\Lambda}, \text{ and } \Lambda = \frac{\lambda}{2\sin\theta}, \quad (2.3)$$

where  $\Lambda$  is the grating spacing,  $\lambda$  is the optical wavelength, and  $\phi_0$  is a constant phase shift arising from the difference between the phases of the two writing beams.

The crystal responds to the intensity distribution, via the photoconductivity property, by the excitation of pairs of electrons and ionised donors, their density being proportional to the intensity. These electrons are mobile and will diffuse from higher to lower electron density; the ionised donors are not mobile and consequently there is a violation of local charge neutrality and an electric field appears. The crystal is also electro-optic, (linear Pockels effect) meaning that an electric field will cause a small change in the relative dielectric constant. The relationship between the dielectric constant and refractive index is discussed in Section 2.5. The intensity interference pattern thus causes a dielectric grating with the same spacing,  $\Lambda$ . The spatial variations of these properties are shown in Fig. 2.2.

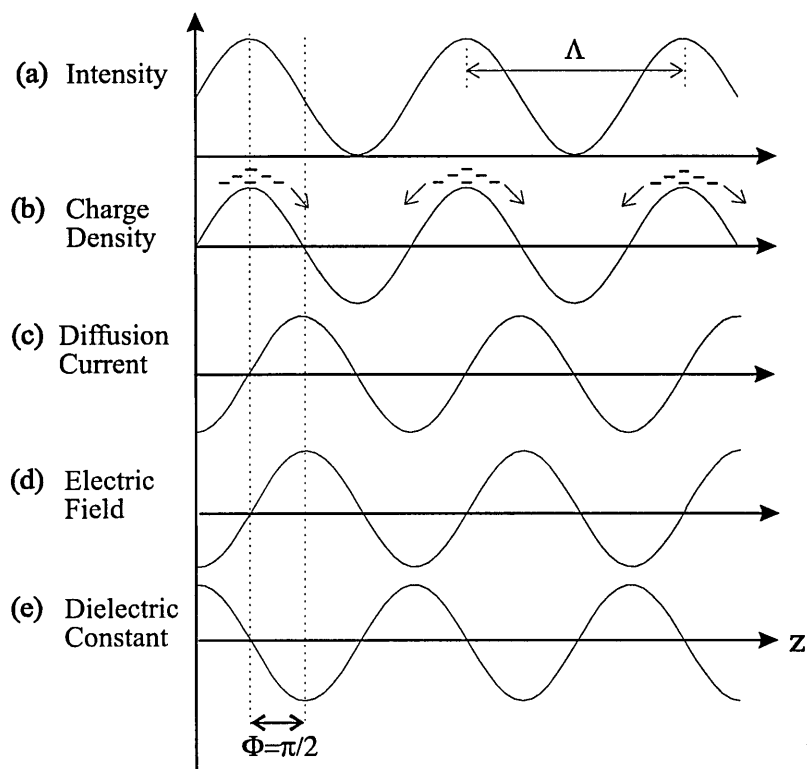


**Fig. 2.2** The response of the material to light: (a) interference pattern, (b) mobile charges migrate, and (c) give rise to a diffusion current, (d) the subsequent space charge distribution gives rise to a space charge field, which (e) modulates the dielectric constant.



The intensity variation (a) causes the charge density distribution in (b), the mobile electrons then diffuse (indicated by arrows) from areas of high to low electron density, and may recombine with ionised donors. This migration of electrons causes the diffusion current, (c) which is 90 degrees out of phase with the electron distribution since it is proportional to the gradient of the electron density (as will be explained following Eq. (2.14)). There is therefore an excess of ionised donors in areas of high electron promotion (high intensity), and a reduced level of donors in areas of low promotion, consequently the electric field appears, (d). This electric field then modulates the dielectric constant, (e) through the linear electro-optic effect which will be discussed in Section 2.3.

The photorefractive effect is classified as nonlinear since light propagating through the material is affected by material properties which are in turn influenced by the passage of the light. Nonlinear optical effects can be described by the following equation which relates the polarisation of a medium,  $P$  to the optical electric field,  $\mathcal{E}$ , (Boyd, 1992)

$$P = \varepsilon_0 \chi_e(\mathcal{E}) \mathcal{E}, \quad (2.4)$$

where

$$\chi_e(\mathcal{E}) = \chi_e^{(1)} + \chi_e^{(2)} \mathcal{E} + \chi_e^{(3)} \mathcal{E}^2 + \dots, \quad (2.5)$$

is the electronic susceptibility, and  $\varepsilon_0$  is the dielectric permittivity of a vacuum. Another nonlinear optical effect which displays a light dependent refractive index is the Kerr effect, which involves the third order susceptibility tensor,  $\chi^{(3)}$ . The associated refractive index change scales with absolute intensity and large power densities ( $\text{MWcm}^{-2}$ ) are necessary to produce observable results. The change of refractive index in the photorefractive effect is, by contrast, due to the linear electro-optic, or Pockel's effect, in which the refractive index change depends linearly on the applied electric field. The Pockel's effect can be described by a second order nonlinear susceptibility,  $\chi^{(2)}$  and can only occur for non-centrosymmetric materials such as BSO. The space charge field changes associated with the photorefractive

effect rely on the modulation of the writing intensities, as will be seen in Section 2.3, and light of very low intensity ( $\text{mWcm}^{-2}$ ) may still produce observable refractive index variations.

These properties are described by the band transport model (Kukhtarev, 1976, 1979) which has come to be accepted as the most generally applicable, and is described in the next section.

## **2.2 The Band Transport Model**

Following from the description of the physical processes involved in grating formation, a quantitative model leading to a partial differential equation for the space-charge field can be formulated. The band transport model is based on two coupled evolution equations, one for free charge carrier (electrons) density, the other for static ionised donor number density. Photoexcitation produces a number of nominally free charge carriers, the number of which is governed by the intensity of light and the number of available un-ionised donors. Ionised donors are assumed to be immobile since they are associated with impurities or imperfections in the crystal lattice, which are fixed. It has been shown from measurements of the response of the longitudinal photocarriers to pulsed-light excitation, (Hou, 1973) that electrons dominate the transport process in undoped BSO crystals. Hou's paper also determines the band edge in BSO to be at 3.25 eV and presents a consistent phenomenological energy-band scheme. An alternative transport model proposed by Feinberg (1980), describes the process as a probabilistic charge hopping mechanism. Although producing similar results to the band transport model for special cases, this is the less general model.

The semi-permanent redistribution of charges in photorefractive crystals suggests the presence of two types of trap sites within the crystal, a number of donor sites capable of giving up electrons are present with a smaller number of acceptor sites. In photorefractive crystals the acceptor sites are assumed to be completely

ionised, the presence of these negatively charged sites ensures that some of the donor sites will be depleted of electrons, even in the dark. Thus a number of ionised donor sites will always be available for capturing mobile electrons, and thus fixing charge distribution patterns.

In materials such as Bismuth Silicon Oxide (BSO) where the diffusion current is dominant over the drift current, induced by the electric field variation, the diffusion length of electrons is shorter than the period of the interference pattern. In this case an electric field must be applied to increase the electron transport length but in consequence the drift process becomes dominant and the phase differs from the  $90^\circ$  given for pure diffusion. Application of an external d.c. voltage increases the magnitude of the space charge field variations, and therefore results in increased modulation of the dielectric grating.

The four parts of the band transport model are:

(i) The rate equation governing the generation and recombination of electrons. The electron generation rate is proportional to the incident intensity, the photoionisation cross-section, and the number of un-ionised donors; therefore

$$g = sI(N_D - N_D^+), \quad (2.6)$$

where  $s$  is the photoionisation coefficient, and thermal generation has been ignored. The generation rate may alternatively be expressed in terms of the number of photons absorbed and a quantum efficiency  $\eta_q$ . If  $\alpha$  is the absorption constant, then the generation rate is

$$g = \frac{\eta_q \alpha I}{\hbar \omega}. \quad (2.7)$$

These generation rate equations require that the conduction band density of states is sufficiently large so as to allow any excited electron into a conduction band state. The spectral sensitivity of BSO becomes apparent when it is noted that the

absorption coefficients at 514nm and 633nm are  $3.02 \text{ cm}^{-1}$  and  $0.76 \text{ cm}^{-1}$  respectively (Soutar, 1991). This spectral sensitivity leads to the useful property of simultaneous writing by Argon ion laser light and reading by He-Ne laser light without degradation by the reading beam.

The recombination rate is proportional to the density of both electrons and ionised donors, and to the probability of capture, given by  $\gamma_R$ , the recombination constant. Hence the rate equation is

$$\frac{\partial N_D^+}{\partial t} = sI(N_D - N_D^+) - \gamma_R n_e N_D^+. \quad (2.8)$$

(ii) In the original band transport model formulated by Kukhtarev, a continuity equation similar to Eq. (2.8) was formulated for the electrons,

$$\frac{\partial n}{\partial t} = sI(N_D - N_D^+) - \gamma_R n_e N_D^+ + \frac{\nabla \cdot \mathbf{J}}{e} \quad (2.9)$$

which takes into account the fact that electrons are mobile and can flow away. Solymar (1996) instead uses an equation for the total current, to give a mathematically simpler formulation. Mathematically the total current equation comes from one of Maxwells equations,

$$\nabla \times \mathbf{H} = \mathbf{J} + \epsilon_s \frac{\partial \mathbf{E}}{\partial t}, \quad (2.10)$$

where  $\mathbf{H}$  is the magnetic field,  $\mathbf{J}$  is the current density,  $\epsilon_s$  is the static dielectric constant, which is used because the space charge field is assumed to vary slowly in time.  $\mathbf{E}$  is the total electric field (including any arising from an applied voltage), and  $t$  is time. Taking the divergence of both sides of this equation, we obtain

$$\nabla \cdot \left( \mathbf{J} + \epsilon_s \frac{\partial \mathbf{E}}{\partial t} \right) = 0, \quad (2.11)$$

and assuming there is variation only in the transverse direction, (the  $z$  direction of Fig. 2.2) the vector operators may be abandoned and the equation integrated to give

$$J + \epsilon_s \frac{\partial E}{\partial t} = J_0, \quad (2.12)$$

where  $J_0$  can be regarded as the total current which has two parts,  $J$  the current due to carrier flow and,  $\epsilon_s \frac{\partial E}{\partial t}$  the displacement current. If an external voltage is applied across the crystal then a current equal to  $J_0$  would flow.

(iii) The total current density  $J$ , due to carrier flow, has two contributions, the drift current and the diffusion current

$$J = e\mu n_e E + k_B T \mu \frac{\partial n}{\partial z}, \quad (2.13)$$

where  $e$  is the charge of the electron,  $\mu$  is the free electron mobility,  $k_B$  is Boltzmann's constant, and  $T$  is the absolute temperature. Note that the diffusion current is proportional to the gradient of the electron distribution giving the  $90^\circ$  phase shift between the intensity and dielectric grating mentioned earlier. The drift current is caused by the drift of charges due to the electric field. For some ferroelectric photorefractive crystals, photovoltaic electric fields would also contribute to the current density but BSO, with which this work is concerned, has no photovoltaic effects.

(iv) The last equation of the model relates the space charge electric field to the charge imbalance. It is given by Poisson's equation in the form

$$\nabla \cdot (\epsilon_s E) = e(N_D^+ - N_A^-). \quad (2.14)$$

We now have a set of non-linear differential equations describing the changes in material properties:

$$\begin{aligned} \frac{\partial N_D^+}{\partial t} &= sI(N_D - N_D^+) - \gamma_R n_e N_D^+, & J + \varepsilon_s \frac{\partial E}{\partial t} &= J_0, \\ J &= e\mu n_e E + k_B T \mu \frac{\partial n}{\partial z}, & \frac{\partial}{\partial z}(\varepsilon_s E) &= e(N_D^+ - N_A^-). \end{aligned} \quad (2.15)$$

To attempt a solution to these equations assumptions and approximations must be made. We shall assume that there is variation only in the transverse, ( $z$ ) direction, and that for small enough perturbations, the system will mirror the variation of the intensity distribution, Eq. (2.1), i.e. there will be a spatially constant term and a periodically varying term, which we may regard as a perturbation.

We can therefore assume that the solution of the differential equations will be of the form

$$X(z,t) = X_0(t) + X_p(z,t), \quad (2.16)$$

where  $X_0$  is independent of space and  $X_p$  is the periodic perturbation. Here  $X$  stands for any of the variables of the system ( $N_D^+$ ,  $n_e$ ,  $J$ , or  $E$ ).

The differential equations may be linearised by neglecting any terms which are multiples of perturbations for example,

$$n_e E \approx n_{e0} E_0 + n_{ep} E_p + n_{ep} E_0. \quad (2.17)$$

Substituting these approximations into the differential equations and separating space-dependent and space-independent terms yields, for the space-dependent case, (Solymar, 1996):

$$\frac{\partial N_{Dp}^+}{\partial t} = sI_p(N_D - N_A^-) - sI_0 N_{Dp}^+ - \gamma_R(n_{e0}N_{Dp}^+ + n_{ep}N_{D0}^+), \quad (2.18)$$

$$0 = e\mu(n_{e0}E_p + n_{ep}E_0) + k_B T\mu \frac{\partial n_{ep}}{\partial t} + \epsilon_s \frac{\partial E_p}{\partial t}, \quad (2.19)$$

$$\epsilon_s \frac{\partial E_p}{\partial t} = eN_{Dp}^+, \quad (2.20)$$

which is a set of linear equations. Now changing the method of representation of the variables to the exponential form, for example, the intensity perturbation becomes

$$I_p = I_1 \exp(-jKz), \quad (2.21)$$

where  $I_1$  is complex and incorporates the phase  $\phi_0$ , ( $I_1$  here has a different meaning from that in Eq (2.2), where it represented the intensity of one of the writing beams).

The space charge field will therefore be given by the combination of a constant term  $E_0$ , equivalent to any applied field, and a spatially varying term  $E_1$ , producing the dielectric grating. The spatial differentiation,  $\partial/\partial z$  can now be replaced by  $-jK$ , and Eqs. (2.18) - (2.20) rewritten in this form. Elimination of variables, (Solymar, 1996) yields the following differential equation in  $E_1$ , the space charge electric field variation

$$\frac{\partial E_1}{\partial t} + pE_1 = mq, \quad (2.22)$$

where  $m$  is the modulation of the interference pattern, as before, and

$$p = \frac{1}{D} \left( 1 + \frac{E_D + jE_0}{E_q} \right), \quad q = j \frac{E_D + jE_0}{D}, \quad D = 1 + \frac{E_D + jE_0}{E_M}. \quad (2.23)$$

the variable is now normalised time,  $t_n$  given by

$$t_n = t / \tau_d, \quad (2.24)$$

where

$$\tau_d = \frac{\epsilon_s}{e\mu n_{e0}}, \quad (2.25)$$

is known as the dielectric relaxation time. The characteristic fields used in this model were introduced by Kukhtarev (1976) and are,

$$E_D = \frac{k_B TK}{e}, \quad E_M = \frac{\gamma_R N_A^-}{\mu K}, \quad E_q = E_{q0}(1-a), \quad E_{q0} = \frac{eN_A^-}{\epsilon_s K}, \quad a = \frac{N_A^-}{N_D}. \quad (2.26)$$

$E_D$  is the diffusion field which is inversely proportional to grating spacing.  $E_M$  is the field which will move an electron a distance  $\lambda/2\pi$  during its lifetime.  $E_{q0}$  is called the saturation field; it is the maximum space charge field that can exist in the material for a sinusoidal charge distribution when  $a \ll 1$ .  $E_q$  is therefore often approximated by  $E_{q0}$ .

The saturation field is explained by considering that at a certain point in the crystal the maximum possible negative charge can occur when none of the donors are ionised (i.e. when electrons have filled the ionised donors) and we see the full negative charge of the acceptors. The maximum positive space charge occurs when the density of ionised donors is twice the density of the ionised acceptors. Hence the maximum sinusoidal distribution can have an amplitude of  $N_A^-$ . According to Poisson's equation

$$\epsilon_s \frac{\partial E_1}{\partial z} = eN_A^- \cos Kz, \quad (2.27)$$

therefore

$$E_1 = \frac{eN_A^-}{\epsilon_s K} \sin Kz = E_{q0} \sin Kz. \quad (2.28)$$



The crystal parameters are not well known, those given by Solymar (1996), which are similar to those given by others (Au, 1988), are:

$$\begin{aligned}
\mu &= 3 \times 10^{-6} \text{ m}^2 \text{ V}^{-1} \text{ s}^{-1}, & \gamma_R &= 1.65 \times 10^{-17} \text{ m}^3 \text{ s}^{-1}, \\
s &= 2 \times 10^{-5} \text{ m}^2 \text{ J}^{-1}, & \varepsilon_s &= 56 \varepsilon_0, \\
N_A^- &= 10^{22} \text{ m}^{-3}, & N_D &= 10^{25} \text{ m}^{-3},
\end{aligned} \tag{2.29}$$

where  $\varepsilon_0$  is the permittivity of free space ( $8.8542 \times 10^{-12} \text{ C}^2 \text{ N}^{-1} \text{ m}^{-2}$ ). These parameters give the following values for the characteristic fields and dielectric relaxation time. A fringe spacing of  $20 \mu\text{m}$ , a total incident intensity of  $5 \text{ mW cm}^{-2}$ , and room temperature are assumed.

$$\begin{aligned}
E_D &= 8.1 \times 10^3 \text{ V m}^{-1}, & E_M &= 175.1 \times 10^3 \text{ V m}^{-1}, \\
E_q &= 10.3 \times 10^6 \text{ V m}^{-1}, & \tau_d &= 17 \text{ ms}.
\end{aligned} \tag{2.30}$$

The differential equation describing the formation of the space charge field Eq. (2.22) has complex coefficients. This makes the equation equivalent to a second-order differential equation with solutions which may be combinations of exponential and oscillatory functions before the space charge field reaches the steady state. Formally with an initial condition

$$E_1 = 0 \quad \text{at} \quad t_n = 0, \tag{2.31}$$

the solution is

$$E_1 = m \frac{q}{p} [1 - \exp(-pt_n)]. \tag{2.32}$$

When  $E_0=0$  all the coefficients are real and the function will rise monotonically, but for  $E_0 \neq 0$  the imaginary part of  $p$  will be non-zero and an oscillatory behaviour occurs, the rise time may be seen to be given by the real part of  $p$ .

For  $E_0 \neq 0$  the space charge field may be seen to be complex. This can lead to energy exchange between the writing beams as will be discussed in Chapter 3. Such

energy exchange between the two optical waves depends on the imaginary part of the space charge field. If the grating is recorded for the purpose of diffracting another optical beam then the quantity of interest is the modulus of the space charge field, which should be maximised to provide the greatest diffraction efficiency, as will be discussed later in this chapter. Such diffraction from the dielectric grating is important when considering correlation applications.

### 2.3 The Steady State Solution

This is the solution in the long time limit when the space charge field is allowed to rise to its saturation limit. Taking  $\frac{\partial}{\partial t} = 0$  in Eq. (2.22) yields

$$E_1 = jm \frac{(E_D + jE_0)E_q}{E_D + E_q + jE_0}. \quad (2.33)$$

From this complex definition the well known expression for the modulus of the space charge field is obtained, (Hall, 1985):

$$|E_1| = mE_q \left[ \frac{E_D^2 + E_0^2}{(E_D + E_q)^2 + E_0^2} \right]^{1/2}. \quad (2.34)$$

The phase mismatch between the grating and the interference pattern is given by (Marrakchi, 1981)

$$\tan \Phi = \frac{1 + \frac{E_D}{E_q} + \frac{E_0^2}{E_D E_q}}{\frac{E_0}{E_D}}, \quad (2.35)$$

giving the result that  $\Phi=\pi/2$  when  $E_0=0$ .

The modulus and imaginary part of the space charge field play important roles in different applications of photorefractive crystals. A computer programme using Eq's (2.33) and (2.34) to model the space charge under a range of conditions was written using IDL software. The results of this modelling are plotted against grating spacing for increasing applied field,  $E_0$  in Figs 2.3 and 2.4.

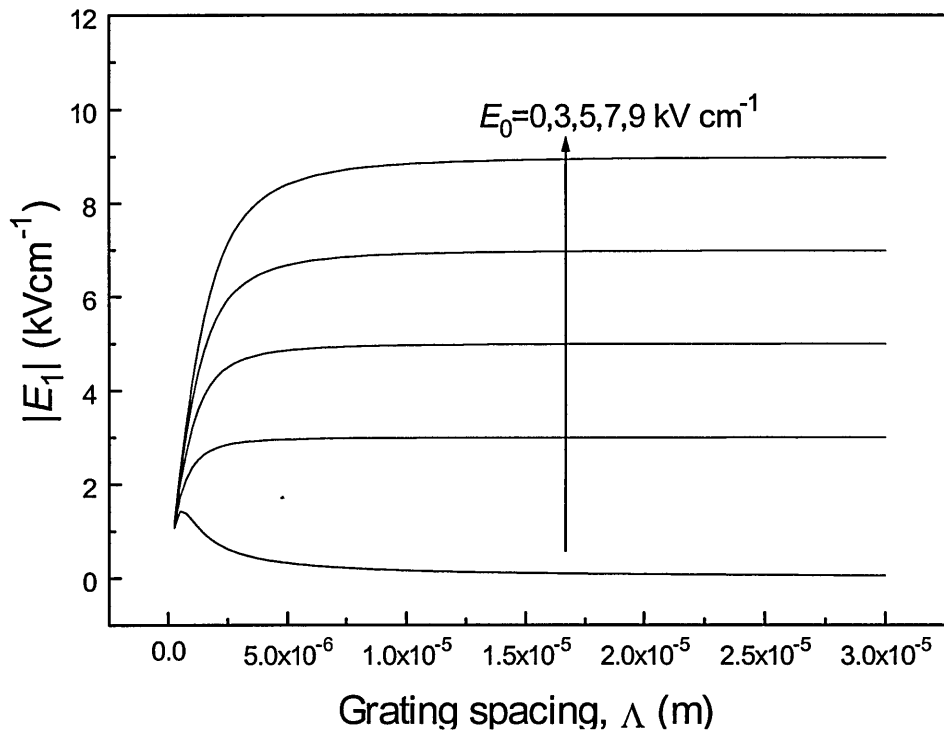


**Fig. 2.3** The modulus of the steady state space charge field as a function of grating spacing for BSO at different applied fields.

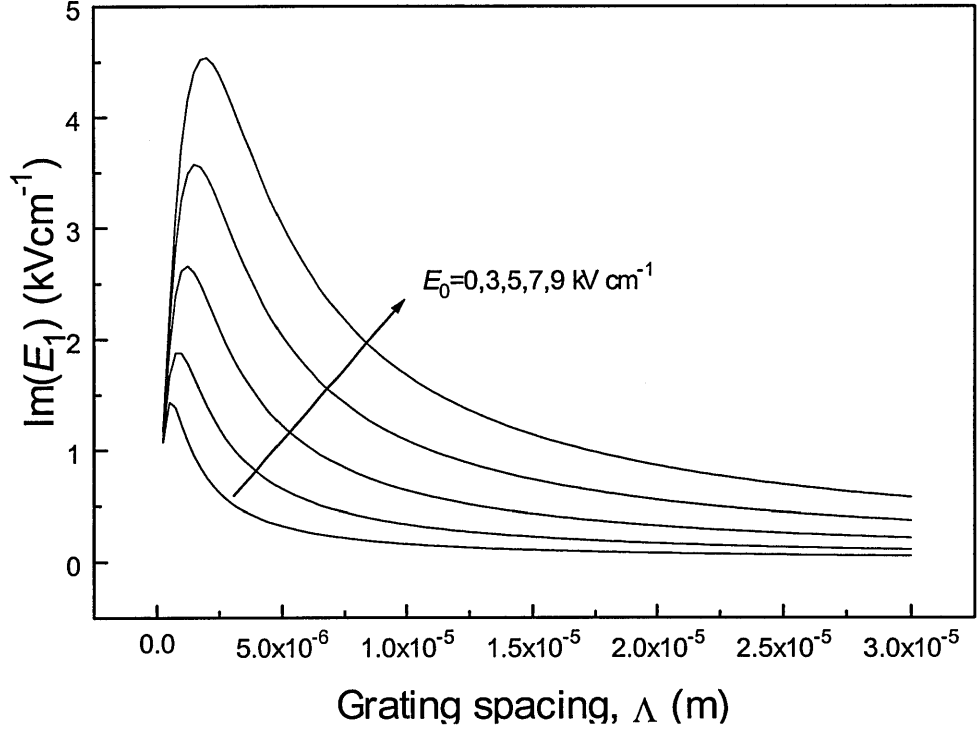


**Fig. 2.4** The imaginary part of the steady state space charge field as a function of grating spacing for BSO at different applied fields.

These figures show that apart from the small grating region there is no great advantage to be had by increasing the applied field as far as the imaginary part is concerned, but it does help to enhance the modulus of the space charge field and therefore increase diffraction efficiency.

The rise time of the space charge field (the time it takes to rise to 63% of its final value) may be obtained from Eq. (2.32) in the form

$$\tau_{nr} = \frac{1}{\text{Re}(p)} = \frac{E_q}{E_M} \frac{(E_M + E_D)^2 + E_0^2}{(E_q + E_D)(E_M + E_D) + E_0^2}, \quad (2.36)$$

which gives the normalised rise time. The real rise time,  $\tau_r$  is proportional to the dielectric relaxation time,  $\tau_r = \tau_{nr} \tau_d$ . For BSO the rise time of the space charge field increases with applied field and decreases with increasing grating spacing. Therefore

a compromise between speed and diffraction efficiency must be found where the limitations imposed by the experimental setup are taken into account.

## 2.4 Refractive Index Changes

$\text{Bi}_{12}\text{SiO}_{20}$  is an electro-optic and photoconductive material, having the cubic point group symmetry  $\bar{4}3m$ . It is optically isotropic if no electric field is applied, its refractive index ellipsoid is a sphere and is given in the standard crystallographic coordinate system  $(x,y,z)$  as (Boyd, 1992; Das, 1991; Yeh, 1993):

$$\frac{x^2}{n_0^2} + \frac{y^2}{n_0^2} + \frac{z^2}{n_0^2} = 1 \quad (2.37)$$

where  $n_0$  is the unperturbed refractive index.

In electro-optic crystals an electric field will cause a linear change in the refractive indices, inducing birefringence. Depending on the form of the electro-optic tensor, which depends on the point group symmetry of the crystal, and on the direction of the induced space-charge field with respect to the crystallographic axes, the magnitude or orientation of the index ellipsoid will be changed.

Electro-optic effects are most commonly described by considering the field-induced changes of the refractive index ellipsoid, given in tensor notation by:

$$\Delta\left(\frac{1}{n^2}\right)_{ij} = \sum_k r_{ijk}(E_1)_k \quad (2.38)$$

where  $r_{ijk}$  is the linear electro-optic tensor (Pockel's effect),  $E_i$  is the space charge field given by Eq. (2.33) and  $(i,j,k) \rightarrow (x,y,z)$ . The electro-optic tensor is symmetric in its first two indices, a symmetry relationship which is valid for all electro-optic crystals (Boyd, 1992), and it is convenient to represent it as a two-dimensional matrix,  $r_{hk}$  using contracted notation according to:

$$h = \begin{cases} 1 \text{ for } ij = 11, \\ 2 \text{ for } ij = 22, \\ 3 \text{ for } ij = 33, \\ 4 \text{ for } ij = 23 \text{ or } 32, \\ 5 \text{ for } ij = 13 \text{ or } 31, \\ 6 \text{ for } ij = 12 \text{ or } 21 \end{cases} \quad (2.39)$$

which yields, (replacing  $hk$  by  $ij$ ):

$$\Delta\left(\frac{1}{n^2}\right)_i = \sum_j r_{ij}(E_1)_j \quad (2.40)$$

where  $r_{ij}$  are known as the electro-optic coefficients and give the rate at which the coefficients  $\left(\frac{1}{n^2}\right)_i$  change with increasing electric field strength.

BSO belongs to the crystallographic class 23 with point group symmetry  $\bar{4}3m$ , which has three equal non-zero linear electro-optic coefficients (Yeh, 1993):

$$r_{41} = r_{52} = r_{63} = 5 \text{ pm } V^{-1} \quad (2.41)$$

giving:

$$\begin{bmatrix} \Delta\left(\frac{1}{n^2}\right)_1 \\ \Delta\left(\frac{1}{n^2}\right)_2 \\ \Delta\left(\frac{1}{n^2}\right)_3 \\ \Delta\left(\frac{1}{n^2}\right)_4 \\ \Delta\left(\frac{1}{n^2}\right)_5 \\ \Delta\left(\frac{1}{n^2}\right)_6 \end{bmatrix} = \begin{bmatrix} 0 & 0 & 0 \\ 0 & 0 & 0 \\ 0 & 0 & 0 \\ r_{41} & 0 & 0 \\ 0 & r_{41} & 0 \\ 0 & 0 & r_{41} \end{bmatrix} \begin{bmatrix} (E_1)_x \\ (E_1)_y \\ (E_1)_z \end{bmatrix} \quad (2.42)$$

The optical properties of the crystal are therefore described by the refractive index ellipsoid, which with an applied field is given by

$$x^2\left(\frac{1}{n^2}\right) + y^2\left(\frac{1}{n^2}\right) + z^2\left(\frac{1}{n^2}\right) + 2r_{41}(E_1)_x yz + 2r_{41}(E_1)_y zx + 2r_{41}(E_1)_z xy = 1 \quad (2.43)$$

The presence of the electric field causes the appearance of cross terms,  $yz$ ,  $zx$ ,  $xy$ , this means that the major axes of the ellipsoid are no longer the  $x$ ,  $y$  and  $z$  crystal axes. For example if the electric field is applied along the  $z$ -axis, the new principal axes of the ellipse are at  $45^\circ$  relative to the crystal axes. By geometric coordinate transformation the ellipsoid can be rewritten in terms of this principal axis system giving:

$$\frac{x'^2}{n_{x'}^2} + \frac{y'^2}{n_{y'}^2} + \frac{z'^2}{n_{z'}^2} = 1 \quad (2.44)$$

where  $x', y', z'$  are the principal-axis based coordinates of the ellipsoid, given by the following transformation:

$$\begin{aligned} x &= x' \cos 45^\circ - y' \sin 45^\circ \\ y &= x' \sin 45^\circ + y' \cos 45^\circ \\ z &= z' \end{aligned} \quad (2.45)$$

As previously mentioned, there are applications where two distinct qualities of the space charge field are utilised, the imaginary part and the modulus. Since the direction of the space charge field relative to the crystallographic axes determines the magnitude and direction of the principal axes of the ellipsoid, different crystal orientations are used depending on the application. Two different geometries have been found (Marrakchi, 1981) which give useful gratings in BSO, these two orientations are represented in Fig 2.5. The first orientation gives better beam

coupling of writing beams, and is known as the two-wave mixing orientation; whilst the second gives maximum diffraction efficiency, and is called the four-wave mixing orientation. In the first instance the electric field  $E_0$  is applied in the  $\langle 001 \rangle$ , ( $z$ ) direction and induces a change of refractive index in the  $x'$  direction of (Gunter, 1989):

$$\Delta n_{x'} = \frac{1}{2} n_0^3 r_{41} E_1 \quad (2.46)$$

while there is no change of refractive index in the  $z'$  direction. In highly photo-conducting electro-optic materials such as BSO, the modulating field can be split into two amplitudes (Marrakchi, 1981), the unshifted and the  $\pi/2$  shifted (imaginary) components of the field. The energy transfer is due to the shifted component and reaches a maximum for the two-wave mixing orientation.

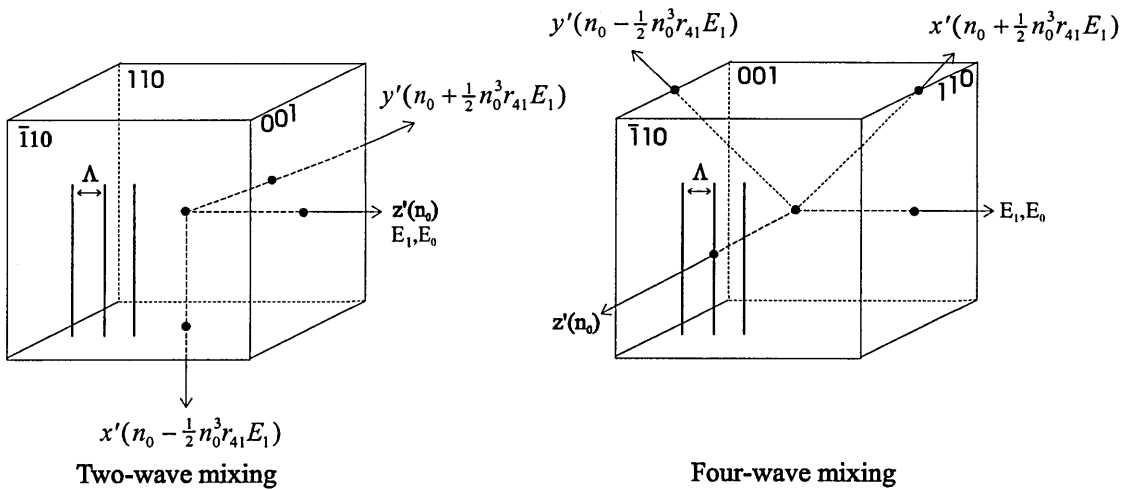


**Fig. 2.5** Two possible orientations of the BSO crystal, in each case the beams are incident near-normal on the  $(\bar{1}10)$  face.



The alternative, four-wave mixing orientation is realised when the electric field is applied along the  $\langle 110 \rangle$  direction, it then induces two new principal electro-optic axes  $x'$  and  $y'$  with the refractive index modulations given by

$$\Delta n_{x'} = +\frac{1}{2} n_0^3 r_{41} E_1, \quad \Delta n_{y'} = -\frac{1}{2} n_0^3 r_{41} E_1 \quad (2.47)$$

With this configuration, the total index modulation seen by the reading beam is  $\Delta n = n_0^3 r_{41} E_1$  which will be shown (Section 2.5) to give a diffraction efficiency four times that of the two-wave mixing orientation.

In addition to the linear birefringence due to the Pockels effect, BSO crystals have strong optical activity ( $\rho_0 = 45^\circ \text{mm}^{-1}$  at  $\lambda = 514 \text{nm}$ , (Gunter, 1989)), thus a circular birefringence is superimposed on the linear birefringence. When such a grating is read by a vertically polarised beam the transmitted and diffracted beams will generally have different elliptical polarisations. This has the advantage that a polariser can be used to reduce coherently scattered noise, giving a better signal to noise ratio.

## 2.5 Static Dielectric Gratings

The previous sections of this chapter have shown that a sinusoidal interference pattern incident on a photorefractive BSO crystal can give rise to a periodic variation of refractive index, or a grating. Many of the useful applications associated with photorefractive effects involve the scattering of light from dielectric gratings. These include wave mixing, phase conjugation and correlation. Volume dielectric gratings are by far the most efficient of all diffraction gratings. Under certain conditions the incident beam can be diffracted with 100% efficiency.

The next step in the investigation of these volume dielectric gratings is to develop an expression describing diffraction from such a grating. All the gratings considered here are transmission gratings where the transmitted and diffracted waves exit from the same side of the material. The model used to derive the coupled

differential equations describing the behaviour of a wave diffracted by a dielectric grating is a simplified form of that developed by Kogelnik, (1969) and assumes that the grating does not vary with time and varies in one direction, ( $z$ ) only. The relative dielectric constant,  $\epsilon_r$  can therefore be written as

$$\epsilon_r = \epsilon_{r0} + \epsilon_{r1} \cos \mathbf{K}z \quad (2.48)$$

where the relative dielectric constant is related to the refractive index by:

$$n^2 = \epsilon_r \Rightarrow (n_0 + \Delta n)^2 = \epsilon_{r0} + \epsilon_{r1} \quad (2.49)$$

$\epsilon_{r0}$  is the background relative dielectric constant,  $\epsilon_{r1}$  is the amplitude of the dielectric grating and  $\mathbf{K}$  is again the grating vector.

The next assumption is that the incident beam arrives at such an angle that it meets the conditions for cumulative diffraction from all the gratings, this is known as the Bragg condition, (Hecht, 1974; Das, 1991). This condition will be met as a matter of course in all the diffraction measurements made in this work. Representing this condition in the form of a vector triangle,

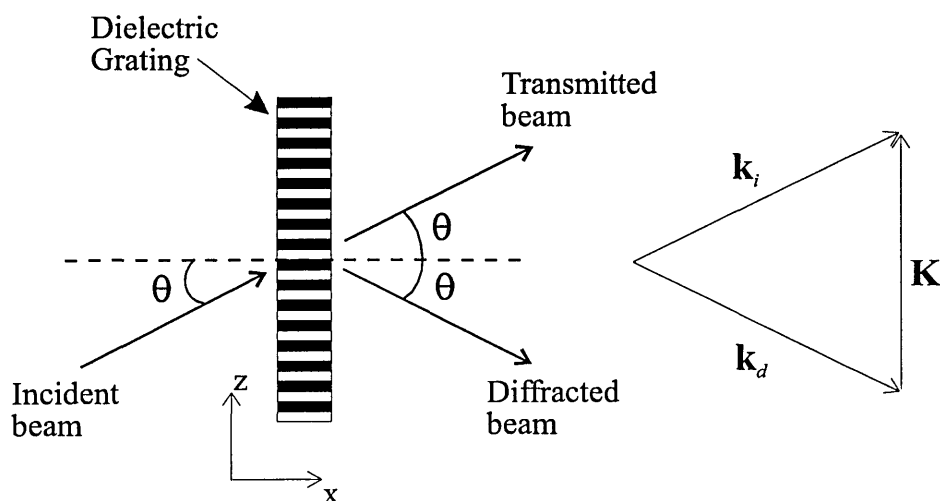


**Fig. 2.6** Bragg diffraction from a dielectric grating.

where  $\mathbf{k}_i$  and  $\mathbf{k}_d$  are the incident and diffracted wave vectors respectively,  $\mathbf{K}$  is the grating vector. The two wave vectors may be written as

$$\mathbf{k}_i = k(\mathbf{i}_x \cos \theta + \mathbf{i}_z \sin \theta) \quad (2.50)$$

$$\mathbf{k}_d = k(\mathbf{i}_x \cos \theta - \mathbf{i}_z \sin \theta)$$

where  $k=2\pi/\lambda$ ,  $\lambda$  is the wavelength in the medium, and  $\mathbf{i}_x$ ,  $\mathbf{i}_z$  are unit vectors in the  $x$  and  $z$  directions respectively. The Bragg condition may be written as

$$\mathbf{k}_i - \mathbf{k}_d = \mathbf{K} \quad (2.51)$$

which is equivalent to

$$\Lambda = \frac{\lambda}{2 \sin \theta} \quad (2.52)$$

The most widely used study of coupled waves in dielectric media is that of Kogelnik (Kogelnik, 1969). The equation to be solved is the scalar wave equation (Boyd, 1992), which for a temporal variation  $\exp(j\omega t)$  is

$$\nabla^2 \mathcal{E} + \omega^2 \mu_0 \varepsilon_0 \varepsilon_r \mathcal{E} = 0 \quad (2.53)$$

where  $\nabla$  (grad) is the two-dimensional vector operator,  $\nabla = \frac{\partial}{\partial x} \mathbf{i}_x + \frac{\partial}{\partial z} \mathbf{i}_z$ . It is assumed that there is no variation in the  $y$ -direction.  $\mathcal{E}$  is the optical electric field,  $\mu_0$  is the free space permeability (the material is assumed to be non-magnetic),  $\varepsilon_0$  is the free space permittivity, and  $\varepsilon_r$  is given by Eq. (2.48).

A useful term is the diffraction efficiency,  $\eta$  of the grating. This is the ratio of the intensity of the first diffraction order to the incident probe intensity. This intensity ratio gives, (Solymar, 1996):

$$\eta = \sin^2 \kappa x \quad (2.54)$$

where  $\kappa$  is a coupling constant given by:

$$\kappa = \frac{\varepsilon_{r1} k}{4\varepsilon_{r0} \cos \theta} \quad (2.55)$$

To convert this efficiency expression into a more practical form, note:

$$\begin{aligned} (n_0 + \Delta n)^2 &= \varepsilon_{r0} + \varepsilon_{r1} \Rightarrow n_0^2 + 2n_0\Delta n \approx \varepsilon_{r0} + \varepsilon_{r1} \\ &\Rightarrow \Delta n \approx \frac{\varepsilon_{r1} n_0}{2\varepsilon_{r0}} \end{aligned} \quad (2.56)$$

where  $n_0$  is the unperturbed index of refraction and  $\Delta n$  is the change in the refractive index. Substituting this expression into Eq. (2.54) gives

$$\eta = \sin^2\left(\frac{\varepsilon_{r1} k L}{4\varepsilon_{r0} \cos \theta}\right) = \sin^2\left(\frac{\varepsilon_{r1} L}{4\varepsilon_{r0} \cos \theta} \frac{2\pi}{\lambda/n}\right) = \sin^2\left(\frac{\pi \Delta n}{\lambda} \frac{L}{\cos \theta}\right) \quad (2.57)$$

where  $L$  is the thickness of the crystal. For most applications, including those in this work, the diffraction efficiency is small and the sinusoidal term may be replaced by its argument:

$$\eta = \left(\frac{\pi \Delta n L}{\lambda \cos \theta}\right)^2 \quad (2.58)$$

Thus giving the result (using Eqs. (2.46) and (2.47)) that the diffraction efficiency for the four-wave mixing orientation is four times that of the two-wave mixing orientation.

The previous sections in this chapter have derived expressions relating the incident writing intensities to the space charge field in the crystal, the modulation of the refractive index and hence the diffraction efficiency of a reading beam. These expressions were derived with the assumption that the modulation,  $m$ , is small, this is

not however always the case. The next section will discuss methods for analysing the space charge field at high modulations.

## 2.6 High Modulation Effects

The highest diffraction efficiencies are achieved for intensity modulations approaching unity, and many correlation experiments are carried out in this regime. This section looks at some of the models which have been developed to describe the photorefractive effect at these high modulations where nonlinear effects become important.

The Kukhtarev band transport model, (Kukhtarev, 1979) described in Section 2.2, has been the most successful at predicting the response of photorefractive materials under a wide variety of conditions. Unfortunately, as the coupled equations presented in the model are nonlinear, no exact solutions for the photorefractive response field have yet been found. A variety of approximate methods have, however been used to obtain information from the system in several limiting cases.

The most commonly applied approximation scheme used in determining the photorefractive response requires that the intensity modulation,  $m \ll 1$ . In this limit Kukhtarev derived a solution linear in  $m$  for the space charge field as a function of material and incident intensity parameters and applied field, yielding Eq (2.33). Although this model is strictly valid only for small  $m$ , it has been shown to be reasonably accurate over a broad range of conditions for values of  $m$  up to roughly 0.5, (Vachss, 1988). When the space charge field is enhanced using the moving grating technique (discussed in the next chapter), departures from linearity have been found for  $m > 0.3$  (Au, 1988) and  $m > 0.02$  (Brost, 1994).

The main problem with Kukhtarev's small  $m$  solution is that it is not applicable in the high  $m$  regime which is where the photorefractive response is generally strongest and where the diffraction efficiency is highest. The small  $m$  solution implicitly linearises the coupled system and will only produce sinusoidal gratings with the same period as the incident intensity. In general, however, the space charge field has a spectrum of harmonic components with spatial frequencies equal

to multiples of the grating frequency, (Vachss, 1988; Au, 1990). For many applications only the fundamental component of the space charge field plays a significant role, if however the modulation is high or the space charge field is enhanced then the higher harmonics can have appreciable amplitudes.

Alternatively, Moharam *et al*, (Moharam, 1979) have presented a solution for the photorefractive response which is valid for values of  $m$  approaching unity, but assumes that the saturation field ( $E_q$ ) is so much larger than the diffusion ( $E_d$ ) or applied field ( $E_0$ ) that its influence on the space-charge field may be ignored. This model indicates that in the regime of high  $m$ , the space charge grating would have a spectrum of harmonic components with amplitudes approaching that of the fundamental grating order.

The nonlinear response at high modulations has been observed in several experiments (Huignard, 1982), in which the magnitude of the photorefractive response observed was several times smaller than that predicted by the models of Kukhtarev and Moharam. A model has been developed by Ochoa *et al* (Ochoa, 1986) which extends Moharam's results by using a second order perturbation and including terms that depend on the saturation field. However these results lose accuracy in the case of a near-unity modulation depth with a strong space charge field, which would give the highest diffraction efficiency. The Ochoa model follows the charge transport model of Kukhtarev to describe the generation and transport of the carriers and hence the formation of the space charge field. The material equations are rewritten in a non-dimensional form and a second order perturbation expansion in  $\gamma$  is used to solve them, where:

$$\gamma = \frac{E_D}{E_M} \tag{2.59}$$

Final results yield the following expression for the space charge field:

$$|E_1|^2 = \left[ \frac{(1-m'^2)^{1/2} - 1}{m'} \right]^2 (E_0^2 + E_D^2) + \frac{E_D}{E_q} \left\{ 2 \left[ \frac{(1-m'^2)^{1/2} - 1}{m'} \right]^2 (E_0^2 - E_D^2) + 2 \left[ \frac{(1-m'^2)^{1/2} - 1}{(1-m'^2)^{1/2}} \right] (E_0^2 + E_D^2) \right\} \quad (2.60)$$

where,

$$m' = \frac{m}{1 + \gamma m} \quad (2.61)$$

Graphical interpretation of this model is shown after the following discussion of the Vachss model applicable to high modulations.

Vachss *et al* (Vachss, 1988) have applied a non-perturbative approach to the Kukhtarev model in the high modulation regime to achieve a relatively simple closed form expression which yields accurate information about the full harmonic spectrum of the steady state space charge field. By restricting the system to the steady state limit it is sufficiently simplified that accurate solutions may be found for several special cases for arbitrary space charge field strength.

The Vachss model again follows the charge transport model of Kukhtarev to describe the formation of the space charge field. The material equations are as they appear in section 2.1. These equations are then rewritten in dimensionless quantities by defining the following variables:

$$\begin{aligned} u &\equiv Kx, & e &\equiv \frac{E_1}{E_q}, & e_D &\equiv \frac{E_D}{E_q}, \\ d &\equiv \frac{N_D^+}{N_D}, & R &\equiv \frac{N_A}{N_D}, & e_A &\equiv \frac{E_0}{E_q} \end{aligned} \quad (2.62)$$

where all other variables have the same meaning as before.

Substituting these expressions into the material equations and combining them yields the following expression for  $e(u)$ , which is a  $2\pi$  periodic function of  $u$ , and is expressed as a Fourier sum:

$$e(u) = \sum_{n=-\infty}^{\infty} e_n \exp(inu) \quad (2.63)$$

where

$$e_n = \frac{1}{2\pi} \int_0^{2\pi} e(u) \exp(-inu) du \quad (2.64)$$

Eq. (2.63) is now substituted into Eq. (2.64), and assuming that the modulation  $m$  is high, several approximations (Vachss, 1988) can be made to yield a final solution for  $e_n$ :

$$e_n \cong (-1)^n e_A \left[ \frac{0.34 + \left(\frac{-2i}{mC}\right)^{1/3} i\delta C}{0.34 + \left(\frac{-2i}{mC}\right)^{1/3} (n + i\delta C)} \right]^{1/4} \times \exp \left\{ \frac{2}{3} \left(\frac{-2i}{mC}\right)^{1/2} \left[ (i\delta C)^{3/2} - (n + i\delta C)^{3/2} \right] \right\} \quad (2.65)$$

where  $\delta = 1 - m$  and

$$C \cong \frac{1.41(1 + 0.6\delta)}{e_A (e_A + 4.67\delta)^{1/2}} \quad (2.66)$$

is a constant determined by boundary conditions. These equations together give an expression for the amplitudes of all the spatial harmonics of  $e(u)$  in terms of elementary functions of  $n$ ,  $m$  and  $e_A$ .



The physical implications may be more readily seen when it is noted that the dependence of  $e_n$  on the above variables is determined primarily by the exponential term, as opposed to the more slowly varying  $1/4$  power term. Considering only this exponential term it may be seen that when  $\delta C \ll 1$ , (i.e.  $m \approx 1$  and  $e_A$  is non-negligible),  $e_n$  decreases in proportion to

$$e_A \exp \left[ \frac{-(1-i)n^{3/2}e_A^{3/4}}{m^{1/2}} \right] \quad (2.67)$$

since  $C$  is proportional to  $e_A^{-3/2}$  for small  $\delta$ .

Therefore in the near-unity modulation regime, an increase in the applied field results in a corresponding exponential decrease of the higher harmonic amplitudes; furthermore, this exponential decrease is more pronounced if the modulation is decreased from unity. Due to the  $(1-i)$  factor in the exponential, this reduction of amplitude with order will also be associated with a phase shift of equal magnitude. This is contrary to the situation described by the Moharam model where there is no phase shift for the higher harmonics. The Eqs. (2.65) and (2.66) have been shown, (Vachss, 1988) to be valid in the range  $0 \leq e_A \leq 1.5$ ; for higher applied fields the amplitude of the harmonics decreases at a rate proportional to the  $n^{\text{th}}$  power of  $m/e_A$ . Comparison of results obtained from this model and an exact numerical integration of the materials equations, have shown that a breakdown in the small  $\delta$  approximation used in Eq. (2.65) may become significant for  $m$  substantially smaller than 0.8.

Eq. (2.65) predicts that, for  $n > 1$ ,  $e_n$  will reach a maximum for some finite value of  $e_A$  and then decrease as  $e_A$  increases further. Fig. (2.7) shows how the moduli of the first four harmonics at modulation  $m = 1$ , vary with the ratio of applied field to saturation field. The data for these graphs were again produced using programmes written for the IDL package.

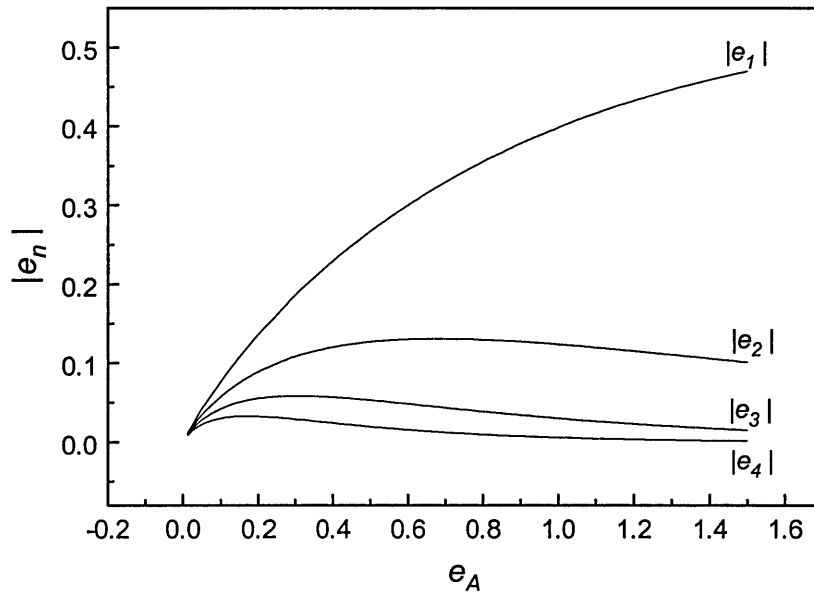


**Fig. 2.7** Moduli of the first four harmonics, predicted by the Vachss model, versus ratio of applied and saturation fields.

Fig. 2.7 shows that for low  $e_A$ , as is often the case for experiments later in this work, the higher harmonics are of appreciable magnitude and a large number of harmonics should be included in the summation to achieve accurate results for the space charge field.

Fig. 2.8 shows the spatial form of  $e(u)$  at unit modulation for different applied fields. The case of  $e_A = 0.05$  shows the highly nonlinear behaviour resulting from the strength of the higher harmonics. This value of  $e_A$  corresponds to the situation in later experiments where a  $5.5\text{kVcm}^{-1}$  applied field is used, and the characteristic fields of Eq. (2.30) are assumed.

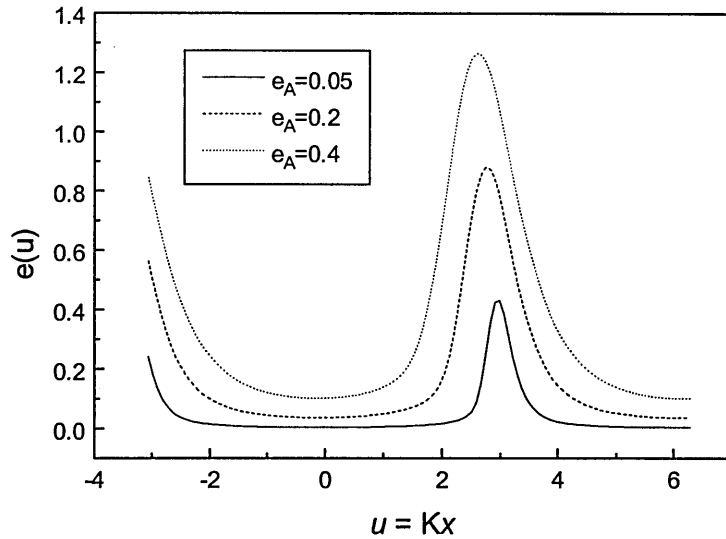


**Fig. 2.8** Form of the space charge field predicted by the Vachss model, for  $m=1$  at three different ratios of applied and saturation fields.

The phase shifts of each harmonic can also be seen to affect the final phase shift of the magnitude of the space charge field, resulting in a larger phase shift of the space charge field as  $e_A$  is reduced.

The spatial form of the space charge field predicted by the Ochoa model, Eq. (2.60) is shown in Fig. 2.9 for the same conditions as used for Fig. 2.8. There is no shift of the space charge field as the field ratio changes and the form remains sinusoidal in all cases.

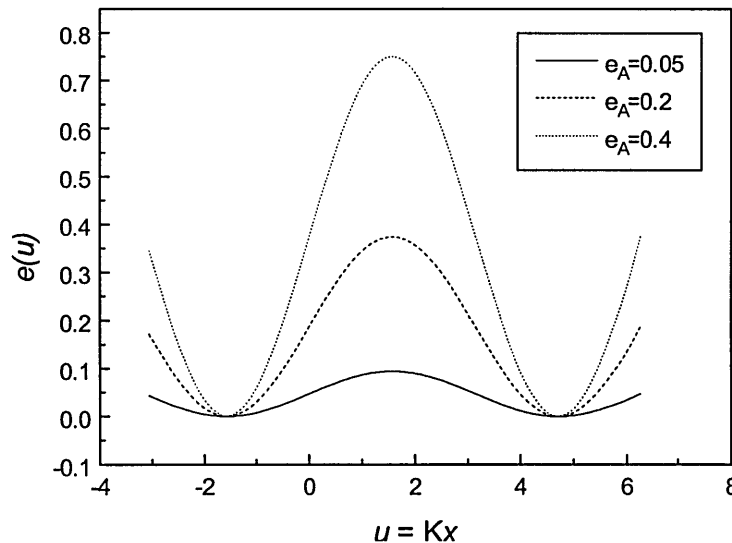


**Fig. 2.9** Form of the space charge field predicted by the Ochoa model, for  $m=1$  at three different ratios of applied and saturation fields.

Fig. 2.10 shows the space charge field dependence on intensity modulation,  $m$ , as predicted by Ochoa. The modulus of the space charge field is seen to increase nonlinearly with  $m$  in contrast to the linear relationship predicted by the Kukhtarev model discussed earlier, Eq. (2.33).

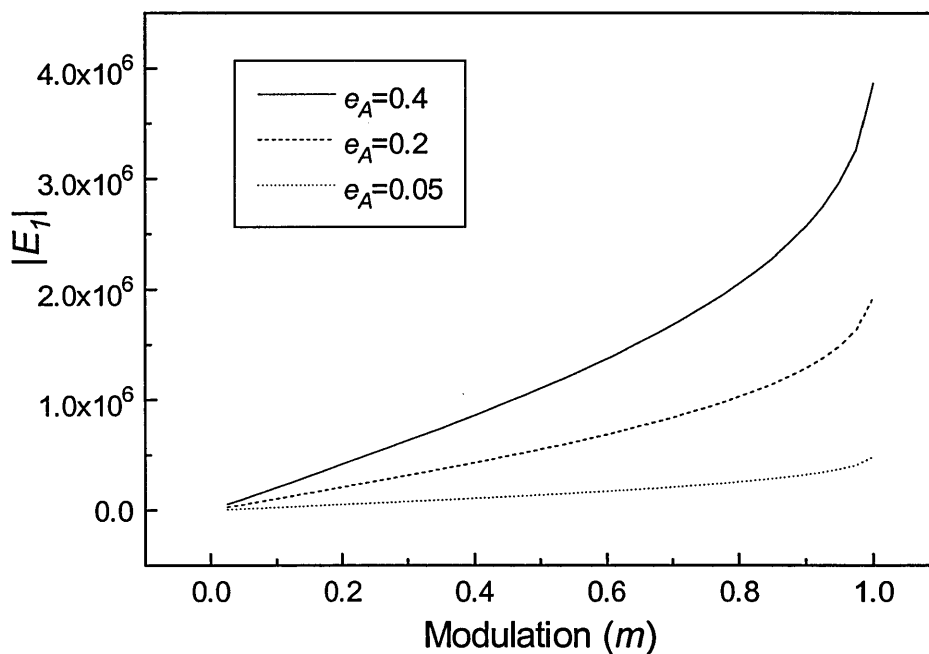


**Fig. 2.10** Nonlinear dependence of space charge field on intensity modulation predicted by Ochoa, at three different field ratios.

This chapter has described how a light interference pattern can form a refractive index grating in photorefractive crystals. The properties of the space charge field which leads to this grating have been described for a range of modulations.

## Chapter 2: References

- Amodei, J.J. 1971, 'Analysis of Transport Processes During Holographic Recording in Insulators', *RCA Rev*, **32**, pp185-198
- Au, L.B. Solymar, L. 1988, 'Space-charge field in photorefractive materials at high modulation', *Opt. Lett.* **13**, No8, pp660-662
- Au, L.B. Solymar, L. 1990, 'Higher harmonic gratings in photorefractive materials at large modulation with moving fringes', *J. Opt. Soc. Am. A*, **7**, No8, pp1554-1561
- Brost, G.A. 1993, 'Numerical analysis of photorefractive grating formation dynamics at large modulation in BSO', *Opt. Comm.* **96**, No1,2,3 pp113-116
- Brost, G.A. Magde, K.M. Larkin, J.J. Harris, M.T. 1994, 'Modulation dependence of the photorefractive response with moving gratings: numerical analysis and experiment', *J. Opt. Soc. Am. B*, **11**, No9, pp1764-1772
- Boyd, R.W. 1992, '*Nonlinear Optics*', San Diego, Academic Press, p120
- Das, P.K. 1991, '*Optical Signal Processing*', Heidelberg, Springer-Verlag, p120
- Feinberg, J. Heiman, A.R. Tanguay, Jr. Hellwarth, R.W. 1980, 'Photorefractive effects and light-induced charge migration in barium titanate', *J. App. Phys.* **51**, No.3, pp1297-1305.
- Gunter, P. Huignard, J.P. 1989, '*Photorefractive Materials and Their Applications II*', Berlin, Springer-Verlag, p213
- Hall, T.J. Jaura, R. Connors, L.M. Foote, P.D. 1985, 'The photorefractive effect - a review', *Prog. Quant. Electr.* **10**, pp77-146
- Hecht, E. Zajac, A. 1974, '*Optics*', Reading, Massachusetts, Addison-Wesley, p364
- Huignard, J.P. Ledu, B. 1982, 'Collinear Bragg diffraction in photorefractive BSO', *Opt. Lett.* **7**, No7, pp310-312
- Hou, S.L. Lauer, R.B. Aldrich, R.E. 1973, 'Transport processes of photoinduced carriers in BSO', *J. Appl. Phys.* **44**, No6, pp2652-2658
- Kogelnik, H. 1969, 'Coupled wave theory for thick hologram gratings', *Bell Syst. Tech. J.* **48**, No9, pp2909

- Khuktarev,N.V. 1976, 'Kinetics of hologram recording and erasure in electrooptic crystals', *Sov. Tech. Phys. Lett.* **2**, No12, pp438-441
- Kukhtarev,N.V. Markov,V.B. Odulov,S.G. Soskin,M.S. Vinetskii,V.L. 1979  
'Holographic storage in electrooptic crystals. I. Steady state', *Ferroelectrics*, **22**, pp949-960
- Marrakchi,A. Huignard,J.P. Gunter,P. 1981, 'Diffraction efficiency and energy transfer in two-wave mixing experiments with BSO crystals', *App. Phys.* **24**, pp131-138
- Moharam,M.G. Gaylord,T.K. Magnusson,R. 1979, 'Holographic grating formation in photorefractive crystals with arbitrary electron transport lengths', *J. Appl. Phys.* **50**, No9, pp5642-5651
- Ochoa,E. Vachss,F. Hesselink,L. 1986, 'Higher-order analysis of the photorefractive effect for large modulation depths', *J. Opt. Soc. Am. A*, **3**, No2, pp181-187
- Solymar,L. Webb,D.J. Grunnet-Jepsen,A. 1996, 'The physics and applications of photorefractive materials', Oxford University Press, Oxford.
- Soutar,C. 1991, 'Optical information processing using photorefractive BSO', PhD thesis, University of Abertay Dundee.
- Vachss,F. Hesselink,L. 1988, 'Nonlinear photorefractive response at high modulation depths', *J. Opt. Soc. Am. A*, **5**, No5, pp690-701
- Yeh,P. 1993, '*Introduction to photorefractive nonlinear optics*', New York, Wiley, p18

## Chapter 3.      **Mixing and Enhancement**

Applications of photorefractive crystals make use of several different architectures. These can be broadly categorised by the principal number of waves involved in the writing process, such as two-wave and four-wave mixing. This chapter describes the coupled nature of such mixing experiments and introduces the moving grating technique as a method for enhancement. Many correlation experiments, as will be seen later, are carried out in the high intensity modulation regime; the consequences of which are discussed.

### **3.1 Derivation of the Coupled Wave Equations**

It has been shown that the refractive index of a photorefractive crystal is perturbed by a spatially varying, time averaged intensity. The simplest intensity variation has a single Fourier component, e.g. that created by the interference of two plane waves. This section deals with the nonlinear coupling of two such plane waves propagating in a photorefractive crystal, called two-wave mixing (2WM). This wave-mixing or intensity coupling is shown to represent a form of coherent optical amplification without stimulated emission, which can be used to amplify a weak signal beam with a much stronger pump beam, (Huignard, 1981 A). The 2WM architecture is also used in many correlation applications, (Javidi, 1989; Khoury, 1994 A).

The physical interpretation of this energy exchange is as follows: in a dynamic material, the self-interference of the incident beam with the diffracted beam creates a new holographic grating which can add to (or subtract from) the original one. Since the diffracted wave is delayed by  $\pi/2$  with respect to the reading beam, the maximum energy transfer is obtained when the intensity fringe pattern and the photoinduced index modulation are shifted by  $\pi/2$ . Two-wave mixing was first reported in BSO by Marrakchi *et al* (Marrakchi, 1981).

To reach a set of equations describing this energy coupling, we must begin with the scalar wave equation, Eq. (2.51). Following Solymar (1996, p68), from the wave equation and assuming several simplifying conditions, such as neglecting absorption and optical activity, we can obtain the coupled equations relating the complex amplitudes of the electric fields of the two beams interacting within the photorefractive crystal. The next section will deal with the moving grating method in which one of the writing beams is slightly detuned, the two beams are therefore assumed to have slightly different frequencies,  $\omega_1$  and  $\omega_2$ . Incorporating the phase angles in the complex amplitudes, we write the total optical field amplitude due to the presence of the two polarised beams as

$$\mathcal{E}(\mathbf{r}, t) = \frac{1}{2} \left[ \mathcal{E}_1(x) \exp j(\omega_1 t - \mathbf{k}_1 \cdot \mathbf{r}) + \mathcal{E}_2(x) \exp j(\omega_2 t - \mathbf{k}_2 \cdot \mathbf{r}) + \text{c.c.} \right], \quad (3.1)$$

where  $\mathbf{k}_i$  is the wave vector of the  $i^{\text{th}}$  beam,  $\mathbf{r}$  is a radius vector,  $\mathcal{E}_i$  is a scalar quantity because the beams are assumed to be polarised in the  $y$  direction, and c.c. means the complex conjugate. Note that when we write an electric field in the complex form we always mean the real part. By introducing the complex conjugate, the optical electric field in Eq. (3.1) is real. We still use the complex amplitudes but we are now no longer restricted to linear differential equations.

It has been seen in Section 2.2 that consideration of the materials equations shows that for small modulation depth this intensity pattern will produce an electric field,  $E$ , within the medium which may be written as

$$E = E_0 + \frac{1}{2} \left\{ E_w m \exp j(\Omega t - \mathbf{K} \cdot \mathbf{r}) + \text{c.c.} \right\}, \quad (3.2)$$

where  $E_0$  is a spatially constant term made up of any externally applied fields,  $\Omega = \omega_1 - \omega_2$  is the detuning frequency,  $\mathbf{K}$  is the grating vector, and  $E_w$  is the normalised space charge field, being independent of modulation and given by



$$E_w = E_1/m, \quad (3.3)$$

where  $E_1$  is the perturbation to the space charge field, Eq. (2.31). We have also previously seen in Section 2.4 that the refractive index change induced in BSO via the linear Pockel's effect can be written as

$$\Delta n = \frac{1}{2} n_0^3 r_{41} E_1, \quad (3.4)$$

this can be rewritten in terms of the change in relative dielectric constant as

$$\varepsilon_{r1} = -\varepsilon_{r0}^2 r_{41} E_1. \quad (3.5)$$

The change in dielectric constant can therefore be written as

$$\varepsilon_{r1} = F \exp j(\Omega t - \mathbf{K} \cdot \mathbf{r}) + \text{c.c.}, \quad (3.6)$$

where

$$F = -\varepsilon_{r0}^2 \frac{\mathcal{E}_1 \mathcal{E}_2^*}{I_0} r_{41} E_w. \quad (3.7)$$

Substituting the above equations into the wave equation, a coupling between the waves arises, resulting in the following nonlinear coupled differential equations

$$\frac{\partial \mathcal{E}_1}{\partial x} + j \frac{F k_0}{2 \varepsilon_{r0}^{1/2} \cos \theta} \mathcal{E}_2 = 0, \quad (3.8)$$

and

$$\frac{\partial \mathcal{E}_2}{\partial x} + j \frac{F^* k_0}{2 \varepsilon_{r0}^{1/2} \cos \theta} \mathcal{E}_1 = 0. \quad (3.9)$$

Eqs (3.8) and (3.9) may now be written in a different form, remembering the phase change of the space-charge field,  $\Phi$ , we may write

$$E_w = |E_w| \exp(j\Phi), \quad (3.10)$$

and, introducing the constant

$$\Gamma = \frac{\varepsilon_{ro}^{1/2} k_o r |E_w|}{\cos\theta}. \quad (3.11)$$

The differential equations take the form

$$\frac{\partial \mathcal{E}_1}{\partial x} - j \frac{\Gamma}{2} \exp(j\Phi) \frac{|\mathcal{E}_2|^2}{I_0} \mathcal{E}_1 = 0, \quad (3.12)$$

and

$$\frac{\partial \mathcal{E}_2}{\partial x} - j \frac{\Gamma}{2} \exp(-j\Phi) \frac{|\mathcal{E}_1|^2}{I_0} \mathcal{E}_2 = 0. \quad (3.13)$$

We can now show that one of the beams may be amplified at the expense of the other. Assuming that beam 1 (pump beam) is much stronger than beam 2 (signal beam), and that the pump beam is undepleted, i.e. the loss of energy is small compared to its initial level, we may write

$$|\mathcal{E}_1|^2 = I_1 \approx I_{10} \approx I_0, \quad (3.14)$$

where  $I_{10}$  is the input intensity of beam 1 at  $x=0$ , Eq. (3.13) can be integrated to give

$$\mathcal{E}_2 = \mathcal{E}_{20} \exp \left[ \frac{\Gamma}{2} (\sin \Phi + j \cos \Phi) x \right], \quad (3.15)$$

where  $\mathcal{E}_{20}$  is the input value of the electric field associated with beam 2. It may now be seen that the amplification depends on the phase change  $\Phi$ . When the space charge electric field is in phase with the interference pattern,  $\Phi$  is zero and only the phase of  $\mathcal{E}_2$  is affected. If however the space charge field is out of phase with the interference pattern,  $\Phi \neq 0$ , which may be induced by detuning one of the writing beams. Then the magnitude of  $\mathcal{E}_2$  is also affected, it is either amplified or attenuated depending on the sign of  $\Phi$ . In the present configuration it must be positive for amplification, the maximum amplification will occur when  $\Phi = \pi/2$  (Solymar, 1996, p72). The case of maximum amplification gives the following expression for the intensity of beam 2

$$I_2 = I_{20} \exp \Gamma x. \quad (3.16)$$

The constant  $\Gamma$  is now seen to be the intensity gain factor per unit length under optimum coupling conditions.

A solution for the case of a general beam ratio may be found by introducing the new variables  $A$  and  $\Psi$  via the relationship

$$\mathcal{E}_{1,2} = A_{1,2} \exp j\Psi_{1,2}, \quad (3.17)$$

where both  $A$  and  $\Psi$  are real. Substituting this expression into Eqs. (3.12) and (3.13) yields the following set of differential equations:

$$\begin{aligned} \frac{dI_1}{dx} + \Gamma \frac{I_1 I_2}{I_1 + I_2} \sin \Phi &= 0, \\ \frac{dI_2}{dx} - \Gamma \frac{I_1 I_2}{I_1 + I_2} \sin \Phi &= 0, \\ \frac{d\Psi}{dx} + \frac{\Gamma}{2} \frac{I_1 - I_2}{I_1 + I_2} \cos \Phi &= 0, \end{aligned} \quad (3.18)$$

where

$$\Psi = \Psi_1 - \Psi_2, \quad (3.19)$$

From this set of differential equations it can be seen that the maximum amplification for beam 2 is still obtained when  $\Psi=\pi/2$ . On the other hand, when  $\Psi=0$ , there is no power transfer and the intensities become uncoupled. There is however phase transfer which could in principal be used to control the phase of one beam with another if it were not for the photorefractive response time which is too slow for such applications.

The direction of power transfer is determined by the sign of the charge carrier which affects the sign of the space charge field and through that the value of  $\Phi$ . The direction of the applied field only affects the sign of the real part of the space charge field and hence the direction of power transfer does not change.

Eqs. (3.18) and (3.19) describe the interaction of two waves polarised in the  $y$  direction, travelling in the  $x$ -direction and being influenced by an electric field in the  $z$ -direction. The orientation of the crystallographic axes relative to the electric field variation will govern whether or not there is a change in the refractive index experienced by light of a given polarisation state.

There are two common crystal geometries, as mentioned in Section 2.4, associated with BSO and other photorefractive crystals (Marrakchi, 1981), in each case the beams are incident on the  $(\bar{1}10)$  face of the crystal. In the 2-wave mixing (or longitudinal) geometry the field is applied in the  $[001]$  direction, the perturbation to the permittivity is given by

$$\varepsilon_0 \varepsilon_{r1} = \varepsilon_0 \varepsilon_{r0}^2 r_{41} \begin{bmatrix} E_z & 0 & 0 \\ 0 & E_z & 0 \\ 0 & 0 & 0 \end{bmatrix}, \quad (3.20)$$

In the 4-wave mixing (or transverse) geometry the field is applied in the [110] direction and the perturbation is

$$\varepsilon_0 \varepsilon_{r1} = \varepsilon_0 \varepsilon_{ro}^2 r_{41} \begin{bmatrix} 0 & 0 & 0 \\ 0 & 0 & -E_z \\ 0 & -E_z & 0 \end{bmatrix}. \quad (3.21)$$

Resulting in the higher refractive index modulation seen in the four-wave mixing orientation, as described by Eq. (2.45).

We are now in a position to be able to determine the orientation of a crystal by the behaviour of the two-wave mixing power transfer. Foote (1987) developed a technique to distinguish between the two principal orientations. The distinguishing feature is that when the crystal is in the longitudinal orientation, there will be energy transfer in one direction only, irrespective of the polarisation of the beams forming the grating; whereas in the transverse orientation, there can be energy transfer in either direction, depending on the writing beams polarisation. Figs. 3.1 and 3.2 show experimental results for energy transfer as a function of beam polarisation for each orientation. These measurements were performed on a BSO crystal with dimensions of 10×9.1×2mm with the smallest dimension in the  $x$ -direction. The crystal has electrodes deposited on the (110) faces, though no voltage is applied for these measurements, and the  $(\bar{1}10)$  faces are polished.

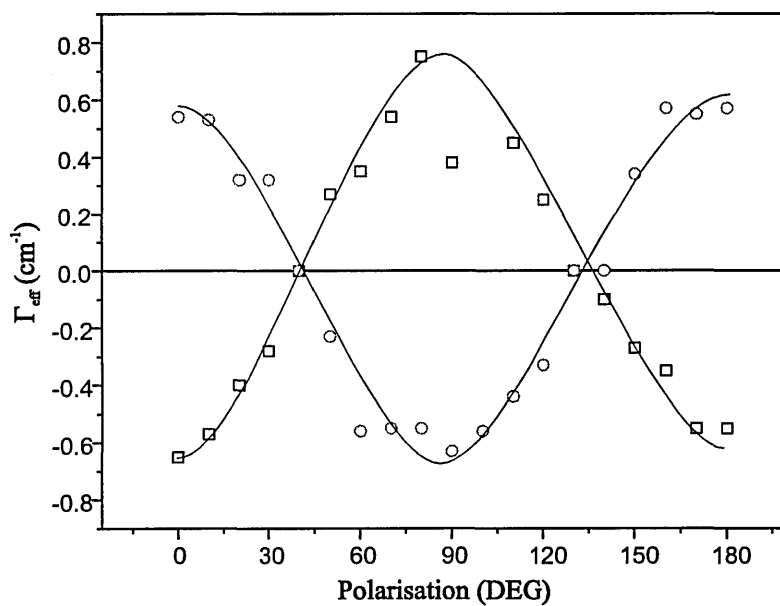


**Fig. 3.1** Energy transfer under the transverse orientation.

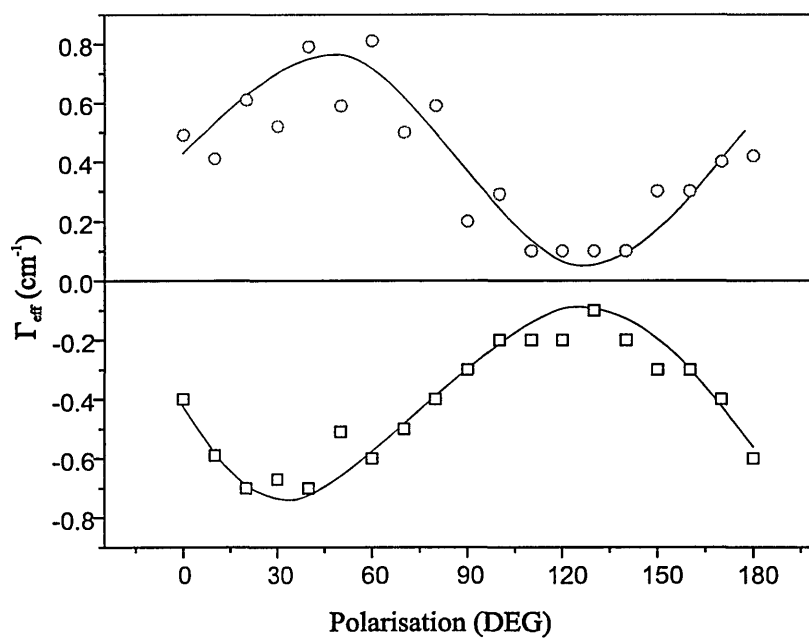


**Fig. 3.2** Energy transfer under the longitudinal orientation.

The energy transfer is measured as (Refregier, 1985)

$$\Gamma_{eff} = \frac{1}{L} \ln \left( \frac{\gamma_0 \beta}{\beta + 1 - \gamma_0} \right), \quad (3.22)$$

where

$$\gamma_0 = \frac{(1 + \beta) \exp(\Gamma L)}{\beta + \exp(\Gamma L)} = \frac{I_i^+}{I_i^-}. \quad (3.23)$$

$I_i^+$  and  $I_i^-$  are the intensities of the transmitted beams with and without the presence of the other writing beam,  $L$  is the length of the crystal, and  $\beta$  is the incident beam ratio.

These figures show the predicted dependence of energy transfer on crystal orientation, allowing us to use the most appropriate orientation when efficient energy transfer or, alternatively, efficient diffraction is desired.

### 3.2 Moving Gratings

It was mentioned in the previous section on two-wave mixing, that power transfer between two beams with similar frequencies reaches a maximum when the phase difference between the intensity interference pattern and the space charge grating is  $\pi/2$ . This condition is fulfilled for BSO when there is no applied field and the transport mechanisms are due to diffusion alone, unfortunately this gives a very weak response and an applied field is necessary to give drift recording and useful operation.

Now again assume that the two waves have slightly different frequencies,  $\omega_1$  and  $\omega_2$  so that

$$\Omega = \omega_1 - \omega_2 \neq 0, \quad (3.24)$$

$\Omega$  is called the detuning frequency and is normally accomplished by detuning one of the beams by reflecting it from a moving mirror; such detuning may also be accomplished by using acousto-optic devices, (Norman, 1994). Wave mixing using the moving grating technique is often referred to as non-degenerate mixing. The intensity interference pattern will now translate in the direction of the grating vector, and drag the refractive index variation along with it. Because the material cannot respond instantaneously to changes in the intensity pattern, the refractive index variation cannot keep up with the motion of the interference fringes and a phase difference is introduced between them. This technique, (Huignard, 1981 B) can be applied to the case of BSO with an applied field to force the phase difference between the intensity interference and the index gratings to its optimum value. The moving grating technique also alters the magnitude of the space charge field and can therefore be used to enhance image processing applications which rely on diffraction from a grating formed by two waves, such as the joint transform correlator which will be investigated later in this work.

When an applied DC field is used in conjunction with frequency detuning, the direction in which the interference pattern moves depends on the sign of detuning, and the direction in which the electrons move will depend on the sign of the electric field. Since the enhancement mechanism depends on the interaction between the moving interference pattern and the space charge wave both the sign of detuning and the direction of the applied field must be considered. If we change one of them the direction of power transfer will change. If both are changed the direction of power transfer is unaffected.

The differential equation describing the space charge field, Eq. (2.21) is:

$$\frac{\partial E_1}{\partial x_n} + pE_1 = mq, \quad (3.25)$$

where

$$p = \frac{1}{D} \left( 1 + \frac{E_D + jE_0}{E_q} \right). \quad (3.26)$$



Enhancement of the space charge is possible because  $p$  is complex, the response of the system will be partly decaying and partly oscillatory. In the presence of an applied field, the space charge field and the other material variables move with a certain velocity before rising in an oscillatory manner, to their steady state values; resonance occurs when the interference pattern moves with the same velocity. Enhancement can be achieved by detuning one of the writing beams to introduce a frequency difference between the two writing beams and hence movement of the interference pattern. The total electric field due to two such beams is given by Eq. (3.1). The intensity pattern then varies as

$$I = I_0 \left[ 1 + \frac{m}{2} \exp \left[ j[(\omega_1 - \omega_2)t - (\mathbf{k}_1 - \mathbf{k}_2) \cdot \mathbf{r}] + c.c. \right] \right]. \quad (3.27)$$

Writing the intensity pattern in the form  $\exp[j(\Omega t - \mathbf{K} \cdot \mathbf{r})]$  it is clear that the interference pattern will move with a velocity,  $v = \Omega / K$ .

The response of the perturbed part of the material variables to this intensity pattern will therefore be of the form

$$X_p = X_1(t) \exp [j(\Omega t - Kz)], \quad (3.28)$$

where  $X$  represents any of the system variables.

Using this new form of the response and solving the material differential equations of Kukhtarev as before, the following expression for the steady state space charge field will be obtained, (Refregier, 1985)

$$E_1 = \frac{-m(E_D + jE_0)}{-\frac{E_0}{E_q} + K\nu\tau_d \left( 1 + \frac{E_D}{E_M} \right) + j \left( 1 + \frac{E_D}{E_q} + K\nu\tau_D \frac{E_0}{E_M} \right)}. \quad (3.29)$$

Assuming that the diffusion field  $E_D$  is negligible compared to the other fields, this being the situation when a large external field is applied to promote drift. The imaginary part of the space charge field is therefore

$$\text{Im}(E_1) = m \left( \frac{E_M^2}{E_0} \right) \left( \frac{\frac{E_0}{E_q} - K v \tau_D}{\left( K v \tau_D + \frac{E_M}{E_0} \right)^2 + \left( \frac{E_M}{E_q} - K v \tau_D \frac{E_M}{E_0} \right)^2} \right), \quad (3.30)$$

which is maximised, and thus yields the optimum energy transfer conditions, for an optimum normalised grating velocity of

$$K v \tau_D = \frac{E_0}{E_q} - \left[ 1 + \left( \frac{E_0}{E_M} \right)^2 \right]^{-1/2} \left[ 1 + \frac{E_0^2}{E_M E_q} \right]. \quad (3.31)$$

This optimum velocity may also be found by considering the differential equation, Eq. (3.25) which is linear with a forcing term  $p$ , which is complex. The detuning results in a harmonic excitation at a frequency  $\Omega$ . The differential equation itself has oscillatory eigensolutions when  $\text{Im}(p) \neq 0$ . Resonance will occur when the eigenfrequency agrees with the detuning frequency

$$\Omega = -\text{Im}(p), \quad (3.32)$$

therefore, neglecting diffusion

$$\Omega = \frac{1}{\tau_d} \text{Im} \left[ \frac{1 + j \frac{E_0}{E_q}}{1 + j \frac{E_0}{E_M}} \right]. \quad (3.33)$$

Assuming  $E_M \ll E_0 \ll E_q$  which is valid for BSO under normal conditions, Eq's (3.31) and (3.33) give the same result for the optimum velocity

$$v = \frac{1}{K\tau_d} \frac{E_M}{E_0}. \quad (3.34)$$

Under the same conditions the magnitude of the space charge field is given by

$$|E_{sc}| = \left[ \frac{m^2 E_0^2}{\left( K v \tau_d - \frac{E_0}{E_q} \right)^2 + \left( 1 + K v \tau_d \frac{E_0}{E_M} \right)^2} \right]^{\frac{1}{2}}, \quad (3.35)$$

which is maximised for the same optimum frequency. Therefore the most efficient diffraction efficiency is obtained when the energy transfer is also maximised. This could cause problems if the diffraction efficiency is to be maximised. The diffraction efficiency is greatest at high modulations; however if this optimum detuning is used energy transfer will cause a reduction in modulation and a decrease in efficiency. It will be seen later that this problem is overcome by an alternative grating velocity arising from nonlinear interactions which provides increased diffraction enhancement away from the imaginary field enhancement regime.

The maximum of the imaginary part of the space charge field, corresponding to the optimum velocity of Eq. (3.34) is given by

$$\text{Im}[E_1] = m \frac{E_0^2 E_q}{E_0^2 + E_M E_q}. \quad (3.36)$$

When the grating is moving at the optimum velocity it is found that, under the previous field approximations, the real part of the space charge field solution goes to zero. Therefore the phase difference between the interference pattern and the

refractive index grating is  $90^\circ$ , and the modulus of the space charge field is approximately the same as the imaginary part.

Recalling that  $E_q$  and  $E_M$  are proportional to the grating spacing,  $\text{Im}(E_1)$  will also be optimised at a particular spacing which is found by differentiating Eq. (3.36) with respect to the grating spacing, giving

$$E_0^2 = E_q E_M, \quad (3.37)$$

consequently the optimum spacing is

$$\Lambda = \frac{2\pi E_0}{N_A} \left( \frac{\epsilon_s \mu}{e\gamma_R} \right), \quad (3.38)$$

and the corresponding space charge field is

$$\text{Im}(E_1) = m \frac{E_q}{2}. \quad (3.39)$$

This expression, derived assuming modulation of the refractive index linear in  $m$ , therefore predicts that a space-charge field of modulus higher than the applied field is possible with moving gratings at high modulation, increased from an optimum of

$$|E_1| = mE_0, \quad (3.40)$$

for stationary gratings.

Numerical simulations carried out by Brost (1994) and others, show that at grating velocities optimising two-wave coupling, the fundamental component of the space charge field is limited in magnitude to values below the applied field. The next section discusses these numerical models, looking particularly at the high modulation regime.

### 3.3 Moving Gratings at High Modulations

When the moving grating technique is used to enhance diffraction efficiency at high modulations, the optimum grating velocity is found to be at a value somewhat less than that predicted by the linearised theory of the previous section, (Wang, 1994). From equations describing the transient behaviour of the space charge field (Au, 1990) it can be shown that the  $r^{\text{th}}$  harmonic of the space charge field moves with an approximate speed of  $v/r^2$ , where  $v$  is the so-called resonance velocity for the fundamental component. Hence there will be resonance of higher harmonics at grating velocities lower than the fundamental.

Brost (1994), (Fig. 3.3) has modelled the formation of the space charge field as a function of grating velocities up to a modulation depth of  $m = 1$ . He found that when the space charge field is enhanced by moving gratings the photorefractive response can differ significantly from the predictions of linearised theory for  $m$  greater than approximately 0.02. This is due to the increased modulation of material variables. A finite difference method was used to calculate the space charge across one grating period, the magnitude and phase of the higher harmonics were then determined by Fourier decomposition of the calculated space charge field. Brost's numerical results are followed by graphs (Fig. 3.4 (a - c)) showing experimental results for the square root of the diffraction efficiency at similar modulations. The square root of the diffraction efficiency is proportional to the magnitude of the space charge field as can be seen from Eqs. (2.45) and (2.56).

Brost's numerical results for small modulations, Fig. 3.3 (a) agree with the linear theory. However at large modulations, Fig. 3.3 (c) a more complicated structure is observed. As the modulation increases a low velocity enhancement of the space charge field is observed and grows as the modulation increases, eventually becoming greater than the space charge at the so-called fundamental grating velocity. The low velocity space charge structure has been shown, (Au, 1988, 1990) to coincide with increased higher harmonic amplitudes.

Although the higher harmonics must be considered in the effort to obtain numerical solutions, the limiting of the space charge field is not due to competition from the higher harmonics. The saturation of the space charge field is due to the

inhibited charge transport when the magnitude of the space charge field is comparable to the applied electric field.

In practice the interaction length, within the crystal, over which moving grating enhancement is achieved is limited since the optimum velocity is a function of intensity, which will change due to absorption and therefore is a function of distance travelled through the crystal. This is less important at high modulations since absorption effects are reduced due to saturation of the space charge field. This has the effect of broadening the enhancement response to grating velocity. The crystal used in this work is thin, (2mm) and modulation changes due to absorption are not critical, especially when our area of interest is large modulations.

Au and Solymar (Au, 1988,1990) have also carried out numerical simulations of the space charge field taking the higher harmonics into account. We can draw the following conclusions from their simulations:

1. As the modulation increases, the space charge field,  $E$ , increases at a lower rate than that predicted by the linear in  $m$  theory, indicating a nonlinear dependence of space charge on fringe modulation.
2. As the modulation increases from low values to 0.6, there is one distinct optimum fringe velocity which increases with modulation. At higher modulations the behaviour gets more complicated and there is more than one region of velocity where the space charge can show enhancement, until at  $m=0.9$ , the optimum fringe velocity shifts to a lower value.

These simulations therefore agree with the main points of Brost's results.

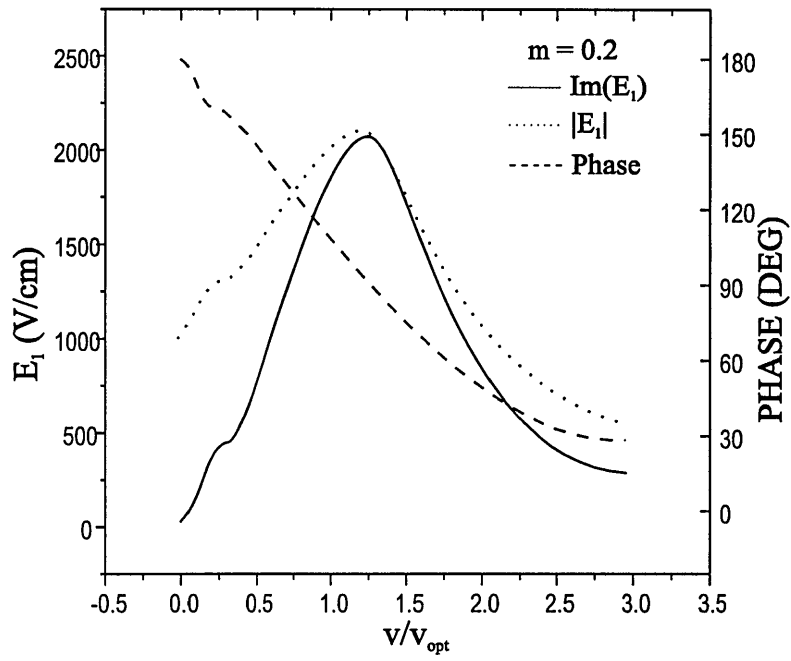


Fig. 3.3 (a)

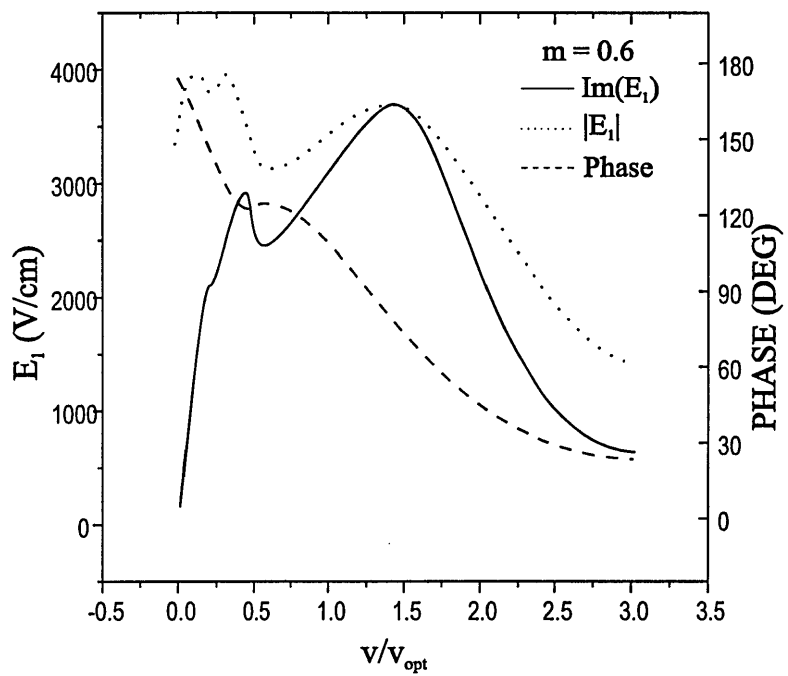


Fig. 3.3 (b)

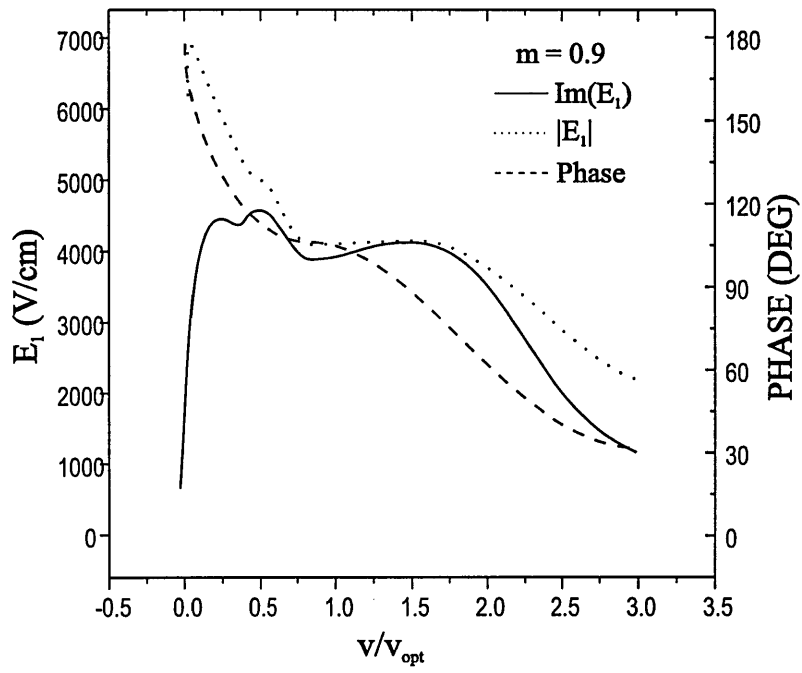


Fig. 3.3 (c)

Fig. 3.3 (a - c) Modulus, imaginary part and phase of the fundamental component of the space charge field at different modulations, (Brost, 1994)

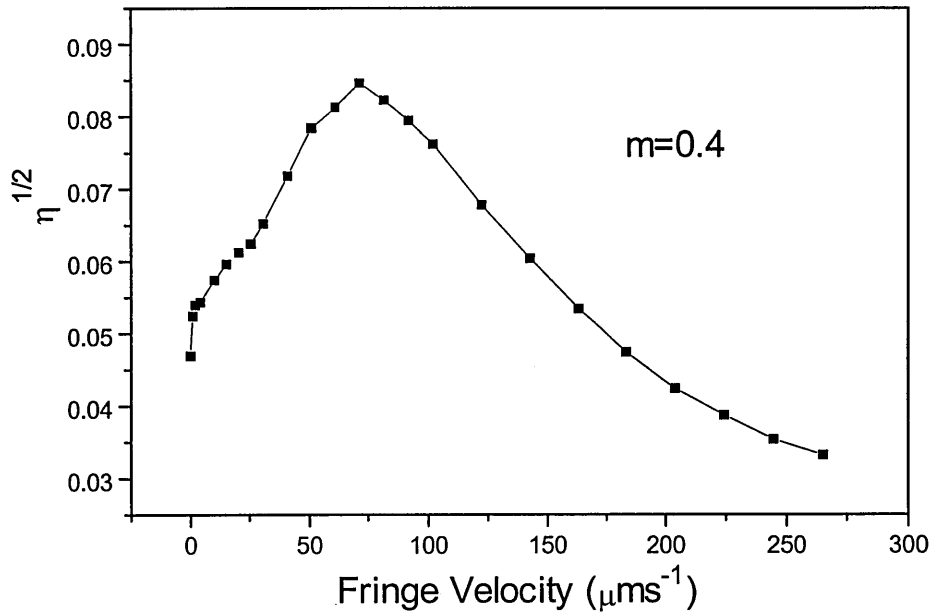


Fig. 3.4 (a)



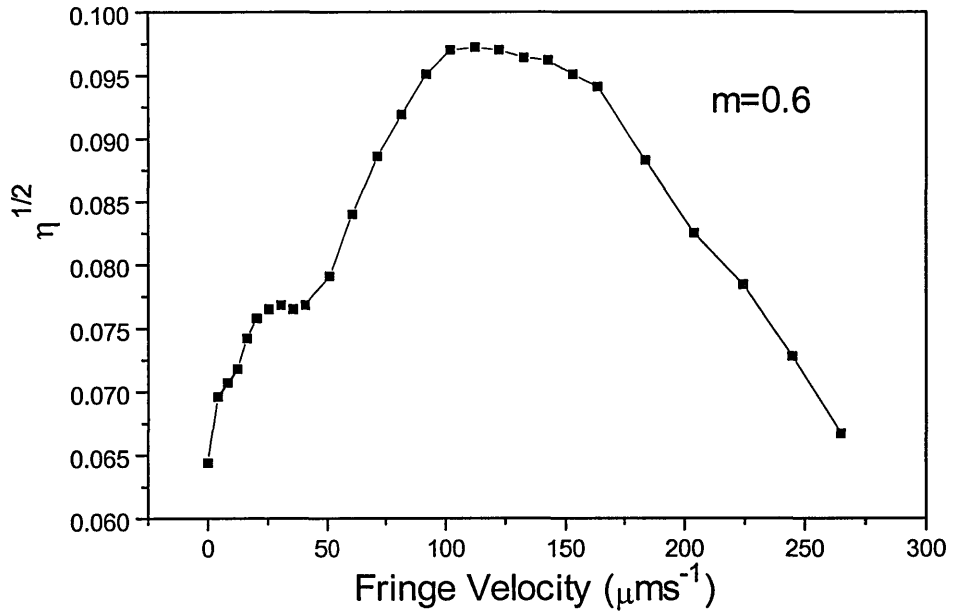


Fig. 3.4 (b)

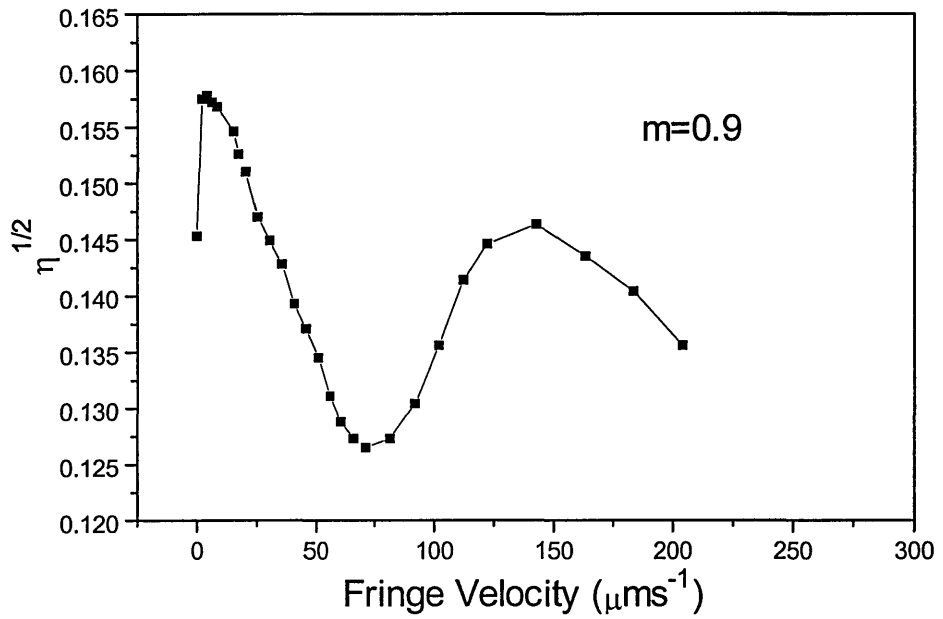


Fig. 3.4 (c)

Fig. 3.4 (a -c) Experimental results showing the square root of the diffraction efficiency at a range of modulations.

The results for the modulus of the space charge field were verified experimentally, during the course of this work using the setup shown in Fig 3.5. The writing beams are incident at the appropriate angle for a grating spacing of  $20\mu\text{m}$ , the

relative intensities of the writing beams may be varied using the combination of a half-wave plate and polarising beam-splitter. The velocity of the interference grating,  $v_g$ , is determined by

$$v_g = \frac{\Omega}{K} = \frac{2\pi}{\lambda K} \frac{v_m}{\cos \phi}, \quad (3.41)$$

where  $\Omega$  is the detuning frequency,  $\lambda$  is the Argon ion wavelength (=514nm),  $v_m$  is the mirror velocity, and

$$\phi = \frac{\pi/2 + \theta}{2}, \quad (3.42)$$

is the incident angle of the beam on the piezomirror, (Physik Instrumente, model PZ47E). The signal generator sent a sawtooth voltage to the piezomirror's control unit which analysed a signal from a position sensor on the piezo to ensure linear expansion to within 0.1%. The 'fly-back' from the sawtooth voltage will disrupt the formation of the space charge field but for these experiments the grating formation time of 10's of milliseconds is sufficiently short compared to the time of the ramped voltage for observations not to be affected. The He Ne beam was diffracted from the refractive index grating and its intensity measured using a Newport optical power meter (Model 840) with wavelength selection.

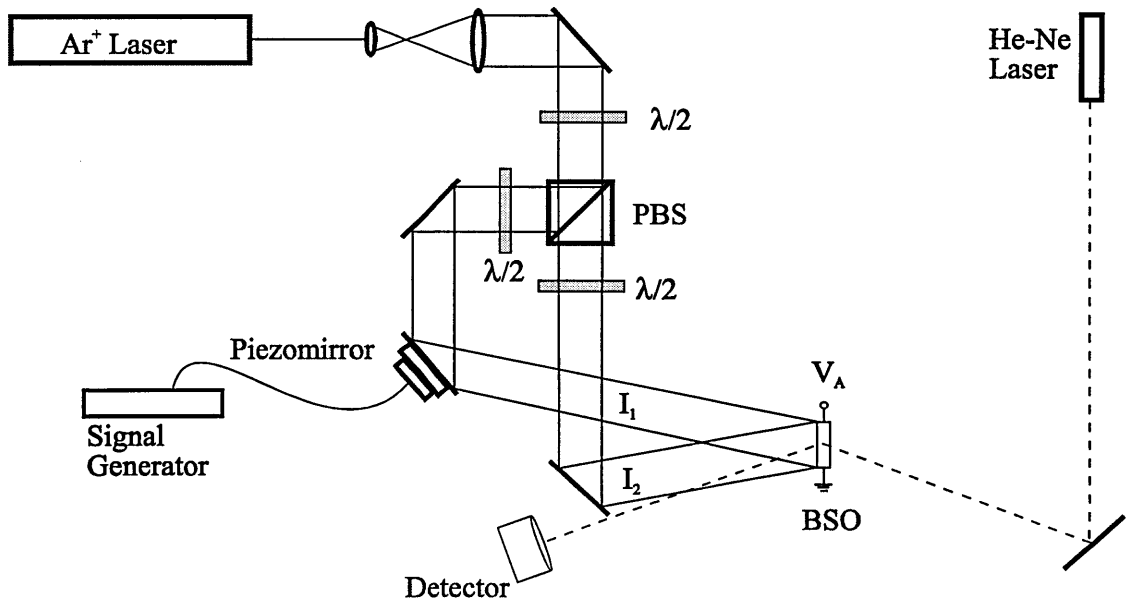


**Fig. 3.5** Schematic diagram of the experimental arrangement for two-wave mixing experiments with moving gratings.

PBS, beam splitter;  $\lambda/2$ , half wave plate.

Looking at Eq's (2.45) and (2.56) it can be seen that the modulus of the space charge field is proportional to the square root of the diffraction efficiency. Fig. 3.4 shows experimental results for the variation of the square root of the diffraction efficiency with grating velocity, for comparison with Brost's numerical predictions with high and lower intensity modulations. The crystal used for these experiments is the same characterised for orientation earlier, and is used in the four-wave mixing orientation. The lowest modulation used was  $m=0.4$ , this was because the diffracted intensities were too low for reliable measurement below this point.

The experimental results of Fig. 3.4 verify the predictions made by Brost's numerical model. At the low intensity modulation of  $m=0.4$ , there is a single region of enhancement at the so-called fundamental grating velocity. As the modulation increases a low velocity enhancement of the diffraction efficiency is observed, becoming greater than the fundamental enhancement somewhere between  $m=0.6$  and  $m=0.9$ . This low velocity enhancement is due to the increased strength of the higher harmonics of the space charge field at high modulations. These higher harmonics will have slower resonant frequencies than the fundamental. Similar diffraction efficiency

measurements with moving gratings have been performed by Wang (1995); the experiments are repeated here for comparison with the high modulation four wave mixing case in the next section.

Using Eq. (3.34), the fundamental velocity for energy transfer and diffraction efficiency at low modulations can be calculated as

$$v_{opt} = \frac{1}{K\tau_d} \frac{E_M}{E_0} = \frac{1}{K} \frac{e\mu s I_0 N_D}{\epsilon_S \epsilon_0 \gamma_R N_A} \frac{\gamma_R N_A}{\mu K E_0}, \quad (3.43)$$

which, using the parameter values given in Section 2.1, gives  $65\mu\text{ms}^{-1}$  for the total incident intensity of  $5\text{mWcm}^{-2}$  used in these experiments. This can be seen to be close to the optimum velocity for the  $m = 0.4$  case, which may be said to approximately comply with the linear in  $m$  model. When BSO is to be used as the recording medium in a correlation system, the diffracted intensity becomes important since a correlation peak threshold is needed to signify recognition. The fact that energy transfer and diffraction efficiency are optimised at the same grating velocity can cause random fluctuations in the diffracted intensity due to energy transfer being sensitive to environmental disturbances such as air flow and fluctuations in the applied field. The increased diffraction efficiency at low grating velocities, away from the optimum energy-transfer velocity, will therefore improve both the signal-to-noise ratio and the stability of correlation peaks. It was noticed during these experiments, and elsewhere, that the moving gratings had the effect of suppressing random diffraction efficiency fluctuations. It has been suggested, (Wang, 1994) that this is due to transient energy transfer being suppressed due to the reduction of the phase transfer mentioned in Section 3.1.

As the modulation increases, the low velocity enhancement predicted by Brost and Solymar appears and grows until, between  $m=0.6$  and  $m=0.9$ , the modulus of the space charge field becomes largest at the low velocity. The higher optimum velocity also falls slightly as the modulation decreases. There are circumstance where the difference in optimum grating velocity at high and low modulations could be a disadvantage, for example if images to be used in a correlation experiment contain a broad range of amplitudes, a fixed grating velocity would only be suitable for a

limited range of modulations. It has been shown that diffraction efficiency can be enhanced for all modulations at the higher grating velocity when a white light optical bias is applied, (Wang, 1996). With no optical bias, the diffraction for higher modulations falls as the grating velocity increases above the ‘slow’ optimum, the optical bias effectively reduces the intensity modulation and a fixed grating velocity can provide enhancement for a broad range of modulations.

Fig. 3.7 shows the variation of the square root of diffraction efficiency with grating velocity for different total incident intensities and a modulation of  $m = 1$ . As the incident intensity decreases, the optimum high velocity falls, though not in the linear fashion predicted by Eq. (3.45) since this equation only applies in the linear, small  $m$  regime. It is also interesting to note that the optimum low velocity also falls as the intensity is reduced

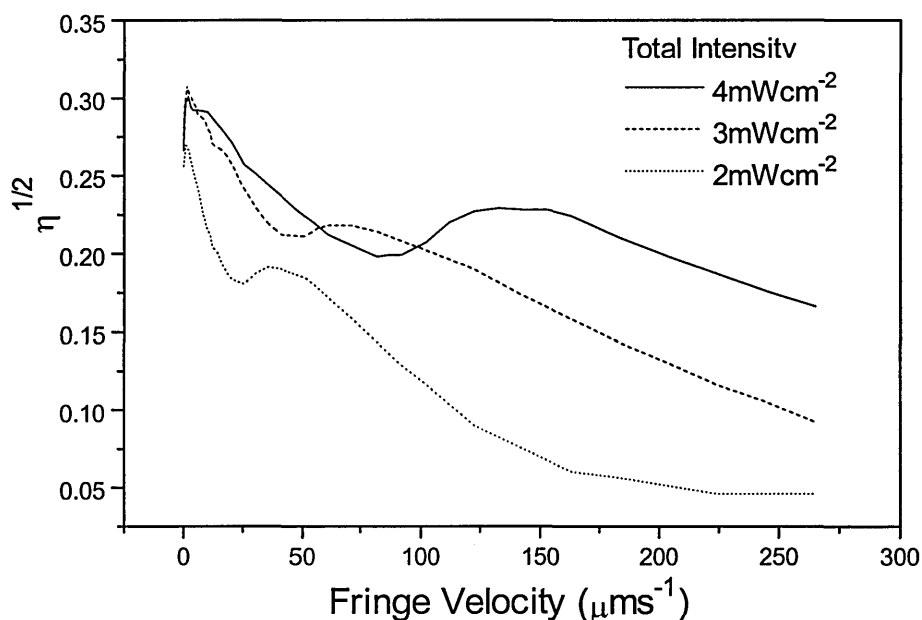
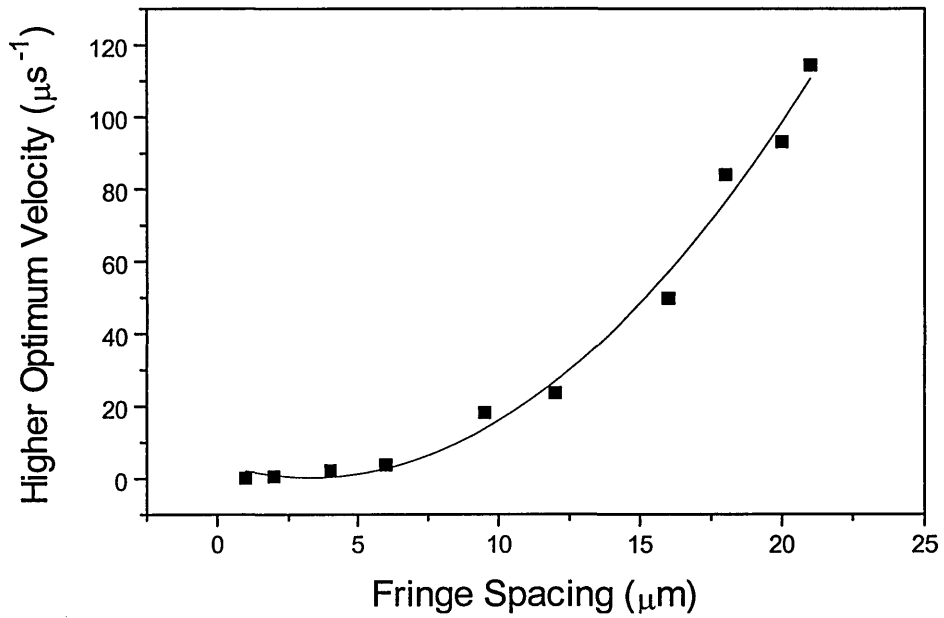


Fig. 3.7 Experimental diffraction results for different total intensities at  $m=1$ .

Fig. 3.8 shows the variation of the higher optimum (low  $m$ ) velocity with fringe spacing. Eq. (3.45) predicts that the optimum velocity will vary quadratically with fringe spacing which is seen to be the case.



**Fig. 3.8** Variation of diffraction efficiency and optimum velocity with fringe spacing at  $m=0.4$ , the line is a quadratic fit.

The theory and experimental results presented in this section show how the enhancement due to moving gratings has a nonlinear form at high modulations. The validity of the linear in  $m$  theory has been verified and experimental results agree with Brost's numerical predictions. The next section will continue the investigation of the moving grating technique in the field of phase-conjugate reflectivity through photorefractive four-wave mixing.

### 3.4 Four-Wave Mixing

Yariv and Pepper, (Yariv, 1977) first applied the formalism of nonlinear optics to the study of four-wave mixing (4WM) in nonlinear media, and predicted that amplified (phase-conjugate) reflection, amplified transmission, and mirrorless self-oscillation were possible. These phenomena have since been observed in several experiments, (Cronin-Golomb, 1984; Huignard, 1979).

One incentive behind four-wave mixing experiments in photorefractive media is the ability to produce the phase-conjugate of a signal beam. This is a useful technique with applications such as correcting aberrations in a laser cavity, or arising from transmission through the atmosphere; it also has applications in image processing and correlation. Phase conjugate reflectivity via four-wave mixing in a photorefractive BSO crystal was first demonstrated by Huignard *et al* (1979). 4WM architectures have also been used to achieve correlation, (White, 1980; Khoury, 1994 B; Asimellis, 1995). One such system, (Asimellis, 1997) applies an incoherent joint power spectrum to partially erase the fringe structure in a standard 4WM configuration, thus modifying the resultant phase conjugate reflected beam. This modified beam contains correlation information and the degree of nonlinearity in the recording process may be controlled by the ratio of the writing and erasure intensities, a useful technique for improving correlation performance (Javidi, 1989), as will be discussed in Chapter 6. Phase conjugate reflectivity by 4WM, its relationship to beam ratios and the possible enhancement of such processes by the moving grating technique are therefore worthy of study.

In this section, the coupled wave equations derived for the case of two-wave mixing in Section 3.1 will be extended to the case where there are four waves interacting within the photorefractive medium. The coupled equations of such a complex system would necessarily be very complicated so several simplifying assumptions are made to extract useful information.

The basic configuration for phase conjugation via four-wave mixing is shown in Fig. 3.9. With the two counter-propagating plane-wave pump beams, beams 1 and 2 illuminating the crystal, any additional signal beam (i.e. beam 4) which is incident on the crystal will be phase conjugated and retroreflected (beam 3). The signal beam

and pump beam 1 may be thought of as producing a dielectric grating which will diffract beam 2. Because beams 1 and 2 are collinear, the diffracted beam will be an exact copy of the signal beam travelling in the opposite direction, hence it is the phase conjugate.

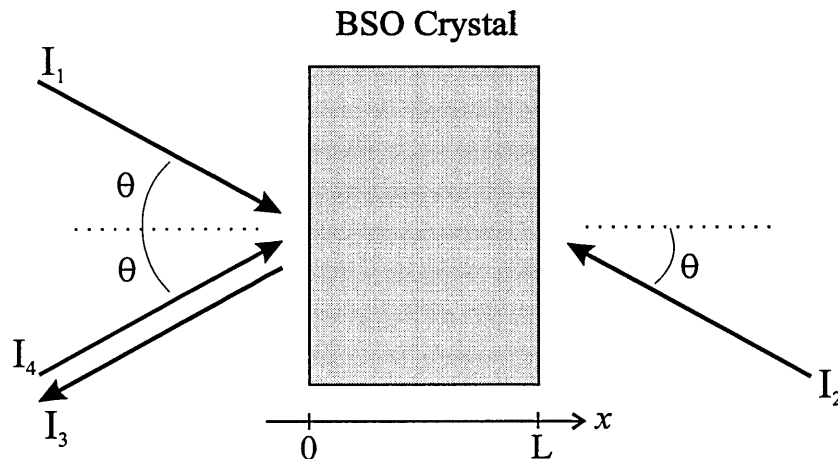


**Fig. 3.9** Generation of a phase conjugate wave via four-wave mixing.

The four beams will interact with one another by setting up four diffraction gratings: one transmission grating, one reflection grating, and two gratings of period  $\lambda/2$  created by the pairs of counterpropagating beams. The propagation directions come in two oppositely directed pairs, given by the wave vectors  $\mathbf{k}_1 = -\mathbf{k}_2$  and  $\mathbf{k}_3 = -\mathbf{k}_4$ , whereas the relative direction of  $\mathbf{k}_3$  and  $\mathbf{k}_1$  is arbitrary.

A complete treatment of the wave interactions involved in the four-wave mixing process would be very difficult. The problem is greatly simplified by using the one-grating approximation (Fischer, 1981), in which it is assumed that only one of the four gratings formed gives rise to strong coupling; in this case the transmission grating created by beam pairs 1 and 4 and also 2 and 3, which have the same grating vector and add coherently. This grating can be made to dominate in many practical situations by the choice of directions and polarisation of the four beams, and the direction of an applied field, relative to the crystal axes. In this case, if absorption and optical activity are neglected then the coupled equations for the amplitudes of the four waves simplify to



$$\frac{d\mathcal{E}_1}{dx} = j\kappa E_w g \mathcal{E}_4, \quad (3.44)$$

$$\frac{d\mathcal{E}_2^*}{dx} = j\kappa E_w g \mathcal{E}_3^*, \quad (3.45)$$

$$\frac{d\mathcal{E}_3}{dx} = -j\kappa E_w g \mathcal{E}_2, \quad (3.46)$$

$$\frac{d\mathcal{E}_4^*}{dx} = -j\kappa E_w g \mathcal{E}_1^*, \quad (3.47)$$

where

$$g = \frac{\mathcal{E}_1 \mathcal{E}_4^* + \mathcal{E}_2^* \mathcal{E}_3}{I_o} \quad \text{and} \quad \kappa = \frac{\pi r_{41} n_0^3}{\lambda \cos \theta}, \quad (3.49)$$

and  $E_w$  is the normalised space charge field, Eq. (3.3). We can simplify the problem further by assuming that the pump beams are undepleted, i.e.  $I_1, I_2 \gg I_3, I_4$ , (Fischer, 1981) This assumption sets  $\mathcal{E}_1$  and  $\mathcal{E}_2$  constant so Eqs. (3.46) and (3.47) can be integrated; using the boundary conditions  $\mathcal{E}_3(L)=0$  and  $\mathcal{E}_4^*(0)$  is known, the solutions for the amplitudes of beams 3 and 4 are, (Fischer, 1981; Solymar, 1996, p257)

$$\mathcal{E}_3(x) = \mathcal{E}_4^*(0) \frac{\mathcal{E}_1}{\mathcal{E}_2} \left[ \frac{\exp(-j\kappa E_w(x-L)) - 1}{r^{-1} \exp(j\kappa E_w L) + 1} \right], \quad (3.50)$$

$$\mathcal{E}_4^*(x) = \mathcal{E}_4^*(0) \left[ \frac{r^{-1} \exp(-j\kappa E_w(x-L)) + 1}{r^{-1} \exp(j\kappa E_w L) + 1} \right], \quad (3.51)$$

where  $r$  is the ratio of the pump intensities  $I_2/I_1$ . These solutions show that the amplitude of beam 3 is directly proportional to the phase conjugate of beam 4. Also Bragg matching conditions require that if beams 1 and 2 are counterpropagating then so are beams 3 and 4, therefore beam 3 is the phase conjugate of beam 4.

The conjugate reflectivity,  $R_c$  is defined as the ratio of beams 3 and 4 at  $x=0$ , from Eq's (3.50) and (3.51) it is given by (Fischer, 1981)

$$R_c = \frac{I_3(0)}{I_4(0)} = \left| \frac{\sinh\left(\frac{-j\kappa E_w L}{2}\right)}{\cosh\left(\frac{-j\kappa E_w L}{2} + \frac{\ln r}{2}\right)} \right|^2. \quad (3.52)$$

The conjugate reflectivity is therefore dependent on the intensity independent term  $\kappa E_w$ , and the pump ratio  $r$  only. The maximum reflectivity occurs when

$$\kappa \text{Im}(E_w)L = \ln(r), \quad (3.53)$$

giving a maximum reflectivity of

$$R_{\max} = \left| \frac{\sinh\left(\frac{-j\kappa E_w L}{2}\right)}{\cos\left(\frac{-\kappa \text{Re}(E_w)L}{2}\right)} \right|^2. \quad (3.54)$$

Looking at the case of a purely imaginary space charge field (i.e. phase change,  $\Phi=\pi/2$ , applicable to diffusion recording), for pump beams of equal intensity ( $r=1$ ), the reflectivity simplifies to,

$$R_c = \tanh^2\left(\kappa |E_w| \frac{L}{2}\right). \quad (3.55)$$

This can never exceed unity; for reflectivity greater than unity (gain) there must be assymmetric pumping.

By comparison if the response of the material is local, (i.e. there is no phase difference between the light interference pattern and the grating) then the optimum reflectivity always occurs for equal pumping, and reflectivities exceeding 100% are

theoretically possible. It may be seen (Fischer, 1981) that the optimum reflectivity occurs when

$$\kappa \operatorname{Im}(E_w)L = \ln(r), \quad (3.56)$$

giving a maximum reflectivity of (Solymar, 1996, p258)

$$R_{c,\max} = \left| \frac{\sinh\left(\frac{-j\kappa E_w L}{2}\right)}{\cos\left(\frac{-\kappa \operatorname{Re}(E_w)L}{2}\right)} \right|^2. \quad (3.57)$$

It is interesting to note that according to Eq. (3.57) it is possible to have infinite reflectivity or so-called self oscillation. What this means is that an output beam can be generated without any input beam. The condition for self-oscillation is

$$\operatorname{Im}(E_w)L = \ln(r) \quad \text{and} \quad k \operatorname{Re}(E_w)L = \pm\pi, \pm3\pi, \dots \quad (3.58)$$

Note that this rules out self-oscillation for  $\Phi=90^\circ$ . Therefore it is necessary to change the phase shift by either applying an electric field or detuning one of the pump beams.

The next section gives details of experiments which were performed to investigate the behaviour of the phase conjugate reflectivity with an applied field and moving gratings (non-degenerate 4WM). Measurements were made at a variety of beam ratios, firstly to confirm the behaviour predicted by the undepleted pumps approximation and then investigate the behaviour when this approximation no longer applies. The beam ratios used are defined as the pump beam ratio,  $r$  defined earlier, and the probe beam ratio,  $\beta$  defined as:

$$\beta = \frac{I_1}{I_4}. \quad (3.59)$$

### 3.5 Four-wave Mixing with Moving Gratings

Phase conjugation by non-degenerate four-wave mixing in BSO has been studied by Rajbenbach (1984), Peterson (1991), Uesu (1994), and others. Yeh (1993, p167) states that the coupled equations for the four amplitudes, Eqs. (3.44) - (3.47), are still valid when considering moving gratings provided a modified coupling constant, which takes into account the characteristic time constant of the grating, is used. Rajbenbach has investigated experimentally the phase-conjugate reflectivity in the regime where the non-depleted pumps approximation is applicable. It was found that, at optimum detuning of pump beam  $I_1$ , there was an optimum pump beam ratio for each probe ratio, and the reflectivity increased as the probe ratio increased, it was also noted that the optimum pump ratio shifted to lower values as the probe ratio increased.

Uesu and Yoshihara (Uesu, 1994), working with BSO, have shown experimentally that the optimum grating velocity is the same for two wave mixing with a beam ratio of  $r=160$  as it is for four-wave mixing with a pump beam ratio of  $r=2$ , implying that the optimum grating velocity for phase conjugation also induces a  $\pi/2$  phase difference between the transmission grating and the intensity interference pattern, though they do not give a probe ratio so it is not certain that the undepleted requirement is fulfilled.

Experiments investigating the relationships between phase conjugate reflectivity via 4WM, beam ratios and grating velocity were carried out as part of this work. Results were obtained for the separate regimes where the undepleted pump beams approximation does and does not apply. The experiment setup during the course of this work and used to achieve these results is shown in Fig. 3.10.

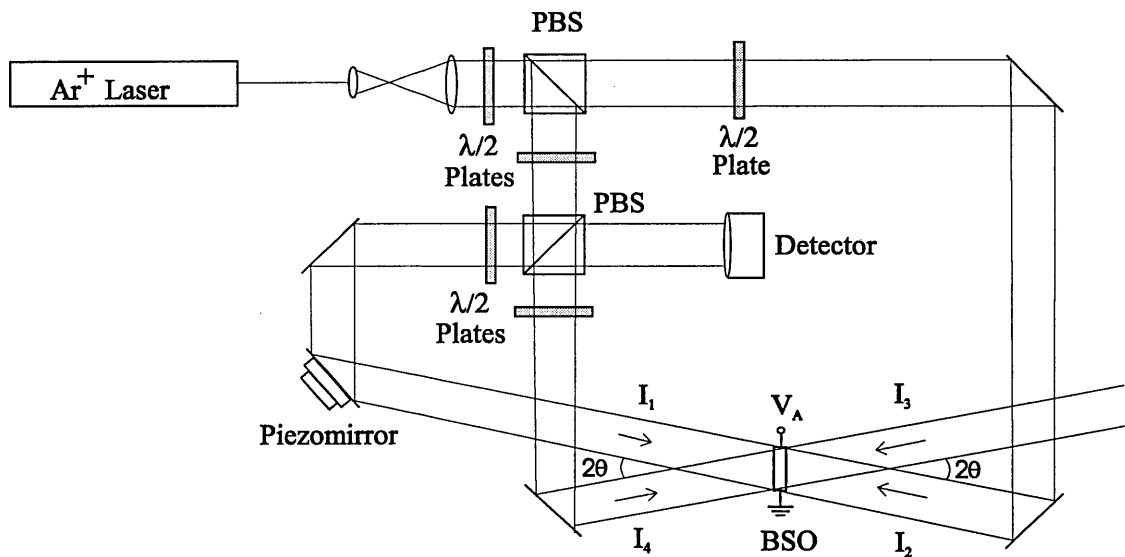


**Fig. 3.10** Experimental setup used to measure the phase-conjugate reflectivity via non-degenerate four-wave mixing. PBS is a polarising beam-splitter,  $V_A$  is the applied voltage, and  $\lambda/2$  is a half wave plate.

An applied field of  $5.5 \text{ kVcm}^{-1}$  was used for these experiments, the piezomirror causes a detuning of pump beam 1 as described in Section 3.3. The angle  $\theta$  was chosen to give a grating spacing of  $20\mu\text{m}$ , and a total incident intensity of  $4\text{mWcm}^{-2}$  was used. The same BSO crystal described in Section 3.1 was used in these experiments.

Looking first at the undepleted pumps case, Fig. 3.11 shows experimental conjugate reflectivity results from non-degenerate 4WM for a probe ratio of  $\beta=32$ . The intensities of all incident beams were adjusted, by means of the polarising beam splitter, for each pump ratio to ensure a constant total intensity.

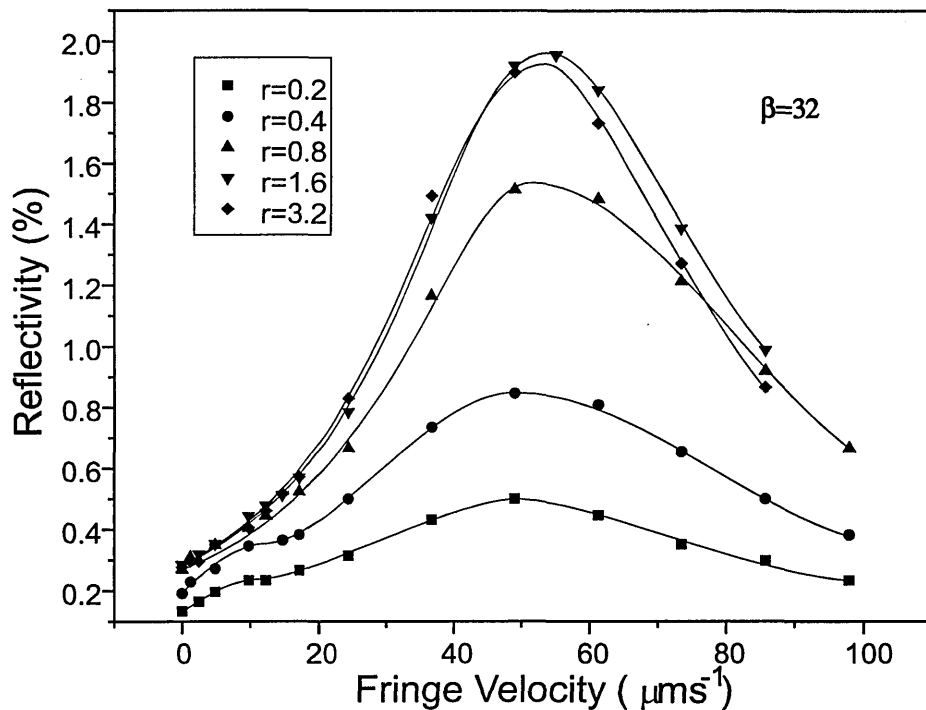


Fig. 3.11 Variation of phase-conjugate reflectivity with fringe velocity at different pump ratios in the undepleted regime.

Fig. 3.11 plots the experimental variation in phase conjugate reflectivity as the fringe velocity is altered; the reflectivity is given by the ratio of the reflected beam  $I_3$  to the incident probe intensity,  $I_4$ . These measurements are similar to those achieved by Rajbenbach *et al* (Rajbenbach, 1984); there is an optimum grating velocity at approximately  $50\mu\text{ms}^{-1}$ , and the reflectivity is optimised for a pump ratio  $r$  between  $r=1.6$  and  $r=3.2$ . It is also apparent that there is a slight shoulder to the reflectivity curve at small velocities and low pump ratios, which will be looked at more closely in Fig. 3.16.

The reflectivity dependence on pump and probe ratios is investigated further using the results shown in Fig's. 3.12 and 3.13. These figures show how the conjugate reflectivity changes at the optimum grating velocity, and for stationary gratings respectively as the pump and probe ratios vary, only some of stationary data are shown for clarity. The results presented in these graphs cover a large range of beam ratios and therefore the undepleted pumps approximation does not always apply.

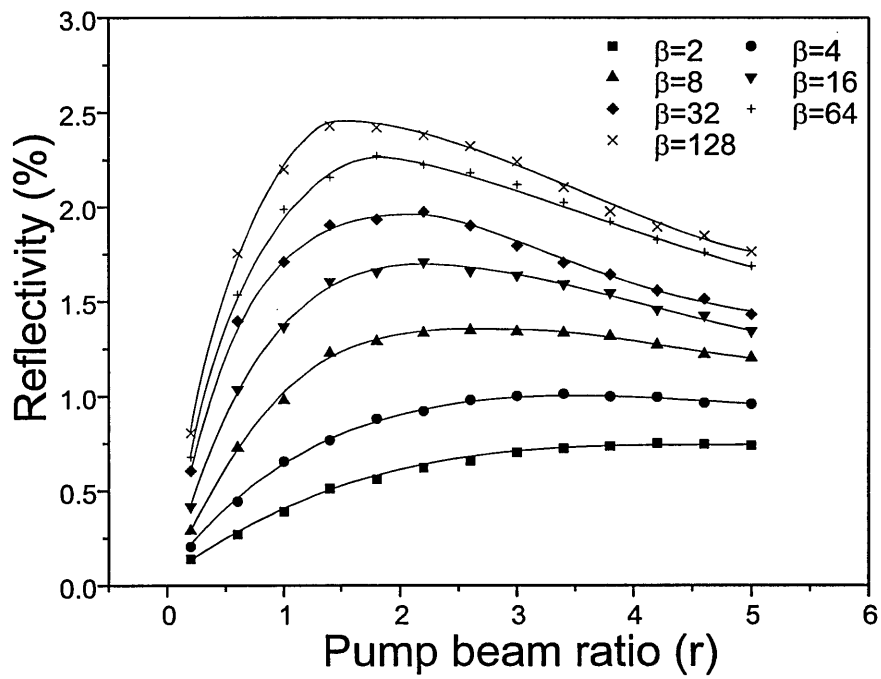


Fig. 3.12 Conjugate reflectivities at the optimum fringe velocity for a range of pump and probe ratios.

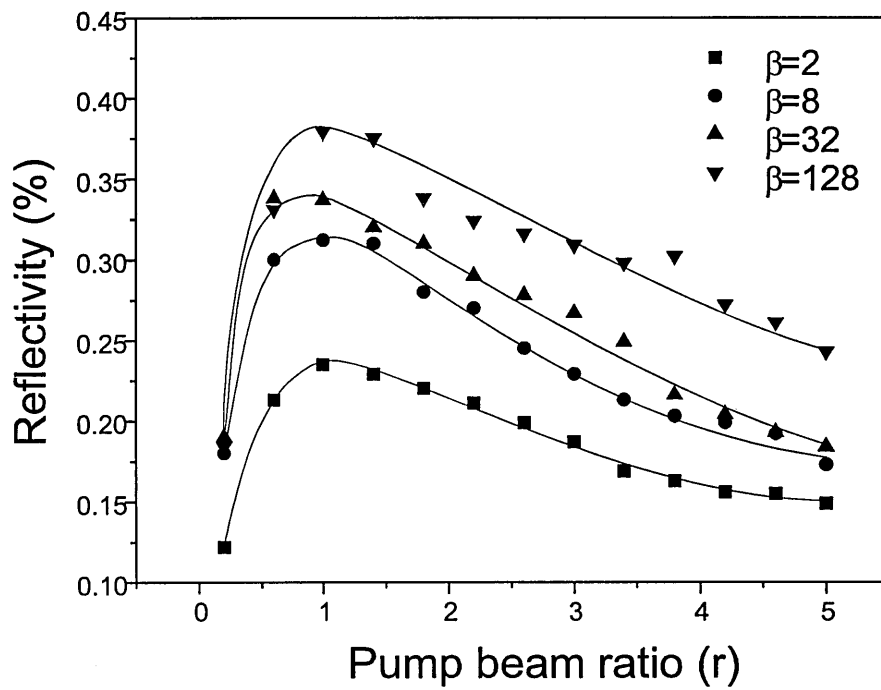
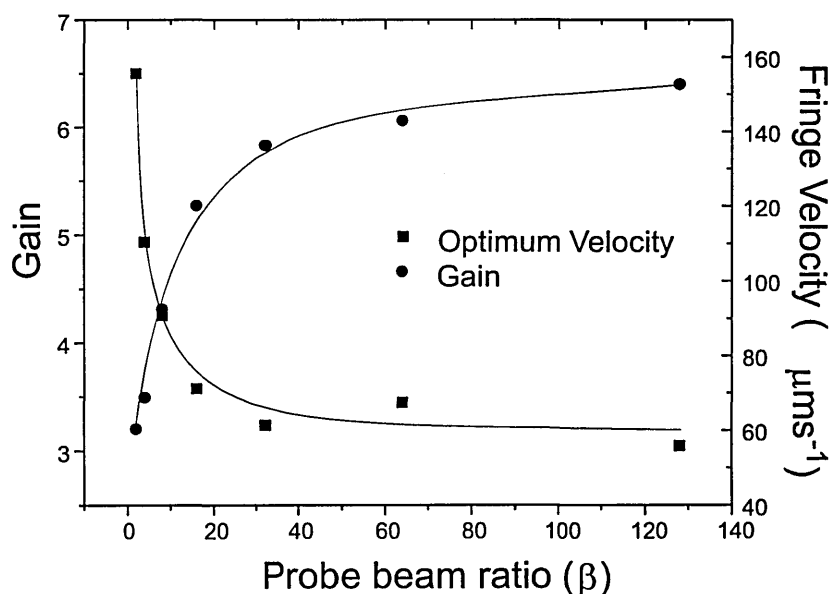


Fig. 3.13 Conjugate reflectivities for stationary gratings for a range of pump and probe ratios.

These reflectivity graphs show that the optimum stationary pump ratio is constant at  $r \approx 1$ , as predicted by the undepleted theory with a local response, i.e. there is no phase difference between the interference pattern and the dielectric grating, due to the applied field. The optimum pump ratio for the moving gratings, Fig. 3.12 gradually shifts to lower values and the peak becomes less broad as the probe ratio increases, in agreement with Rajbenbach, (1984). The stationary reflectivity, Fig. 3.13 increases with  $\beta$  until  $\beta=64$ , above which it remains roughly constant. The moving reflectivity is still increasing at  $\beta=128$ , though the rate of increase is slowing as is seen in Fig. 3.14. This graph shows the gain in reflectivity due to moving gratings and optimum velocity versus probe ratio. Each gain point is the ratio of optimum moving to optimum stationary reflectivity at a particular probe ratio. The gain due to moving gratings is seen to increase sharply then level out at higher values. The optimum velocity falls sharply as  $\beta$  increases before levelling off at approximately  $60\mu\text{ms}^{-1}$ . This would have positive implications when the phase-conjugate of an image with a range of amplitudes is sought since the optimum velocity would apply across a broad range of probe ratios. Therefore the reflectivity and hence the signal to noise ratio in correlation experiments could be improved by using the moving grating technique.



**Fig3.14** Gain due to moving gratings, and optimum velocity as a function of probe ratio.



When the undepleted pumps assumption no longer applies, it becomes harder to find an analytical solution which yields any useful information, in this case numerical solutions have been attempted. Numerical simulations (Cronin-Golomb, 1984), and experiments (Kwong, 1985) have been carried out for the depleted pumps case with stationary gratings. These results show that there is an optimum probe ratio at high pump ratios; but at lower pump ratios, the case in these experiments, the reflectivity increases to a maximum as the probe beam weakens. The experimental results presented here show that, when the optimum grating velocity is used, this is also the case up to the limit of the weakest probe beam used in these experiments.

The numerical results of Cronin-Golomb *et al* are reproduced below in Fig. 3.15. Note that the main surface only has been reproduced; this corresponds to the case where the phase-conjugate wave (PCW) is generated so that the grating formed between itself and beam 2 is in phase with the interference pattern formed between the forward going beams 1 and 4, i.e. it is assumed that the grating is made up of both pairs of transmission gratings in phase.

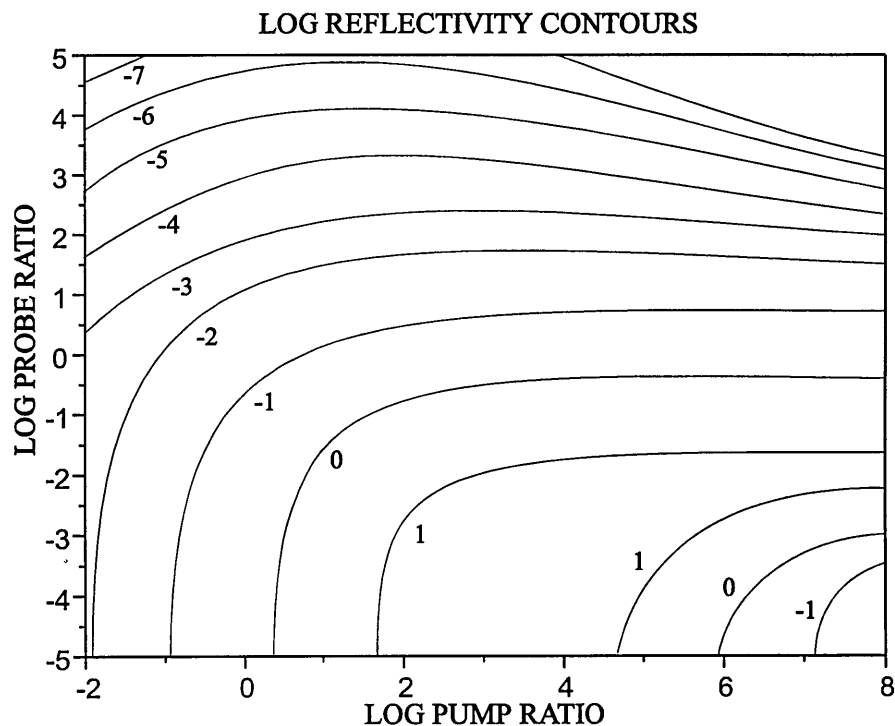


**Fig. 3.15** Numerical results of Cronin-Golomb *et al* predicting the conjugate reflectivity as a function of beam ratios.

Note that Cronin-Golomb *et al* define the probe ratio,  $q$  slightly differently as:

$$\ln\{q\} = \ln\left\{\frac{I_4(0)}{I_1(0) + I_2(L)}\right\}, \quad (3.60)$$

whilst the pump beam ratio is as given earlier. Given the range of beam ratios used in the earlier experiments, the logarithms of the ranges of these parameters thus become

$$\begin{aligned} \beta &= 128 \text{ to } 1 & \text{and} & & r &= 0.2 \text{ to } 5 \\ \Rightarrow \ln(q) &= -6.6 \text{ to } -0.18 & \text{and} & & \ln(r) &= -1.6 \text{ to } 1.6 \end{aligned} \quad (3.61)$$

The results of Fig. 3.12 show that as  $\beta$  increases the optimum pump ratio decreases, this would seem to show that applying the moving grating, has the same effect as shifting the pump ratio to a higher range, to above the optimum  $r$ , given by Cronin-Golomb, rather than below it.

Another consideration in producing the phase conjugate wave, apart from the conjugate reflectivity, is the quality of the conjugate phase. Kwong *et al* (1986) have shown that for undepleted and depleted pumps, the phase of the phase-conjugate wave, (beam 3) is given by

$$\psi_3(0) = \psi_1(0) + \psi_2(L) - \psi_4(0), \quad (3.62)$$

when there is a  $\pi/2$  phase shift between the refractive index grating and the light interference fringes, which is the case for no external field or appropriate detuning. More generally,  $\psi_3(0)$  is a function of a complex coupling constant and the pump ratio. Kwong *et al* also give numerically calculated curves of  $\psi_3$  which show that the effect of changing the pump ratio on the system is similar to that of changing the phase difference between the interference pattern and the dielectric grating,  $\Phi$ . This agrees with the earlier, experimental result that a moving grating, and the phase change this induces, has the same effect as an increase in pump ratio.

It is interesting to note from Kwong's calculations that, by an appropriate decrease in  $\Phi$ , or increase in  $r$ , the phase of the PCW,  $\psi_3$  can be made approximately independent of probe ratio. This could again be of importance when the probe beam is carrying information and hence likely to vary spatially in intensity. By making the conjugate phase independent of probe ratio, there will be no phase variation across the conjugate wavefront induced by different probe ratios. If such phase variation did occur, this could degrade the quality of correlation information which relies on a Fourier transform of the conjugate wave.

Looking more closely at the case where the undepleted pumps assumption is no longer valid, i.e. the probe beam intensity is comparable with the pump beam; or, in the terminology of the previous chapter, the high modulation regime. Fig. 3.16 shows the variation of the conjugate reflectivity with grating velocity as the probe ratio is increased from unity for fixed  $r=0.2$ . The following figure (Fig. 3.17) shows the reflectivity variation for fixed  $\beta=1$  as the pump ratio is increased.

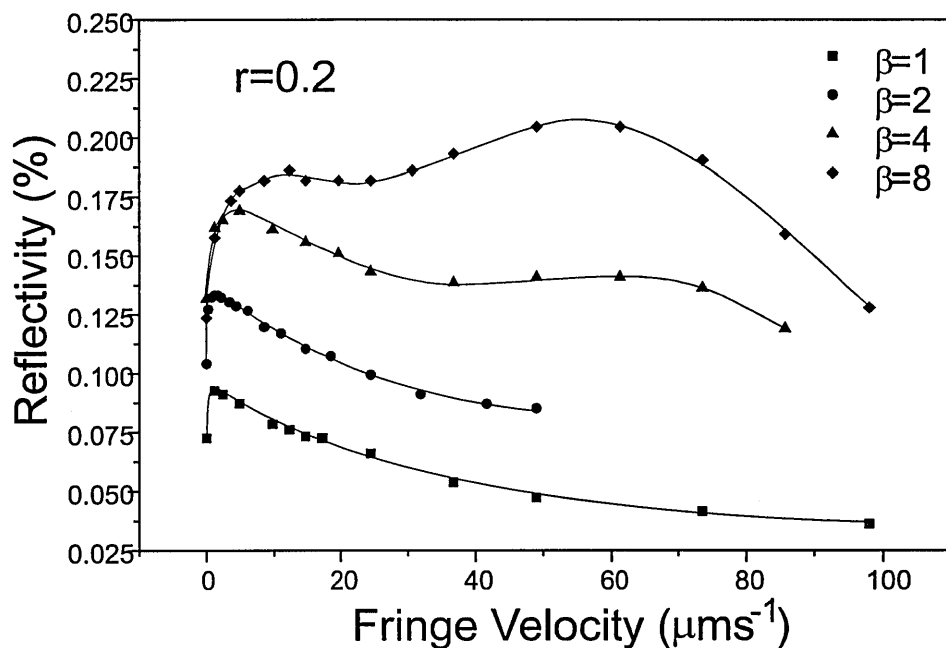


**Fig. 3.16** Reflectivity variation with fringe velocity for a constant pump ratio as the probe increases from unity.

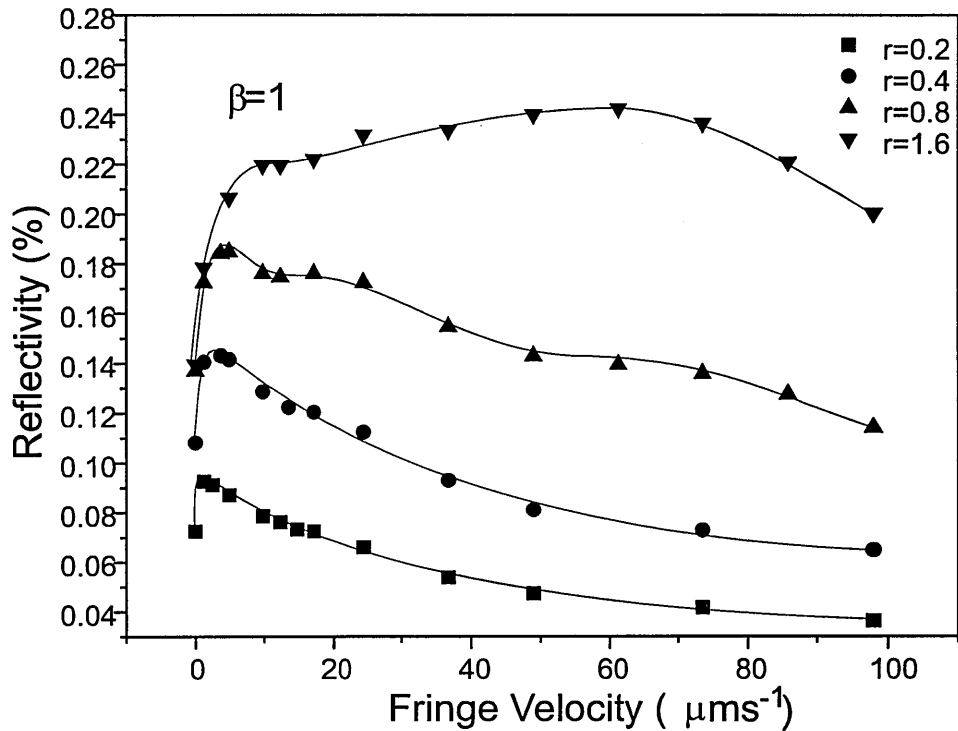


**Fig. 3.17** Reflectivity variation with fringe velocity for a constant probe ratio as the pump increases from low values.

These graphs show that there is a low velocity enhancement similar to that seen in the two-wave mixing case, again the low velocity enhancement is replaced by the higher velocity enhancement as the probe or pump ratio increases. The similarity of these two graphs shows that the effect of raising probe ratio is much the same as raising the pump ratio.

The experimental results have been presented in terms of the reflectivity for the purpose of comparing the influence of beam ratios and grating velocity, and initially the 2.5% reflectivity achieved with  $r = 1.5$  and  $\beta = 128$  (Fig. 3.12) would seem to outperform that of 0.1% achieved with  $r = 0.2$  and  $\beta = 1$  (Fig. 3.16). The object of the process is however to maximise the intensity of the phase conjugate beam. If the limited total input intensity ( $I_1 + I_2 + I_d$ ) is unity then the reflected phase conjugate intensities in these two cases, expressed as a percentage of the total input, are  $7.8 \times 10^{-3} \%$  and  $45 \times 10^{-3} \%$  respectively; the high probe ratio, low velocity case will therefore give a higher reflected intensity.

This section has demonstrated the relationship between grating velocity and phase conjugate reflectivity in 4WM experiments. The moving gratings enhance the reflectivity by altering the magnitude of the space charge field, and modifying the phase difference between the intensity interference pattern and the refractive index grating. The assumption of undepleted pumps has been shown to apply across a broad range of beam ratios with the predicted relationship between beam ratios and reflectivity. It is not until the probe beam is of a similar intensity to the pump beams that there is a significant departure from the predicted behaviour. In this case there is a low velocity moving grating enhancement, similar to that observed in the two-wave mixing case. To our knowledge this is the first time such a low velocity enhancement has been observed in 4WM experiments.

The phase quality of the reflected phase conjugate beam is also affected by the phase difference between the interference pattern and the dielectric grating. The moving grating technique could also provide a way to minimise phase deterioration. Correlation applications would therefore benefit from increased signal power and greater control of the quality of phase conjugation.

The wave mixing experiments in this chapter would have been improved if a greater laser power had been available. A greater range of beam ratios would have been possible and higher diffraction and reflection efficiencies would have improved the reliability of the results.

This chapter has looked at two of the mixing architectures used most often in processing experiments involving photorefractive crystals. The next chapter will introduce the mathematical analysis used to study optical processing before such a system is described in more detail later.

### Chapter 3: References

- Asimellis,G. Khoury,K. Kane,J. Woods,C 1995, 'Two-port photorefractive joint-transform correlator', *Opt. Lett.* **20**, No24, pp2517-2519
- Asimellis,G. Khoury,J. Woods,C.L. 1997, 'Experimental demonstration of the holographic incoherent-erasure joint-transform correlator', *Opt. Eng.* **36**, No.9, pp2392-2399
- Au,L.B. Solymar,L. 1988, 'Space-charge field in photorefractive materials at high modulation', *Opt. Lett.* **13**, No8, pp660-662
- Au,L.B. Solymar,L. 1990, 'Higher harmonic gratings in photorefractive materials at large modulation with moving fringes', *J. Opt. Soc. Am. A.* **7**, No8, pp1554-1561
- Brost,G. Magde,K.M. Larkin,J.J. Harris,M.T. 1994, 'Modulation dependence of the photorefractive response with moving gratings: numerical analysis and experiment', *J. Opt. Soc. Am. B.* **11**, No9, pp1764-1772
- Cronin-Golomb,M. Fischer,B. White,J.O. Yariv,A. 1984, 'Theory and applications of four-wave mixing in photorefractive media', *IEEE J. Quant. Electr.* **20**, No1, pp12-30
- Fischer,B. Cronin-Golomb,M. White,J.O. Yariv,A. 1981, 'Amplified reflection, transmission, and self-oscillation in real-time holography', *Opt. Lett.* **6**, No11, pp519-521
- Foote,P.D. 1987, 'Optically induced anisotropic light diffraction in photorefractive crystals', *PhD thesis*, University of London, p321
- Huignard,J.P. Herriau,J.P. Aubourg,P. Spitz,E. 1979, 'Phase-conjugate wavefront generation via real-time holography in BSO crystals', *Opt. Lett.* **4**, No1, pp21-23
- Huignard,J.P. Marrakchi,A. 1981 A, 'Two-wave mixing and energy transfer in BSO crystals: application to image amplification and vibration analysis', *Opt. Lett.* **6**, No12, pp622-624

- Huignard, J.P. Marrakchi, A. 1981 B, 'Coherent signal beam amplification in two-wave mixing experiments with photorefractive BSO crystals', *Opt. Comm.* **38**, No4, pp249-254
- Javidi, B. 1989, 'Nonlinear joint power spectrum based optical correlator', *App. Opt.* **28**, No12, pp2358-2367
- Javidi, B. Caulfield, H.J. Horner, J.L. 1989, 'Image deconvolution by nonlinear signal processing', *App. Opt.* **28**, No15, pp3106-3111
- Khoury, J. Cronin-Golomb, M. Gianino, P. Woods, C. 1994 A, 'Photorefractive two-beam coupling nonlinear joint-transform correlator' *J. Opt. Soc. Am. B*, **11**, No11, pp2167-2174
- Khoury, J. Kane, J.S. Asimellis, G. Cronin-Golomb, M. Woods, C. 1994 B, 'All-optical joint Fourier transform correlator', *App. Opt.* **33**, No.35, pp8216-8225
- Kwong, S. Chung, Y. Cronin-Golomb, M. Yariv, A. 1985, 'Experimental studies of phase conjugation with depleted pumps in photorefractive crystals', *Opt. Lett.* **10**, No7, pp359-361
- Kwong, S. Yariv, A. Cronin-Golomb, M. Fischer, B. 1986, 'Phase of phase conjugation and its effect in the double phase conjugate resonator', *J. Opt. Soc. Am. A* **3**, No1, pp157-160
- Macdonald, K.R. Feinberg, J. 1985, 'Enhanced four-wave mixing by use of frequency shifted optical waves in photorefractive BaTiO<sub>3</sub>', *Phys. Rev. Lett.* **55**, No8 pp821-824
- Marrakchi, A. Huignard, J.P. Gunter, P. 1981, 'Diffraction efficiency and energy transfer in two-wave mixing experiments with BSO crystals', *Appl. Phys.* **24**, pp131-138
- Norman, J.B. Hong, J.H. Chang, T.Y. 1994, 'Accurate measurements of the frequency dependence of photorefractive grating formation in BSO', *J. App. Phys.* **75**, No.10, pp4873-4877
- Peterson, P.M. 1991, 'Theory of one-grating nondegenerate four-wave mixing and its application to a linear photorefractive oscillator', *J. Opt. Soc. Am. B* **8**, No8, pp1716-1722

- Refregier, Ph. Solymar, L. Rajbenbach, H. Huignard, J.P. 1985, 'Two-beam coupling in photorefractive  $\text{Bi}_{12}\text{SO}_{20}$  crystals with moving grating: Theory and experiments', *J. Appl. Phys.* **58**, No1, pp45-57
- Rajbenbach, H. Huignard, J.P. Refregier, P. 1984, 'Amplified phase-conjugate beam reflection by four-wave mixing with photorefractive  $\text{Bi}_{12}\text{SO}_{20}$  crystals', *Opt. Lett.* **9**, No12, pp558-560
- Solymar, L. Webb, D.J. Grunnet-Jepsen, A. 1996, 'The physics and applications of photorefractive materials', Oxford University Press, Oxford.
- Uesu, Y. Yoshihara, T. 1994, 'Moving grating method in phase conjugation- principle, method and its application', *J. Kor. Phys. Soc.* **27**, pp124-130
- Wang, Z.Q. Gillespie, W.A. Cartwright, C.M. 1994 'Holographic-recording improvement in a bismuth silicon oxide crystal by the moving-grating technique', *App. Opt.* **33**, No. 32, pp7627-7633
- Wang, Z.Q. Gillespie, W.A. Cartwright, C.M. Cook, N.J. 1996, 'Effects of optical bias on moving gratings in bismuth silicon oxide', *App. Opt.* **35**, No. 20, pp3829-3834
- White, J.O. Yariv, A. 1980, 'Real-time image processing via four-wave mixing in a photorefractive medium', *App. Phys. Lett.* **37**, No1, pp5-7
- Xie, P. Dai, J. Wang, P. Zhang, H. 1996, 'Numerical studies of externally pumped phase conjugation in photorefractive crystals with applied electric fields', *Opt. Comm.*, **130**, pp302-306
- Yariv, A. Pepper, D.M. 1977, 'Amplified reflection, phase conjugation and oscillation in degenerate four-wave mixing', *Opt. Lett.* **1**, No1, pp16-18



**4.1 Linear Space Invariant Systems**

Optical information processing is an attractive area of research in fields dealing with high parallelism and where large, fast processing capacities are requirements. One of the most typical examples of this processing capacity is the optical implementation of the correlation and convolution operations, which are closely connected and have been implemented successfully. This chapter will provide an introduction to the physical optics of optical information processing and describe how these operations can be implemented.

The fundamental principles of optical signal processing are similar to those developed for digital or electronic signal processing. It was shown (Cutrona, 1960) that optical spatial filtering techniques could be used to process electronic signals once those signals had been represented as an image on a photographic film. Concepts developed in communication theory and signal processing, such as spectrum analysis and linear filtering, are used almost without modification for analysing optical signal-processing systems.

The mathematical analysis used to study signal processing is based on the theory of linear systems (Das, 1991; Goodman, 1968; VanderLugt, 1992; Yu, 1983). If attention is restricted to deterministic systems, defined below, then a specified input must map into a unique output. It is not necessary that each output corresponds to a unique input. A deterministic (non-random) signal has finite total power as characterised by:

$$0 < \int_{-\infty}^{\infty} |f(x)|^2 dx < \infty. \quad (4.1)$$

An example of a non-deterministic signal is a random signal that is unbounded in space which has finite average energy.

A convenient representation of an optical system is a mathematical operator,  $L\{\}$ , which operates on input excitation to produce output response. Thus if the functions  $f_i(x_1, y_1)$  represent the inputs to a system, and  $g_i(x_2, y_2)$  represent the corresponding outputs, where  $(x_1, y_1)$  and  $(x_2, y_2)$  are the coordinate systems of the input and output planes respectively. Then by the definition of  $L\{\}$ , the two functions are related through:

$$L\{f_i(x_1, y_1)\} = g_i(x_2, y_2). \quad (4.2)$$

A system is said to be linear if the following superposition property is obeyed for all input functions  $f_i(x, y)$  and all complex constants  $c_i$

$$L\left\{\sum_i c_i f_i(x_1, y_1)\right\} = \sum_i c_i L\{f_i(x_1, y_1)\} = \sum_i c_i g_i(x_2, y_2). \quad (4.3)$$

The great advantage offered by linearity is the ability to express the response of the system to an arbitrary input in terms of responses to certain “elementary” functions into which the input has been decomposed. Such a decomposition is achieved by the so-called sifting property (Goodman, 1968) of the impulse  $\delta$  function, which states that

$$f(x_1, y_1) = \int_{-\infty}^{\infty} \int_{-\infty}^{\infty} f(x_0, y_0) \delta(x_1 - x_0, y_1 - y_0) dx_0 dy_0, \quad (4.4)$$

expressing  $f(x, y)$  as a linear combination of weighted and shifted  $\delta$  functions. The output of the linear optical system may now be written as

$$\begin{aligned}
g(x_2, y_2) &= L\{f(x_1, y_1)\} \\
&= L\left\{\int_{-\infty}^{\infty} \int_{-\infty}^{\infty} f(x_0, y_0) \delta(x_1 - x_0, y_1 - y_0) dx_0 dy_0\right\}, \\
&= \int_{-\infty}^{\infty} \int_{-\infty}^{\infty} f(x_0, y_0) L\{\delta(x_1 - x_0, y_1 - y_0)\} dx_0 dy_0
\end{aligned} \tag{4.5}$$

$f(x_0, y_0)$  is simply a weighting factor and the linearity property allows the operator  $L\{\}$  to act on the individual impulse functions.

Introducing the impulse response,  $h$ , of the system as the response at point  $(x_2, y_2)$  in output space to a  $\delta$  function input at point  $(x_0, y_0)$

$$h(x_2, y_2; x_0, y_0) = L\{\delta(x_1 - x_0, y_1 - y_0)\} \tag{4.6}$$

and, furthermore if the linear system is space-invariant, i.e. if the image of a displaced point source changes only in location, not in functional form, or

$$L\{f(x_1 - x_0, y_1 - y_0)\} = g(x_2 - x_0, y_2 - y_0), \tag{4.7}$$

then the impulse response function can be written as

$$h(x_2, y_2; x_0, y_0) = h(x_2 - x_0, y_2 - y_0), \tag{4.8}$$

and the output of the optical linear space invariant can be written as

$$g(x_2, y_2) = \int_{-\infty}^{\infty} \int_{-\infty}^{\infty} f(x_0, y_0) h(x_2 - x_0, y_2 - y_0) dx_0 dy_0, \tag{4.9}$$

which is a two dimensional convolution of the object function with the impulse response of the system. Thus the output response for an arbitrary input function can be obtained by first calculating the response for an impulse at the point  $(x_0, y_0)$  of the

input plane, and then convoluting it with the object function. Eq. (4.9) can be written more simply as

$$g = f * h, \quad (4.10)$$

where  $*$  denotes the convolution operation.

Looking at a temporal system to demonstrate the convolution operation, the output signal  $a(t)$  of a linear system having an impulse response function  $h$  and being fed with an input signal  $e(t)$  is given by, see Fig. 4.1

$$a(t) = (e * h)(t). \quad (4.11)$$

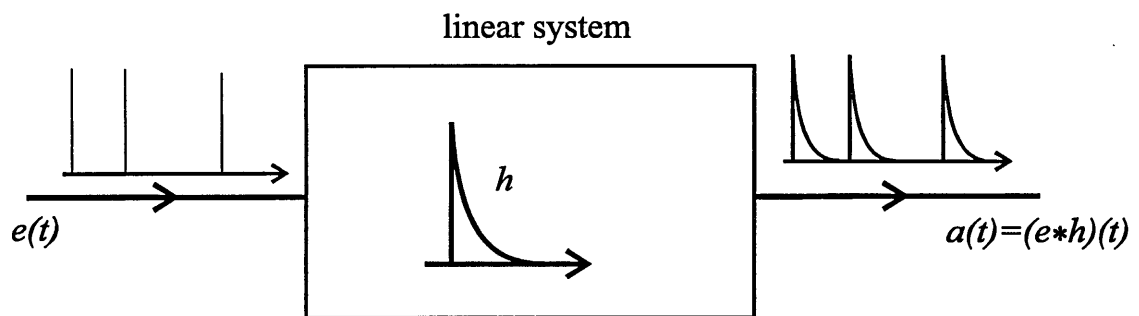


**Fig. 4.1** The output signal,  $a(t)$  of a linear system is given by the convolution of the input signal,  $e(t)$  and the impulse response function,  $h$ .

Many optical systems can be considered as a linear system and thus can be assigned an impulse response function. The simplicity of invariant systems is evident when we note the form of the convolution relation after Fourier transformation, which is introduced in the next section.

## 4.2 The Fourier Transform

The Fourier transform, (Das, 1991; Goodman, 1968; VanderLugt, 1992; Yu, 1983) is a widely used tool in the physical sciences for signal analysis. Its principal value is that it generates a function that displays the frequency content of a signal. As a result, certain features are more easily analysed or detected in the frequency domain than in the spatial domain.

Coherently illuminated systems are most useful for performing optical processing operations such as convolution, cross-correlation, and spectral analysis because the Fourier transform of an optical signal physically exists and can therefore be measured or modified.

The basic idea behind the Fourier transform is that if  $f(x)$  is a periodic signal so that  $f(x+L) = f(x)$  where  $L$  is the period of the signal, the frequency content is revealed if we expand  $f(x)$  into a series of the form

$$f(x) = a_0 + \sum_{n=1}^{\infty} \left[ a_n \cos\left(\frac{2\pi nx}{L}\right) + b_n \sin\left(\frac{2\pi nx}{L}\right) \right], \quad (4.12)$$

which is known as a Fourier series.

If  $f(x)$  is not periodic the basic interval  $L$  is extended to infinity and the fundamental spatial frequency, given by  $u_0 = 1/L$ , tends to zero. In this case the summation becomes an integral and the discrete frequency components become the Fourier transform,  $F(u)$  of the nonperiodic signal, given by

$$F(u) = \int_{-\infty}^{\infty} f(x) \exp(-jux) dx, \quad (4.13)$$

where

$$u = \frac{2\pi\alpha}{\lambda f} \quad (4.14)$$

is the spatial frequency coordinate,  $\alpha$  is the frequency plane coordinate system,  $\lambda$  is the optical wavelength, and  $f$  is the focal length of the transform lens. The corresponding inverse Fourier transform is

$$f(x) = \int_{-\infty}^{\infty} F(u) \exp(jux) du. \quad (4.15)$$

To develop the Fourier transform in optics (VanderLugt, 1992), consider the one lens system, of focal length  $f$ , shown in Fig. 4.2

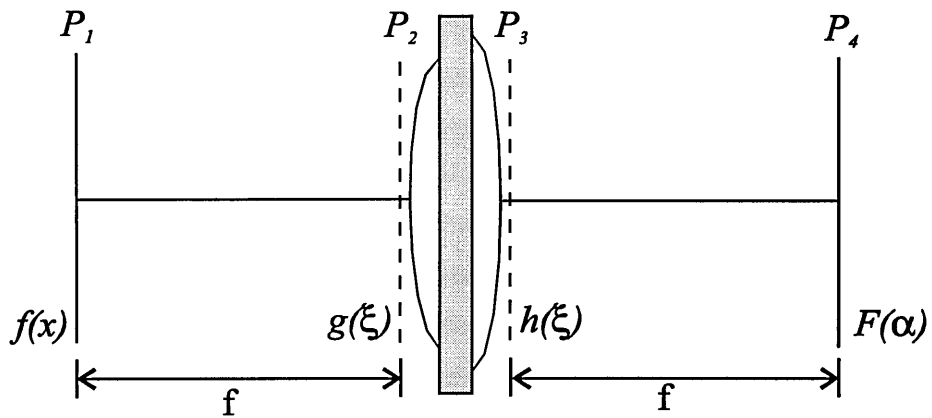


Fig. 4.2 Basic Fourier transform lens.

To simplify the mathematics we use a one dimensional notation to find the light distribution  $F(\alpha)$  at the back focal plane of the lens and we place  $f(x)$  at the front focal plane of the lens. The distribution  $g(\xi)$  is obtained by applying a Fresnel transform, (Vanderlugt, 1992) which relates distributions across free space.  $h(\xi)$  is then obtained by multiplying  $g(\xi)$  by the lens function which may be thought of as a phase transformation in which the incident wavefront is delayed by an amount proportional to the thickness of the lens. The back focal plane distribution is obtained by a further Fresnel distribution, giving

$$F(\alpha) = \sqrt{\frac{j}{\lambda f}} \int_{-\infty}^{\infty} f(x) \exp\left(\frac{-jx2\pi\alpha}{\lambda f}\right) dx, \quad (4.16)$$

which is the Fourier transform of the signal  $f(x)$  in terms of the physical coordinate  $\alpha$  of the Fourier plane.

To emphasise that the Fourier transform is a function of the spatial frequency  $u$ , and extending the result to two dimensions, we can express the result as

$$\mathbf{F}\{f(x, y)\} = F(u, v) = \int \int_{-\infty}^{\infty} f(x, y) \exp[-j(ux + vy)] dx dy, \quad (4.17)$$

where  $\mathbf{F}\{\}$  denotes the Fourier operation, and  $(u, v)$  are the orthogonal spatial frequencies. The scaling constant  $\left(\sqrt{\frac{j}{\lambda f}}\right)$  is generally dropped when the transform is written in this form. The original object  $f(x, y)$  can be obtained from its Fourier spectrum,  $F(u, v)$  by an inverse transform, given by

$$f(x, y) = F^{-1}\{F(u, v)\} = \int \int_{-\infty}^{\infty} F(u, v) \exp[j(ux + vy)] du dv, \quad (4.18)$$

where  $F^{-1}\{\}$  denotes the inverse Fourier transform. This can be achieved by a succeeding transform lens at the back focal plane of the first lens, which gives an output identical to  $f(x, y)$  but with reversed coordinates.

An important property of the Fourier transform is translation invariance, if the input object shifts to a position  $(x_0, y_0)$  then Eq. (4.17) gives

$$\begin{aligned} \mathbf{F}\{f(x - x_0, y - y_0)\} &= \int_{-\infty}^{\infty} \int_{-\infty}^{\infty} f(x - x_0, y - y_0) \exp[-j(ux + vy)] dx dy \\ &= \exp[-j(ux_0 + vy_0)] F(u, v) \end{aligned} \quad , \quad (4.19)$$

i.e. the translation of an input object causes a linear phase shift in the Fourier spectrum without a change in position.

Now returning to look at the Fourier transform of the convolution of two signals, which can be written, in one dimension for simplicity, as

$$\begin{aligned} G(u) &= \int_{-\infty}^{\infty} g(x) \exp(-jux) dx = \int_{-\infty}^{\infty} \left[ \int_{-\infty}^{\infty} f(\alpha) h(x - \alpha) d\alpha \right] \exp[-jux] dx \\ &= \int_{-\infty}^{\infty} f(\alpha) \exp(-ju\alpha) d\alpha \int_{-\infty}^{\infty} h(x - \alpha) \exp[-ju(x - \alpha)] dx \\ &= F(u) H(u) \end{aligned} \quad , \quad (4.20)$$

which is known as the convolution theorem and states that the Fourier transform of the convolution of two signals is equal to the product of the Fourier transforms of the two signals,  $H$  is called the transfer function of the system.

The convolution theorem may be regarded as indicating that the input may be decomposed into complex exponential functions of various spatial frequencies, rather than the  $\delta$  functions. This leads to further useful properties of the Fourier transform.

The autocorrelation of a function  $f$ , written symbolically as  $f \otimes f$ , is defined by

$$[f(x, y) \otimes f(x, y)](\alpha, \beta) = \int_{-\infty}^{\infty} \int_{-\infty}^{\infty} f(x, y) f^*(x - \alpha, y - \beta) dx dy, \quad (4.21)$$

where the superscript  $*$  denotes the complex conjugate. This expression is related to the convolution product Eq. (4.9) because for a real-valued function we have  $f \otimes f = (f * f)^{(-)}$ , where  $f^{(-)}$  denotes the function obtained from  $f$  by reflecting the coordinates at the origin (Das, p250)



$$f^{(-)}(x,y) = f(-x,-y). \quad (4.22)$$

A connection between the autocorrelation of a function and its Fourier transform is established by the Wiener-Khinchin theorem, which states that the autocorrelation and the power spectrum of a function are Fourier transforms of one another, i.e

$$FT\{R(\alpha,\beta)\} = FT\left\{\int\int_{-\infty}^{\infty} f(x,y)f^*(x-\alpha,y-\beta)dxdy\right\} = |F(u,v)|^2, \quad (4.23)$$

where  $R(\alpha,\beta)$  is known as the autocorrelation function. Conversely, we have

$$FT^{-1}\{|F(u,v)|^2\} = R(x,y). \quad (4.24)$$

The crosscorrelation theorem can be stated as follows. If  $f_1(x,y)$  and  $f_2(x,y)$  are two Fourier transformable functions then

$$FT\{R_{12}(\alpha,\beta)\} = FT\{f_1(x,y) \otimes f_2^*(x,y)\} = F_1(u,v)F_2^*(u,v) \quad (4.25)$$

and

$$FT\{R_{21}(\alpha,\beta)\} = FT\{f_1^*(x,y) \otimes f_2(x,y)\} = F_1^*(u,v)F_2(u,v), \quad (4.26)$$

where

$$R_{12}(\alpha,\beta) = \int\int_{-\infty}^{\infty} f_1(x+\alpha,y+\beta)f_2^*(x,y)dxdy \quad (4.27)$$

and

$$R_{21}(\alpha,\beta) = \int\int_{-\infty}^{\infty} f_1^*(x-\alpha,y-\beta)f_2(x,y)dxdy, \quad (4.28)$$

are the crosscorrelation functions. Correlation is a measure of the similarity between the two functions  $f_1(x,y)$  and  $f_2(x,y)$  as a function of the variables  $(u,v)$ . The Fourier

transform property of lenses leads to interesting optical applications in the field of optical processing and in particular pattern recognition, the basic ideas of which, and some specific applications are developed in the next section.

### 4.3 Pattern Recognition

Optical correlation may be demonstrated using the setup shown in Fig. 4.3 where two lenses are used to form the image of an illuminated object transparency. The first lens may be considered as generating the Fourier transform of the object in the Fourier plane, the second lens then performs the inverse transform of the resulting field distribution. A filter inserted at the Fourier plane can modify the spatial frequencies of the distribution and Fourier plane filtering is therefore known as spatial filtering. A spatial filter is a mask or transparency that has an amplitude response (through attenuation) and a phase response (through an optical path difference).

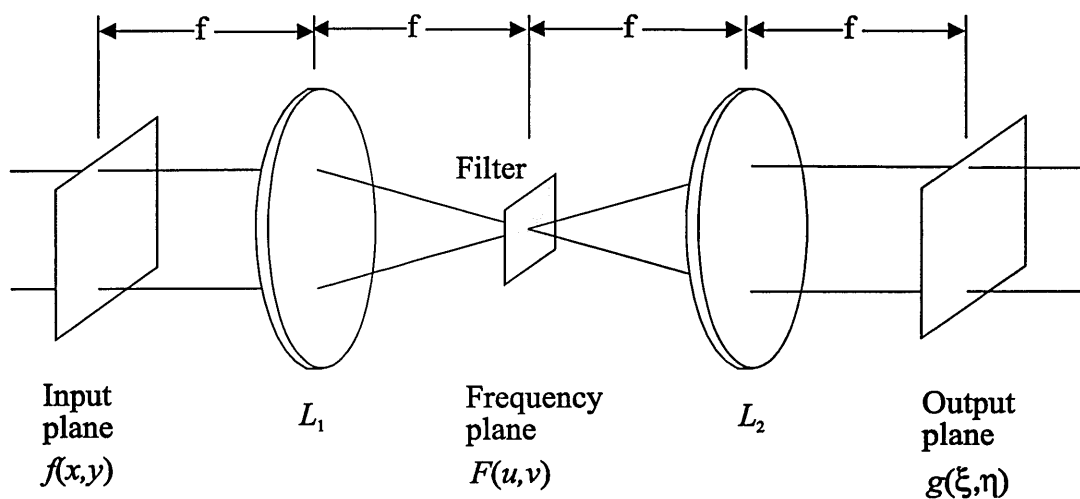


**Fig. 4.3** The  $4f$  system for optical correlation.  $L_1$  and  $L_2$  are lenses, of focal length  $f$ .

An important problem in optical information processing is the detection of a signal corrupted by random noise (VanderLugt, 1992). If the input distribution to such a system is the sum of a deterministic signal  $s(x,y)$  and stationary additive noise  $n(x,y)$ , the spectral density of which is  $R_n(u,v)$ , i.e.

$$f(x,y) = s(x,y) + n(x,y). \quad (4.29)$$

The aim is to develop a filter which will maximise the ratio of the intensity of the peak signal to mean-square noise at the output of the system, this signal to noise ratio (SNR), given by

$$\text{SNR} = \frac{|g(0,0)|^2}{r_n(0,0)} = \frac{\left| \int_{-\infty}^{\infty} \int_{-\infty}^{\infty} S(\alpha,\beta) H(\alpha,\beta) d\alpha d\beta \right|^2}{\int_{-\infty}^{\infty} \int_{-\infty}^{\infty} R_n(\alpha,\beta) |H(\alpha,\beta)|^2 d\alpha d\beta}, \quad (4.30)$$

where, due to translational invariance, the filter is designed such that  $|g(0,0)|^2$  is maximised.

Suppose that  $h(x,y)$  is the impulse response of a linear, space-invariant filter  $H(u,v)$ , the response of which must be optimised. It is found that the highest SNR is achieved when

$$H(u,v) = \frac{S^*(u,v)}{R_n(u,v)}. \quad (4.31)$$

The magnitude of the optimum filter is therefore proportional to the magnitude of the Fourier transform of the signal and inversely proportional to the noise spectral density. Because the phase of the optimum filter is conjugate, or matched, to the phase of the Fourier transform of the signal,  $H(u,v)$  is called a matched filter. For the special case where the additive noise is white, i.e. the spectral density is uniform for all spatial frequencies, the optimum filter becomes

$$H(u, v) = S^*(u, v), \quad (4.32)$$

which is also referred to as a matched filter. The field transmitted by such a matched filter is entirely real (proportional to  $SS^*$ ) and all phase variation is eliminated across the Fourier domain. Consequently the final lens focuses an amplitude-weighted plane wave to a bright spot denoting recognition. If the filter is not matched there will be no spot. The matched filter system will therefore not recognise the input signal. If the input is not centred at the origin, the bright correlation spot in the output plane simply shifts by a proportional distance.

The output of the system for the special case of Eq. (4.32) is

$$g(\xi, \eta) = \int \int_{-\infty}^{\infty} F(u, v) S^*(u, v) \exp[-j(ux + vy)] du dv. \quad (4.33)$$

By using the convolution theorem, Eq. (4.20) this can be expressed as

$$g(\xi, \eta) = \int \int_{-\infty}^{\infty} f(x, y) s^*(x - \xi, y - \eta) dx dy, \quad (4.34)$$

which is a correlation operation.

The matched filter is difficult to use in practice; it contains amplitude and phase information which can be difficult to calculate and control, and if the images have a high space-bandwidth product, the positional alignment may cause problems.

The problems of calculation and control of phase information were solved by the VanderLugt filter (VanderLugt, 1964). In his technique a hologram was recorded by exposing a film to the interference produced by a plane wave and the Fourier transform of the object. The hologram therefore enables an arbitrary phase and amplitude response to be incorporated in a spatial carrier frequency. After development, the hologram is replayed by the Fourier transform of the reference image to generate, via a probe beam, the correlation of the object and reference images. It is not necessary to record the Fourier hologram optically. The filter can be

produced as a synthetic or computer-generated hologram, giving much greater speed and flexibility.

The problem with positional sensitivity was removed with the development of the joint transform correlator (JTC) (Weaver, 1966). This system records the joint power spectrum of the Fourier transforms of the object and reference images. After development the hologram is replayed by a plane wave so the position of the filter is not critical, the cross-correlation of the two images is present in the output.

#### 4.4 Unconventional Correlators

Many efforts have been made to improve optical correlation techniques to gain higher flexibility, less sensitivity to object modification, better signal discrimination and the use of incoherent light or higher light efficiency (Horner, 1987; Kumar, 1992; Javidi, 1994).

The recognition process is also sensitive to changes in scale and rotations of one or both input functions, and additional transformations have been proposed to avoid this sometimes unwanted sensitivity, (Casasent, 1976).

The discovery that, in the Fourier plane, phase information is considerably more important than amplitude information, led to the development of the phase-only filter (Horner, 1984). One way to obtain such a filter is to omit the amplitude information of the matched filter

$$F_2'(u, v) = \frac{F_2^*(u, v)}{|F_2^*(u, v)|} = \exp[-j\psi(u, v)], \quad (4.35)$$

where  $F_2^*(u, v)$  is the matched filter of input function  $F_2(u, v)$ . The phase-only filter delivers optimum light efficiency because there is no attenuation due to amplitude modulation. Besides the improvement in efficiency, the output peak structure for the recognition process is also enhanced. This may be understood by thinking of the phase-only filter as the application of a spatial high pass filter to the conventional matched filter, since the neglected amplitude information is chiefly contained in the

low frequency component of the transformation. This results in a strongly enhanced autocorrelation peak. Hence the signal to noise ratio or discrimination ability of the filter is improved. On the other hand this filter is more sensitive to modifications of the input function.

The performance of these and other filters is tested below using the images of the similar letters 'O' and 'G' shown in Fig. 4.4. The noiseless images are made up of the two grey levels 0 and 255. The noise is white additive Gaussian noise with standard deviation,  $\sigma = 100$ .

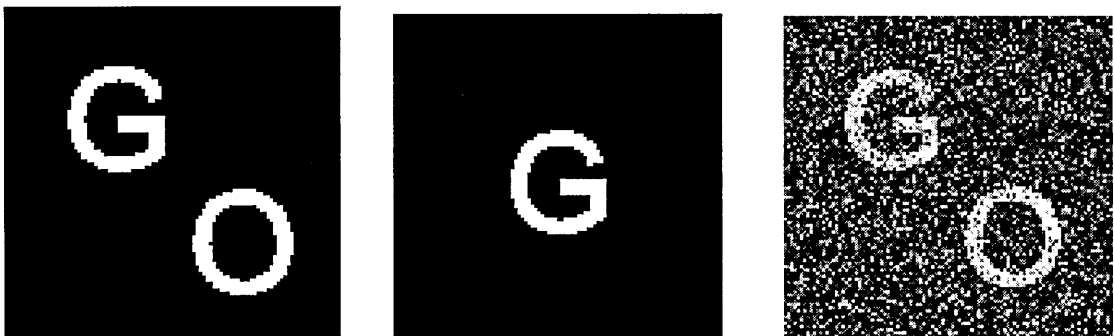


**Fig. 4.4** The reference (left), object (middle), and noisy reference (right) images used in the correlation simulations.

The VanderLugt correlator makes use of the Wiener-Khinchin theorem to perform its correlation

$$R(x,y) = FT^{-1}\{F(u,v) \cdot G(u,v)\}, \quad (4.36)$$

where  $R(x,y)$  is the cross-correlation function, and  $F(u,v)$  and  $G(u,v)$  are the Fourier transforms of the reference image and filter respectively. The filter is calculated from the object function  $o(x,y)$ , the Fourier transform of which may be written as

$$FT\{o(x,y)\} = O(u,v) = |O(u,v)|\exp[j\phi(u,v)]. \quad (4.37)$$

The matched, phase-only and amplitude-only filters are therefore given by

$$\begin{aligned}
 G(u, v) &= O^*(u, v) = |O^*(u, v)| \exp[-j\phi(u, v)] && \text{matched,} \\
 G(u, v) &= \frac{O^*(u, v)}{|O^*(u, v)|} = \exp[-j\phi(u, v)] && \text{phase - only,} \\
 G(u, v) &= |O^*(u, v)| && \text{amplitude - only.}
 \end{aligned} \tag{4.38}$$

A fourth filter is also tested for comparison, it is called the inverse filter and is given by

$$G(u, v) = \frac{cO^*(u, v)}{|O^*(u, v)||O(u, v)|} = \frac{c \exp[-j\phi(u, v)]}{|O(u, v)|}, \tag{4.39}$$

where  $c$  is a constant needed to keep the filter passive. The constant solves the problem associated with mathematical poles; when the modulus is tending to zero the filter will become phase only at these points (Vallmitjana, 1995).

The results of the correlations using each of these filters are shown in Fig's 4.5 and 4.6 for the noiseless and noisy references respectively. These correlations were calculated using an IDL program written for this thesis. The 3-D plots show the square of Eq. (4.36) since the correlation  $R$  is proportional to amplitude and a physical detector responds to intensity.

The intensity plots show the auto and cross-correlation of the letters 'G' and 'O'. The auto-correlation is always the higher. The correlations show that the phase-only filter offers an improvement over the matched filter and the amplitude-only filter causes a degradation in the correlation peak, as a consequence of the greater importance of phase information in the Fourier plane. The low level structure of the peaks is a reflection of the original image. For the noiseless case, the inverse filter gives a further enhancement of the correlation peak. However Fig. 4.6 shows that the signal to noise ratio for the inverse filter decreases rapidly when noise is added to the reference scene.

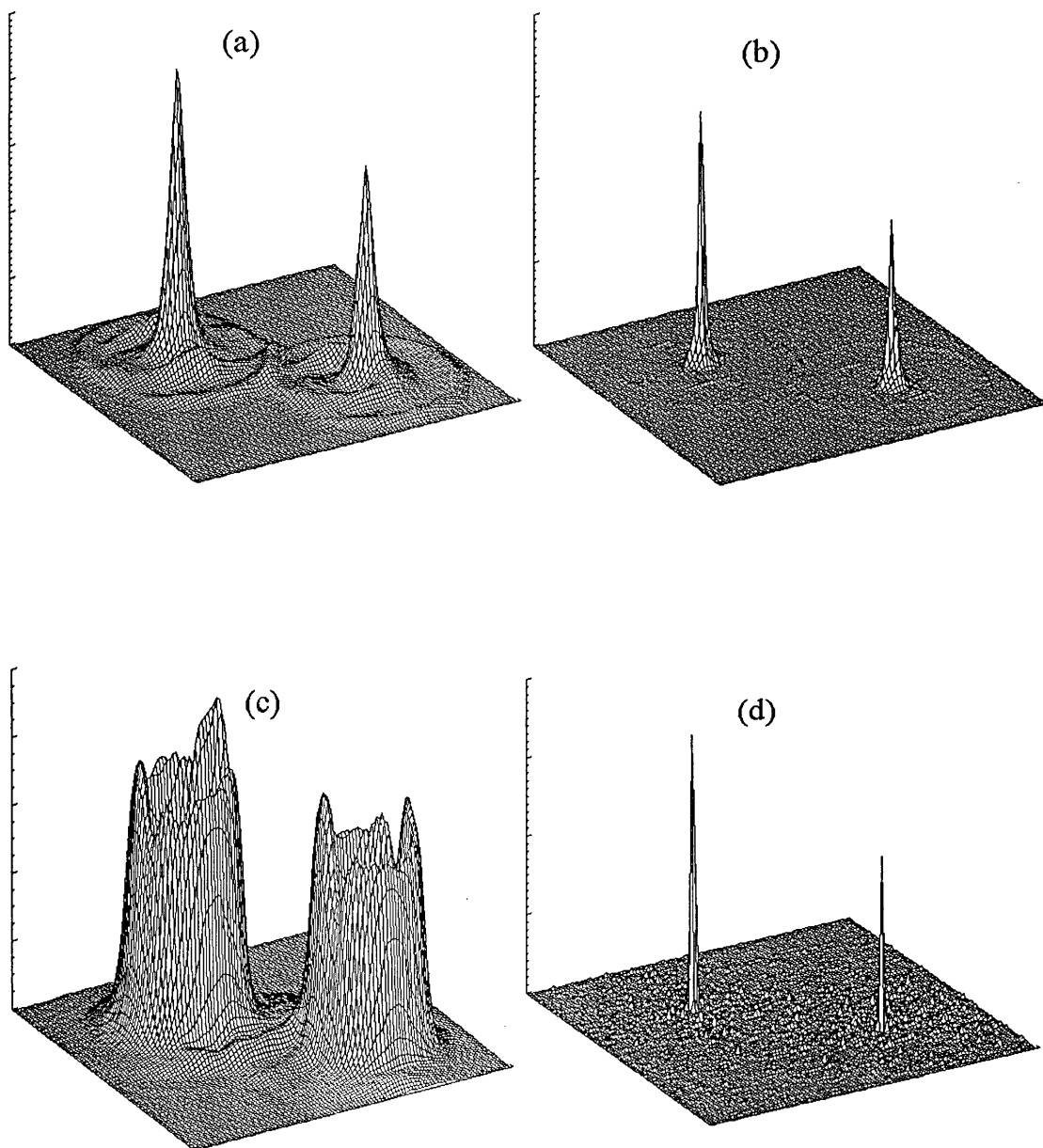


**Fig. 4.5** Simulated noiseless correlations using different filters.  
(a) Matched, (b) Phase-only, (c) Amplitude-only, (d) Inverse.



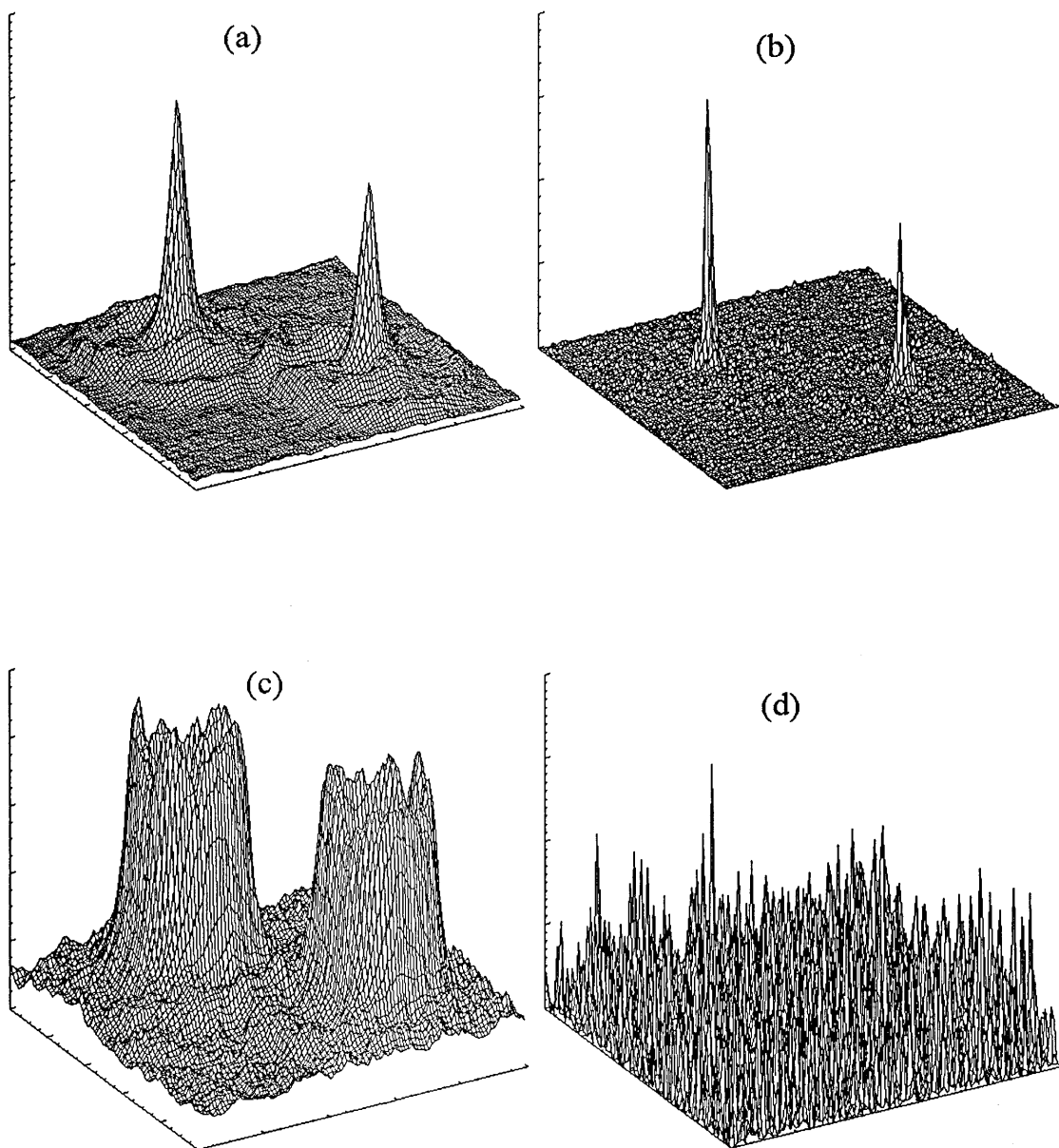


**Fig. 4.6** Simulated noisy correlations using different filters.  
(a) Matched, (b) Phase-only, (c) Amplitude-only, (d) Inverse.

With noise added to the reference scene the phase-only filter still offers an improvement over the matched filter, however the correlation achieved using the inverse filter is so degraded that there is no discrimination. The inverse filter (VanderLugt, 1992) not only corrects the phase, as does the matched filter, but also maximises the peak signal at the output, by setting the magnitude of the correlation in the Fourier plane equal to unity. The signal to noise ratio (SNR) is, however, not maximised and if  $O(u,v)$  has any zeros a large amount of noise passes through the system because the filter transmittance is highest at those frequencies where the SNR is lowest.

The filters mentioned are only a small selection of the large number which have been developed to cater for the requirements of different applications. For example if the phase-only filter is restricted to binary operation (Psaltis, 1984; Horner, 1985;) then real-time spatial light modulators (SLM's) such as the magneto-optic SLM, can be employed in the filter plane.

Another important class of filters is the synthetic discriminant function (SDF) (Casasent, 1984). The SDF can be described as a linear combination of reference images to create a composite, which is then cross-correlated with the inputs. The weights for the linear combination are selected so that the cross-correlation output at the origin is the same for all images belonging to one class. Further enhancements to the SDF include that made by Kumar (1986), who introduced the minimum variance SDF (MVSDF) which maximised the noise tolerance.

As well as a large number of filter designs there are also other possible correlator architectures apart from the classic  $4f$  system described earlier (Javidi, 1994). One of these alternatives, the joint transform correlator (JTC), is described in Chapter 6.

## 4.5 Performance Measures

The final section of this chapter looks at the various measures which have been developed to compare the performance of different correlation systems (Kumar, 1990). The main performance measures are light efficiency, signal-to-noise ratio, peak sharpness, and discriminability; methods of estimating these properties are detailed below.

The behaviour of filters under the conditions of additive white Gaussian noise is often used to grade their performance. This noise model does not reflect all realities, but it does inject an uncertainty component into the input signal and provides a useful tool for comparing performance.

*Light Efficiency:*

In optical correlators it is important that the output intensity at the correlation plane is maximised, so that detectors in this plane can respond quickly and accurately. The light efficiency was originally quantified using the following measure, called the Horner efficiency (Caulfield, 1982)

$$\begin{aligned}\eta_H &= \frac{\iint |f_1(x, y) * f_2(x, y)|^2 dx dy}{\iint |f_1(x, y)|^2 dx dy} \\ &= \frac{\text{Total energy in the output}}{\text{Total energy in the input signal}}\end{aligned}\tag{4.40}$$

*Signal-to noise Ratio (SNR):*

When random noise is added to the input signal, the output will fluctuate from experiment to experiment. It is desirable to keep this fluctuation to a minimum, and the output as large as possible for each noise level. This is achieved by maximising the following conventional correlation peak SNR measure which is

defined as the ratio of the expected value squared of the correlation peak amplitude to the variance of the correlation peak amplitude

$$SNR = \frac{|E[g(0,0)]|^2}{\text{var}[g(0,0)]}, \quad (4.41)$$

where  $E[g(0,0)]$  is the expected peak amplitude (or ensemble average) and  $g(0,0)$  is the peak amplitude. This measure of the SNR is not suitable for defining output peak sharpness. Higher SNR values indicate a better noise tolerance and a higher probability of correct detection in random noise. The numerator in Eq. (4.41) represents the average of values at the origin obtained from different noise samples, the denominator represents the variance of these values. The above SNR measure cannot, therefore be estimated using one correlation experiment.

The above SNR measure is not the same as that used to design the matched filter, which was given in Eq. (4.29)

$$SNR = \frac{|g(0,0)|^2}{r_n(0,0)} = \frac{\left| \int_{-\infty}^{\infty} \int_{-\infty}^{\infty} S(\alpha, \beta) H(\alpha, \beta) d\alpha d\beta \right|^2}{\int_{-\infty}^{\infty} \int_{-\infty}^{\infty} R_n(\alpha, \beta) |H(\alpha, \beta)|^2 d\alpha d\beta}, \quad (4.42)$$

and is described as the peak signal intensity divided by the noise power, both measured at the origin.

*Peak Sharpness:*

The accuracy of detection of the inputs will be increased for sharper correlation peaks. One such measure of the sharpness of correlation peaks is the peak-to-sidelobe ratio (PSR), given by

$$\text{PSR} = \frac{|E[g(0,0)]|^2}{\text{var}[g(x',y')]}, \quad (4.43)$$

where  $(x',y')$  represents a point in the output correlation far from the origin. It is therefore similar to the SNR measure given by Eq. (4.41) except that the denominator is now the variance at some point away from the correlation peak.

Another measure of peak sharpness is referred to as the peak-to-root mean square ratio (PRMSR)

$$\text{PRMSR} = \frac{|g(0,0)|^2}{g_{rms}^2}, \quad (4.44)$$

where the peak is once again assumed to occur at the origin. If  $\Omega$  denotes the set of output pixels for which the output values are below 50% of the peak value and  $N_\Omega$  denotes the number of pixels in this set, then  $g_{rms}$  is defined according to

$$g_{rms} = \left[ \frac{1}{N_\Omega} \sum_{i \in \Omega} |g(i)|^2 \right]^{\frac{1}{2}}. \quad (4.45)$$

A third measure of the peak sharpness is given by the peak-to-correlation energy (PCE) defined as follows

$$\text{PCE} = \frac{|g(0,0)|^2}{\int \int_{-\infty}^{\infty} |g(x,y)|^2 dx dy}, \quad (4.46)$$

where the denominator is the total correlation plane energy. For sharp correlation peaks most of the energy in the correlation plane will be in the peak, and the PCE will be large, for broad peaks the PCE will tend to zero.

This third technique for defining the peak sharpness gives a smooth measure because of the averaging involved in finding the total energy, Kumar (1990) recommends this technique as being analytically tractable.

#### *Discriminability:*

Discriminability refers to the ability to detect one class of deterministic signal whilst rejecting others; it is different from the SNR measurement which refers to detection of a deterministic signal in random noise. It is relatively easy to discriminate against known false inputs, this is achieved using the following matched filter

$$H(\alpha, \beta) = S_1^*(\alpha, \beta) - S_2^*(\alpha, \beta), \quad (4.47)$$

where  $s_1(x, y)$  and  $s_2(x, y)$  are the desired and false inputs respectively;  $S_1^*(\alpha, \beta)$  and  $S_2^*(\alpha, \beta)$  are the conjugates of their Fourier transforms.

A good measure of discrimination between two inputs in random noise is given by the Fisher ratio (Kumar, 1990)

$$FR = \frac{|E\{g_1(0,0)\} - E\{g_2(0,0)\}|^2}{[\text{var}\{g_1(0,0)\} + \text{var}\{g_2(0,0)\}]/2} \quad (4.48)$$

Higher FR values indicate better discrimination between the two signal inputs. The denominator accounts for the fact that good discrimination also depends on low variance in the correlation peak heights.

Using the measures defined above the following table gives values, at three different noise levels, for the performance of the previously defined matched spatial filter and phase-only filter. 'AUTO' and 'CROSS' refer to correlations obtained for the auto-correlation of the letter 'G' and the cross-correlation with the letter 'O'.

	$\sigma=2$		$\sigma=50$		$\sigma=100$	
Matched Filter	AUTO	CROSS	AUTO	CROSS	AUTO	CROSS
Peak Max	0.99	0.67	0.85	0.59	0.72	0.52
$\eta_H$	18.8%	19.7%	6.5%	7.2%	2.5%	3.0%
PCE	$10.7 \times 10^{-3}$	$8.5 \times 10^{-3}$	$2.3 \times 10^{-3}$	$1.7 \times 10^{-3}$	$0.64 \times 10^{-3}$	$0.47 \times 10^{-3}$
SNR	$5.5 \times 10^6$	$4.7 \times 10^6$	$1.2 \times 10^4$	$0.9 \times 10^4$	$2.4 \times 10^3$	$2.3 \times 10^3$
FR	$2.0 \times 10^6$		$3.8 \times 10^3$		$7.5 \times 10^2$	
Phase-only Filter	AUTO	CROSS	AUTO	CROSS	AUTO	CROSS
Peak Max	12.0	4.1	8.8	3.0	6.1	2.0
$\eta_H$	100%	100%	100%	100%	100%	100%
PCE	0.21	0.08	$6.1 \times 10^{-2}$	$2.0 \times 10^{-2}$	$1.3 \times 10^{-2}$	$0.5 \times 10^{-2}$
SNR	$7.5 \times 10^4$	$7.9 \times 10^4$	$1.3 \times 10^2$	$1.1 \times 10^2$	40.6	34.7
FR	$7.5 \times 10^4$		$1.2 \times 10^2$		39	

**Table 4.1** Performance Measures of matched and phase-only filters for increasing noise levels, (SNR from Eq. (4.40)).

The performance data in the above table was calculated using the IDL computer programme, 'Perform.PRO' shown in Appendix A of this work. Each set of data was calculated from a series of 40 correlations, each using different noise arrays.

The Horner efficiency,  $\eta_H$ , is 100% for the phase-only filter because it has unit amplitude and hence zero absorption.

'Peak Max' is the maximum height of the correlation peak at the origin,  $|g(0,0)|^2$ , it is given as a multiple of the autocorrelation peak height of the noiseless matched filter which has an absolute value of unity. At the very low noise level of  $\sigma=2$  the phase only auto-correlation peak height is 12.0, much higher than unity, showing the greater sharpness achieved with the phase-only filter.

The signal to noise ratio is higher for the matched filter case, which is appropriate since this is a consideration in its design. The signal-to-noise ratio is very high at the low noise level due to the very small variance of the correlation peak. This led to great variation in the SNR data and 40 correlations were not sufficient to achieve a reliably constant figure, the figures given are nonetheless useful for a comparison between the filter designs.

It is somewhat surprising that the discriminability, measured by the Fisher ratio, is higher for the matched filter, since the correlation peaks of Figs. 4.5 and 4.6 would seem to indicate otherwise. This is explained by its reliance on the variance of the correlation peaks rather than the peak sharpness.

The next chapter discusses the characterisation of the inexpensive liquid crystal television to be used as a spatial light modulator in later correlation experiments. The following chapter will then discuss joint transform correlator systems, including those using photorefractive BSO as the recording medium.



## Chapter 4: References

- Casasent,D. Psaltis,D. 1976, 'Position, rotation, and scale invariant optical correlation', *Appl. Opt.* **15**, No7, pp1795-1799
- Casasent,D. 1984, 'Unified synthetic discriminant function computational formulation', *Appl. Opt.* **23**, No10. pp1620-1627
- Caulfield,H.J. 1982, 'Role of the Horner efficiency in the optimization of spatial filters for optical pattern recognition', *Appl. Opt.* **21**, No4, pp4391-4393
- Cutrona,L.J. Leith,E.N. Palermo,C.J. Porcello,L.J. 1960, 'Optical data processing and filtering systems', *IRE Trans. Inf. Theory*, **IT-6**, pp386-400
- Das,P.K. 1991, *Optical Signal Processing*, Heidelberg, Springer-Verlag, Ch.3,
- Goodman,J.W. 1968, *Introduction to Fourier Optics*, New York, McGraw-Hill, Ch.1.
- Horner,J.L. Gianino,P.D. 1984, 'Phase-only matched filtering', *Appl. Opt.* **23**, No6, pp812-816
- Horner,J.L. Leger,J.R. 1985, 'Pattern recognition with binary phase-only filters', *Appl. Opt.* **24**, No5, pp609-611
- Horner,J.L. (Ed), 1987, *Optical Signal Processing*, San Diego, Academic Press, Ch. 2.2. Javidi,B. Horner,J.L. (Ed's), 1994, *Real-Time Optical Information Processing*, San Diego, Academic Press, Part 1.
- Kumar,B.V.K. 1986, 'Minimum-variance synthetic discriminant functions', *J. Opt. Soc. Am. A.* **3**, No10, pp1579-1584
- Kumar,B.V.K. Hassebrook,L. 1990, 'Performance measures for correlation filters', *Appl. Opt.* **29**, No20, pp2997-3006
- Kumar,B.V.K, 1992, 'Tutorial survey of composite filter designs for optical correlators', *Appl. Opt.* **31**, No23, pp4773-4801
- Psaltis,D. Paek,E.G. Venkatesh,S.S. 1984, 'Optical image correlation with binary spatial light modulator', *Opt. Eng.* **23**, No6, pp698-704
- Vallmitjana,S. Carnicer,A. Martín-Badosa,E. Juvells,I. 1995 'Nonlinear filtering in object and Fourier space in a joint transform optical correlator: comparison and experimental realization', *Appl. Opt.* **34**, pp3942-3949

- VanderLugt, A. 1964, 'Signal detection by complex spatial filtering', *IEEE Trans.on Inf. Theory*, **IT-10**, pp139-145
- VanderLugt,A. 1992, *Optical Signal Processing*, New York, Wiley-Interscience, Chs.3,5.
- Weaver,C.S. Goodman,J.W. 1966, 'A technique for optically convolving two functions', *Appl. Opt.* **5**, pp1248-1249
- Yu,F.T.S. 1983, *Optical Information Processing*, New York, Wiley-Interscience, Ch.1.

## **Chapter 5. Characterisation of the Liquid Crystal Television**

### **5.1 Liquid Crystal Displays**

Because of its commercial availability and low cost, the liquid crystal television (LCTV) has been used in a variety of optical processing applications as a spatial light modulator (SLM) where the light amplitude is modulated, (Soutar, 1992; Jutamulia, 1987; Gregory, 1986; Liu, 1985). However, because of the birefringence of liquid crystals (LC's), an LCTV also acts as a spatial phase modulator. Both amplitude modulation and phase modulation are dependent on the polarisation of the light being modulated and the voltage applied to the liquid crystal cells. In most applications either pure amplitude modulation, with no phase modulation (Gregory, 1991), or vice versa, is needed. There are applications (Gregory, 1992; Gorecki, 1996) where phase and intensity are both modulated, in these cases two LCTV's can be used to provide independent phase and amplitude modulation.

The twisted nematic liquid crystal is an anisotropic medium that can be treated locally as a homogeneous uniaxial crystal whose optical axis is parallel to the direction of the molecules. Because of a twist, see Fig. 5.1, induced by scratches on the surface of the sandwiching electrodes, the molecules gradually rotate in a helical fashion, usually through  $90^\circ$ . Thus the material is inhomogeneous, and the optical axis follows the molecular twist.

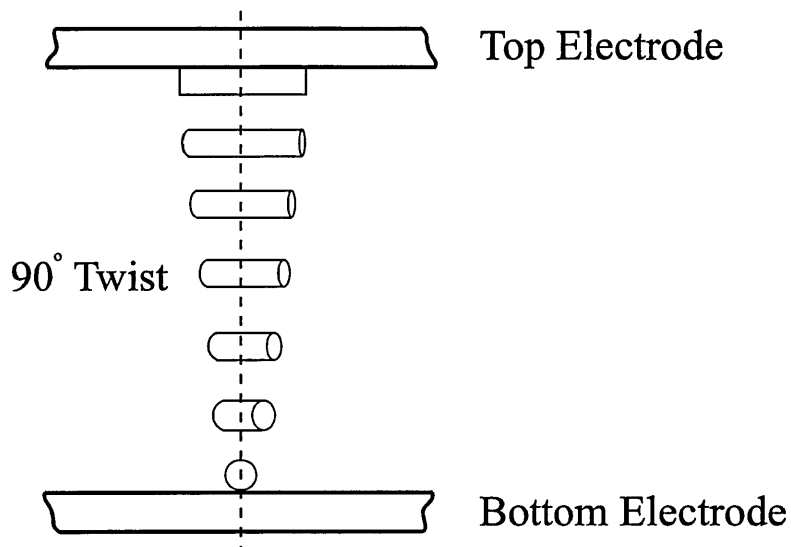


**Fig. 5.1** Molecular director orientation in a slice through a twisted nematic liquid crystal cell.

When an electric field is applied the molecules away from the surfaces tend to realign in a direction approximately parallel to the applied field and normal to the surface. This realignment causes changes in the transmission of polarised light and the liquid crystal acts as a birefringent medium whose characteristics depend on the applied voltage.

The response of the transmitted amplitude and phase change to applied field is coupled and complex and the LCTV must be characterised to determine the operating curve. Prior knowledge of this is essential to correct any filter algorithms accordingly. In this work all the filters are designed to modulate amplitude (or intensity) and a minimum phase change is therefore desired.

## 5.2 The Epson Liquid Crystal Television

The LCTV used in this work was taken from the Epson Liquid Crystal Video Projector (model VP-100PS). The projector has three LCTV screens for the red, green and blue components of the colour video signal, each screen has 326×264 (rows by columns) thin film transistor (TFT) pixels (Gorecki, 1996) arrayed in a 32mm diagonal area, each having a size of 80×90 $\mu\text{m}$  and an active area of 55×60 $\mu\text{m}$ , giving a fill factor of 46%, with an approximate transmission efficiency of 43% at 633nm. One of the LCTV's was removed from the video projector and, the original, poor quality, plastic film polarisers which sandwiched the screen were removed and higher quality polarisers on rotational mounts were substituted. The 23 conductor flat lead cable connecting the LCTV to the drive electronics was replaced by a longer ribbon cable.

The voltage applied to the LCTV cells consists of two parts. First a bias voltage across every cell produces the transmittance and can be largely controlled by adjustment of the 'brightness' level on the video projector. Additional control is provided by the 'contrast' level which modifies the contrast ratio between a fully 'on' and a fully 'off' pixel. The 'brightness' and 'contrast' levels on the video projector can be adjusted according to a hardware fixed scale between 0 and 10. The second part of the voltage is applied individually to each pixel and controls the continuous 256 grey level mode.

The update rate of the LCTV is determined by the addressing speed of the driving electronics which is based on the composition of a video frame. A single video frame of approximately 600 lines consists of two interlaced fields which write to odd and even lines on a television giving a refresh rate of 25Hz. The LCTV operates in a slightly different way writing each field to every line, resulting in a 50 Hz update rate. Soutar (1994) found that, under the most stringent operating conditions, i.e. frame by frame switching between grey levels 0 and 255, a refresh rate of 7Hz was needed to avoid averaging between frames.

Phase mostly modulation (Kirsch, 1992) can be achieved by using an appropriate applied voltage bias when the polarisation of the light is oriented parallel

to the LC molecule director. For this mode of operation, the directions of polariser and analyser, which sandwich the LCTV, will be  $0^\circ$  and  $90^\circ$  respectively, where the direction of the LC molecular director at the front face of the LCTV is also  $0^\circ$ . Phase mostly modulation is achieved under a small bias voltage where the LC directors are slightly perturbed and their twist angle distribution is close to the unperturbed case where no bias is applied. In this configuration the LCTV produces phase-mostly modulation with small amplitude modulation.

Amplitude mostly modulation can be achieved for a bias voltage above a certain threshold level. The mode of operation is therefore partially determined by the 'brightness' setting. The polariser should be at  $90^\circ$ , perpendicular to the molecular director at the front face and the analyser should be parallel to the polariser. With large applied voltage the LC molecular directors are almost untwisted, and there is little or no phase variation.

Linear polarised light that enters an LCTV parallel to the molecular director will undergo a phase change of

$$\phi = \frac{2\pi n_e d}{\lambda}, \quad (5.1)$$

and emerge linearly polarised,  $d$  is the thickness of the LC.

Light polarised perpendicular to the director will undergo a phase change of

$$\phi = \frac{2\pi n_o d}{\lambda}, \quad (5.2)$$

but will still emerge linearly polarised.  $n_o$  and  $n_e$  are the ordinary and extraordinary refractive indices of the birefringent LC, and  $n_e - n_o > 0$ , giving positive dielectric anisotropy.

To find the correct configuration, the orientation of the molecular directors at the front face of the LCTV must be determined as follows. Intensity nulls for an LCTV sandwiched between polariser and analyser with zero applied voltage, can only be achieved if the input polarisation is either parallel or perpendicular to the

molecular director, (Kirsch, 1992). Light entering the front face polarised at any other angle will emerge elliptically polarised. The polarisation state of the exit light can therefore be used to determine two possible orientations of the molecular director at the front face.

Using this experimental method intensity nulls were found for incident polarisations of  $4^\circ$ ,  $94^\circ$ ,  $184^\circ$  and  $274^\circ$  to the vertical. Using the property of LC's that predicts the maximum phase modulation only for incident light polarised parallel to the molecular director, it was determined that the molecular director at the front face was inclined at  $4^\circ$  to the vertical. The phase and amplitude mostly configurations can be verified using the experimental setup shown in Fig 5.2, which consists of a Mach-Zender interferometer and imaging system. The 'brightness' control was set to mid-range for this first approximate characterisation.

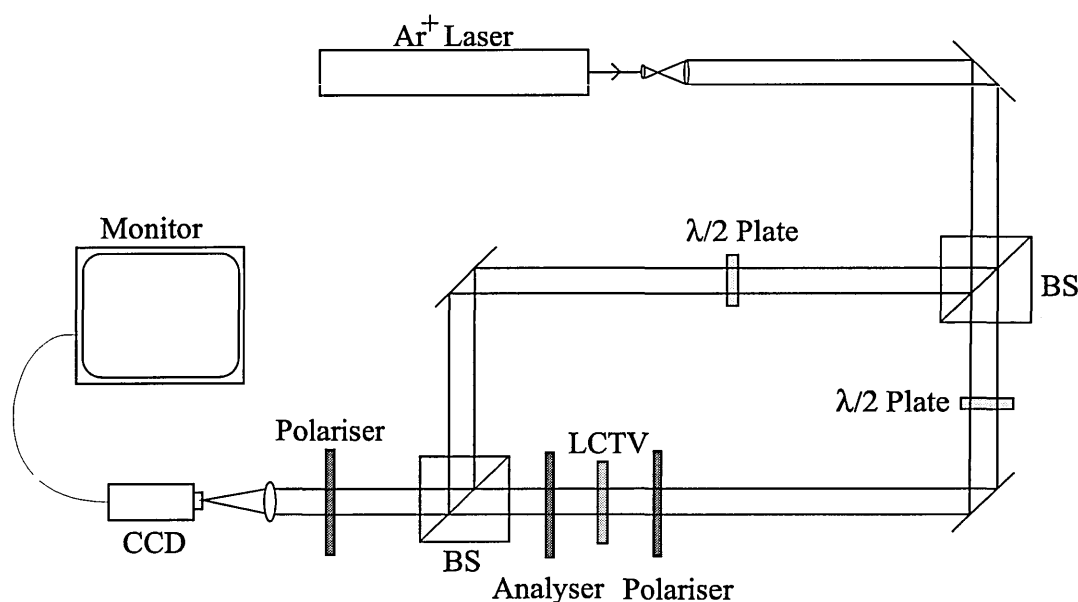


**Fig. 5.2** Experimental setup for verifying the molecular director orientation.

BS is a beam splitter,  $\lambda/2$  is a half-wave plate, CCD is a charge coupled device camera.

Light from an argon ion laser operating at the 514.5nm wavelength was used to characterise the LCTV since this is the wavelength used for later processing applications. The beams are aligned so that the final image seen on the monitor has a region showing the original LCTV image and another region where this image has been allowed to interfere with the second beam. An image consisting of alternate regions of high and low grey level is displayed on the LCTV. If there is no phase variation between the high and low grey levels then continuous interference fringes will be seen, otherwise there will be a displacement at each grey region border. The polariser before the CCD camera is to reduce the intensity if necessary.

The results from this demonstration are shown in Fig. 5.3, where the upper image shows the continuous interference fringes resulting from minimum phase modulation and the lower image shows discontinuous fringes resulting from a phase mismatch between the different grey levels, verifying that the molecular director is at  $4^\circ$  to the vertical. Each image was obtained with the polariser and analyser in the appropriate modulation orientation. These images also show the high degree of optical flatness of the LCTV screen, if there were an appreciable thickness variation across the screen, the concentric fringes would be distorted.



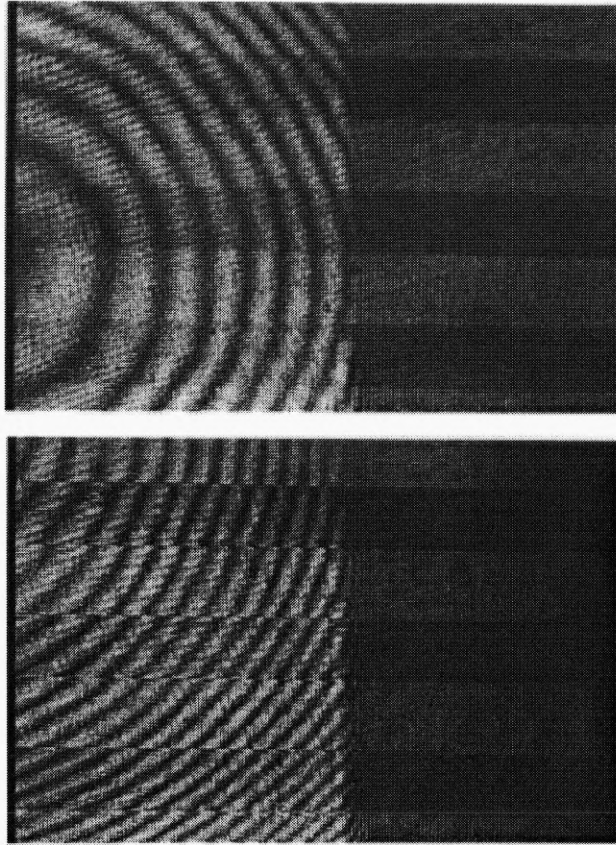


**Fig. 5.3** Interference fringes showing amplitude and phase mostly operation of the LCTV.

Now that the orientation of the molecular director has been determined we can carry out a more in-depth characterisation of the amplitude and phase modulation and how it is affected by variations in the ‘brightness’ level and hence bias voltage. The LCTV is to be used as a pure amplitude modulator, the aim is therefore to minimise the phase modulation and maximise the contrast ratio, (the ratio of maximum to minimum transmitted intensity). Amplitude mostly operation is therefore achieved when the ‘contrast’ is set at the maximum level of 10 (Gorecki, 1996).

The system used to measure the variation of phase with grey level is shown in Fig. 5.4 (Soutar, 1994), it is basically an imaging system with a spatial filtering element. A Ronchi grating was placed in the path of an unexpanded, circularly

polarised Ar<sup>+</sup> laser beam. An achromatic lens was positioned at a distance of twice its focal length (2f) from the grating, which produced an image a distance 2f from the lens, and the zero order diffraction from the pixel structure of the LCTV is magnified onto a CCD camera. A spatial filter is used to block all but the two first order diffractions from the Ronchi grating, each of these beams passes through one half of the LCTV and forms a simple two beam interference pattern at the CCD. The magnification is adjusted until four or five fringes are seen on the monitor screen.

One half of the LCTV is then set at grey level 0 whilst the other is varied; depending on the phase shift introduced by the altered half of the LCTV, the interference pattern will move accordingly. It can be shown that the relative phase (in radians) between the two beams will be given by

$$\phi = 2\pi\left(\frac{\Delta}{\Lambda}\right), \quad (5.3)$$

where  $\Delta$  is the interference fringe displacement and  $\Lambda$  is the fringe period. The final values were calculated from the average of a series of six measurements, the displacement and period of the fringes was measured directly from the monitor screen.

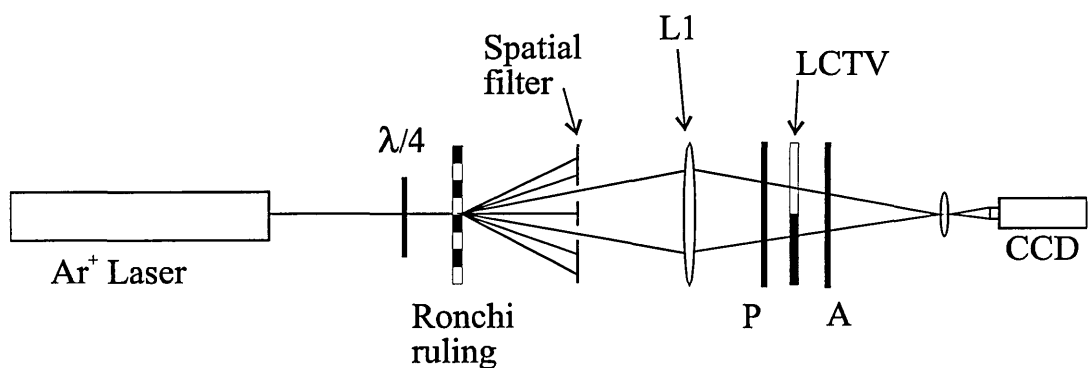


**Fig. 5.4** Experimental configuration for measuring the phase modulation of the LCTV. P and A are polariser and analyser respectively, L1 is an achromatic lens, and  $\lambda/4$  is a quarter wave plate.

The phase shift introduced by grey levels from 0 to 255 is shown for various 'brightness' levels in Fig. 5.5. The minimum phase shift was found with the 'brightness' set at 6.5 which gave a maximum phase variation of less than  $\pi/4$  radians across the whole grey level range.

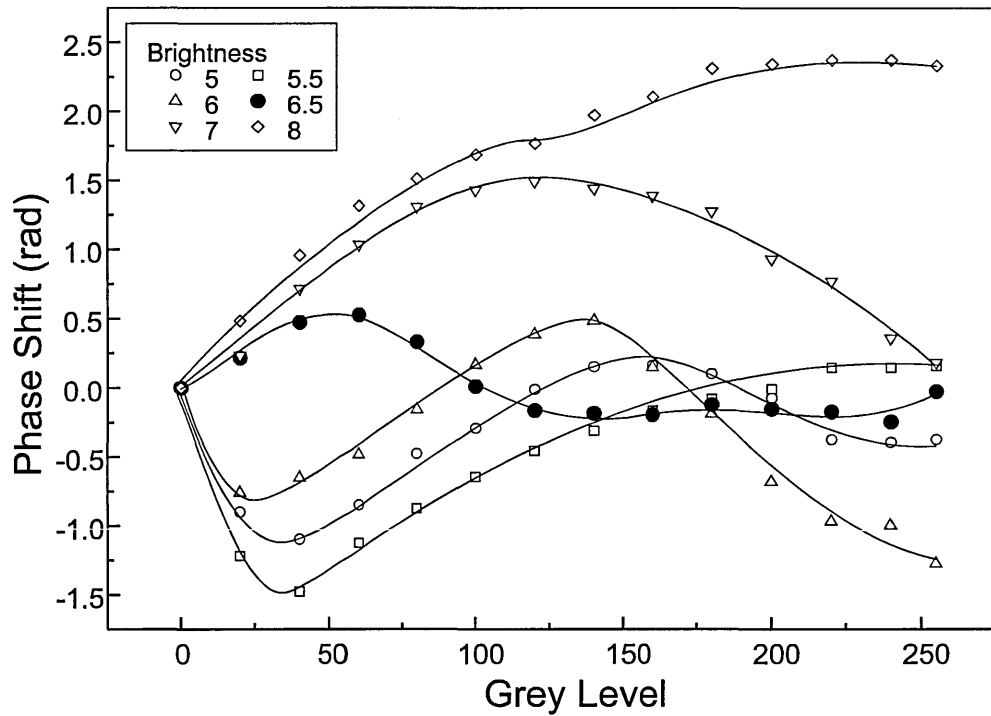


**Fig. 5.5** Phase shift dependence on grey level of the LCTV for various 'brightness' levels.

Problems were encountered as the varying grey level became very bright since the fringes were not visible due to the very low modulation. This was solved by placing neutral density filters in the path of the bright beam then using the horizontal shift of the monitor to adjust the fringe pattern position to compensate for any phase change introduced by the filter.

The LCTV must also be characterised for amplitude, and therefore intensity, modulation. The grey level modulation of transmitted amplitude changes for different polariser and analyser positions, so once the minimum phase configuration has been found, the amplitude modulation must be determined. This was accomplished using a

Newport power meter with wavelength selection to measure the intensity of the zeroth diffraction order. The results are shown in Fig. 5.6, the minimum phase modulation configuration gives a contrast ratio of 30:1. Contrast ratios up to 1000:1 and phase modulation of over 360° have been reported (Laude, 1993) with a similar Epson LCTV, but neither was obtained for a true amplitude or phase mostly configuration.

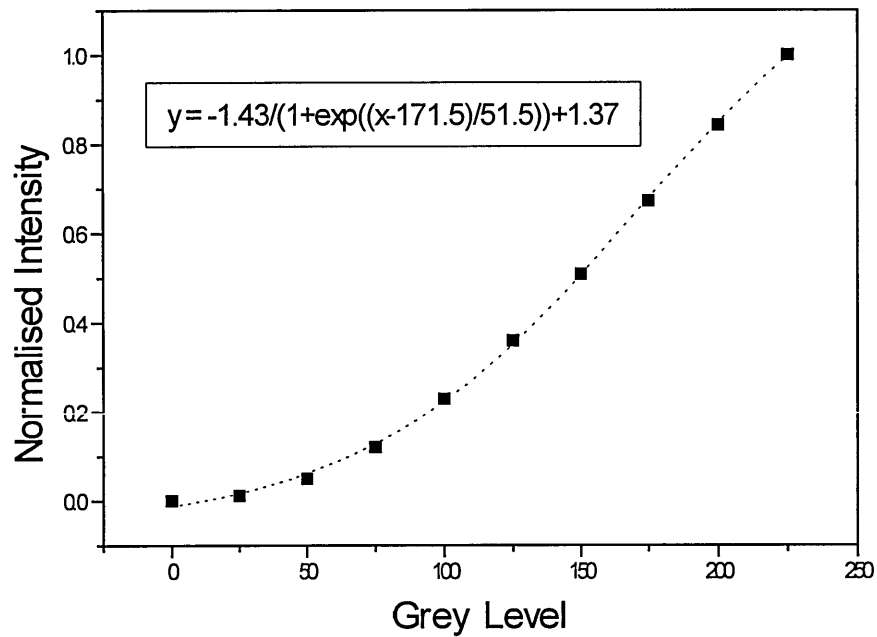


**Fig. 5.6** Normalised transmitted intensity as a function of grey level for the amplitude mostly configuration.

The normalised intensity modulation is well described by the Boltzman distribution shown on the graph. This function can be inverted to give

$$\text{Grey level} = 255 \times \left\{ 51.5 \times \ln \left[ \left( \frac{-0.06 - 1.37}{y - 1.37} \right) - 1 \right] + 171.5 \right\}, \quad (5.4)$$

where  $y$  is the desired normalised intensity. This formula will be used in later IDL routines to provide a linear grey scale used in preprocessing to manipulate the grey levels of any images to be displayed. This is essential for any processing applications where the grey scale information is important and a linear relationship between image grey scale and transmitted intensity is necessary.

### **5.3 Pixel Registration**

The Epson LCTV has three possible signal inputs; composite video (accepting PAL and SECAM, the European and French television coding systems respectively), digital RGB (Red, Green, Blue) and analogue RGB. Several methods of image signal input were tested to determine a satisfactory method giving controllable and reliable pixel registration and grey level control.

The images to be displayed are generated and stored by a personal computer and these images must be displayed by some software package, before a signal is sent to the electronics controlling the LCTV. Most software packages that were tested (e.g. GDS and GWS) were found to dither the grey levels (i.e. form a grey level by mixing two other levels), or form an image of an inappropriate size. The best solution was found by using a Vision-EZ (model DT55) framegrabber board which has its own display software (Global Lab Acquire) and an analogue RGB output. The framegrabber board displays PCX (Zsoft paintbrush) files of size 768×512 pixels with 256 grey levels, which are sampled in some way to be displayed on the LCTV. These files must therefore be processed in order that this sampling results in reliable pixel registration on the 326×264 pixel LCTV.

The active area of the LCTV does not necessarily include all the pixels and seems to depend on the method and size of input signal, similarly not all pixels in the original framegrabber file are necessarily displayed. The process of developing a pixel registration strategy is therefore to identify the active area of the LCTV and determine a scaling factor that will reduce the 768×512 image in the framegrabber to the active area whilst being able to control each individual pixel. The active area is

identified by displaying a series of files with different rows and columns set to a high grey level and inspecting the magnified LCTV displayed images through a CCD camera. The scaling factor is found through trial and error, though a starting point is provided by the ratio of utilised framegrabber pixels to active area pixels. By this process the active areas were identified as those shown in Fig. 5.7, i.e an area of  $712 \times 506$  pixels from the image file is displayed in a  $319 \times 253$  region of the LCTV.

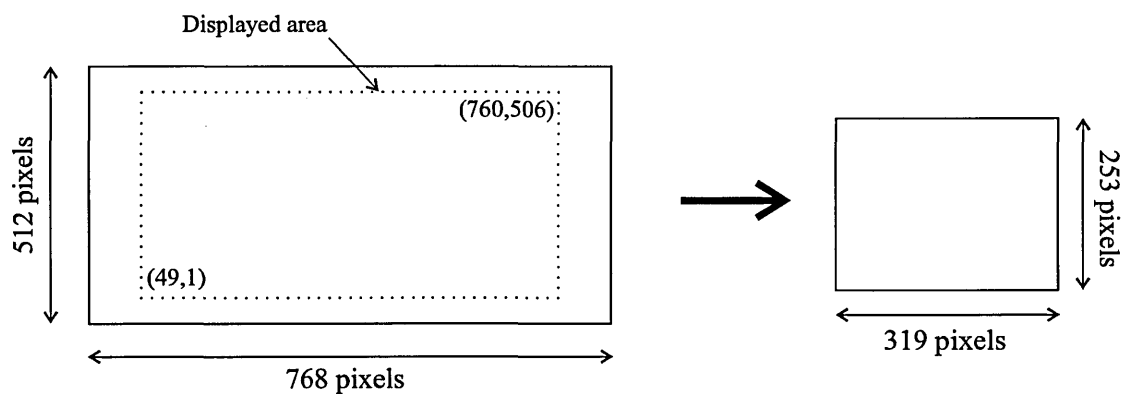


**Fig. 5.7** Active region of framegrabber mapping onto active region of LCTV.

This gives an initial estimate for the scaling factor of 2.232 for the horizontal, and 2 for the vertical. The simple factor of 2 was found to give exact registration in the vertical, the horizontal factor was varied and tested with various images to check the registration. The best, though not perfect, solution was found for a factor of 2.2305, some test files and captured images for this scaling factor are shown below in Fig. 5.8; Liu (1985) also had problems with horizontal pixel registration. The pixel registration was found to drift with time, probably due to temperature changes in the driving electronics, the scaling factor adopted provided stable operation at the stable operating temperature of the electronics.

The laser-printer used to produce this document does not have true grey level reproduction, hence some dithering may be seen in the captured images. It is still

possible nonetheless to see that approximately true pixel registration has been achieved. There are still regions where the scaling factor causes a slight drift and pixels can ‘spill’ over to the adjacent horizontal pixels.

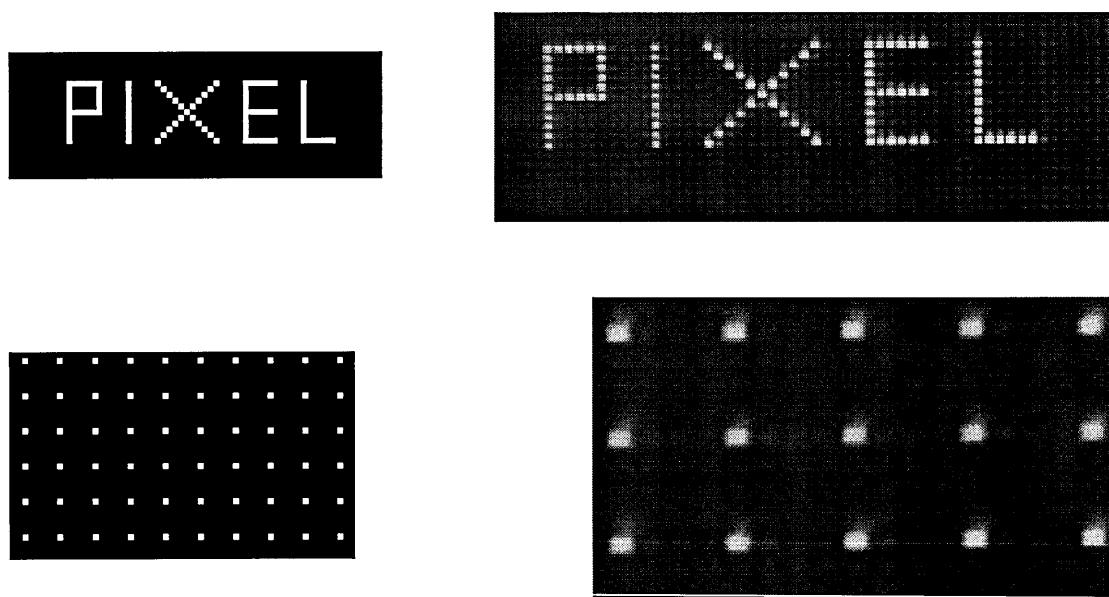


**Fig. 5.8** Test files displayed on LCTV (left) and images captured by the CCD camera (right). The word ‘PIXEL’ is made up of single lines of pixels and the grid has every fifth pixel, horizontally and vertically, at a high grey level.

The next figure shows an original grey level image of a satellite, which will be used in later experiments, and how the processed version appears as it is sent to the framegrabber board. In the processed version the vertical and horizontal addresses of each pixel has been multiplied by 2 and 2.2305 respectively, and the 0 to 255 grey levels have been recalculated according to Eq. 5.4.

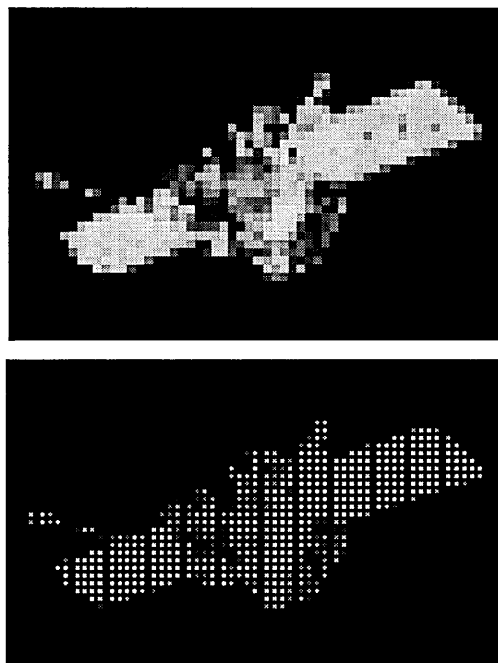


**Fig. 5.9** Original grey scale image and the processed version as it is sent to the framegrabber.

The vertical 'gaps' in the processed image are the points where the sampling misses information from the framegrabber as the image is mapped to the LCTV active area.

Having now determined a method giving linear transmission and correct, reliable pixel registration; it is now possible to use the LCTV as an amplitude mostly spatial light modulator (SLM) for displaying images. The next chapter goes on to discuss joint transform correlators where this LCTV may find applications.



## Chapter 5: References

- Gregory,D.A. 1986, 'Real-time pattern recognition using a modified liquid crystal television in a coherent optical correlator', *App. Opt.* **25**, No4, pp467-469
- Gregory,D.A. Loudin,J.A. Kirsch,J.C. Tam,E.C. Yu,F.T.S. 1991, 'Using the hybrid modulating properties of liquid crystal television', *App. Opt.* **30**, No11, pp1374-1378
- Jutamulia,S. Lin,T.W. Yu,F.T.S. 1987, 'Real-time noncoherent correlator using liquid crystal television', *Opt. Comm.* **64**, No2, pp115-119
- Kirsch,J.C. Gregory,D.A. Thie,M.W. Jones,B.K. 1992, 'Modulation characteristics of the Epson liquid crystal television', *Opt. Eng.* **31**, No5, pp963-969
- Laude,V. Maze,S. Chavel,P. Refregier,Ph. 1993, 'Amplitude and phase coding measurements of a liquid crystal television', *Opt. Comm.* **103**, pp33-38
- Liu,H-K. Davis,J.A. Lilly,R.A. 1985, 'Optical-data-processing properties of a liquid crystal television spatial light modulator', *Opt. Lett.* **10**, No12, pp635-637
- Soutar,C. Wang,Z.Q. Cartwright,C.M. Gillespie,W.A. 1992, 'Real-time optical intensity correlator using photorefractive BSO and a liquid crystal television', *J. Mod. Opt.* **39**, No4, pp761-769
- Soutar,C. Monroe,S.E. Knopp,J. 1994, 'Measurement of the complex transmittance of the Epson liquid crystal television', *Opt. Eng.* **33**, No4, pp1061

## Chapter 6. The Joint Transform Correlator

### 6.1 The Linear Joint Transform Correlator

The concept of the joint transform correlator (JTC) was introduced by Weaver and Goodman (1966). The JTC enabled a reference function to be displayed alongside the input scene in the input plane, as opposed to spatial filter based systems which required a pre-processed filter function. In addition, the JTC is less sensitive to optical system alignment compared to spatial filter based correlators such as the Vanderlugt correlator, (Vanderlugt, 1964)

The basic arrangement of the joint transform correlator is shown in Fig. 6.1. The reference and input scene functions are displayed on SLM1 in positions  $\left(-x_0/2, y_0\right)$  and  $\left(x_0/2, y_0\right)$  respectively. The joint power spectrum (JPS) of these two functions is linearly recorded by the CCD camera; the joint power spectrum is the intensity of the interference formed by the Fourier transforms of the two functions. In general, the Fourier plane recording device requires a large dynamic range to record the JPS linearly. The captured JPS is then displayed on a second SLM and a further Fourier transform yields correlations at the output plane, amongst which is the cross-correlation of the reference and input scene functions. The output can be captured using another CCD camera, and the correlations displayed on a monitor or captured by a framegrabber card for further analysis.

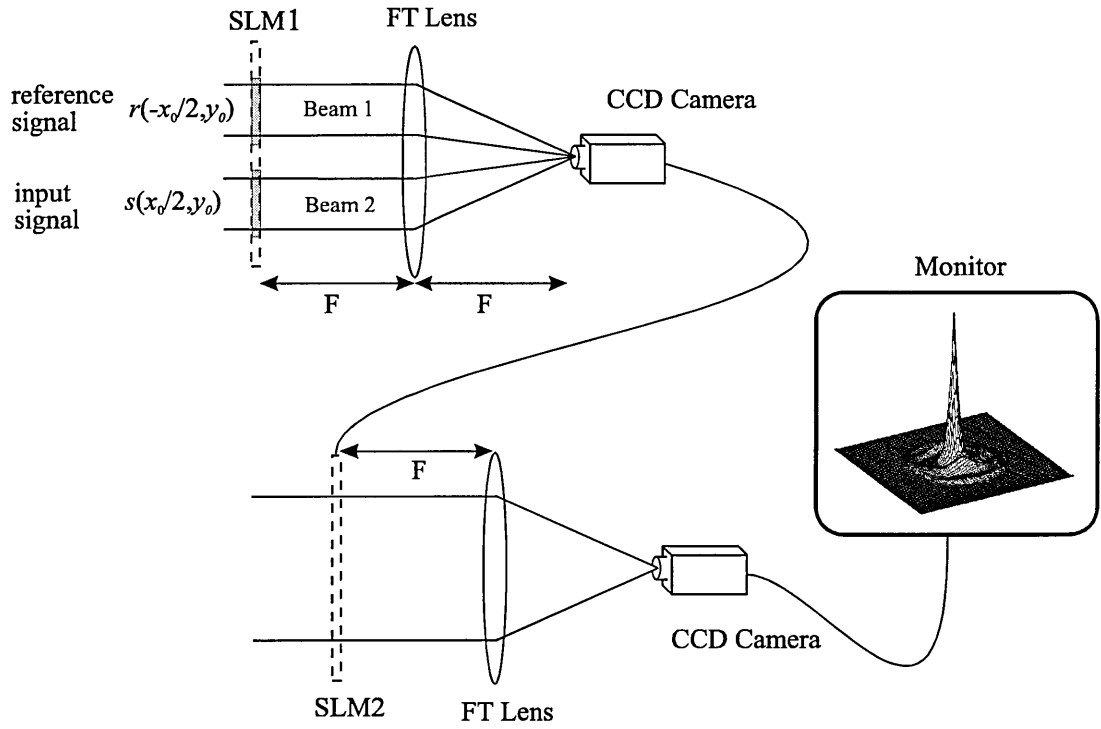


**Fig. 6.1** The joint transform correlator. SLM is a spatial light modulator. CCD is a charge coupled device. FT lens is a Fourier transform lens.

The input plane contains the reference signal  $r(-x_0/2, y_0)$  and the input scene signal  $s(x_0/2, y_0)$ . The joint power spectrum of the two input images is

$$\begin{aligned}
 I(u, v) &= \left| S(u, v) \exp\left(\frac{jx_0 u}{2}\right) + R(u, v) \exp\left(-\frac{jx_0 u}{2}\right) \right|^2 \\
 &= |S(u, v)|^2 + |R(u, v)|^2 \\
 &\quad + |S(u, v)| \exp[-j\phi_s(u, v)] |R(u, v)| \exp[+j\phi_R(u, v)] \exp(-jx_0 u) \\
 &\quad + |S(u, v)| \exp[+j\phi_s(u, v)] |R(u, v)| \exp[-j\phi_R(u, v)] \exp(jx_0 u)
 \end{aligned} \tag{6.1}$$

where  $(u, v)$  are the spatial frequency coordinates, and  $S(u, v) = |S(u, v)|\exp[j\phi_S(u, v)]$  and  $R(u, v) = |R(u, v)|\exp[j\phi_R(u, v)]$  correspond to the Fourier transforms of the input scene and reference signal,  $s(x, y)$  and  $r(x, y)$  respectively. Eq. (6.1) can be rewritten as

$$I(u, v) = |S(u, v)|^2 + |R(u, v)|^2 + 2|S(u, v)||R(u, v)|\cos[x_0 u + \phi_S(u, v) - \phi_R(u, v)] \quad (6.2)$$

In the conventional, linear case the inverse Fourier transform of Eq. (6.1) can produce the following correlation signals at the output plane

$$C(x', y') = R_{11}(x', y') + R_{22}(x', y') + R_{12}(x' - x_0, y') + R_{21}(x' + x_0, y') \quad (6.3)$$

where

$$\begin{aligned} R_{21}(x', y') &= R_{12}(-x', -y') = \iint s(\xi, \zeta)r(\xi - x', \zeta - y')d\xi d\zeta, \\ R_{11}(x', y') &= \iint s(\xi, \zeta)s(\xi - x', \zeta - y')d\xi d\zeta, \text{ and} \\ R_{22}(x', y') &= \iint r(\xi, \zeta)r(\xi - x', \zeta - y')d\xi d\zeta. \end{aligned} \quad (6.4)$$

In Eq. (6.3) the first two terms are the on-axis autocorrelation terms. The terms of interest are the third and fourth terms which are the cross-correlations of the reference with the scene signal, and yield the same output as a matched filter. These cross-correlations are recovered in the Fourier transformed JPS. For correct operation of the JTC there should be a sufficient separation between the reference signal and the input scene to avoid overlap between the on-axis auto-correlation terms and the off axis cross-correlation terms.

## 6.2 The Binary Joint Transform Correlator

It is not necessary for the JPS to be recorded linearly, and nonlinear transformation of the JPS, such as binarisation can give very good correlation results. Such JTC's with a nonlinear transformation in the Fourier plane are called nonlinear JTC's (Javidi, 1994, Ch. 4). Nonlinear transformations can improve light efficiency, correlation peak size, and discriminability for many typical images (Javidi, 1989, 1990, 1991). Another important advantage of binary JTC's is hardware availability, binary or high-contrast optical recording devices are more easily made than continuous devices with a large dynamic range.

The incentive for studying nonlinear JTCs arises from the success of unconventional correlators, (Horner, 1985) discussed in Section 4.4, that use nonlinear transformation in the Fourier plane. In one of these unconventional correlators, the phase-only filter, the Fourier magnitude of the reference function is removed giving improved correlation performance. Javidi (1989) shows that a square-root nonlinearity applied to the JPS in the Fourier plane gives results similar to a phase-only correlator, and that hard clipping, or thresholding, causes it to behave like an inverse filter correlator.

In the last few years, there have been many papers published in the pattern recognition field which have analysed different correlation systems in order to increase the discrimination capability. In particular, the binarisation of the joint power spectrum (JPS) has been widely used and has been shown to be a reliable method (Javidi, 1989, 1991). The binary JTC is described below for later comparison with a development of the photorefractive JTC.

The binary joint power spectrum  $I_b(u, v)$  is obtained by assigning the values 0 or +1 to  $I(u, v)$ , as below

$$I_b(u, v) = \begin{cases} 1 & \text{for } I(u, v) \geq I_T(u, v) \\ 0 & \text{for } I(u, v) < I_T(u, v) \end{cases}, \quad (6.5)$$

where  $I_T(u, v)$  is a predetermined threshold function. This bipolar function can be expressed as a Fourier expansion

$$I_b(u, v) = \sum_{n=0}^{\infty} H_n[R(u, v), S(u, v)] \cos\{n[x_0u + \phi_S(u, v) - \phi_R(u, v)]\}. \quad (6.6)$$

Thresholding the JPS results in an infinite sum of harmonic terms, the correct phase information about the correlation signal is recovered from the first order harmonic of the thresholded JPS. An appropriate threshold function  $I_T(u, v)$  is given by (Javidi, 1991)

$$I_T(u, v) = |R(u, v)|^2 + |S(u, v)|^2. \quad (6.7)$$

This threshold function maximises the first-order amplitude modulation and, as a result, maximises the first-order correlation peak. This threshold function also relaxes the separation requirement between the reference function and the input signal, and eliminates even-order harmonic terms and correlations between different elements of the input scene.

When the above  $I_T$  is used for binarisation, the amplitude modulation of the binarised joint power spectrum can be expressed as

$$H_n[R(u, v), S(u, v)] = \begin{cases} 0 & \text{for } n = \text{even}, n > 0 \\ \frac{2}{\pi n} (-1)^{\frac{n-1}{2}} & \text{for } n = \text{odd}, n \geq 1 \end{cases}. \quad (6.8)$$

The Fourier component of the transmittance function that generates the first-order correlation signals for  $n = 1$  is

$$I_1(u, v) = \frac{2}{\pi} \cos[x_0u + \phi_S(u, v) - \phi_R(u, v)]. \quad (6.9)$$

Therefore by neglecting terms  $n > 1$ , which are very weak in terms of intensity, the correlation can be written by Fourier transforming Eq. (6.9) to give

$$c(x, y) = \delta(x - x_0, y) + \delta(x + x_0, y), \quad (6.10)$$

which is the ideal output from a correlator. It is evident that the binary JTC using this threshold function removes the Fourier amplitudes of both the reference signal and the input image for the first-order Fourier transmittance component, thus the first-order correlation is based only on their Fourier phases.

One limitation of bipolar joint transform correlators is the presence of redundant self-correlation terms due to the  $n$ -order harmonics in Eq. (6.6). To avoid this problem, the elimination of part of the Fourier plane information has been proposed. To remove the intra-class terms of Eq. (6.2), the intensity of the Fourier transform of the scene and the reference can be evaluated separately, and the subtraction between Eqs. (6.2) and (6.7) may then be obtained by computer (Osugi, 1994).

To obtain ideal  $\delta$ -like correlations, other solutions have been proposed by different authors. One possible way is based on the direct processing of the JPS (Carnicer, 1995) and in another, inverse-filter solutions have been suggested (Vallmitjana, 1995; Cheng 1993).

The nonlinear binary joint transform correlator can therefore produce a sharp peak with a large peak-to-sidelobe ratio. The next section discusses the behaviour of a joint transform correlator with a photorefractive BSO crystal as the recording medium. A method for encoding images to provide a performance analogous to that of the binary JTC is also described.

### 6.3 The Photorefractive Joint Transform Correlator

Photorefractive recording materials offer the advantage of simultaneous recording and read-out of the hologram, removing the need for development and thus avoiding the positional constraints previously encountered by the Vanderlugt filter (Vanderlugt, 1964). The use of spatial light modulators (SLM) to display the images offers the possibility of continuous update of the hologram, and the combination of photorefractive crystals and SLMs can be used to design real-time pattern recognition systems.

There are other advantages gained by using a photorefractive crystal as the JPS processor, rather than a CCD/SLM setup, such as increased resolution in the Fourier plane. The pitch of the pixels in the CCD camera and LCTV, used later in this work are approximately  $10\mu\text{m}$  and  $80\mu\text{m}$  respectively, (though SLM's with a smaller pitch are available). The BSO crystal would operate as a continuous recording surface. Also the performance is not degraded by Fourier plane quantisation (Osugi, 1996). As mentioned earlier a continuous device with a large dynamic range is required to record the JPS accurately. CCD cameras record intensity as a limited number of quantisation levels, the greater the number the closer the approximation to continuity. Javidi *et al* (1991, B) have reported serious deterioration in the performance of a binary JTC with input scene noise for quantisation levels below  $2^{12}$ . The inexpensive hardware components used in later experiments each have  $2^8$  quantisation levels, therefore this hardware would result in such deterioration of performance.

The fact that the magnitude of the photorefractive space charge field depends on the modulation of the intensity, rather than its absolute value which is the case for linear detectors, can be used to implement Fourier plane nonlinearities. The degree of the nonlinearity may be adjusted by varying beam ratios. Khoury (1994) has reported a photorefractive correlator that operates by using two-beam coupling to implement nonlinearity in the Fourier plane, correlations similar to inverse filters and phase-only filters were obtained.



Referring to Figs. 6.1 and 7.1, which show the classic and photorefractive JTC's respectively; and assuming that the two writing beams, beams 1 and 2 are of a suitable wavelength to enable hologram formation in the crystal, in these experiments the 514nm line from an argon-ion laser is used. Let us look at the response of the material to the interference pattern formed between the fields  $r\left(-x_0/2, y_0\right)$  and  $s\left(x_0/2, y_0\right)$ . We also assume that the photorefractive crystal is thin, in the sense that the two fields are constant across the thickness of the crystal, and we can neglect any coupling between the two waves. In this case the amplitude of the refractive index variation induced in the material that gives rise to the first order cross-correlations is obtainable from Eq (2.45) as

$$\Delta n = n_0^3 r_{41} E_1(m(u, v)), \quad (6.11)$$

where  $E_1(m(u, v))$  is calculated as a function of the modulation but also contains the phase information of the JPS, and may be written as

$$E_1(m(u, v)) = |E_1(m(u, v))| \cos[x_0 u + \phi_S(u, v) - \phi_R(u, v)]. \quad (6.12)$$

The JPS incident on the photorefractive BSO crystal has a certain modulation  $m(u, v)$  for each spatial frequency

$$m(u, v) = \frac{2\sqrt{I_S(u, v)I_R(u, v)}}{I_S(u, v) + I_R(u, v)}, \quad (6.13)$$

where  $I_S(u, v) = |S(u, v)|^2$  and  $I_R(u, v) = |R(u, v)|^2$  are the intensities of the two Fourier transformed incident fields, which are now acting as the writing beams.

We next assume that a third, plane-wave probe beam is Bragg-matched to the grating produced by the two writing beams and furthermore it is arranged that the presence of the probe beam does not perturb the grating. This is easily achieved for

BSO since a He-Ne beam can be used as the third probe beam, and BSO is less sensitive to 633nm light. The probe beam is diffracted from the grating to produce a beam which, when inverse Fourier transformed, will give the desired correlation output.

Assuming that the diffraction efficiency is low and ignoring absorption, the amplitude diffraction efficiency,  $\eta'$  is derived from the intensity diffraction efficiency, Eq. (2.56)

$$\eta' = \frac{\pi \Delta n L}{\lambda \cos \theta}, \quad (6.14)$$

and therefore the amplitude of the diffracted probe. The probe is assumed to have unit amplitude, may be obtained using Eq's (6.11) - (6.14) to give

$$-\frac{\pi L n_0^3 r_{41}}{\lambda \cos \theta} |E_1(m(u, v))| \cos[x_0 u + \phi_S(u, v) - \phi_R(u, v)], \quad (6.15)$$

which is of the form of the cross-correlations given in Eq. (6.2). So photorefractive materials can be used as the active media for real-time correlation and convolution processes.

The Fourier component of the transmittance function that generates the first-order correlation intensity signal can therefore be expressed as having the form

$$|E_1(m(u, v))| \cos[x_0 u + \phi_S(u, v) - \phi_R(u, v)]. \quad (6.16)$$

The choice of model used to describe the modulation of the space charge field depends on the particular characteristics of the system, in particular the intensity modulation, as described in Chapter 2.

The next section of this chapter deals with a method, developed as part of this work, to improve the performance of a photorefractive JTC by additional processing of the reference and scene functions. We note that if  $|R(u, v)| = |S(u, v)|$  for all  $(u, v)$

then  $m(u,v)=1$ , leading to a maximised, constant modulation of the space-charge field. This high modulation for all spatial frequencies will improve diffraction efficiency, increase the information contribution from the high frequency component, and result in phase-only correlation. This can be achieved for all  $(u,v)$  in practical terms by setting  $|R(u,v)| = |S(u,v)| = 1$ , which is possible by encoding the scene and reference to give phase-only distributions in the Fourier plane. The cross-correlation term of the JPS will therefore be formed by two fields of unit amplitude, resulting in a constant modulation of the Fourier plane cosinusoidal term, similar to the binarised JPS described earlier, Eq. (6.9) without the unwanted higher harmonic terms.

## 6.4 Object-Plane Phase-Only Filters

The object-space distribution giving a phase-only Fourier transform is calculated as follows: Let  $F(u,v)=|F(u,v)|\exp[i\phi(u,v)]$  be the Fourier transform of a two-dimensional distribution  $f(x,y)$ . Let us define the phase-only version of  $f(x,y)$  in object space  $f_{PO}(x,y)$  as

$$f_{PO}(x,y) = FT^{-1} \left[ \frac{F(u,v)}{|F(u,v)|} \right] = FT^{-1} \left\{ \frac{FT[f(x,y)]}{|FT[f(x,y)]|} \right\}, \quad (6.17)$$

where FT and  $FT^{-1}$  are the Fourier and inverse Fourier transform operators respectively. The original input,  $f(x,y)$ , is real and positive so the inverse transform of the frequency plane phase-only filter,  $f_{PO}(x,y)$  is real, with positive and negative values. Since the LCTV is only capable of displaying real, positive amplitude information, the filters must be encoded to provide the negative amplitude information at the Fourier plane. This is achieved by a further simplification of Lee's method of generating holograms by computer, (Lee, 1970) in which a complex function is decomposed into four real, positive components. Since the object plane filters are real they can be encoded using two real, positive components, or pixels. The technique used for encoding the positive and negative values is derived from the

method of subtraction based on the decomposition of the function in two parts (Vallmitjana, 1995), the positive and negative, and encoding in Ronchi gratings with the same frequency but with a  $\pi$  phase difference. This provides the subtraction of amplitudes in Fourier space.

A real two-dimensional function  $h(x, y)$  may be expressed as the sum of two functions

$$h(x, y) = h^+(x, y) - h^-(x, y), \quad (6.18)$$

where

$$\begin{aligned} h^+(x, y) &= h(x, y) && \text{when } h(x, y) > 0, \\ &= 0 && \text{when } h(x, y) < 0, \\ h^-(x, y) &= -h(x, y) && \text{when } h(x, y) < 0, \\ &= 0 && \text{when } h(x, y) > 0. \end{aligned} \quad (6.19)$$

Both  $h^+(x, y)$ , and  $h^-(x, y)$  are real, positive functions and are called bipolar filters.

The transmission of a Ronchi grating may be presented by its Fourier series expansion, (Vallmitjana, 1995)

$$r^+(x, y) = 1 + \sum r_n \sin\left(\frac{2\pi nx}{p}\right), \quad (6.20)$$

where  $p$  is the spatial period. If the Ronchi grating is displaced by  $p/2$ , its transmission is

$$r^-(x, y) = 1 - \sum r_n \sin\left(\frac{2\pi nx}{p}\right). \quad (6.21)$$

Note that  $r^+$  and  $r^-$  alternate the values 0 and 1 along the  $x$ -axis and that they are complementary gratings.

Now consider the following function

$$\begin{aligned}
 h_c(x, y) &= h^+(x, y)r^+(x, y) + h^-(x, y)r^-(x, y) \\
 &= [h^+(x, y) + h^-(x, y)] + [h^+(x, y) - h^-(x, y)]. \\
 &\quad \times \sum r_n \sin(2\pi nx/p)
 \end{aligned} \tag{6.22}$$

Its two-dimensional Fourier transform is given by

$$\begin{aligned}
 H_c(x, y) &= [H^+(u, v) + H^-(u, v)] \\
 &\quad + [H^+(u, v) - H^-(u, v)] \otimes \sum r_n \delta(u - n/p) \\
 &= [H^+(u, v) + H^-(u, v)] \\
 &\quad + H(u, v) \otimes \sum r_n \delta(u - n/p)
 \end{aligned} \tag{6.23}$$

Finally by taking the Fourier transform of only one diffraction order we obtain the desired function  $h(x, y)$ .

The encoding of a digital function is carried out by representing each sampled value by using four pixels. Both left pixels are given the original value if it is positive, while the two right pixels remain at zero. Similarly, both right pixels are given the absolute of the original value if it is negative and the two left ones remain zero. Each set of two vertical pixels therefore forms part of a grating, the gratings arising from the positive and negative values are complementary and provide subtraction of amplitudes in the Fourier plane. Each sampled value was chosen to be represented by two vertical pixels after testing of other possibilities as part of this work.

In the experimental realisation of such object plane filters, the transmission of the encoded reference filter is usually lower than that of the encoded scene filter. This is caused by the necessary scaling of the encoded filters to the 256 grey levels supported by the LCTV. The grey level of the filter was scaled by calculating a new maximum to be used by the IDL 'BYTSCL' procedure which scales a range of numbers to the required 256 levels. The relationship between this maximum and the

transmitted intensity was calculated and used to calculate the appropriate scaling factor, this scaling procedure may be seen in the IDL program shown in Appendix C which is described in Section 7.1. Optimum diffraction efficiency is obtained for an intensity modulation of  $m = 1$ , this can be achieved if the encoded reference filter,  $r(x,y)$  is multiplied by a scaling constant,  $k$ , such that

$$k = \left[ \frac{\langle |s(x,y)|^2 \rangle}{\langle |r(x,y)|^2 \rangle} \right]^{\frac{1}{2}}, \quad (6.24)$$

i.e. the average transmitted intensity of the two images in the object plane should be equal.

The end product of calculating the object-plane phase-only filter and applying the Ronchi grating encoding procedure is shown in Fig. 6.2 for an image of a single satellite which is used as a reference image in later experiments. The form of the Ronchi gratings can be seen in the encoded version as an array of vertical pixel pairs.

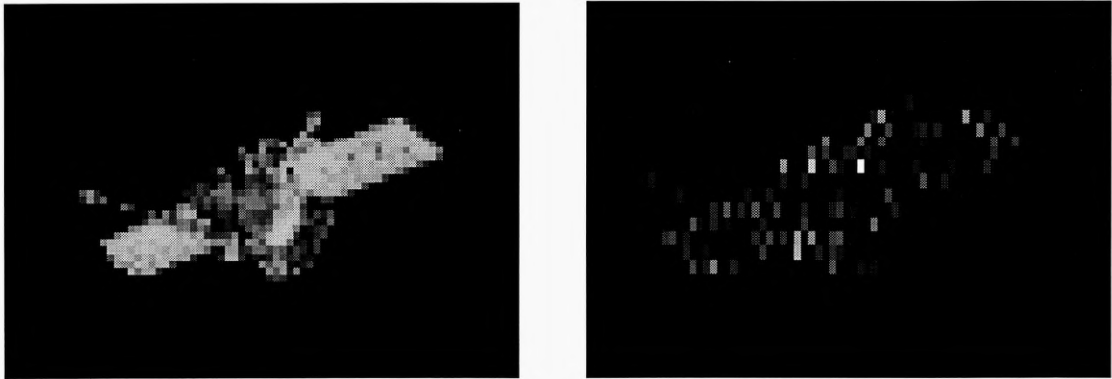


**Fig. 6.2** Original (left) and object-plane encoded (right) images of a satellite.

The programme written to calculate the object plane filters, POF.PRO, is listed in Appendix B.

## 6.5 Processing requirements of binary and photorefractive JTC's

It has been shown that the correlation performance of a phase-only photorefractive joint transform correlator (POPJTC) can be equivalent to a binary JTC (BJTC) by using input distributions which give phase-only information at the Fourier plane. The better operating characteristics of BSO with respect to a CCD, e.g. resolution and lack of quantisation, give additional reasons for its use as a Fourier plane recording material. In the POPJTC, the scene is displayed as an encoded distribution and this means that digital preprocessing according to Eq. (6.17) must be carried out. This is the main time-bottleneck in the recognition process, and processing time is an important consideration since many scenes may have to be analysed.

To compare the processing times of the two techniques, we must evaluate the number of floating point operations needed to preprocess the scene in order to obtain the encoded distribution. Note that only the scene is taken into account because the reference is calculated at a previous stage. The time requirements to carry out the correlation using a POPJTC will be compared with the processing time involved in the generation of a binary JPS in a BJTC. These calculations were first performed by Artur Carnicer (Cook, 1998).

The number of floating point operations (flop) needed to calculate a  $N \times N$  point FFT is (Nussbaumer, 1982)

$$flop = 5N^2(\log_2 N - 2) + 32N. \quad (6.25)$$

To obtain an object-space encoded image, we need to divide each point of the Fourier transform by its modulus, so we add  $5N^2$  more floating operations. Finally we inverse Fourier transform the results so the total number of operations is

$$5N^2(\log_2 N - 2) + 32N + 5N^2 + 5N^2(\log_2 N - 2) + 32N =$$

$$5N^2(2\log_2 N - 3) + 64N \quad (6.26)$$

In our case, the scene consists of  $128 \times 128$  pixels to match the LCTV resolution, so the number of floating point operations is  $0.91 \times 10^6$ . By means of a benchmark test, we can determine the rate of MFlops of the computer that manages the optical system. For example, our inexpensive personal computer based on a Pentium processor at 120MHz performs at 13 MFlops (Cook, 1998), so the preprocessing time is under 0.1 s. A further comparison of a quarter of the pixels and an integer operation for each pixel are needed, resulting in approximately  $N^2$  ops which is small compared to Eq. (6.26).

On the other hand, as was pointed out in Section 6.2, the binary JPS is obtained by registering separately the JPS and the power spectra of the scene and the reference. As an ordinary CCD works at video rates (1/30 s for frame), the theoretical time requirements to store these three images is 0.1s (in practice, this time is higher because we do not take into account other factors related with computer hardware).

The next step is to compute the binary JPS processing time: 2 integer operations and a comparison are required to determine the value of each pixel of the BJPS, so we need to calculate  $3N^2$  integer operations (op). Note that in this case the number of points is assumed to be  $512 \times 512$  according to the sampling capability of the digitiser board. Consequently,  $3N^2 \approx 0.8\text{Mop}$ , and the total processing time is  $> 0.1$  s. Despite the fact that the POPJTC requires the calculation of two two-dimensional FFTs, the bottleneck imposed by the recording of three spectra in a BJTC allows us to conclude that a POPJTC performs correlations at a similar speed to a BJTC using current equipment.

The computational requirements of the POPJTC or the BJTC can be improved by using appropriate hardware. For instance, the use of specific FFT hardware or faster video cameras and digitiser boards respectively, substantially reduces the time involved in calculations.



## Chapter 6: References

- Carnicer,A. Martin-Badosa,E. Juvells,I. Vallmitjana,S. 1995, 'Spatial envelop-free nonlinear joint transform correlator', *Opt. Comm.* **114**, pp336-343
- Cheng,F. Yu,F.T.S. Gregory,D.A. 1993, 'Multitarget detection using spatial synthesis joint transform correlator', *Appl. Opt.* **32**, No32, 6521-6526
- Cook,N.J. Carnicer,A. Vallmitjana,S. Juvells,I. Cartwright,C.M. Gillespie,W.A. 1998, 'Implementation of a Photorefractive Binary Joint Transform Correlator', *J. Opt. Soc. B.* (To be published)
- Horner,J.L. Leger,J.R. 1985, 'Pattern recognition with binary phase-only filters', *Appl. Opt.* **24**, No5, pp609-611
- Javidi,B. 1989, 'Nonlinear joint power spectrum based optical correlation', *Appl. Opt.* **28**, No12, pp2358-2367
- Javidi,B. 1990, 'Comparison of nonlinear joint transform correlator and nonlinear matched filter based correlator', *Opt. Comm.* **75**, No1, pp8-13
- Javidi,B. Wang,J. Tang,Q. 1991, A, 'Multiple-object binary joint transform correlation using multiple-level threshold crossing', *Appl. Opt.* **30**, No29, pp4234-4244
- Javidi,B. Ruiz,J. Ruiz,C. 1991,B, 'Performance of the binary nonlinear joint transform correlators in the presence of the Fourier plane quantization', *Opt. Commun.* **80**, pp275-284
- Javidi,B. Tang,Q. 1992, 'Binary encoding of grey scale nonlinearly transformed filters for optical pattern recognition', *Appl. Opt.* **31**, No20, pp4034-4041
- Javidi,B. Horner,J.L. (Ed's), 1994, *Real-Time Optical Information Processing*, San Diego, Academic Press
- Khoury,J. Cronin-Golomb,M. Gianino,P. Woods,C. 1994, 'Photorefractive two-beam coupling nonlinear joint-transform correlator', *J. Opt. Soc. Am. B*, **11**, No.11, pp2167-2174
- Lee,W.H. 1970, 'Sampled Fourier transform hologram generated by computer', *Appl. Opt.* **9**, pp639-643
- Nussbaumer,H.J. 1982 *Fast Fourier Transform and Convolution Algorithms*, Series

in Information Sciences, Berlin, Springer-Verlag

- Osugi, Y. Zhan, Q. Minemoto, T. 1994 'Hybrid binary subtracted joint transform correlator for a large number of reference patterns using a  $\text{Bi}_{12}\text{SiO}_{20}$  (BSO) spatial light modulator and a laser scanner', *Opt. Rev.* **1**, pp159-162
- Osugi, Y. Mizukawa, H. Minemoto, T. 1996, 'Quantization and truncation conditions of Fourier power spectrum for good performance in a binary subtracted joint transform correlator', *Opt. Rev.* **3**, pp161-170
- Vallmitjana, S. Carnicer, A. Martín-Badosa, E. Juvells, I. 1995 'Nonlinear filtering in object and Fourier space in a joint transform optical correlator: comparison and experimental realization', *Appl. Opt.* **34**, pp3942-3949
- VanderLugt, A. 1964, 'Signal detection by complex spatial filtering', *IEEE Trans. on Inf. Theory*, IT-10, pp139-145
- Weaver, C.S. Goodman, J.W. 1966, 'A technique for optically convolving two functions', *Appl. Opt.* **5**, pp1248-1249

## Chapter 7. The Phase-Only Photorefractive Joint Transform Correlator

### 7.1 Experimental Realisation of the POPJTC

The experimental setup of the phase-only photorefractive JTC (POPJTC) is shown in Fig. 7.1. The input scene and reference function are presented to the LCTV by a framegrabber as described in Chapter 5. The polariser and analyser, before and after the LCTV, are oriented to provide amplitude mostly operation of the LCTV. With amplitude mostly operation a half-wave plate should also be inserted before the BSO crystal to rotate the polarisation of the incident argon ion light to the vertical for optimum refractive index modulation.

The arguments presented in Chapter 4 concerning the formation of the Fourier transform rely on the input to the lens being placed in the object plane, a distance equal to the focal length in front of the lens. The figure showing the experimental setup shows that the LCTV is placed close to the lens, this simplifies the positioning of the LCTV and lens, and can be allowed by considering that the change in distance from the lens will introduce a phase curvature in the Fourier transform of each of the input images. Since we have earlier assumed that the input images are located at  $\left(-x_0/2, y_0\right)$  and  $\left(x_0/2, y_0\right)$ , these phase differences will cancel in the final joint power spectrum, (Goodman, 1968).

The array of pixels which makes up the LCTV produces many diffraction orders at the Fourier plane, the correct phase information for the JPS is contained in the zeroth order. The zeroth order formed at the photorefractive crystal had an Ar<sup>+</sup> laser power of approximately 50  $\mu$ W. The crystal was cut to give the four-wave mixing orientation and hence maximise the refractive index modulation as described in Section 2.3. A d.c. voltage of 5kV was applied to the crystal in the  $\langle 110 \rangle$  direction, to promote the drift of electrons and enhance the space charge field. The

same  $10 \times 9 \times 2$  mm crystal described in Section 3.1 was used for these correlation experiments.

The JPS is analysed using a narrow, low power He-Ne beam which diffracts from the grating formed by only the zeroth order of the diffraction pattern caused by the pixelation of the LCTV, thus satisfying the condition that only one order of Eq (6.22) is transformed. The combination of pixel pitch and choice of lens results in a separation of approximately 2mm between LCTV diffraction orders at the BSO crystal. Assuming that the transform of the joint-scene is weighted by a sinc function, appropriate to the transform of two apertures, there will be negligible overlap between adjacent orders. Since only one diffraction order was analysed by the narrow, low power HeNe laser, separate spatial filtering was not required before the final inverse transform which gives the correlation output.

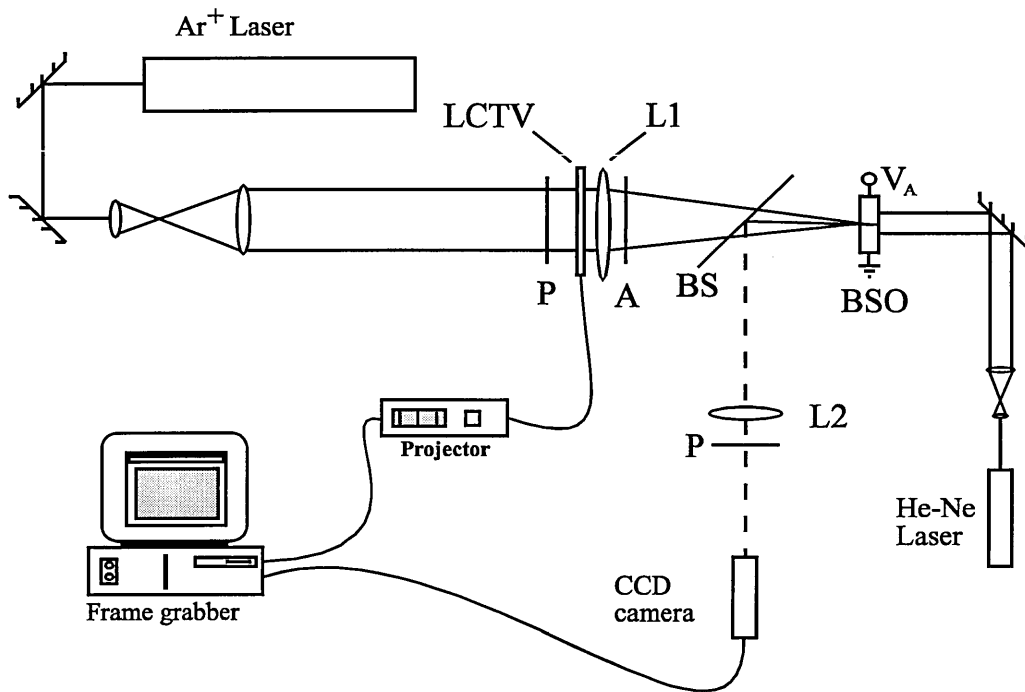


**Fig. 7.1** The photorefractive joint transform correlator. P and A are polariser and analyser respectively, L1 and L2 are Fourier transform lenses, BS is a 20% beamsplitter.

The intensity of the He-Ne beam was adjusted for each correlation so that the maximum intensity of the correlation peak, measured as a grey level, is approximately constant as this ensures that meaningful comparisons of performance measures can be made between filters. A grey level of 230 was chosen as this allowed correlations up to a high noise level to be obtained.

The joint-scene to be presented to the LCTV is shown in conventional form in Fig 7.2; the scene in the upper image has zero added noise, while the lower has added white Gaussian noise with a standard deviation of  $\sigma=70$  grey levels. The reference image, on the left, and any filters calculated from it measure  $64\times 64$  pixels, the input scene and its calculated filters measure  $128\times 128$  pixels.

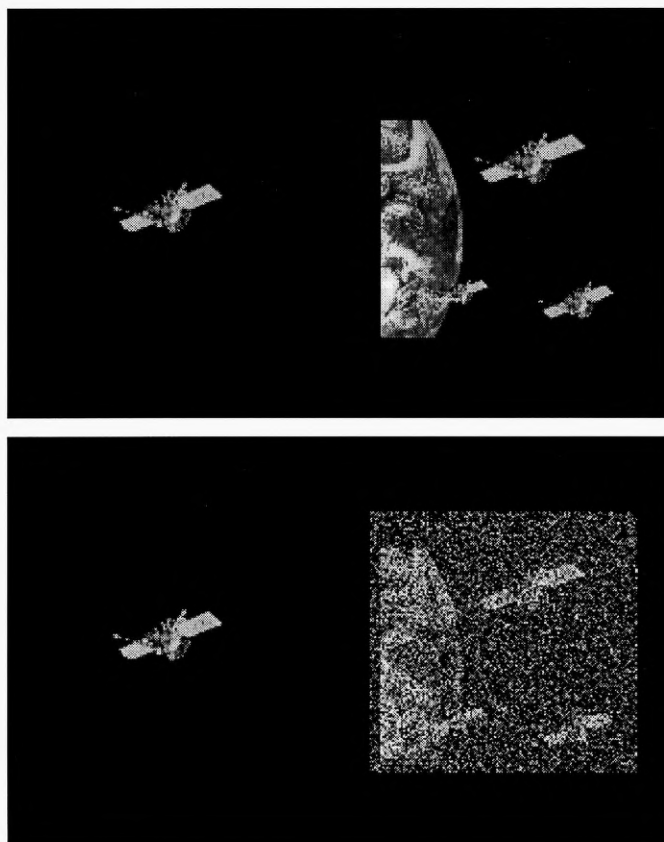


**Fig. 7.2** Conventional, matched scene to be presented to the LCTV; upper scene has no added noise, lower has  $\sigma = 70$ .

A series of joint scenes were calculated with added white Gaussian noise varying from  $\sigma = 0$  to  $\sigma = 100$ . Since the added noise is random, noise arrays of the same standard deviation can yield markedly different results. To ensure that the experimental results are not adversely affected by an untypical noise array, the theoretical correlations for twenty joint scenes with independent noise arrays were calculated using, for the sake of simplicity, the form of the fundamental of the Moharam model mentioned in Section 2.6. The average peak-to-correlation energy (PCE) was then calculated according to Eq. (4.46) and further noise arrays generated until one giving a PCE result close to the average was found. This IDL listing, 'CORRELATE.PRO', is shown in Appendix C.

Again to ensure that a meaningful comparison between filters is made, the noise array that was used in each conventional matched scene is also used when calculating the encoded phase-only joint-scene. The averaging and encoding procedures are carried out by the programme listed in Appendix C.

## 7.2 Theoretical Models and Results

Section 2.6 of this work mentioned that a number of models have been developed to describe the formation of the space charge field within photorefractive crystals. Each of these theories was developed to apply under different modulation conditions; the earlier models, (Kukhtarev, 1976) applied only to low modulation conditions after which, (Moharam, 1979; Ochoa, 1986; Vachss, 1988) efforts were made to extend the theory to high modulations.

To decide which of these models would be most useful in modelling the photorefractive phase-only correlator, we must look at the range of modulations encountered in the photorefractive correlations. Fig. 7.3 shows histograms for the modulations present in the JPS of the conventional matched input and the encoded phase-only input; the upper graph shows results from the noiseless scenes, and the lower from input scenes with added  $\sigma = 80$  noise. Although the encoded filters are designed to give unit amplitude at all spatial frequencies in the Fourier plane, the

necessary scaling of filter values to the 256 grey levels supported by the LCTV results in an imperfect output.

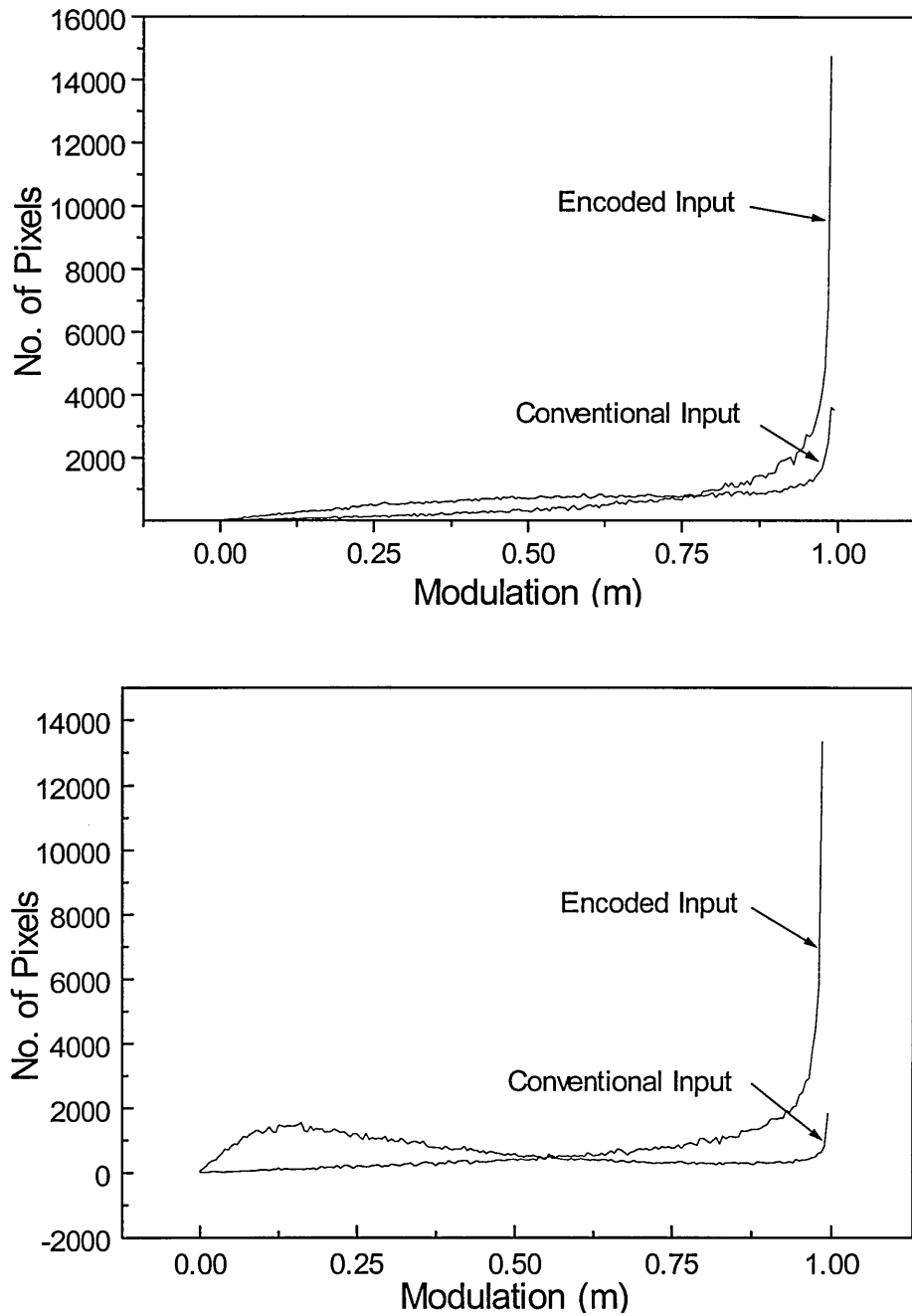


**Fig. 7.3** Histograms of the modulation present in the JPS for noiseless (upper) and  $\sigma = 80$  (lower) inputs.

The upper histogram shows that for the noiseless case the conventional JPS modulations are spread across all levels with a small increase towards  $m=1$ , but the JPS from the encoded input has most information concentrated in the highest modulation levels. The JPS from the conventional input shows a large increase in low modulation levels when noise is added. This increase is not present in the encoded version which still shows most of the information to be concentrated at the highest modulation levels, as expected from the phase-only nature of the JPS. The relationship between noise and average modulation of the JPS is shown for all noise levels in Fig. 7.4 for both conventional and encoded input. As mentioned in Section 6.4 the encoded reference is scaled to give equal average intensities in the JPS, or equivalently, to maximise the modulation.

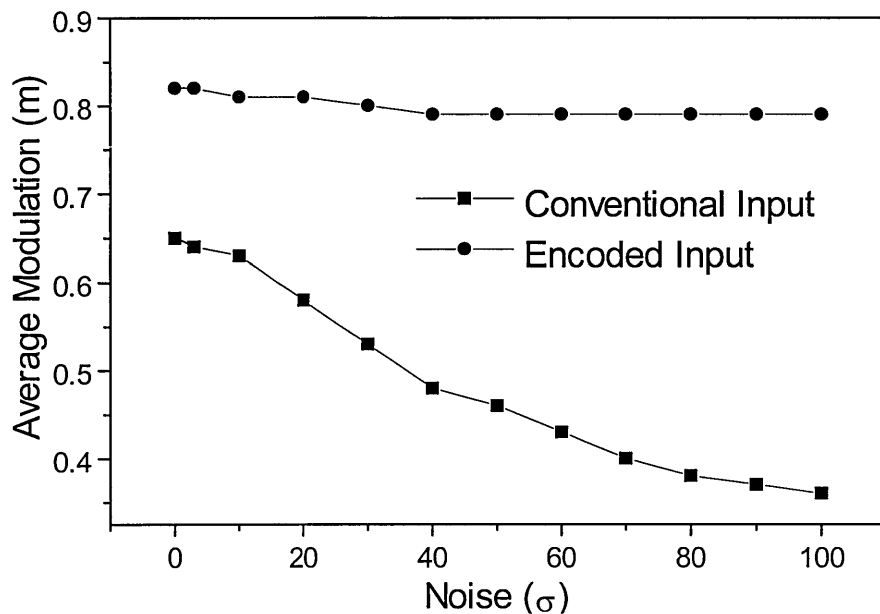


**Fig. 7.4** Average modulation of the JPS as a function of noise for conventional and encoded input.

From the graph in Fig. 7.4 we can see that encoding the input results in a consistently high modulation across all noise levels; this differs from the conventional case where the average modulation of the JPS gradually decreases as more noise is added to the input scene.



With this information we can proceed to choose an appropriate model of the space-charge field to simulate the photorefractive correlation. Since the conventional case results in a range of modulation levels falling from 0.65 to 0.35, the model developed by Ochoa would seem to be most apt. The Ochoa model will not cover the case of encoded input due to the higher modulations, and the theory developed by Vachss should be used. Unfortunately because each model is limited to a certain modulation range, they can strictly only be applied to one type of input. It is nevertheless worthwhile simulating both types of inputs using both models to see if either provides a useful comparison with the experimental correlations.

To this end IDL routines were written to calculate the correlations for conventional and encoded inputs using both models. To get statistically meaningful performance characteristics 100 correlations, using unique noise arrays, were performed for each noise level. The following two figures show 3-dimensional representations of the intensity at the correlation plane for noiseless and high ( $\sigma = 70$ ) noise cases. Note that all noiseless cases, whether conventional or encoded, and calculated using either model, have a similar appearance so only the following example is given. These correlations were generated using the Ochoa model.

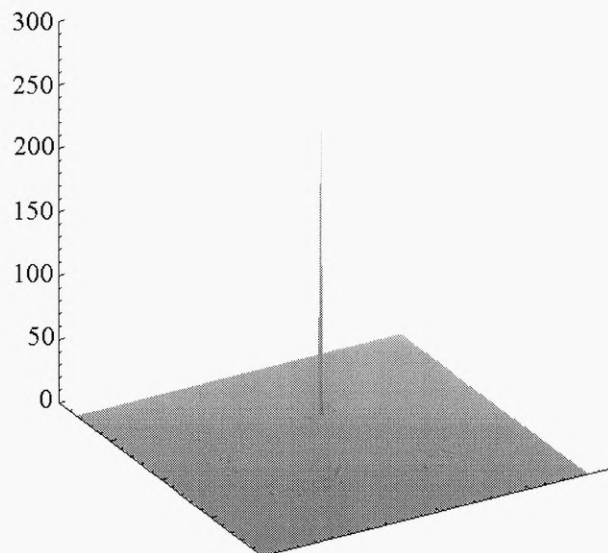


**Fig. 7.5** Intensity at correlation plane arising from noiseless encoded input.

## Ochoa Model

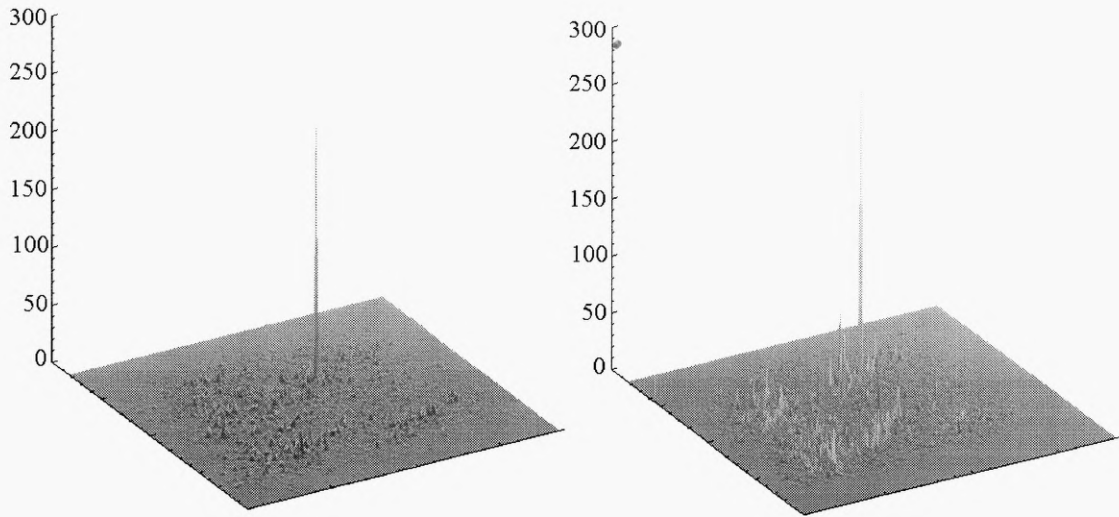


**Fig. 7.6** Noisy correlations arising from conventional (left) and encoded (right) inputs, using the Ochoa model.

The intensity plot in Fig. (7.5) shows an ideal delta type correlation as described by Eq. (6.10). Small signals arising from the earth background and false targets can also be seen.

As noise is added, Fig. 7.6, differences in the correlations arising from each type of filter become apparent. In the conventional case the addition of input noise results in a general increase of background noise in the correlation whereas the encoded case produces a more spiky background.

The performance measures obtained using the Ochoa model are shown in the following figures.

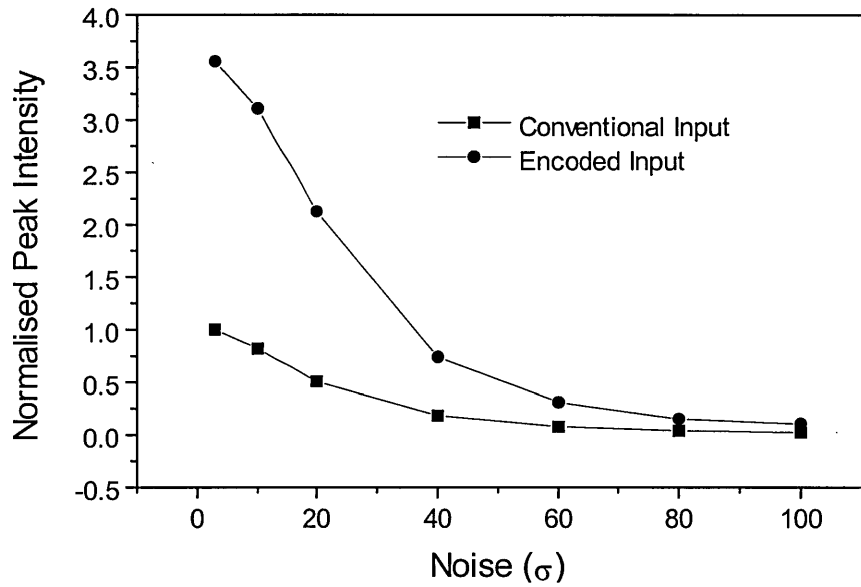


**Fig. 7.7** Normalised peak intensity dependence on noise, as predicted by the Ochoa model.

The peak intensities in Fig. 7.7 are normalised with respect to the noiseless conventional case. The graph shows that the noiseless correlation peak resulting from the encoded input is over 3.5 times the height of that from the conventional input, this ratio rises to 7.5 for the case of added ( $\sigma = 100$ ) noise.

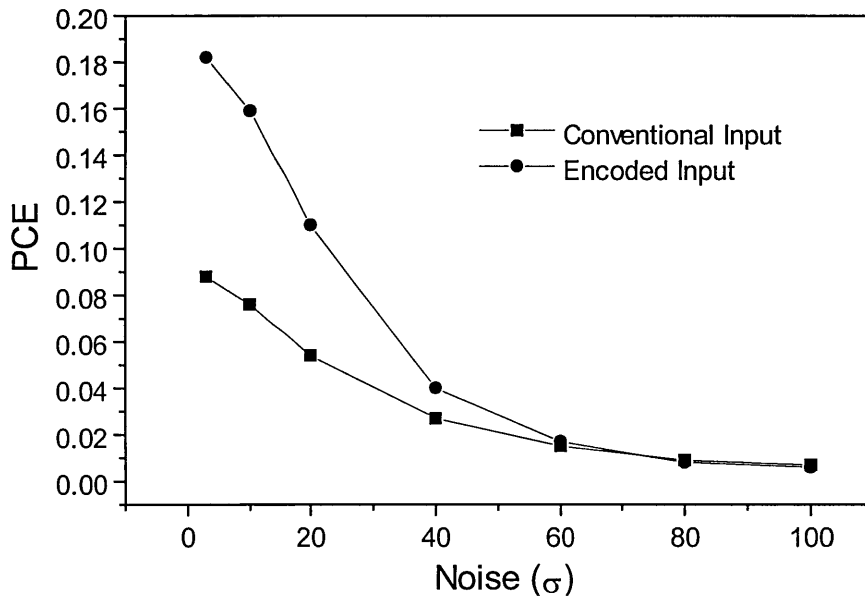


**Fig. 7.8** Peak to correlation energy dependence on noise, as predicted by the Ochoa model.

The peak to correlation energy ratio (PCE, Eq. 4.46) gives a measure of the sharpness of the correlation peak. The nonlinear recording nature of the photorefractive crystal gives a sharp peak for both types of input as was seen in Fig. 7.6. The Ochoa model does, however, predict an improvement when the input is encoded, especially at low noise levels. The peak to root-mean-square ratio (PRMSR, Eq. 4.44) gives another measure of peak sharpness and is very similar in form to the PCE variations.

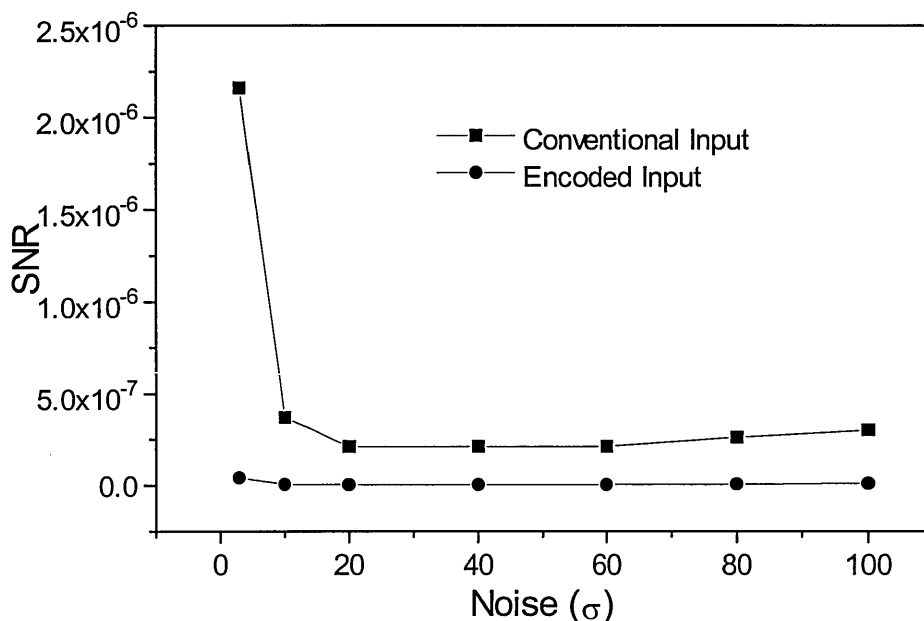


**Fig. 7.9** Signal to noise ratio dependence on noise, as predicted by the Ochoa model.

The signal to noise ratio (SNR) given by Eq. (4.41) gives a measure of the stability of the correlation peaks from a large number of correlations with random noise. The graph shows that the conventional input is predicted to give a much more stable peak than the encoded input for low noise levels. This large advantage falls quickly as the noise level is increased but the stability is still greater at higher noise levels.

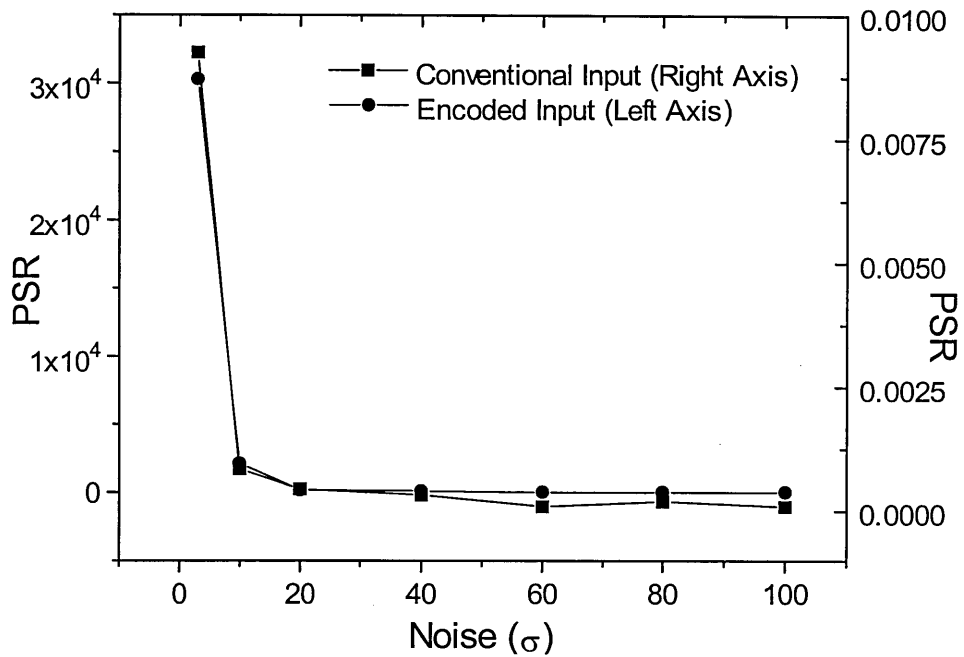
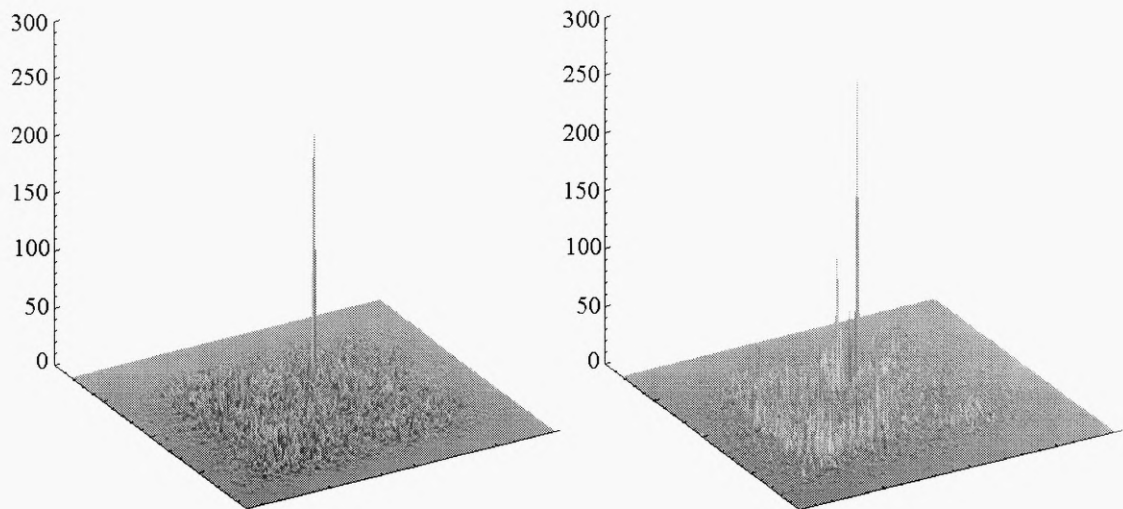


**Fig. 7.10** Peak to sidelobe ratio dependence on noise, as predicted by the Ochoa model.

The peak to sidelobe ratio (PSR, Eq. 4.43) gives a measure of the correlation detection ability in surrounding noise. The above graph shows that the two types of input give a similar form for the behaviour of the PSR, but the encoded input gives values up to six orders of magnitude greater than the conventional input. Since we have seen from the previous graph that the correlation peak from encoded input is less stable, these PSR results imply that the background noise is much more stable for encoded input. The PSR calculations were repeated for several different points in the correlation plane and whilst the absolute values varied between locations, the ratios between the results from the two filter types were similar.

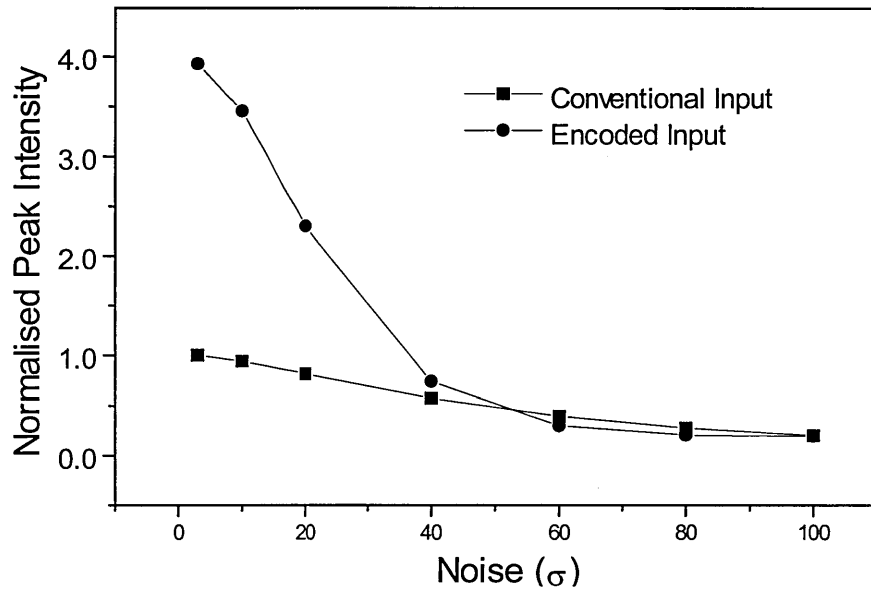
## Vachss Model

Fig. 7.11 shows the correlation peaks obtained for a typical noise array with  $\sigma=70$ , obtained using the Vachss model, (Vachss, 1988). The correlation from the encoded input, on the right, again produces a more spiky output



**Fig. 7.11** Noisy correlations arising from conventional (left) and encoded (right) inputs, using the Vachss model.

The following graphs detail the same performance measures of correlations calculated using the Vachss model as were calculated for the Ochoa model.



**Fig. 7.12** Normalised peak intensity dependence on noise, as predicted by the Vachss model.

The correlation peak intensities are again normalised to that achieved for the noiseless conventional input. A similar improvement in peak height is seen for the noiseless encoded input as was predicted by the Ochoa model, but the peak heights at higher noise levels are now similar.

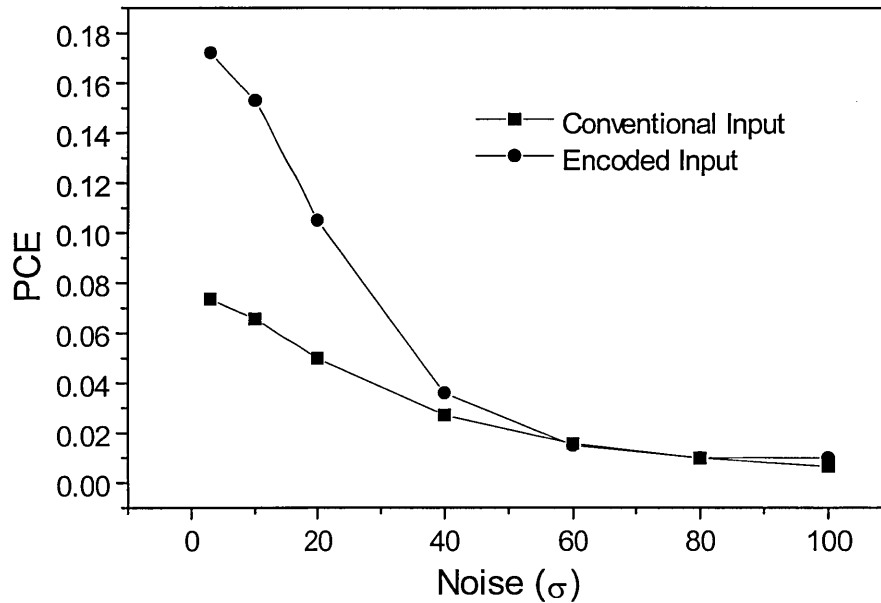


**Fig. 7.13** Peak to correlation energy dependence on noise, as predicted by the Vachss model.

The PCE results of the two models are very similar, both predicting an improvement in peak sharpness at low noise levels. The figures calculated for the peak to root-mean-square ratio (PRMSR) again have a similar form to those shown for the PCE.

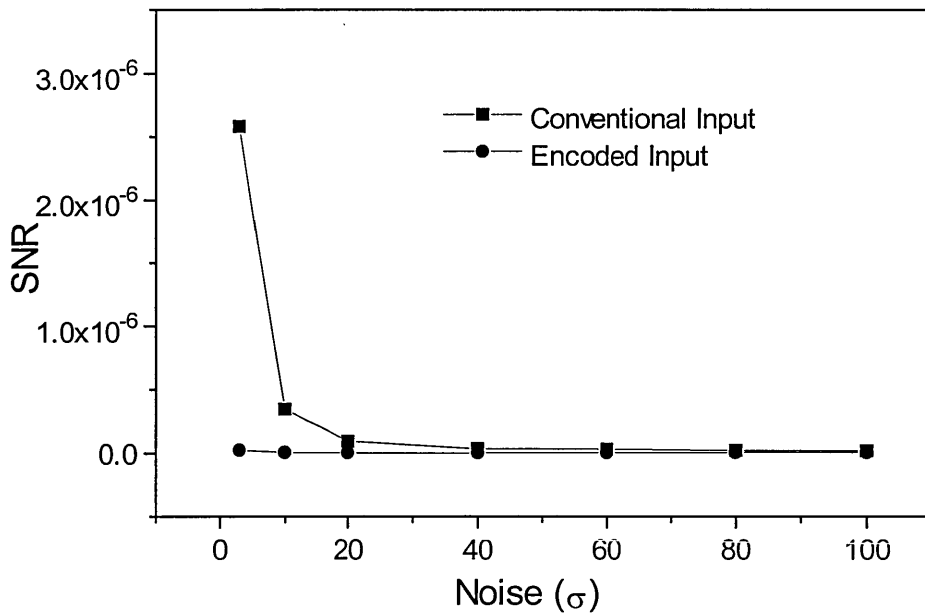


**Fig. 7.14** Signal to noise ratio dependence on noise, as predicted by the Vachss model.

The SNR predicted by the Vachss model, Fig 7.14, has a similar form to that predicted by the Ochoa with a much higher stability achieved by the conventional input at low noise levels. However this advantage over the encoded input quickly disappears as more noise is added with very similar results obtained at the higher levels.



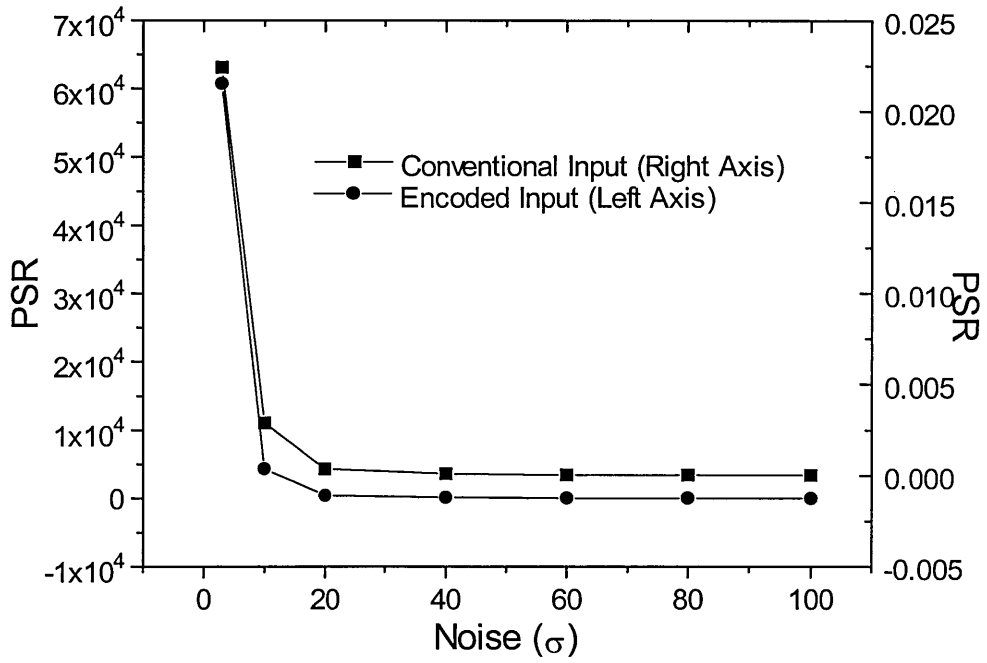
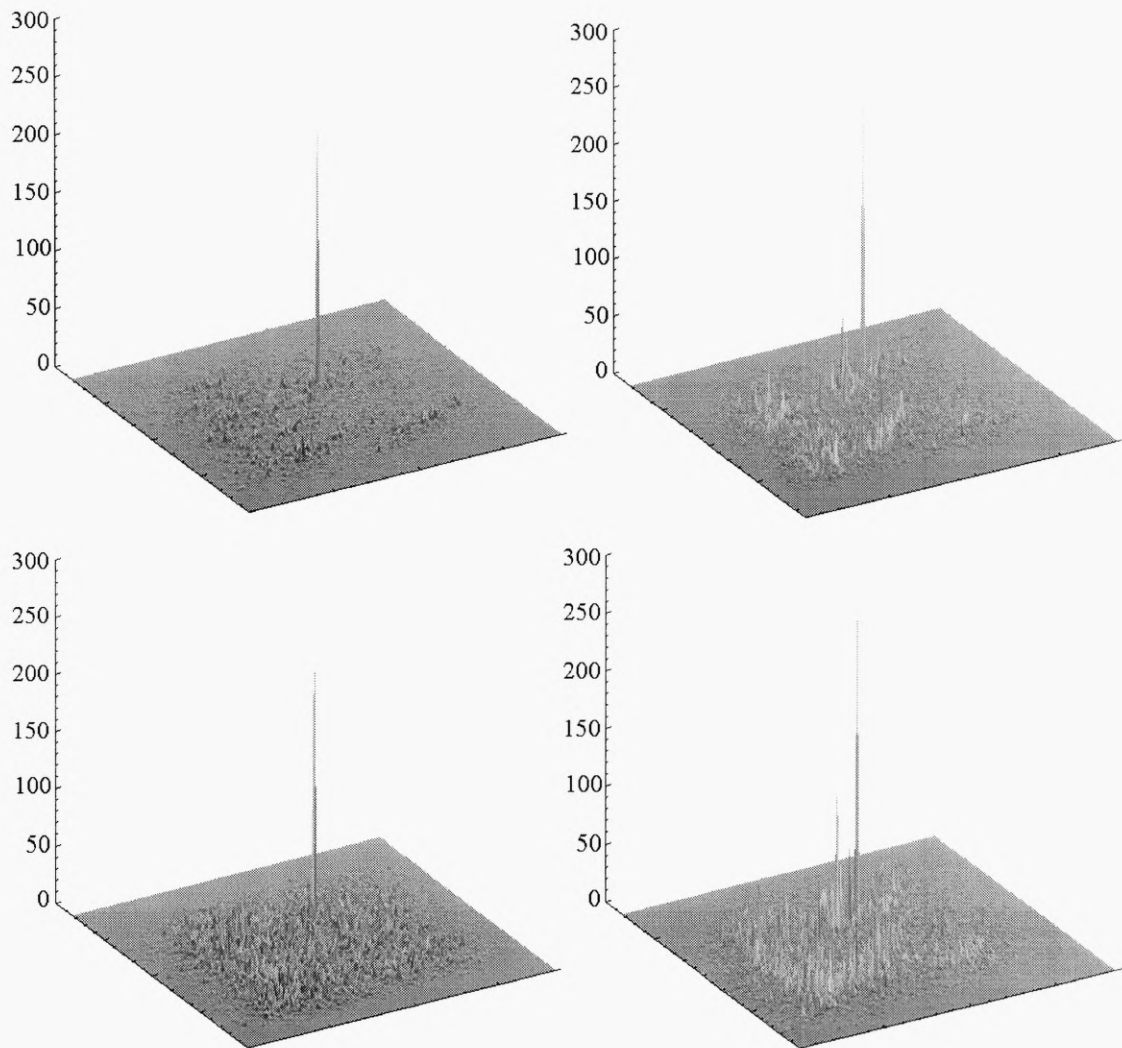


**Fig. 7.15** Peak to sidelobe ratio dependence on noise, as predicted by the Vachss model.

The Vachss model predicts a similar peak to sidelobe ratio (PSR) increase with encoded input as predicted by the Ochoa model

## Combined Models

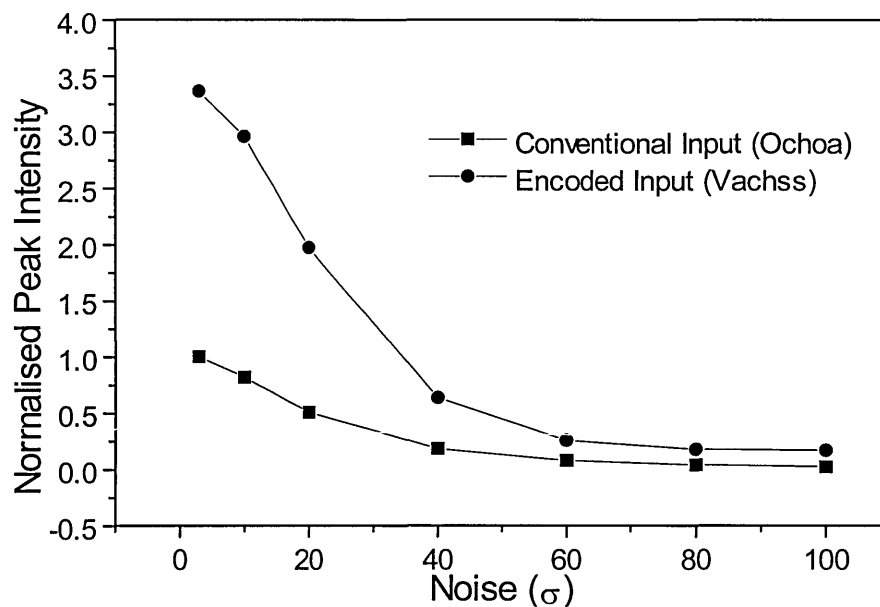
As mentioned previously, the two models apply to different modulation regimes and each can therefore only be applied to one of the two filter types. To compare the performance measures of the different types of filter the Ochoa model should be used for the conventional input, with mid-range modulations, and the Vachss model used for the encoded input, with modulations close to unity. The simulated correlations from Figs. 7.6 and 7.11, corresponding to the Ochoa and Vachss models respectively are reproduced here for comparison.



**Fig. 7.16** Noisy correlations arising from conventional (left) and encoded (right) inputs, using the Ochoa (top) and Vachhs (bottom) models.

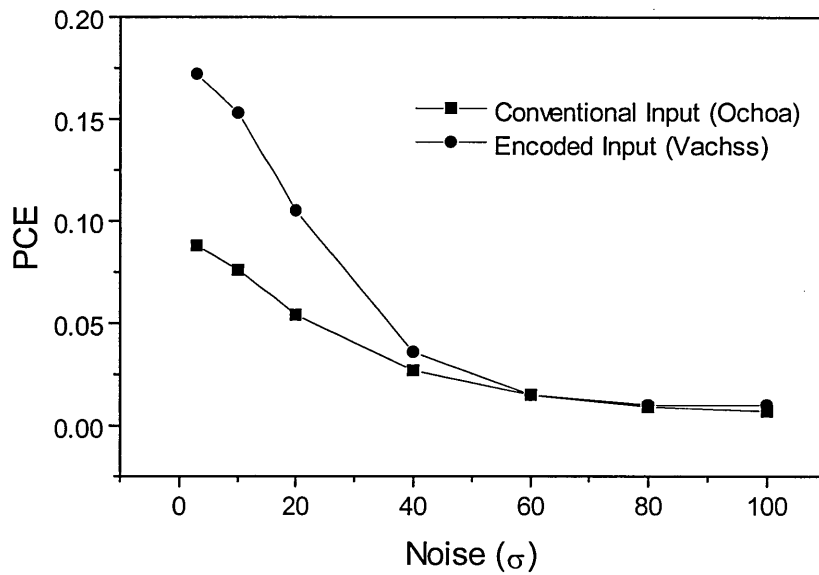
The graphs in Fig. 7.16 show a generally more noisy correlation resulting from the Vachss model in both cases. Since the Vachss model is used to simulate the performance of the encoded filter, the improvements obtained by using these filters may well be greater than predicted by the following graphs.

The resulting graph of peak intensity, normalised to the conventional (Ochoa) case, is shown in Fig. 7.17.



**Fig. 7.17** Normalised peak intensity dependence on noise, as predicted by the appropriate model.

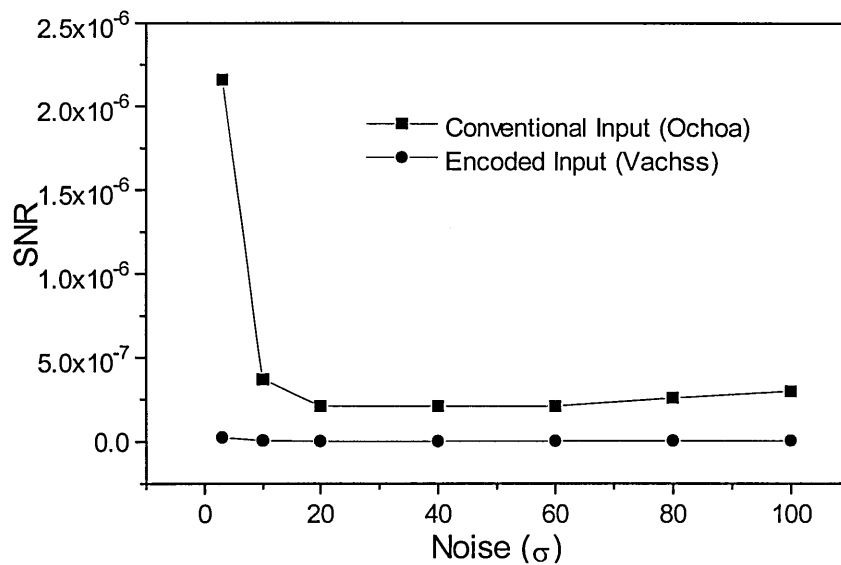
The combined models predict a higher peak intensity for the encoded input at all noise levels with a ratio changing from approximately 3.5 for the lowest noise level to 7.5 for the highest noise level.



**Fig. 7.18** Peak to correlation energy dependence on noise, as predicted by the appropriate model.

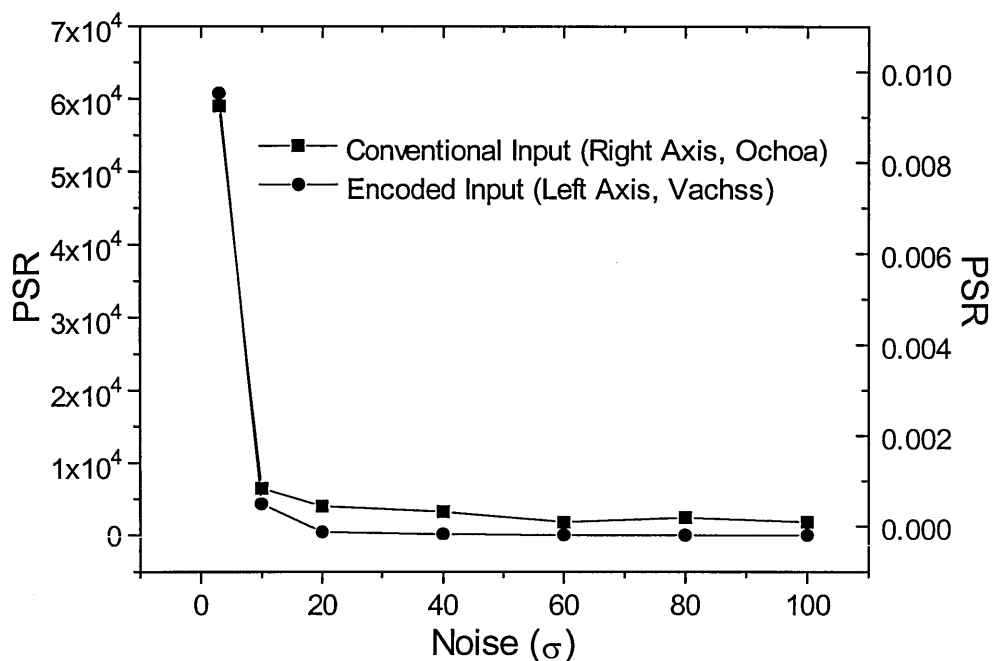
The graph shows that the combined models predict that the encoded input will have a superior performance, in terms of peak sharpness, up to high noise levels; again the peak to root-mean-square ratio is very similar.

Fig. 7.19 shows the results of SNR calculations when the Ochoa model is applied to conventional input and the Vachss model to encoded input.



**Fig. 7.19** Signal to noise ratio dependence on noise, as predicted by the appropriate model.

Using different models to calculate the SNR for each filter type predicts that the correlation peak from the conventional input will be more stable than that from the encoded input at all noise levels, with a greater advantage at the lowest noise levels.



**Fig. 7.20** Peak to sidelobe ratio dependence on noise, as predicted by the appropriate model.

Fig. 7.20- shows the variation of peak to sidelobe ratio with added noise, using the appropriate model for each filter type. These measurements predict that the noise in the correlation output will be much less unstable for encoded input than for conventional input.

There are problems when we seek to compare the performance of the experimental correlations, detailed in the next section, to these simulated correlations. Because it would take a prohibitive amount of time to record a large number of correlations for each noise level, we are limited in the performance measures we can calculate for the experimental correlations. Any performance

measure which relies on the variance of a particular co-ordinate in a large number of correlations (e.g. SNR and PSR) cannot be measured for an individual correlation.

For the purpose of this comparison, an alternative signal to noise ratio is therefore defined as

$$\text{Alternative SNR} = \frac{|g(0,0)|^2}{\text{var}\left\{g(x,y) < \frac{|g(0,0)|^2}{2}\right\}}. \quad (7.1)$$

Which is a simple ratio of peak intensity to the variance of all other points, and describes the effect of the total background noise on the quality of the correlation. The variation of this alternative SNR with increasing noise is shown in Fig. 7.21, where the appropriate model was used for each filter type.

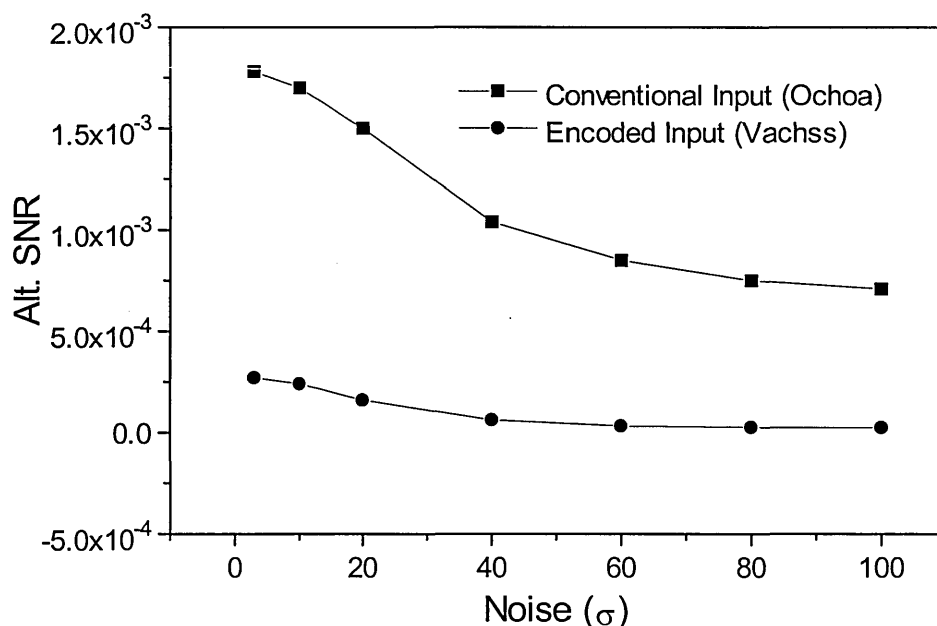


**Fig. 7.21** Alternative SNR dependence on noise, as predicted by the appropriate model.

This alternative measure gives better results for the conventional input at all noise levels. This is to be expected because of the more ‘spiky’ nature of correlations resulting from the encoded input.

In summary, two models of the photorefractive space charge field have been applied to calculating correlations from conventional and encoded input with added noise. These models were developed to describe the different modulation regimes that the two filter types produce at the Fourier plane, and each can therefore strictly only be applied to one type of filter. Nonetheless the two models give similar performance characteristics, which may be regarded as a positive indication of their usefulness.

The performances of the two filters were compared using the model appropriate to each modulation regime, and the results were presented in Figs. 7.16 - 7.20. These results would indicate that the technique of encoding the input to achieve phase-only JPS recording will produce enhanced peak sharpness and less background noise variation at the expense of correlation peak stability, when compared to conventional input. The greatest improvement was in the peak to sidelobe ratio measurement which would indicate that the background noise in the encoded correlations was much more stable than those from conventional correlations. This would improve detection ability since it would enable noise subtraction between different correlations of the same scene. The performance of the two filter types is determined experimentally in Section 7.3 for comparison with the simulated performance.

To end this section, it is interesting to see how the two filter types perform when a square law receiver, such as a charge coupled device (CCD) camera, rather than the BSO crystal, is used to record the JPS. Figs. 7.22 and 7.23 show the correlations achieved for noiseless and noisy ( $\sigma = 70$ ) scenes respectively, calculated for conventional (left) and encoded (right) inputs.

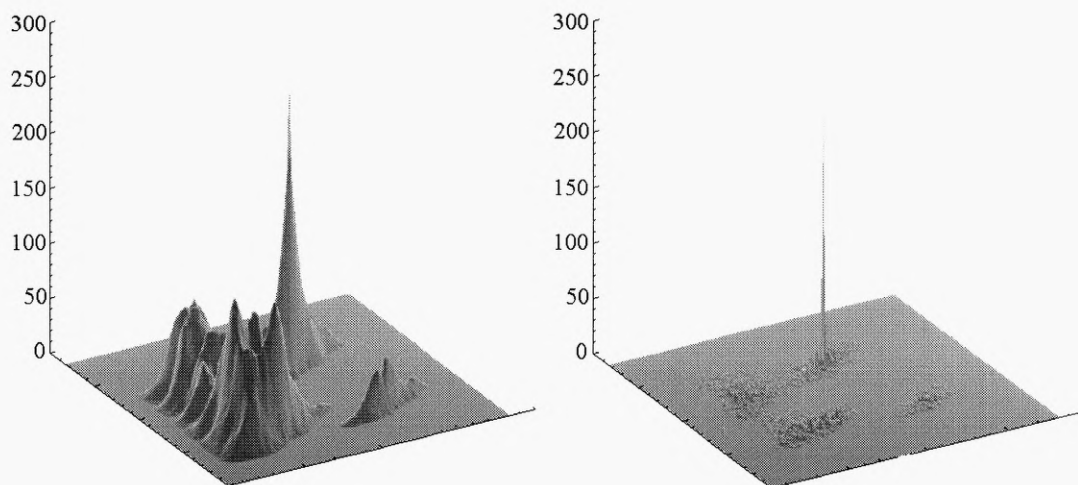


**Fig. 7.22** Correlations for noiseless scene, conventional (left) and encoded (right) inputs using a square law receiver.

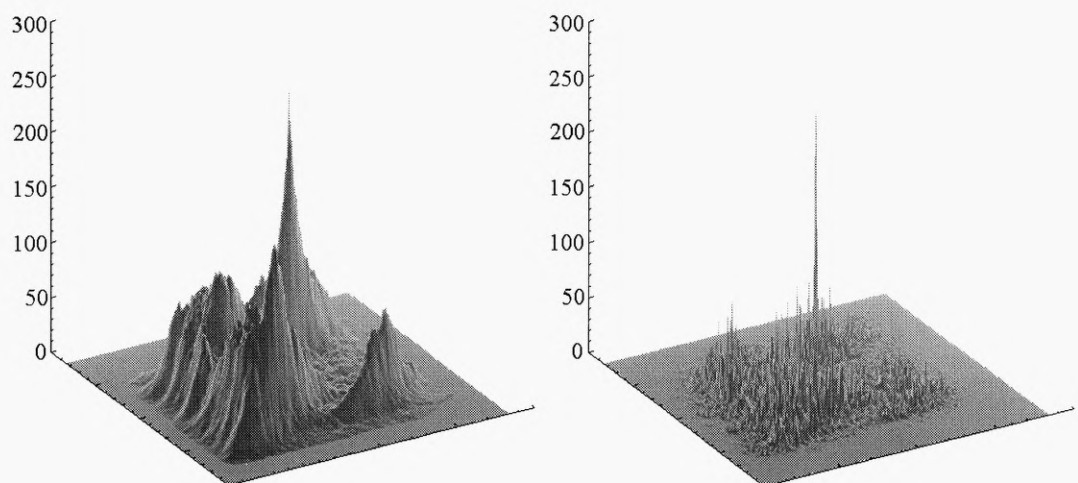


**Fig. 7.23** Correlations for noisy ( $\sigma = 70$ ) scene, conventional (left) and encoded (right) inputs using a square law receiver

These correlation simulations show that the square law receiver with conventional input gives correlations similar in form to those from the matched filter seen in Figs. 4.5 and 4.6. The encoded input results in output similar to the phase-only filter, as expected. Comparing the matched correlations produced using the square law receiver to the simulations using the BSO crystal (Figs. 7.6 and 7.10) shows that the crystal yields results closer to the phase-only case. This is due to the nonlinear recording nature of the BSO which, as was mentioned in Section 6.3, can be used to produce phase-only type correlations.



### 7.3 Experimental results

This section presents and discusses the experimental correlations obtained using the setup shown in Fig. 7.1. Conventional, Fig. 7.2, and encoded input scenes with a range of additive noise were presented to the LCTV and the resulting correlations recorded by a CCD camera connected to a frame grabber. These recorded correlations were stored as GIF files, with 256 grey levels, for later analysis. Figs. 7.24 and 7.25 show the experimental correlations obtained for noiseless input scenes. The first image was obtained from the conventional input and the second from the encoded input. The  $x$  and  $y$  axes show the number of pixels stored by the frame grabber in each direction, the stored area covers the whole input scene, the angle of view has been set to show the correlation peak clearly.

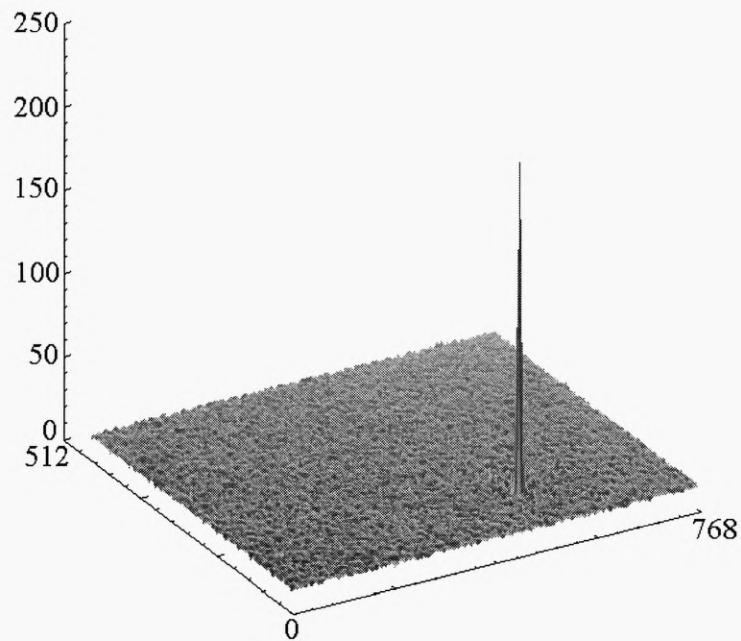


**Fig. 7.24** Experimental correlation from noiseless scene with conventional input.

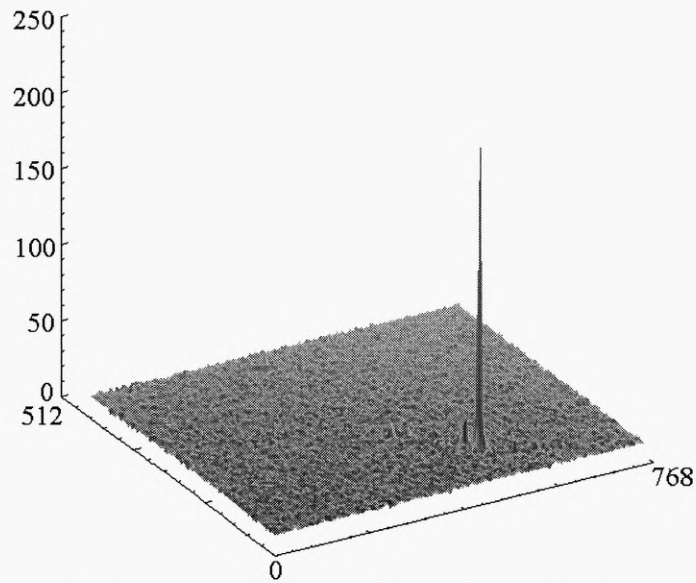


**Fig. 7.25** Experimental correlation from noiseless scene with encoded input.

Both types of input yield a delta type correlation peak as predicted by both theoretical models. The photorefractive BSO will always tend to produce a more delta-type correlation than a quadratic system since the recording mechanism depends on the modulation rather than the absolute of the intensity. The higher frequencies, which generally have lower intensities, will therefore contribute more information in the photorefractive case leading to a sharp peak. With no added noise there is very little background noise in the correlation and no false signals from the earth or smaller satellites shown in the scene of Fig. 7.2

Figs. 7.26 and 7.27 show similar intensity plots of the experimental correlations obtained with added noise of standard deviation,  $\sigma = 70$ .

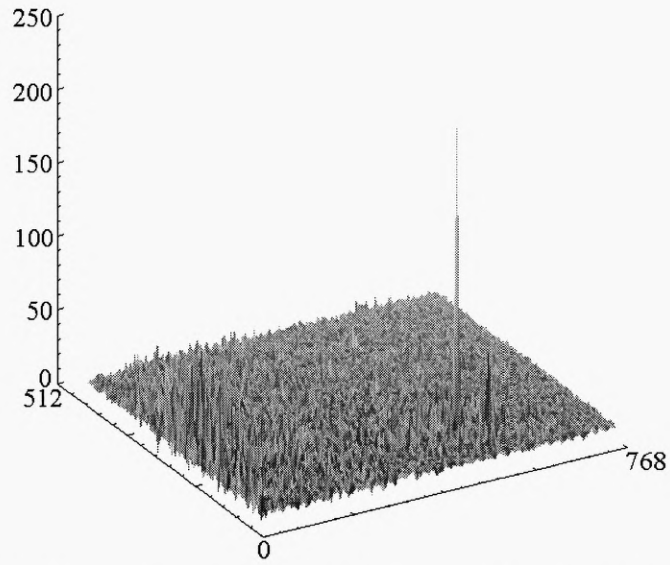


**Fig. 7.26** Experimental correlation from noisy ( $\sigma = 70$ ) scene with conventional input.

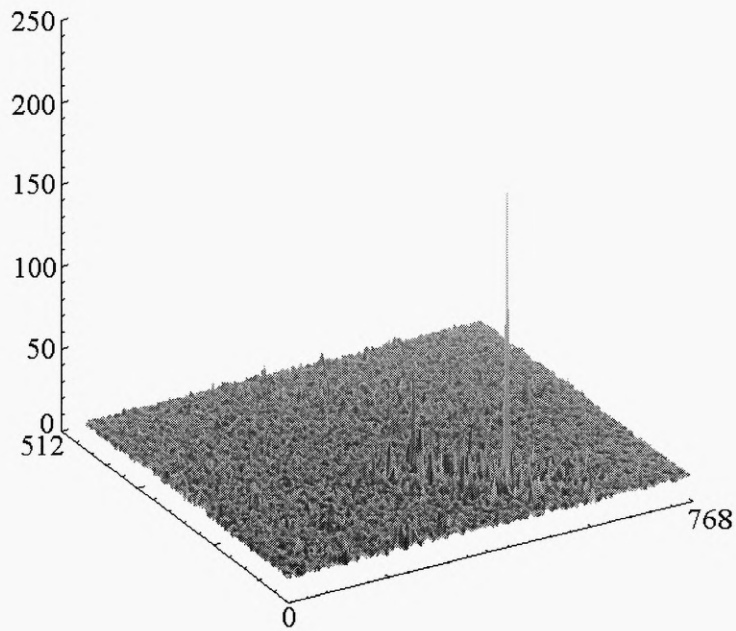


**Fig. 7.27** Experimental correlation from noisy ( $\sigma = 70$ ) scene with encoded input.

These correlation plots for the noisy scene show that the correlation from the conventional input has more background noise, especially from the false objects such as the earth which causes the higher noise level on the left edge of the plot.

As mentioned in the previous section, only some of the performance measures may be calculated for individual experimental correlations. These measures, PCE, PRMSR and the alternative SNR are shown in the following figures.

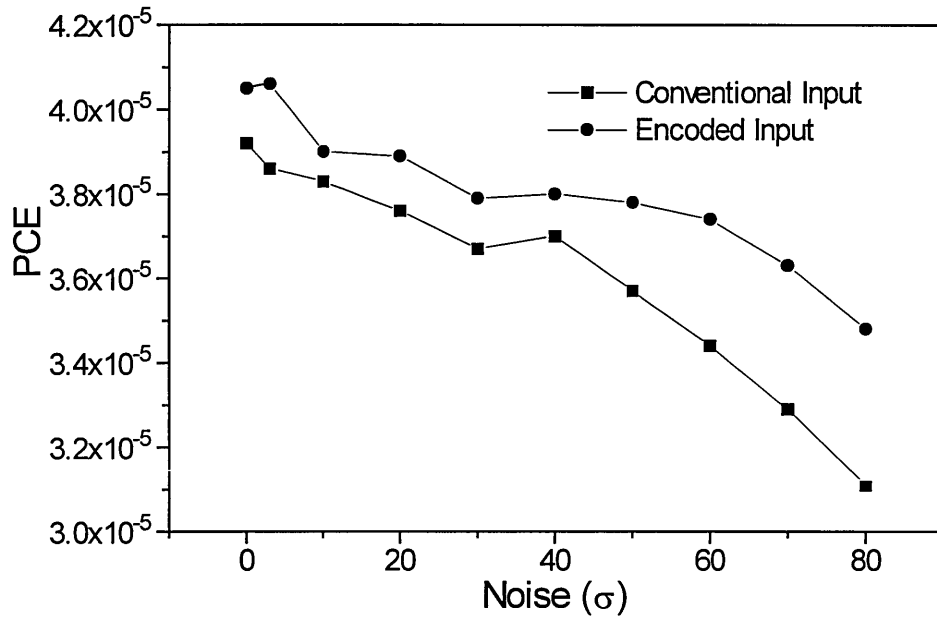


Fig. 7.28 Experimental peak to correlation energy dependence on noise, for comparison with Fig. 7.18.

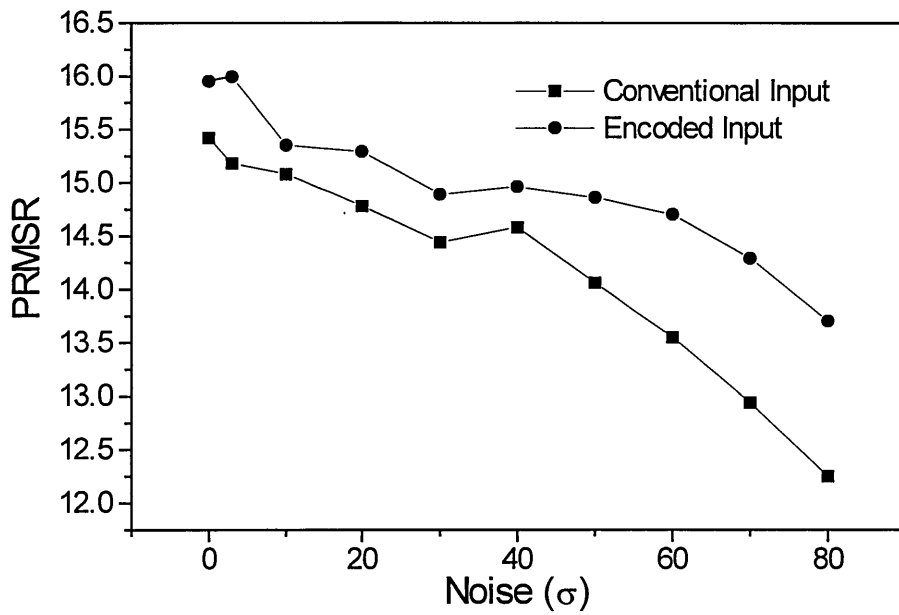


Fig. 7.29 Experimental peak to root-mean-square ratio dependence on noise, again for comparison with form of Fig. 7.18.

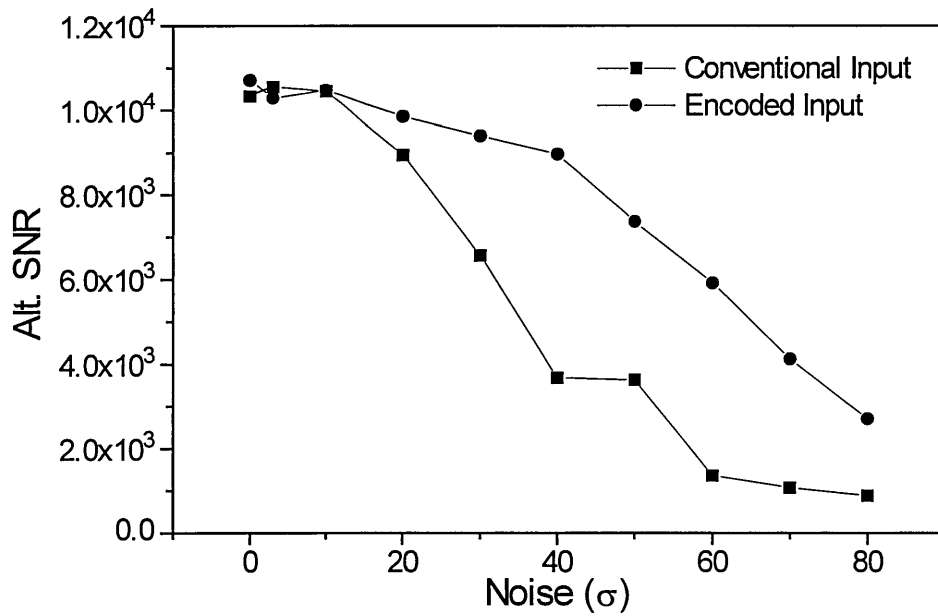


Fig. 7.30 Experimental alternative signal to noise ratio dependence on noise, for comparison with Fig. 7.21.

As with the theoretical prediction of the last section there is very little difference between the experimental PCE and PRMSR variation with noise, hence they should both be compared to Fig. 7.18. These two measures and the alternative SNR measure show improved performance from the encoded input. The experimental PCE and PRMSR results are very much smaller than the simulated results because both measures rely in some way on the total background intensity which will be higher in the experimental case. On the other hand, the experimental 'Alternative SNR' measurements give higher figures than the simulated measurements, this implies that the variance of the background noise is less in the experimental case. Little importance can be placed on the absolute values of the performance figures since these will change between different systems. There are a few points which may be made when comparing Figs. 7.28 and 7.29 with Fig. 7.18:

- (i) The large advantage that encoded input has at low noise levels would not necessarily be expected in the experimental results since there will always be a certain level of noise pollution from dust and pixel registration faults in the LCTV.
- (ii) During these experiments there were variations in the diffraction efficiency over time caused by air currents, fluctuations in the applied voltage and possible energy exchange between writing beams. This changing diffraction efficiency led to difficulties in recording consistent correlations, and sometimes several frames were captured before a peak height close to the chosen constant value of 230 was found. Again the problem of capturing a large number of correlations meant that those used are not truly typical leading to the slightly erratic nature of the data in the experimental graphs.
- (iii) The experimental performance measures show an improved performance from the encoded input over the conventional input at all noise levels. This is not the case for the theoretical predictions where the performance is similar at medium to high noise levels.

The experimental results show an improvement when the encoded input is used that was not predicted by the theoretical results. One possible explanation for this improvement over the predicted performance at medium-to-high noise levels could be the increased diffraction efficiency of the grating formed by the JPS from the encoded input. The encoded filters ensure the optimum high modulation conditions at the crystal

at all noise levels, and therefore reduce performance degradation due to scene noise. A measure of the degradation due to decreasing experimental diffraction efficiency is shown in Fig. 7.31. The experimental diffraction efficiency,  $\eta_e$  is calculated as the ratio of the correlation peak grey level to the He-Ne beam intensity used, and the measure of degradation is given by

$$\text{Performance Degradation} = \left(1 - \frac{1}{\eta_e}\right). \quad (7.2)$$

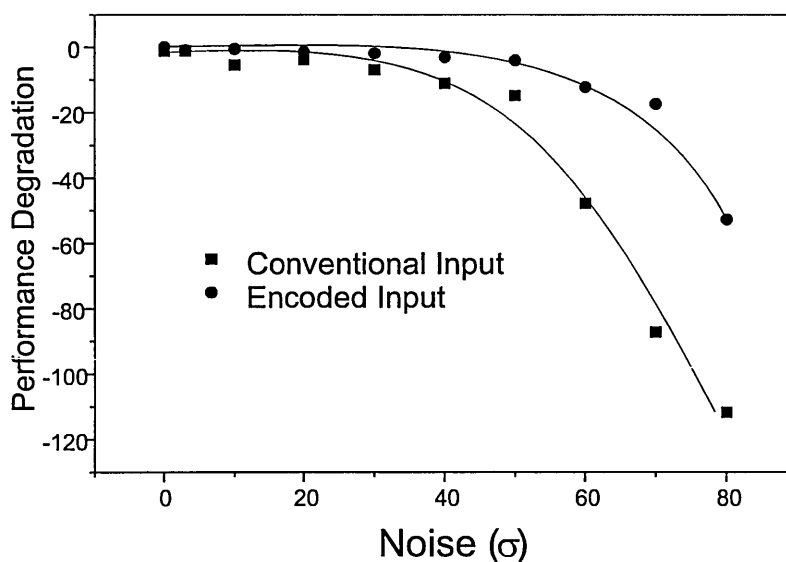


**Fig. 7.31** Experimental performance degradation due to decreasing diffraction efficiency.

This measure shows that as the noise level increases a higher He-Ne power is required to reach the constant grey level set as a requirement earlier. The He-Ne level must be increased because the diffraction efficiency falls as noise is added. The graph shows that the encoded input is more resistant to this degradation than the conventional input. This would result in a relatively better performance from the encoded input at medium-to-high noise levels as was seen in the experimental performance measure results.

## Chapter 7: References

Goodman, J.W. 1968, *Introduction to Fourier Optics*, New York, McGraw-Hill, Ch.1.

Khuktarev, N.V. 1976, 'Kinetics of hologram recording and erasure in electrooptic crystals', *Sov. Tech. Phys. Lett.* **2**, No12, pp438-441

Moharam, M.G. Gaylord, T.K. Magnusson, R. 1979, 'Holographic grating formation in photorefractive crystals with arbitrary electron transport lengths', *J. Appl. Phys.* **50**, No9, pp5642-5651

Ochoa, E. Vachss, F. Hesselink, L. 1986, 'Higher-order analysis of the photorefractive effect for large modulation depths', *J. Opt. Soc. Am. A*, **3**, No2, pp181-187

Vachss, F. Hesselink, L. 1988, 'Nonlinear photorefractive response at high modulation depths', *J. Opt. Soc. Am. A*, **5**, No5, pp690-701



This thesis has presented a discussion of the photorefractive effect with particular regard to the field of optical image correlation.

The work started with a description of the physical processes and material properties behind the photorefractive effect. The band transport model which describes the redistribution of charge in photorefractive crystals was then discussed and the linearised form of the space charge field at low modulations was given.

The technique of photorefractive image processing relies on the modulation of the material properties, in particular the refractive index, by incident light. The modulation of the refractive index by the space charge field was therefore discussed for the particular case of photorefractive BSO which is used as the recording medium in later experiments.

Many processing applications achieve their best performance under high modulation conditions where diffraction efficiency is optimised. Further models of the space charge field were therefore presented which extend the band transport model to the medium and high modulations regimes.

Optical processing applications make use of many architectures where the number of beams interacting within the crystal changes. Two of these architectures, called two-wave and four-wave mixing, were described and experiments performed to investigate the enhancement technique known as the moving grating method. The quality which is of most importance to image processing via two-wave mixing is the diffraction efficiency. The moving grating technique can improve the diffraction efficiency by enhancing the space charge field, this enhancement is well described analytically by the band transport model for low modulations. At high modulations, numerical simulations have shown that higher harmonics of the space charge field become important and a complicated response to grating velocity results. The response of diffraction efficiency to grating velocity was investigated experimentally for a range of modulations up to the high modulation regime, and results in agreement with the numerical results were obtained. Of particular importance is the low velocity enhancement at the highest modulations since this increases diffraction efficiency without increasing energy transfer. This high modulation enhancement of diffraction

efficiency can lead to better stability and improved signal to noise measurements in optical processing applications.

The quality which is of interest in four-wave mixing applications is the phase-conjugate reflectivity. The relationship between this reflectivity and grating velocity was therefore investigated for a range of beam ratios. When the two pump beams have intensities much greater than the probe beam, the undepleted pumps assumption may be used and analytical expressions for the reflectivity are possible. Four-wave mixing experiments were performed and the reflectivity response was found to be consistent with these analytical expressions, as has previously been shown elsewhere. When the undepleted pumps approximation no longer applies, numerical solutions are necessary to yield useful information. Two such numerical models were discussed and show that a phase change which could be induced by the moving grating technique has a similar effect to an increase in pump ratio. Evidence of this induced shift to higher pump ratios was found in the experimental results. Another consideration when studying phase conjugate reflectivity is the quality of the conjugate phase. One of the numerical models discussed shows that by an appropriate phase shift it is possible to have a conjugate phase that is independent of probe ratio. This would be of importance when the probe beam is carrying information and a range of probe ratios is present since the conjugate phase would not be degraded. The final reflectivity experiments performed show that when the pump and probe beams have comparable intensities a low velocity enhancement of the reflectivity is possible. To our knowledge this is the first demonstration of such a low velocity enhancement in 4WM experiments.

The mathematical analysis used to study optical processing was then discussed, leading to the concept of optical correlation. Examples of unconventional correlators were given, and the performance measures used to study such correlations defined. These performance measures show how the relative importance of phase over amplitude in the Fourier plane can lead to improved performance. The liquid crystal television (LCTV) which was used as a spatial light modulator (SLM) in later correlation experiments was then characterised, as part of this work, to give amplitude mostly operation.

The joint transform correlator (JTC) was then introduced and improvements in performance by nonlinear transformation of the joint power spectrum (JPS), such as binarisation, were discussed. It was then shown that, with appropriate preprocessing, it

is possible to obtain object plane filters which yield phase-only information in the Fourier plane. The combination of this phase-only correlation with the high modulation recording characteristics of BSO was then shown to give ideal  $\delta$ -like correlations similar to those achieved by binarisation of the JPS. The computational requirements for the preprocessing of the filters was then calculated, and found to compare favourably with that required for the binarisation of the JPS.

Two models of the photorefractive effect which are valid in the medium to high modulation regimes, Ochoa and Vachss respectively, were then studied. These models were used to model the performance of the phase only photorefractive JTC and compare it with the performance of a matched filter, which performs well in photorefractive JTC's. The simulations performed using these models predicted that for four out of the six performance measures considered the encoded filters, which yield phase-only information, will perform better than the conventional matched filters. A photorefractive JTC system was then constructed to perform correlation experiments to compare the encoded and conventional filters. Because of the difficulties in recording a high number of correlations, not all the performance measures could be obtained. Those which were possible, however, showed an improvement when the encoded filters were used.

The experimental performance measures show a slight improvement from the encoded filters across all noise levels with the improvement increasing slightly as the noise reaches the highest levels. There are therefore two major differences between the simulated and experimental results. The large improvement at low noise levels predicted by the simulations was not seen and an unexpected improvement at high noise levels was seen. The first difference may be explained by considering that the simulations at low noise are considering a perfect case with very low noise levels, whereas there will always be noise in the experimental case even before any Gaussian noise is added. One possible explanation of the second difference is that these models did not provide an accurate interpretation of the form of the space charge field variation with intensity modulation, and the diffraction efficiency could therefore not be predicted reliably. The high modulation which results from the encoded filters leads to a higher diffraction efficiency. This higher efficiency will become more important as the added noise reaches a high level since the encoded filters will preserve a high modulation whereas the modulation of the JPS resulting from the matched filters will decrease rapidly. An

expression for the signal degradation due to falling diffraction efficiency is introduced and gives the form of the experimental performance measures.

This thesis has shown that it is possible to achieve a high performance with a phase-only photorefractive JTC. The LCTV used as an SLM in these experiments did not provide perfect pixel registration. This led to deterioration in the performance of the encoded filters and improved hardware could further improve the performance of these filters.

## Appendices. Computer Programme Listings

### Appendix A:

Matched and phase-only correlations are performed and performance measures are calculated, as described in Sections 4.4 and 4.5.

```
PRO PERFORM
;REGISTER ARRAYS
A1=BYTARR(100,100,/NOZERO)
A2=BYTARR(100,100,/NOZERO)
B=BYTARR(100,100,/NOZERO)
R1=DBLARR(200,200)
R2=DBLARR(200,200)
R3=DBLARR(200,200)
R4=DBLARR(200,200)
O=DBLARR(200,200)
FTA1=DCOMPLEXARR(200,200,/NOZERO)
FTA2=DCOMPLEXARR(200,200,/NOZERO)
FILT1=DCOMPLEXARR(200,200,/NOZERO)
FILT1=DCOMPLEXARR(200,200,/NOZERO)
CORR1=DBLARR(200,200)
CORR2=DBLARR(200,200)
PEAK1=DBLARR(40)
PEAK2=DBLARR(40)
;READ IMAGES
READ_GIF,'H:\MDL40\LET1.GIF',A1
R1(50:149,50:149)=FLOAT(A1)
READ_GIF,'H:\MDL40\LET3.GIF',A2
R2(50:149,50:149)=FLOAT(A2)
READ_GIF,'H:\MDL40\LET1.GIF',B
O(50:149,50:149)=FLOAT(B)
;MATCHED FILTER
FT=CONJ(FFT(O,-1,DOUBLE=1))
;FILT1=FT
;PHASE-ONLY FILTER
FILT1=FT/ABS(FT)
;READ NOISE LEVEL
READ,SIG,PROMPT='ENTER SIGMA ~'
FOR K=0,39 DO BEGIN
```

```

IF (SIG EQ 0.0) THEN BEGIN
GOTO, JUMP1
ENDIF
NOISE=SIG*RANDOMN(SEED,200,200)
R3=R1+NOISE
R4=R2+NOISE
FOR J=0,199 DO BEGIN
FOR I=0,199 DO BEGIN
IF (R3(I,J) GT 255.0) THEN BEGIN
R3(I,J)=255.0
ENDIF
IF (R3(I,J) LT 0.0) THEN BEGIN
R3(I,J)=0.0
ENDIF
IF (R4(I,J) GT 255.0) THEN BEGIN
R4(I,J)=255.0
ENDIF
IF (R4(I,J) LT 0.0) THEN BEGIN
R4(I,J)=0.0
ENDIF
ENDFOR
ENDFOR
;AUTO TRANSFORM
FTA1=FFT(R3,-1,DOUBLE=1)
;CROSS TRANSFORM
FTA2=FFT(R4,-1,DOUBLE=1)
CORR1=SHIFT(ABS(FFT(FTA1*FIL1,1,DOUBLE=1))^2,50,50)
CORR2=SHIFT(ABS(FFT(FTA2*FIL1,1,DOUBLE=1))^2,50,50)
;NB HEIGHT OF MATCHED AUTO-CORRELATION = 486357.17
PEAK1(K)=MAX(CORR1)/486357.17
PEAK2(K)=MAX(CORR2)/486357.17
ENDFOR
;NOISELESS CASE
JUMP1:
IF (SIG EQ 0.0) THEN BEGIN
FTA1=FFT(R1,-1)
FTA2=FFT(R2,-1)
CORR1=SHIFT(ABS(FFT(FTA1*FIL1,1,DOUBLE=1))^2,50,50)
CORR2=SHIFT(ABS(FFT(FTA2*FIL1,1,DOUBLE=1))^2,50,50)
;PERFORMANCE MEASURES
PRINT,'AUTO MAX = ',MAX(CORR1)/486357.17
PRINT,'CROSS MAX = ',MAX(CORR2)/486357.17
ENDIF
;HORNER
HIGH1=WHERE(CORR1 GT MAX(CORR1)/2.0)
ETAH1=TOTAL(CORR1(HIGH1))/TOTAL(ABS(R1)^2)
HIGH2=WHERE(CORR2 GT MAX(CORR2)/2.0)

```

```

ETAH2=TOTAL(CORR2(HIGH2))/TOTAL(ABS(R2)^2)
PRINT,'AUTO HORNER = ',ETAH1
PRINT,'CROSS HORNER = ',ETAH2
;PCE
PCE1=MAX(CORR1)/TOTAL(CORR1)
PCE2=MAX(CORR2)/TOTAL(CORR2)
PRINT,'AUTO PCE = ',PCE1
PRINT,'CROSS PCE = ',PCE2
IF (SIG EQ 0.0) THEN BEGIN
GOTO, JUMP2
ENDIF
;AVERAGE PEAK
MAXC1=(TOTAL(PEAK1))/40.0
PRINT,'AVERAGE AUTO MAX = ',MAXC1
MAXC2=(TOTAL(PEAK2))/40.0
PRINT,'AVERAGE CROSS MAX = ',MAXC2
RESULT1=MOMENT(PEAK1)
RESULT2=MOMENT(PEAK2)
;SNR
SNR1=MAXC1/RESULT1(1)
SNR2=MAXC2/RESULT2(1)
PRINT,'AUTO SNR = ',SNR1
PRINT,'CROSS SNR = ',SNR2
;FR
FR=2.0*(MAXC1-MAXC2)/(RESULT1(1)+RESULT2(1))
PRINT,'FISHER RATIO = ',FR
JUMP2:
RETURN
END

```

## Appendix B.

The object-plane filters described in Section 6.4 are calculated and the encoding procedure performed to yield the target filter data which is stored for later use.

```

PRO POF
;REGISTER ARRAYS
S=DBLARR(128,128,/NOZERO)
A=DBLARR(200,200)
B=DCOMPLEXARR(200,200,/NOZERO)
D=DBLARR(200,200,/NOZERO)

```

```

C=DCOMPLEXARR(200,200,/NOZERO)
OUTPUT=DBLARR(200,200,/NOZERO)
OUT=DBLARR(200,200)
INV=DBLARR(160,200)
POF=BYTARR(160,200)
;READ SCENE FILE
READ_GIF,'H:\IDL40\SATS.GIF',S
OPENW,2,'H:\IDL40\POF2.RAW'
S=FLOAT((S))
WINDOW,0,XSIZE=160,YSIZE=200
TV,S
A(68:131,68:131)=S(44:107,64:127)
;CALCULATE PHASE-ONLY FILTER
B=FFT(A,-1,DOUBLE=1)
D=ABS(B)
C=CONJ(B)/D
;INVERSE TRANSFORM TO OBJECT PLANE
OUTPUT=IMAGINARY(COMPLEX(0,1)*FFT(C,1,DOUBLE=1))
;CREATE RONCHI GRATING
FOR I=0,99 DO BEGIN
FOR J=0,99 DO BEGIN
IF (OUTPUT(2*I,2*J) LT 0) THEN BEGIN
OUT(2*I,2*J)=-OUTPUT(2*I,2*J)
OUT(2*I,2*J+1)=OUT(2*I,2*J)
ENDIF ELSE BEGIN
OUT(2*I+1,2*J)=OUTPUT(2*I,2*J)
OUT(2*I+1,2*J+1)=OUT(2*I+1,2*J)
ENDELSE
ENDFOR
ENDFOR
;MAXIMUM FILTER VALUE FOR LATER GREY SCALING
LIM=MAX(ABS(OUTPUT))
PRINT,'MAX ABS(POF) VALUE = ',LIM
FOR I=0,63 DO BEGIN
FOR J=0,63 DO BEGIN
INV(112-I,132-J)=OUT(68+I,68+J)
ENDFOR
ENDFOR
POF=BYTSCL(INV^2,MAX=LIM^2)
WINDOW,1,XSIZE=160,YSIZE=200
TV,POF
;WRITE RAW FILTER DATA TO FILE
WRITEU,2,INV^2
CLOSE,2
RETURN
DELVAR,A,B,C,D,OUTPUT,OUT,POF,S,IMAGE,INV
END

```



## Appendix C

The fundamental of the Moharam model of the photorefractive space charge field is used to calculate the peak to correlation energy of a number of correlations with a certain level of added noise, as described in Section 7.1. The program can then be used to generate further noise arrays until one giving results close to the average is found and used to generate experimental filters

```
PRO CORRELATE
;REGISTER ARRAYS
A2=DBLARR(128,128,/NOZERO)
A3=DBLARR(128,128,/NOZERO)
C2=DBLARR(128,128,/NOZERO)
B2=DBLARR(160,200,/NOZERO)
FOBJ=DCOMPLEXARR(400,400,/NOZERO)
IT=DCOMPLEXARR(400,400,/NOZERO)
OUTPUT=DBLARR(400,400,/NOZERO)
RAW=DBLARR(160,200,/NOZERO)
M=DBLARR(405,405,/NOZERO)
A1=DCOMPLEXARR(405,405,/NOZERO)
B1=DCOMPLEXARR(405,405,/NOZERO)
F=DCOMPLEXARR(405,405,/NOZERO)
G=DBLARR(405,405,/NOZERO)
H=DBLARR(405,405,/NOZERO)
;READ ORIGINAL SCENE
READ_GIF,'SATS.GIF',A2
A2=DOUBLE(TEMPORARY(A2))
A3=A2
;ADD NOISE
READ,SIG,PROMPT='ENTER SIGMA ~'
TPTE=0.0
FOR K=0,19 DO BEGIN
OBJ=DBLARR(400,400)
OUT=DBLARR(400,400)
POF=DBLARR(160,200)
C=DBLARR(320,200)
A=DBLARR(405,405)
B=DBLARR(405,405)
MATCH=DBLARR(320,200)
A2=A3+SIG *RANDOMN(SEED,128,128)
FOR J=0,127 DO BEGIN
FOR I=0,127 DO BEGIN
IF (A2(I,J) GT 254.0) THEN BEGIN
```

```

C2(I,J)=254.0
ENDIF
IF (A2(I,J) LT 0.0) THEN BEGIN
C2(I,J)=0.0
ENDIF ELSE BEGIN
C2(I,J)=A2(I,J)
ENDELSE
ENDFOR
ENDFOR
OBJ(136:263,136:263)=C2
FOBJ=FFT(OBJ,-1,DOUBLE=1)
IT=(CONJ(FOBJ))/ABS(FOBJ)
OUTPUT=IMAGINARY(COMPLEX(0,1)*FFT(IT,1,DOUBLE=1))
FOR I=0,199 DO BEGIN
FOR J=0,199 DO BEGIN
IF (OUTPUT(2*I,2*J) LT 0) THEN BEGIN
OUT(2*I,2*J)=-OUTPUT(2*I,2*J)
OUT(2*I,2*J+1)=OUT(2*I,2*J)
ENDIF ELSE BEGIN
OUT(2*I+1,2*J)=OUTPUT(2*I,2*J)
OUT(2*I+1,2*J+1)=OUT(2*I+1,2*J)
ENDELSE
ENDFOR
ENDFOR
LIM=MAX(ABS(OUTPUT))
FOR I=0,127 DO BEGIN
FOR J=0,127 DO BEGIN
POF(144-I,164-J)=OUT(136+I,136+J)
ENDFOR
ENDFOR
POF=BYTSCSCL(TEMPORARY(POF)^2,MAX=LIM^2)
POF=DOUBLE(TEMPORARY(POF))
;READ PREVIOUSLY STORED TARGET FILE
OPENR,2,'POF2.RAW'
READU,2,RAW
CLOSE,2
TOTALS=TOTAL(POF)*0.294
;SCALE TARGET FILTER
MULT=(-2.7319-21.54)/(1+EXP((TOTALS-44607)/22012))+21.6
RAW=BYTSCSCL(TEMPORARY(RAW),MAX=(5519.1526^2)/MULT)
RAW=DOUBLE(TEMPORARY(RAW))
PRINT,'MULT = ',MULT,' / RATIO = ',TOTAL(RAW)/TOTAL(POF)
C(0:159,0:199)=RAW
C(160:319,0:199)=POF
WINDOW,0,XSIZE=320,YSIZE=200
TV,BYTE(C)
A(120:279,100:299)=C(0:159,0:199)
B(120:279,100:299)=C(160:319,0:199)

```

```

A1=((FFT(A,-1,DOUBLE=1)))
B1=((CONJ(FFT(B,-1,DOUBLE=1))))
F=(A1*B1)/ABS(A1*B1)
A=ABS(A1)^2
B=ABS(B1)^2
M=2.0*SQRT(A*B)/(A+B)
F=((1.0-SQRT(1.0-(M^2)))/M)^2*TEMPORARY(F)
G=SHIFT(ABS(FFT(F,-1,DOUBLE=1))^2,202,202)
H=BYTSC(L(G)
PTE=MAX(H)/TOTAL(H)
PRINT,'No. ',K,'PTE = ',PTE
CON=""
READ,CON,PROMPT='CONTINUE WITH ANOTHER RUN? (Y/N)'
IF (CON EQ 'N' OR CON EQ 'n') THEN BEGIN
GOTO, JUMP1
ENDIF
TPTE=TPTE+PTE
ENDFOR
JUMP1:
C=BYTE(TEMPORARY(C))
;WRITE ENCODED FILE
S1=""
READ,S1,PROMPT='ENTER POF FILENAME'
WRITE _GIF,S1,C
;WRITE CONVENTIONAL FILE
S2=""
READ,S2,PROMPT='ENTER MATCH FILENAME'
MATCH(47:110,67:130)=A3(44:107,64:127)
MATCH(175:302,35:162)=C2
MATCH=BYTE(TEMPORARY(MATCH))
WRITE _GIF,S2,MATCH
PRINT,' TOTAL PTE = ',TPTE+1
RETURN
DELVAR,A,B,C,A1,B1,F,G,H,A2,C2,A3,$
OBJ,FOBJ,IT,OUTPUT,OUT,POF,RAW,MATCH
END

```

## **Appendix D      List of Publications**

The following publications and conference presentations were based on the work presented in this thesis. These publications are reproduced at the end of the thesis.

### **Publications:**

Wang,Z.Q. Cartwright,C.M. Gillespie,W.A. Cook,N.J. 1996 'Effects of optical bias on moving gratings in BSO at large modulations', *App. Opt.* **35**, No.20, pp3829-3834

Cook,N.J. Carnicer,A. Vallmitjana,S. Juvells,I. Cartwright,C.M. Gillespie,W.A. 1998, 'Implementation of a Photorefractive Binary Joint Transform Correlator', *J. Opt. Soc. Am. B.* (To be published, July 1997)

### **Conference Presentations:**

Cook,N.J. Wang,Z.Q. Cartwright,C.M. Gillespie,W.A. 'Enhancement of phase conjugate beam reflectivity of photorefractive BSO by the moving grating technique', Photorefractive Materials Effects and Devices PR'95, Colorado, USA, June 1995.

Cartwright,C.M. Gillespie,W.A. Wang,Z.Q. Cook,N.J. 'The effects of optical bias on moving gratings in BSO at large modulations', Photorefractive Materials Effects and Devices PR'95, Colorado, USA, June 1995.

Vallmitjana,S. Cartwright,C.M. Carnicer,A. Cook,N. Juvells,I. Gillespie,W.A. 'Joint transform correlator using photorefractive BSO using improved discrimination', Conf. Optical systems design and production, Glasgow, May 1996, (Published in Proc. SPIE 2774, pp766-773, 1996)

Cartwright,C.M. Vallmitjana,S. Carnicer,A. Cook,N.J. Juvells,I. Gillespie,W.A.

‘Optical implementation of a binary joint transform correlator using object space filters’, Photorefractive Materials Effects and Devices PR’97, Chiba, Japan, June 1997.

Cartwright,C.M. Vallmitjana,S. Cook,N.J. Gillespie,W.A. Juvells,I. ‘Optical object identification by means of a joint transform phase-only correlator using BSO in the Fourier domain’, European Symposium on Lasers and Optics in Manufacturing, Munich, 1997, (Published in Proc. SPIE 3101, pp119-128, 1997)

Carnicer,A. Cartwright,C.M. Cook,N.J. Vallmitjana,S. Gillespie,W.A. Juvells,I. ‘Photorefractive phase-only joint transform correlator’, 5a. Reunion Nacional de Optica, Valencia, 1997.

**The full text of the following published papers has been removed from the e-thesis due to copyright restrictions:**

**Wang,Z.Q. Cartwright,C.M. Gillespie,W. A. Cook,N.J. 1996 ‘Effects of optical bias on moving gratings in BSO at large modulations’, A p p . O p t. 35, No.20, pp.3829-3834**

**Vallmitjana,S. Cartwright,C.M. Camicer,A. Cook,N. Juvells,I. Gillespie,W.A. ‘Joint transform correlator using photoreff active BSO using improved discrimination’, Conf. Optical systems design and production, Glasgow, May 1996, (Published in Proc. SPIE 2774, pp.766-773, 1996)**

**Implementation of a Photorefractive Binary  
Joint Transform Correlator.**

**N. J. Cook**

School of Engineering, University of Abertay-Dundee, Dundee DD1 1HG, Scotland

**A. Carnicer, S. Vallmitjana and I. Juvells**

Laboratori d'Optica, Departament de Fisica Aplicada i Electronica, Universitat de Barcelona,  
E08028 Barcelona, Spain

**C. M. Cartwright and W. A. Gillespie**

School of Engineering, University of Abertay-Dundee, Dundee DD1 1HG, Scotland

## **Abstract**

The use of photorefractive materials such as  $\text{Bi}_{12}\text{SiO}_{20}$  as a dynamic holographic medium is becoming an interesting alternative to current liquid crystal based modulators in real-time optical image processing. In this paper we present an experimental realisation of optical correlation for pattern recognition by means of a photorefractive joint transform correlator. The correlator operates with a liquid crystal television as the input and a photorefractive crystal at the recording plane. We consider two possible ways of registering the Fourier plane information: conventional detection of the joint power spectrum and utilising only phase information at the Fourier plane by suitable pre-processing of the scene and reference at the object plane. We also compare the latter case with the performance of a binary joint transform correlator. Analysis, simulations and experimental results are presented.

**KEY WORDS:** Real-time optical pattern recognition, binary joint transform correlation, BSO photorefractive crystals, phase-only information.

## **1. Introduction**

In the field of pattern recognition, optical techniques are usually based on the analysis of the cross-correlation function between the two-dimensional functions representing the scene and the reference to be recognised. These techniques have been widely developed and improved by the introduction of two important methods: the matched filter by VanderLugt<sup>1</sup>, and two years later the development of the joint transform correlator (JTC) by Weaver and Goodman<sup>2</sup>. Initially the image inputs were dependent on photographic and holographic media with their inherent delayed time for development. The development of spatial light

modulators (SLM) and the inclusion of CCD cameras in conjunction with frame grabbers represented an important step in the field of pattern recognition<sup>3,4</sup>. These devices allow one to combine the main advantages of the optical technique (high speed and parallel processing capability) with the versatility of the digital methods. As a consequence, a reliable real-time correlation process can be achieved. Among the different SLM, liquid crystal displays removed from videoprojectors have proved a less expensive alternative for the implementation of real-time correlators<sup>5</sup>. Also photorefractive materials such as  $\text{Bi}_{12}\text{SiO}_{20}$  (Bismuth Silicon Oxide, BSO) have been incorporated as a dynamic holographic recording medium in the Fourier domain<sup>6,7</sup>. In order to improve the correlation the use of nonlinear methods has been shown to be very effective. These techniques can be applied in two different ways when using a JTC: nonlinear processing of the joint power spectrum<sup>8</sup> or the use of suitable spatial correlation filters designed to be the reference in the joint input image<sup>9</sup>. In this paper we implement a conventional photorefractive joint transform correlator (PJTC) which uses matched filters. To enhance the detection capability of the correlator we also use encoded filters in the input plane to give phase-only information in the Fourier plane, we denote this case as phase-only photorefractive JTC (POPJTC). Both correlators operate with an Epson 1000 videoprojector as the SLM<sup>10</sup> at the input and a BSO crystal in the Fourier plane. We analyse theoretically the correlator working in matched and phase-only mode and we compare the behaviour of the correlator in both situations. We also show that a POPJTC operates in a similar way to a binary joint transform correlator (BJTC). Simulations and experimental optical results are presented.

In section 2 a review of the BJTC is presented while in section 3 we show that a POPJTC operates in a similar way to a BJTC. In section 4 we describe the technique for encoding the object plane filters to give phase-only information in the Fourier plane. In section 5, we compare theoretically the BJTC and the POPJTC in terms of time requirements:



digital calculations are required in both correlators so we evaluate this drawback. In section 6 we study by digital simulation the response of the PJTC and the BJTC/POPJTC when the scene was corrupted by zero mean Gaussian additive noise. In section 7 we present some experimental results and finally, the conclusions are presented in section 8.

## 2. Binary Joint transform correlation review

Joint transform correlators<sup>2</sup> have been shown to be powerful coherent processors for optical pattern recognition. Since 1966, several improvements in this architecture have been proposed in order to obtain real-time detection by using liquid crystal devices<sup>11</sup>. In the last few years, most of the papers published in the pattern recognition field, have analysed different systems in order to increase the discrimination capability. In particular, the binarisation of the joint power spectrum (JPS) has been widely used and has been shown to be a reliable method<sup>8</sup>. Fig. 1 shows a conventional JTC setup, scene and reference (joint-scene) are displayed on the input LCTV. The system is illuminated by a coherent plane wave and the JPS is recorded in the focal plane of the Fourier lens by means of a video-camera (CCD). In a second stage, the JPS is displayed on the LCTV and the correlation is recorded by the CCD. The JPS is described by the following equation:

$$\begin{aligned}
 I(u, v) = & |F_R(u, v)|^2 + |F_S(u, v)|^2 \\
 & + 2|F_R(u, v)||F_S(u, v)| \cos[x_0 u + y_0 v + \phi_S(u, v) - \phi_R(u, v)]
 \end{aligned} \tag{1}$$

where  $|F_R(u, v)|\exp[i\phi_R(u, v)]$  and  $|F_S(u, v)|\exp[i\phi_S(u, v)]$  are the Fourier transforms (FT) of the reference  $f_R(x, y)$  and the scene  $f_S(x, y)$  respectively. We assume that the scene is located at

$(x_0/2, y_0/2)$  and the reference is at  $(-x_0/2, -y_0/2)$  The binary joint power spectrum  $I_b(u, v)$  is obtained by assigning the values +1 or -1 to  $I(u, v)$ , as below:

$$I_b(u, v) = \begin{cases} 1 & \text{if } I(u, v) \geq I_T(u, v) \\ -1 & \text{if } I(u, v) < I_T(u, v) \end{cases} \quad (2)$$

where  $I_T(u, v)$  is a predetermined threshold function. This bipolar function can be expressed as a Fourier expansion<sup>8</sup>:

$$I_b(u, v) = \sum_{n=1}^{\infty} A_n[u, v; I_T(u, v)] \cos\{n[x_0u + y_0v + \phi_S(u, v) - \phi_R(u, v)]\} \quad (3)$$

An appropriate threshold function  $I_T(u, v)$  is presented in Eq. (4)<sup>12</sup>

$$I_T(u, v) = |F_R(u, v)|^2 + |F_S(u, v)|^2 \quad (4)$$

To remove the intra-class terms of Eq. (1), the intensity of the Fourier transform of the scene and the reference can be evaluated separately, and then, the subtraction between Eqs. (1) and (4) is obtained by computer<sup>13,14</sup>. By using this threshold function, Eq. (3) becomes

$$\begin{aligned} I_b(u, v) &= \sum_{n=0}^{\infty} \frac{1}{2n+1} \cos\{(2n+1)[x_0u + y_0v + \phi_S(u, v) - \phi_R(u, v)]\} \\ &= \cos[x_0u + y_0v + \phi_S(u, v) - \phi_R(u, v)] + \dots \end{aligned} \quad (5)$$

and Fourier transforming Eq. (5) and neglecting terms  $n > 1$ , which are very weak in terms of intensity, the correlation can be written as:

$$c(x, y) = \delta(x - x_0, y - y_0) + \delta(x + x_0, y + y_0) \quad (6)$$

To obtain  $\delta$ -like correlations, other solutions have been proposed by different authors. One possible way is based on the direct processing of the JPS<sup>15,16</sup> and in another, inverse-filter solutions have been suggested<sup>9,17,18</sup>.

### 3 Photorefractive JPS recording

In this section we shall describe the recording process of the photorefractive BSO crystal and how the use of encoded objects with only phase information in the Fourier plane gives an effectively quantised refractive index grating analogous to the binarised JPS discussed in the previous section.

When two beams intersect inside a photorefractive crystal, an optically induced refractive-index grating is produced<sup>19,20</sup>. This grating is formed by the excitation of photoelectrons which migrate by diffusion and drift forming a local space-charge modulation which modifies the refractive index via the linear electro-optic effect. The joint power spectrum incident on the photorefractive BSO crystal has a certain modulation  $m(u, v)$  for each spatial frequency,

$$m(u, v) = \frac{2\sqrt{I_S(u, v)I_R(u, v)}}{I_S(u, v) + I_R(u, v)} \quad (7)$$

where  $I_S(u, v) = |F_S(u, v)|^2$  and  $I_R(u, v) = |F_R(u, v)|^2$  are the intensities of the two writing beams. The intensity distribution incident on the crystal will be recorded as a nearly sinusoidal variation in refractive index. Eq. (1), which describes the JPS intensity at the crystal, can be rewritten in terms of  $m(u, v)$  as,

$$I(u, v) = [I_R(u, v) + I_S(u, v)] \left\{ 1 + m(u, v) \cos[x_0 u + y_0 v + \phi_S(u, v) - \phi_R(u, v)] \right\} \quad (8)$$

The refractive index grating which the JPS gives rise to has a modulation given by,

$$|\Delta n| = \frac{n^3 r |E|}{2} \quad (9)$$

where  $n$  is the unperturbed refractive index,  $r$  is the appropriate electro-optic coefficient, and  $E$  is the space-charge field caused by the photo-electrons which is a function of  $m(u, v)$ . This grating may be analysed using a low power HeNe beam which will diffract with an efficiency  $\eta$ , which assuming negligible absorption is given by,

$$\eta = \sin^2 \left( \frac{\pi \Delta n d}{\lambda_2 \cos \theta_2} \right) \approx \left( \frac{\pi \Delta n d}{\lambda_2 \cos \theta_2} \right)^2 \quad (10)$$

Where  $\lambda_2$  and  $\theta_2$  are the wavelength and incident angle of the HeNe beam, and  $d$  is the crystal thickness. The Fourier component of the transmittance function that generates the first-order correlation signal can therefore be expressed as,

$$|E|^2 \cos[x_0 u + y_0 v + \phi_S(u, v) - \phi_R(u, v)] \quad (11)$$

Moharam et al<sup>21</sup> have modelled the modulation of the space-charge field and hence the behaviour of the diffraction efficiency. This derivation gives the space-charge field for intensity modulations up to  $m=1$  but becomes less accurate as the applied field is increased. The fundamental component of the space-charge field is given by

$$E = \left[ \frac{(1-m^2)^{1/2} - 1}{m} \right] (E_a^2 + E_d^2)^{1/2} \quad (12)$$

Where  $E_a$  and  $E_d$  are the applied field and diffusion field respectively

Ochoa et al<sup>22</sup> derive an expression for the space charge field which is valid for large modulations and for applied fields which approach the saturation field, a situation we will not encounter. The space-charge field is given by

$$\begin{aligned} |E|^2 = & \left[ \frac{(1-m'^2)^{1/2} - 1}{m'} \right]^2 (E_a^2 + E_d^2) \\ & + \frac{E_d}{E_q} \left\{ 2 \left[ \frac{(1-m'^2)^{1/2} - 1}{m'} \right]^2 (E_a^2 - E_d^2) \right. \\ & \left. + 2 \left[ \frac{(1-m'^2)^{1/2} - 1}{(1-m'^2)^{1/2}} \right] (E_a^2 + E_d^2) \right\} \end{aligned} \quad (13)$$

where

$$m' = \frac{m}{1 + \left( \frac{E_d}{E_q} \right) m} \quad (14)$$

The saturation field  $E_q$  depends on the concentration of acceptor sites, which is of the order of  $N_a=10^{22}\text{m}^{-3}$ .  $E_q=qN_a/\epsilon K=62\text{kVcm}^{-1}$  at this concentration, where  $q$  is the charge on an electron,  $\epsilon$  is the static dielectric constant, and  $K$  is the grating spatial frequency.  $E_a$  and  $E_d (=Kk_B T/q$  where  $k_B$  is Boltzmann's constant and  $T$  is the absolute temperature) are determined by the experimental setup, in this case they are  $5.6\text{kVcm}^{-1}$  and  $0.14\text{kVcm}^{-1}$  respectively.

$|E|^2$  is plotted in Fig. 2 against the modulation  $m$  using the expressions of Moharam and then Ochoa for different trap concentrations. It is seen that the space-charge deviates further from the Moharam predictions as the acceptor concentration decreases. This deviation increases if the refractive index grating spacing is reduced or the applied field increased. Since the diffraction efficiency of the refractive index grating is proportional to  $|E|^2$ , the performance of the JTC will therefore deteriorate for lower modulation or greater deviation from the Moharam model. The different modulation regimes shown in Fig. 2 were used in the simulation of the photorefractive joint transform correlator, the results of these simulations are presented and discussed in section 6.

However we note that if  $I_R(u,v) = I_S(u,v)$  for all  $(u,v)$  then  $m(u,v)=1$ , leading to a maximised, constant modulation of the space-charge field. This can be achieved for all  $(u,v)$  in practical terms by setting  $I_R(u,v)=I_S(u,v)=1$ , which is possible by encoding the scene and reference to give phase-only distributions in the Fourier plane. The cross-correlation term of the JPS will therefore be quantised, which is qualitatively analogous to the binarised JPS given by Eq. (5)<sup>16</sup>.

The object-space distribution giving phase-only output is calculated as follows: Let  $F(u,v)=|F(u,v)|\exp[i\phi(u,v)]$  be the Fourier transform of a two-dimensional distribution  $f(x,y)$ . Let us define the phase-only version of  $f(x,y)$  in object space  $f_{PO}(x,y)$  as

$$f_{PO}(x,y) = FT^{-1} \left[ \frac{F(u,v)}{|F(u,v)|} \right] = FT^{-1} \left\{ \frac{FT[f(x,y)]}{|FT[f(x,y)]|} \right\} \quad (15)$$

where FT and  $FT^{-1}$  are the Fourier and inverse Fourier transform operators respectively. The original joint-scene,  $f(x,y)$ , is real and positive so the inverse transform of the frequency plane phase-only filter,  $f_{PO}(x,y)$  is real, with positive and negative values.

There are other advantages gained by using a photorefractive crystal as the JPS processor, rather than a CCD/SLM setup, such as increased resolution; useful diffraction is possible with a grating spacing of  $5\mu\text{m}$ , whereas the pitch of the CCD pixels is approximately  $40\mu\text{m}$ . Also the performance is not degraded by Fourier plane quantisation<sup>23</sup>. Javidi et al<sup>24</sup> report serious deterioration in the performance of a binary JTC with input scene noise for quantisation levels below  $2^{12}$ , the frame grabber used in these experiments has  $2^8$  quantisation levels. Lower quantisation values may be used when the low spatial frequency pixel values are nonlinearly compressed.

#### 4. Coding of phase-only information

In object space, the distribution  $f_{PO}(x,y)$  that results in the phase-only information in the Fourier plane is a real function taking positive and negative values in different zones. This implies that some form of coding is necessary because of the negative values. The technique used for coding the negative values of the objects was derived from the method of subtraction based on the decomposition of the function into two parts, the positive and the negative parts were encoded in Ronchi gratings with the same frequency but opposite phase. This provides the subtraction of amplitudes in Fourier space. Note that this encoding method is a further simplification of the well known Lee's detour-phase hologram method<sup>25</sup>. A real two dimensional function  $h(x,y)$  may be expressed as  $h(x,y) = h^+(x,y) - h^-(x,y)$

$$\begin{aligned} h^+(x,y) &= h(x,y) & \text{if } h(x,y) \geq 0 \\ &= 0 & \text{if } h(x,y) < 0 \end{aligned} \quad (16)$$

$$\begin{aligned} h^-(x,y) &= h(x,y) & \text{if } h(x,y) \leq 0 \\ &= 0 & \text{if } h(x,y) > 0 \end{aligned} \quad (17)$$

Both  $h^+(x,y)$  and  $h^-(x,y)$  are positive functions. The transmission of a Ronchi grating may be represented by its Fourier series expansion

$$r^+(x,y) = 1 + \sum_n r_n \sin\left(\frac{2\pi nx}{p}\right) \quad (18)$$

where  $p$  is the spatial period. If the Ronchi grating is displaced  $p/2$  its transmission will be

$$r^-(x,y) = 1 - \sum_n r_n \sin\left(\frac{2\pi nx}{p}\right) \quad (19)$$

Note that  $r^+(x,y)$  and  $r^-(x,y)$  alternate between the values of 0 and 1 along the x-axis and that they are complementary gratings. Let us consider the following function  $h_c(x,y)$

$$\begin{aligned} h_c(x,y) &= h^+(x,y)r^+(x,y) + h^-(x,y)r^-(x,y) \\ &= [h^+(x,y) + h^-(x,y)] \\ &\quad + [h^+(x,y) - h^-(x,y)] \sum_n r_n \sin\left(\frac{2\pi nx}{p}\right) \end{aligned} \quad (20)$$



Its two dimensional Fourier transform is given by

$$\begin{aligned}
H_c(x,y) &= [H^+(u,v) + H^-(u,v)] \\
&\quad + [H^+(u,v) - H^-(u,v)] \otimes \sum_n r_n \delta\left(u - \frac{n}{p}\right) \\
&= [H^+(u,v) + H^-(u,v)] \\
&\quad + H(u,v) \otimes \sum_n r_n \delta\left(u - \frac{n}{p}\right)
\end{aligned} \tag{21}$$

Finally, by taking the Fourier transform of only one diffraction order, we shall obtain the desired function  $h(x,y)$ . Coding of a digital function was carried out by representing each sampled value using four pixels. Both left pixels are switched on together when the original value was positive. Analogously, the right hand ones are switched on when the value was negative, the other two pixels remain zero.

## 5. Comparison between processing time requirements in a binary joint transform correlator and a photorefractive JTC

As we have pointed out in the previous section, the correlation performance of a POPJTC can be equivalent to a BJTC by using input distributions which give phase-only information at the Fourier plane. Moreover the better operating characteristics of BSO with respect to a CCD is an additional reason to use it. Nevertheless, the scene should be displayed as an encoded distribution and this means that digital preprocessing according to Eq. (15) should be carried out. This is the main time-bottleneck in the recognition process.

In this section we evaluate the number of floating point operations needed to preprocess the scene in order to obtain the encoded distribution. Note that only the scene is taken into account because the reference is calculated at a previous stage. We will compare

the time requirements to carry out the correlation using a POPJTC with the processing time involved in the generation of a binary JPS in a BJTC.

The number of floating point operations (flop) needed to calculate a  $N \times N$  point FFT is<sup>26</sup>

$$flop = 5N^2(\log_2 N - 2) + 32N \quad (22)$$

To obtain an object-space encoded image, we need to divide each point of the Fourier transform by its modulus, so we add  $5N^2$  more floating operations. Finally we inverse Fourier transform the results so the total number of operations is

$$\begin{aligned} 5N^2(\log_2 N - 2) + 32N + 5N^2 + 5N^2(\log_2 N - 2) + 32N = \\ 5N^2(2\log_2 N - 3) + 64N \end{aligned} \quad (23)$$

In our case, the scene consists of  $128 \times 128$  pixels to match the LCTV resolution, so the number of floating point operations is 0.91 Mflops. By means of a benchmark test, we can determine the number of MFlops of the computer that manages the optical system<sup>27</sup>. For example, our inexpensive personal computer based on a Pentium processor at 120MHz performs at 13 MFlops per second, so the preprocessing waste of time is under 0.1 s.

On the other hand, as was pointed out in section 2, the BJPS is obtained by registering separately the JPS and the power spectra of the scene and the reference. As an ordinary CCD works at video rates (1/30 s for frame), the theoretical time requirements to store these three images is 0.1 s (in practice, this time is higher because we do not take into account other factors related with computer hardware).

The next step is to compute the BJPS processing time: 2 integer operations and a comparison are required to determine the sign of each pixel of the BJPS, so we need to calculate  $3N^2$  integer operations (op). Note that in this case the number of points is  $512 \times 512$  according to the sampling capability of the digitiser board. Consequently,  $3N^2 \approx 0.8\text{Mop}$ , and the total processing time is  $> 0.1$  s. Despite the fact that the POPJTC requires the calculation of two two-dimensional FFTs, the bottleneck imposed by the recording of three spectra in a BJTC allows us to conclude that a POPJTC performs correlations at a similar speed to a BJTC using current equipment.

The computational requirements of the PJTC or the BJTC can be improved by using appropriate hardware. For instance, the use of specific FFT hardware or faster video cameras and digitiser boards respectively, substantially reduces the time involved in calculations.

## 6. Performance of the POPJTC in presence of noise

In this section we analyse how the POPJTC/BJTC performs in the presence of zero mean additive Gaussian noise. The results are compared with those obtained with a conventional PJTC. An image of a single satellite ( $64 \times 64$  pixels) as shown on the left-hand side of Fig. 3 (the scene on the right hand side ( $128 \times 128$  pixels) has added noise,  $\sigma=70$ ) has been used as a reference image, the joint-scene has  $319 \times 200$  pixels. The digital simulation of the correlation was carried out by using Eqs. (12) and (13) to simulate both the POPJTC and the PJTC. The standard deviation of the noise added to the scene varies from  $\sigma = 3$  to 70. The simulations and experiments are assessed using the peak-to-total-correlation-energy ratio (PTE), (given as PCE in reference 28),

$$PTE = \frac{(f \otimes g)(0,0)}{\int_{R^2} (f \otimes g)(x,y) dx dy} \quad (24)$$

The simulation was run twenty times for each noise level to find the average PTE at each level. Noise arrays were then generated and tested to find one that gave results close to the average for each level, for later use in the experiment. The results for the simulated PTE measurements are shown in Fig. 4, the simulations show that the PTE results for the POPJTC (solid line) do not change appreciably for different acceptor levels, and the conventional PJTC results (other lines) improve as the space-charge modulation deviates further from the Moharam model. The best advantage of the POPJTC over the conventional JTC is achieved for the situation where Moharam's results are valid, this coincides with the situation where the acceptor concentration is high. The advantage of the POPJTC over the PJTC as predicted by the simulation is only slight. We believe however that as a consequence of the phase-only technique the diffraction efficiency of the phase-only grating will be superior to the conventional case and this will improve the phase-only advantage as noise increases, this is investigated in the next section.

## 7. Optical results

The experimental BSO joint transform correlator setup is shown in Fig. 5. A  $5.6 \text{ kVcm}^{-1}$  ( $E_a$ ) field was applied to the crystal using deposited electrodes to achieve drift-mode recording (see reference 20 for an overview of the photorefractive effect and its applications). The scene and reference images were displayed side by side on the LCTV. The distance between the scene and reference, combined with the choice of lens L1 gave a fringe spacing of  $12 \mu\text{m}$ , this ensured Bragg matching for objects throughout the scene. The different

objects in the scene should not be so far apart that their intra-correlation signals coincide with the cross-correlation field. The LCTV was taken from an Epson VP-100PS projector, it has 326×264 pixels (rows by columns) arrayed in a 32mm diagonal area, each having a size of 80×90μm and an active area of 55×60μm. In this setup it has 319×200 available pixels and a contrast ratio of 30:1. The images were sent to the LCTV using a 768×512 framegrabber board, the images were appropriately scaled to ensure correct pixel registration. The polariser (P) and analyser (A) were aligned to give amplitude mostly modulation<sup>5</sup>.

The Fourier transform was formed at the BSO crystal (10×9×2mm) by lens L1 (focal length 300mm), the zeroth order Ar<sup>+</sup> laser power at the crystal was approximately 50 μW. The combination of pixel pitch and choice of lens results in a separation of approximately 2mm between LCTV diffraction orders at the BSO crystal. Assuming that the transform of the joint-scene is weighted by a sinc function, appropriate to the transform of two apertures, there will be negligible overlap between adjacent orders. Since only one diffraction order was analysed by a narrow, low power HeNe laser, (this does not degrade the grating due to the spectral sensitivity of BSO) separate spatial filtering was not required. The diffracted HeNe beam (dotted line) was sampled using a 20% beam-splitter (BS), and the correlation output was formed by lens L2, then captured by a CCD camera linked to the same frame grabber.

With this arrangement it is possible to perform correlations at high rates. The response time of BSO would permit frame rate throughput but the main limitation in our present setup is the rate at which the LCTV can be realistically updated which has been shown to be about 8 frames per second<sup>10</sup>. Note that the calculations in section 4 have been carried out considering 30 frames per second.

The use of a photorefractive crystal as the recording medium has a number of advantages over and above the potential for real-time operation. It is found that, for example, configurations of this kind are quite robust and are not susceptible to minor misalignments

and these benefits have been further developed in the design of an incoherent correlator based upon the use of Fresnel transforms<sup>29</sup>.

Optical results for a noise level of  $\sigma = 70$  are presented in Figs. 6 (using conventional input) and 7 (using encoded phase-only input), the target to detect is the bigger satellite. It can be seen that the noise contribution from the earth background is obvious in the conventional JTC result but virtually absent from the phase-only correlation. The higher peaks near the autocorrelation peaks are false correlations due to the high noise level, discrimination is however still achieved. Measuring the signal-to-noise-ratio (SNR) as

$$\text{SNR} = \frac{\text{correlation peak max.}}{\text{variance of intensities} < \left( \frac{\text{max}}{2} \right)} \quad (25)$$

gives the conventional PJTC SNR as 10.1 and the POPJTC SNR as 40.2 at this noise level.

The experimental PTE results obtained using the representative noise arrays are shown in Fig. 8. The HeNe intensity used was sufficient to achieve the same correlation peak maximum for all noise levels. When these results are compared with those predicted by the simulation (Fig. 4) there is little similarity. This disparity is, we believe, due to the effect of diffraction efficiency on the signal to noise ratio. For the encoded filters the modulation of the JPS will always be very close to  $m=1$  at all noise levels. The modulation of the conventional JPS however will fall as the noise is increased. It can be seen from the space-charge versus modulation graph in Fig. 2 that the space-charge and hence the diffraction efficiency falls sharply as the modulation is reduced from  $m=1$ . For example, at low noise ( $\sigma=3$ ) the encoded filter requires a HeNe intensity of  $65\mu\text{W}$  and the conventional filter requires  $100\mu\text{W}$ ; at high noise ( $\sigma=70$ ) the intensities required are  $0.9\text{mW}$  and  $4.3\text{mW}$  respectively. Fig. 9. shows a measure of the effect that the diffraction efficiency will have on the signal to noise

measurements,  $\eta$  is the normalised diffraction efficiency, calculated from the ratio of correlation peak height to the HeNe beam intensity. This relationship between the diffraction efficiency and noise bears some resemblance to the PTE curves, hence we suggest that the improved phase-only PTE results are due to a combination of the phase-only (binarised) correlation and the improved diffraction efficiency of the gratings. The improvement in diffraction efficiency is all the more impressive when it is considered that in all cases the intensity of  $\text{Ar}^+$  light reaching the crystal is much lower for the phase-only filters.

## 8. Summary

Correlations equivalent to those obtained using a binary JTC can be obtained by using phase only information from the encoded scene and reference in object space as the input to a photorefractive JTC. The main advantages of this procedure are i) no computer control is needed to deal with the threshold function and ii) the use of BSO crystals improves the spatial bandwidth of the usual recording systems. On the other hand, both scene and reference must be detour-phase encoded in the input LCTV.

We have also analysed the time requirements to obtain the encoded scene and we have shown that this time is similar to the time required to compute the BJPS in a BJTC. The noise analysis shows that the POPJTC performs better than PJTC, when the scene is corrupted by Gaussian noise, the values of the metric considered are always higher when using POPJTC rather than PJTC.

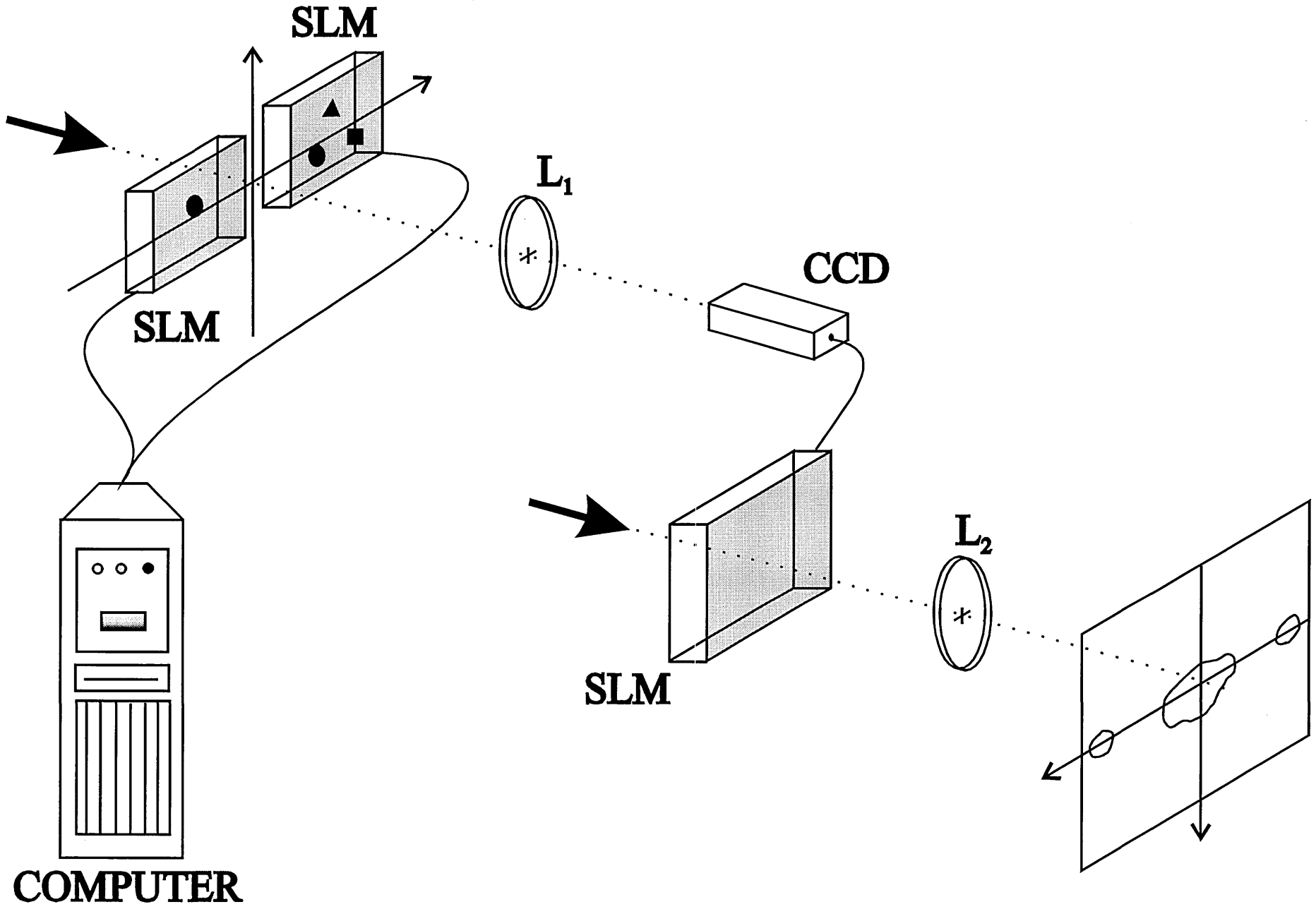
Experimental realisation of optical correlation using i) conventional matched input and ii) encoded phase-only joint-scene, in a real-time JTC using a BSO crystal to record the joint power spectrum has been presented. The performance of the JTC in case ii) was improved across a range of noise due in part to the binarisation of the JPS and also to the

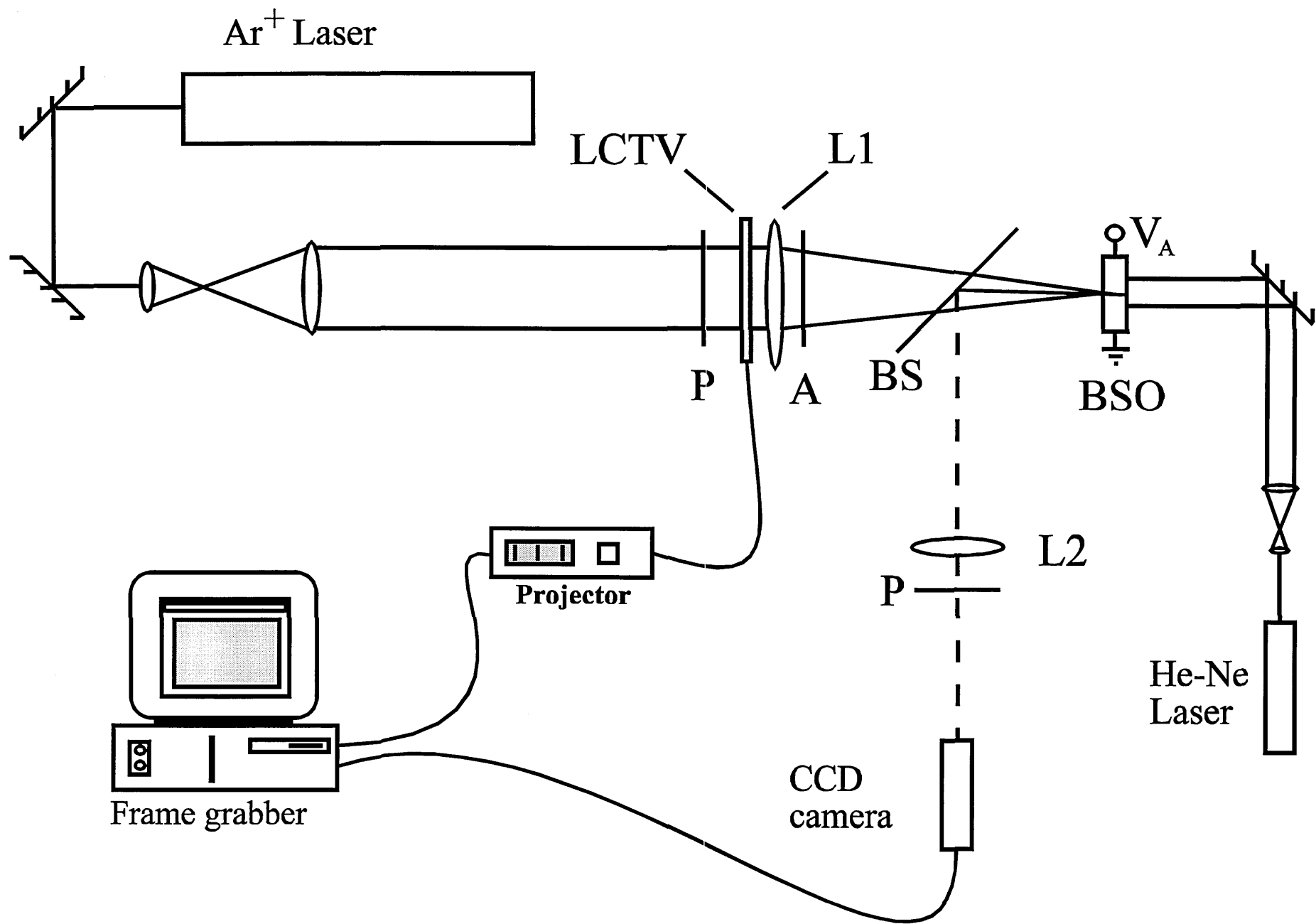
increased diffraction efficiency resulting from the maximised modulation inherent in the phase-only Fourier plane distributions.

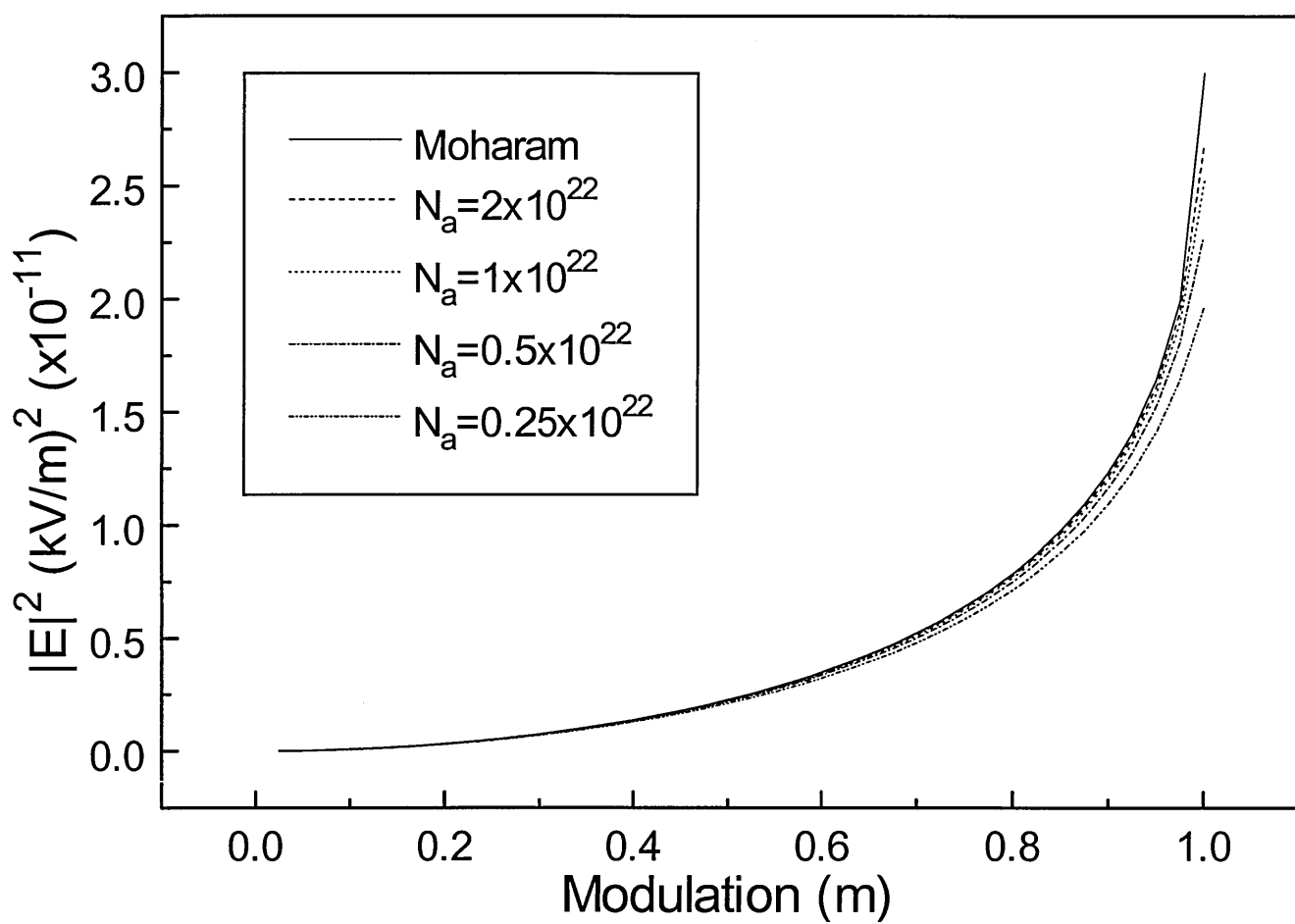
### **Acknowledgements**

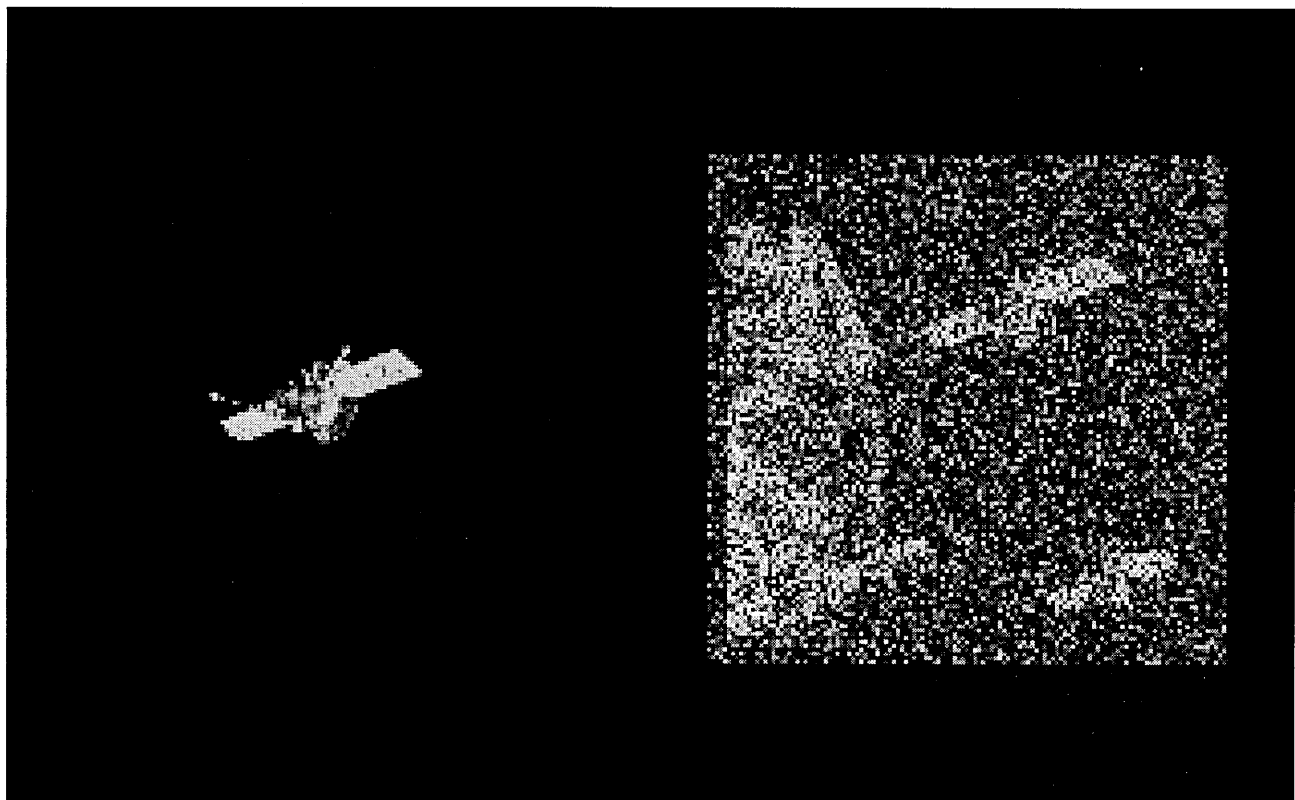
This paper has been supported in part by the *CICYT (Comision Interministerial de Ciencia y Tecnologia)*, project TAP94-0303. The authors thank Dr Mario Montes-Usategui for helpful suggestions.

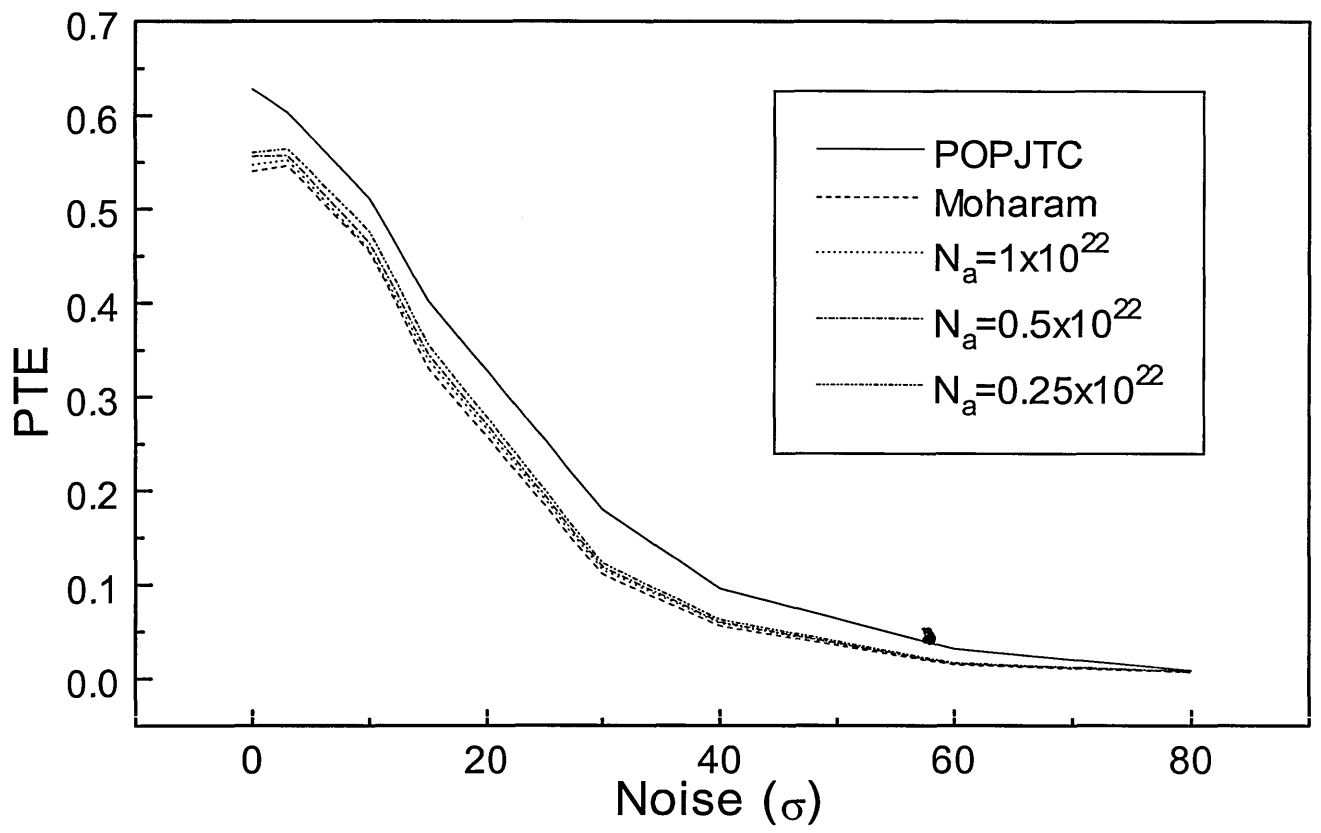


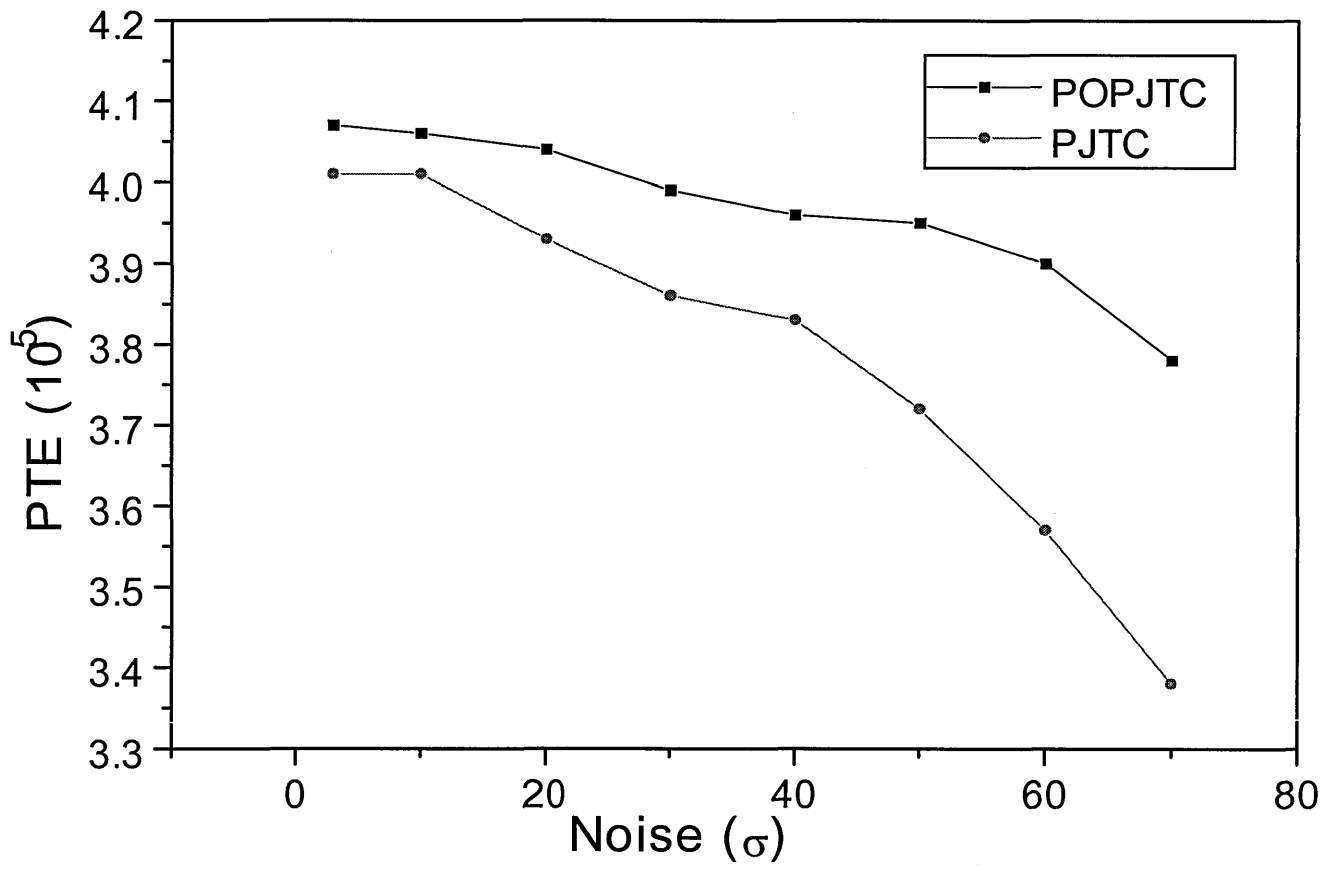


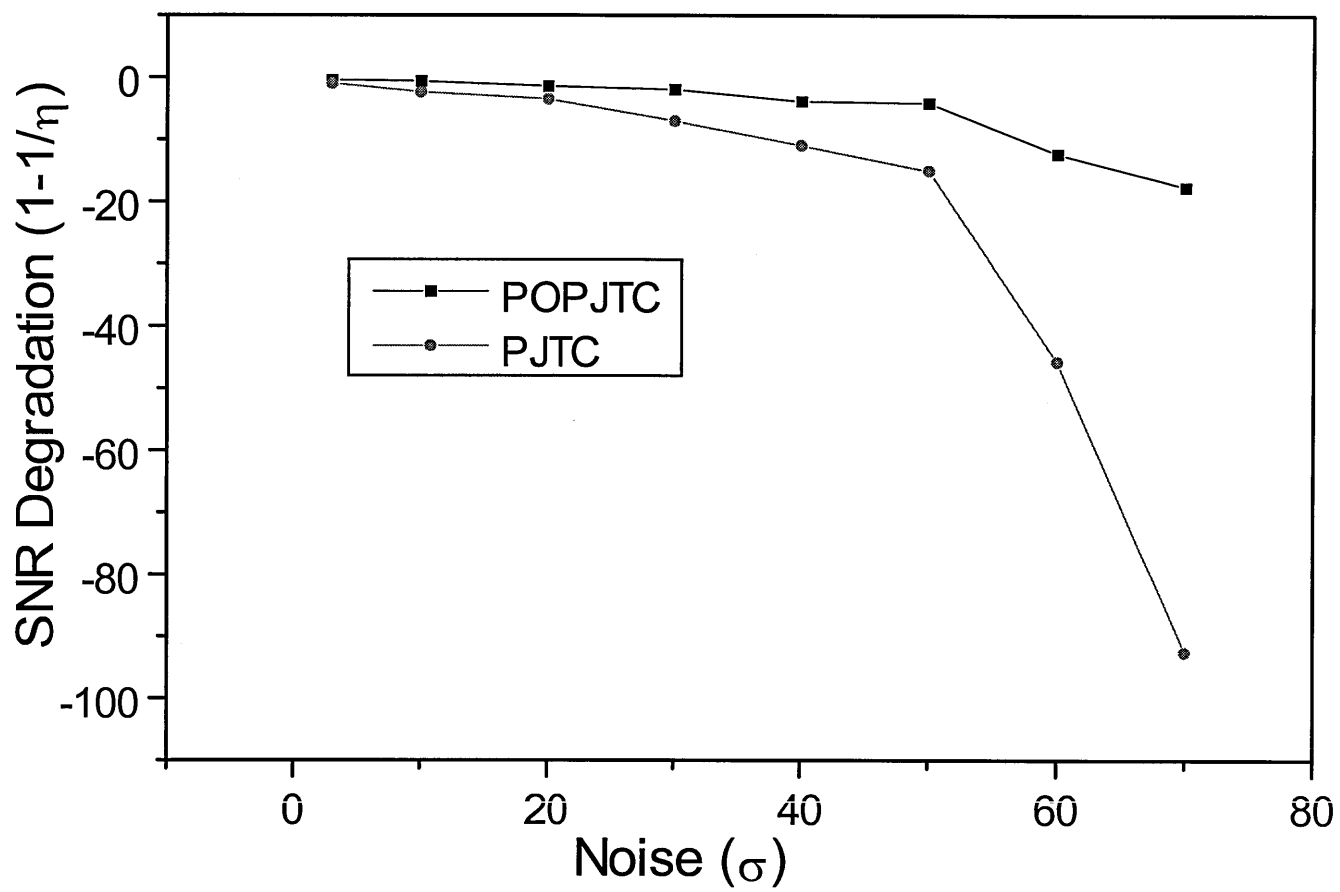












## References.

1. A. Vander Lugt, "Signal detection by complex spatial filtering", IEEE Trans. Inform. Theory **IT-10**, 139-145 (1964).
2. C. S. Weaver and J. W. Goodman, "A technique for optically convolving two functions", Appl. Opt. **5** 1248-1249 (1966).
3. S. Yu and X. J. Lu, "A real-time programmable joint transform correlator", Opt. Comm. **52**, 10-16 (1984).
4. Liu, J. A. Davis and R. A. Lilly, "Optical data processing properties of a liquid crystal television spatial light modulators", Opt. Lett. **10**, 635-637 (1985).
5. C. Kirsch, D. A. Gregory, M. W. Thie and B. K. Jones, "Modulation characteristics of the Epson liquid crystal television", Opt. Eng. **31**, 963-969 (1992).
6. L. Pichon and J. P. Huignard, "Dynamic joint-Fourier transform correlator by Bragg diffraction in photorefractive  $\text{Bi}_{12}\text{SiO}_{20}$  crystals", Opt. Comm. **36**, 277-280 (1981).
7. C. Soutar, Z. Q. Wang, C. M. Cartwright and W.A. Gillespie, "Real-time optical intensity correlator using photorefractive BSO and liquid crystal television", J. Mod. Opt. **39**, 761-769 (1992).
8. B. Javidi, "Nonlinear correlation joint transform correlation", Appl. Opt. **28**, 2358-2367 (1989).
9. S. Vallmitjana, A. Carnicer, E. Martín-Badosa and I. Juvells, "Nonlinear filtering in object and Fourier space in a joint transform optical correlator: comparison and experimental realization", Appl. Opt. **34**, 3942-3949 (1995).
10. C. Soutar, S. E. Monroe Jr. and J. Knopp, "Complex characterisation of the Epson liquid crystal television", Proc. SPIE **1959**, 269-277 (1993).



11. F. T. S. Yu, S. Jutamulia, T. W. Lin and D. A. Gregory, "Adaptive real-time pattern-recognition using a liquid crystal TV based joint transform correlator", *Appl. Opt.* **26**, 1370-1372 (1987).
12. B. Javidi, J. Wang and Q. Tang, "Multiple-object binary joint transform correlation using multiple level threshold crossing", *Appl. Opt.* **30**, 4234-4244 (1991).
13. Q. Zhan, T. Minemoto, "Successful pattern matching with a large number of reference patterns using a joint Fourier-transform correlator", *Jpn. J. Appl. Phys.* **32**, 3471-3476, (1993)
14. Y. Osugi, Q. Zhan, T. Minemoto, "Hybrid binary subtracted joint transform correlator for a large number of reference patterns using a  $\text{Bi}_{12}\text{SiO}_{20}$  (BSO) spatial light modulator and a laser scanner", *Opt. Rev.* **1**, 159-162, (1994)
15. K. Chalasinska-Macukow and C. Gorecki, "Optoelectronic implementation of a quasi-phase correlator", *Opt. Commun.* **93**, 11-18 (1992).
16. A. Carnicer, E. Martin-Badosa, I. Juvells and S. Vallmitjana, "Spatial envelop-free nonlinear joint transform correlator", *Opt. Commun.* **114**, 336-343 (1995).
17. D. Feng, H. Zhao and S. Xia, "Amplitude modulated joint transform correlator for improving correlation discrimination", *Opt. Commun.* **86**, 260-264 (1991).
18. F. Cheng, F. T. S. Yu and D. A. Gregory, "Multitarget detection using spatial synthesis joint transform correlator", *Appl. Opt.* **32**, 6521-6526 (1993).
19. H. Gunter, P. H. Higuard, *Photorefractive materials and their applications II*, Topics in Applied Physics **62**, Springer-Verlag, Berlin (1989).
20. T. J. Hall, R. Jaura, L. M. Connors and P. D. Foote, "The photorefractive effect. A review", *Prog. Quant. Electron.* **10**, 77-146 (1985).

21. M.G.Moharam, T.K.Gaylord, R.Magusson, L. Young, "Holographic grating formation in photorefractive crystals with arbitrary electron transport lengths", J. App. Phys, **50**, 5642-5651, (1979)
22. E.Ochoa, F.Vachss, L.Hesselink, "Higher order analysis of the photorefractive effect for large modulation depths", J. Opt. Soc. Am. A, **3**, 181-187 (1986)
23. Y. Osugi, H. Mizukawa and T. Minemoto, "Quantization and truncation conditions of Fourier power spectrum for good performance in a binary subtracted joint transform correlator", Opt. Rev. **3**, 161-170, (1996)
24. B. Javidi, J. Ruiz and C. Ruiz, "Performance of the binary nonlinear joint transform correlators in the presence of the Fourier plane quantization", Opt. Commun. **80**, 275-284 (1991).
25. W. H. Lee, "Sampled Fourier transform hologram generated by computer", Appl. Opt. **9**, 639-643 (1970).
26. H. J. Nussbaumer, *Fast Fourier Transform and Convolution Algorithms*, Series in Information Sciences, Springer-Verlag, Berlin (1982).
27. The number of floating operation for second can be obtained by using a performance test. Specialized algorithms to deal with Fourier transforms are also available. The C code to test the marks of our computed has been obtained from anonymous ftp at <ftp://ftp.nosc.mil/pub/aburto/tfftdp.c>. Further details of compiler requirements to carry out the test can be found in <http://www.netlib.org/performance/html/PDSreports.html>
28. B. V. K. Vijaya Kumar and L. Hassebrook, "Performance measures for correlation filters", Appl. Opt. **29** 2997-3006 (1990).
29. C. Soutar, W. A. Gillespie and C. M. Cartwright, "The effect of optical bias on grating formation dynamics in photorefractive BSO", Opt. Comm. **90**, 329-334 (1992).

## List of Figures.

Fig. 1. Standard joint transform correlator experimental setup. SLM stands for spatial light modulator, CCD is a charge coupled device camera,  $L_1$  and  $L_2$  are lenses.

Fig. 2. Variation of square modulus of the space-charge field, (proportional to refractive index) with intensity modulation for a range of acceptor concentrations.

Fig. 3. The matched joint-scene with zero mean Gaussian additive noise of standard deviation,  $\sigma=70$ .

Fig. 4. The simulated PTE results for the POPJTC and the PJTC with increasing noise.

Fig. 5. The BSO joint transform correlator experimental setup. LCTV stands for liquid crystal television, BS is a 20% beam splitter,  $L_1$  and  $L_2$  are lenses, P and A are polariser and analyser respectively

Fig. 6. Experimental correlation of conventional input with noisy scene, ( $\sigma=70$ ).

Fig. 7. Experimental correlation of encoded phase-only input with noisy scene, ( $\sigma=70$ ).

Fig. 8. Experimental PTE results for the POPJTC and PJTC.

Fig. 9. Measure of signal degradation due to increasing noise.

# Enhancement of Phase Conjugate Beam Reflectivity of Photorefractive $\text{Bi}_{12}\text{SiO}_{20}$ by the Moving Grating Technique.

N.J.Cook, Z.Q.Wang, C.M.Cartwright, W.A.Gillespie.

Department of Electronic Engineering,  
University of Abertay Dundee,  
Bell Street,  
Dundee DD1 1HG,  
UK.

Telephone: 01382 308000  
FAX: 01382 308877  
eMail: N.J.COOK@TAY.AC.UK

## ABSTRACT

The use of moving gratings to enhance two wave mixing processes in BSO is well established. In the past we have used this technique to demonstrate increased diffraction efficiency for the purpose of correlation. We now investigate phase conjugate beam reflectivity as a function of incident beam ratio, pump beam ratio and grating velocity.

## SUMMARY

The use of photorefractive BSO in both two wave and four wave mixing geometries has been well reported, for example see: [1]. The moving grating technique has been applied to such dynamic holographic processes and has been shown to reduce energy coupling and allow a larger refractive index modulation: [2].

We have previously reported the enhancement of the diffraction efficiency of dynamic gratings recorded in a BSO crystal at high modulation: [3]. The optimum fringe velocity for the maximum diffraction efficiency was found to vary in a complicated manner as the fringe modulation increased: [4]. The enhancement by moving grating also has the effect of suppressing random fluctuations in energy transfer.

In this paper we investigate the nonlinear effects of a moving grating on phase conjugate reflection by four-wave mixing at high modulation: [5]. We also look at the dependence of reflectivity on fringe modulation and pump beam ratio. A thin and a thick crystal were studied. The experimental configuration used is shown in Figure 1.

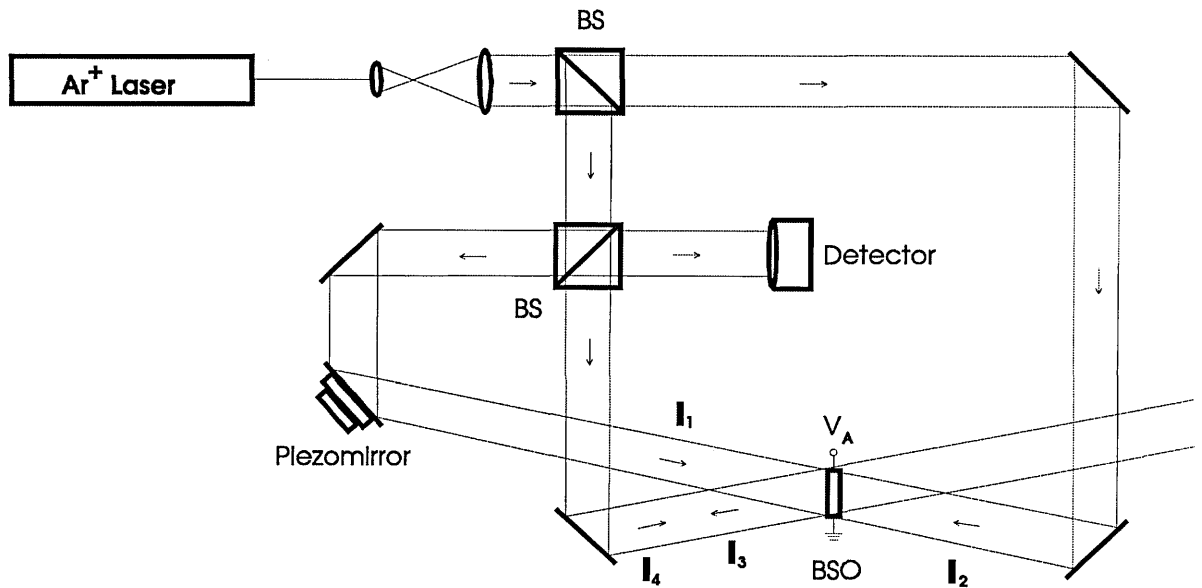


Figure 1. Schematic diagram of the four-wave mixing system. an aperture may be used to limit the spatial extent of the signal beam,  $I_4$ .

The beams enter the  $(\bar{1}10)$  plane of polished BSO, the external field, of  $5\text{kVcm}^{-1}$ , was applied along the  $[110]$  direction, parallel to the grating vector, giving the optimum four-wave mixing orientation. The crystals have dimensions  $10\times 9\times 2\text{mm}$  and  $10\times 9\times 5\text{mm}$ . The reference pump beam,  $I_1$  and the signal beam,  $I_4$  interfere in the crystal volume. Beam  $I_2$ , counterpropagating to the plane wave reference, generates the conjugate beam,  $I_3$ . The frequency detuning,  $\delta\omega$ , of the pump beam  $I_1$ , is accomplished using a piezomirror, and generates a conjugate beam of frequency  $\omega_0+\delta\omega$ .

The reflectivity is found to have an unusual dependence on fringe velocity at high modulation with a low pump beam ratio. Figures 2. and 3. show the variation of phase conjugate reflectivity with fringe velocity (in  $\mu\text{ms}^{-1}$ ) for high and low signal beam ratios,  $\beta=I_1/I_4$  respectively, and at different pump beam ratios,  $r=I_2/I_1$ .

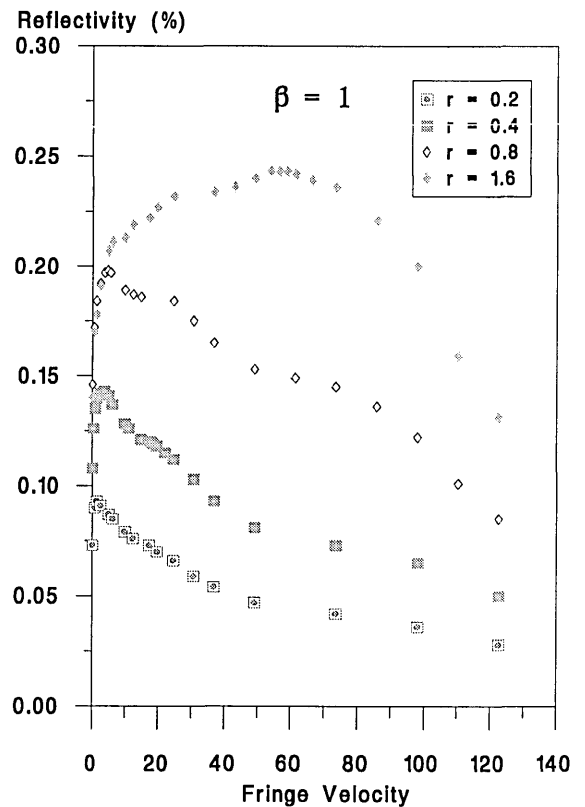


Figure 2. Phase conjugate reflectivity variation with fringe velocity at high modulation.

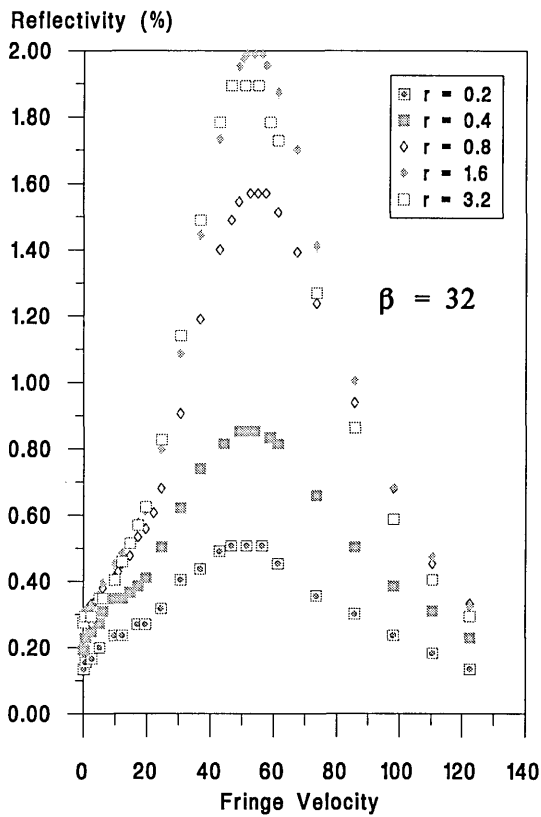


Figure 3. Phase conjugate reflectivity variation with fringe velocity at low modulation.

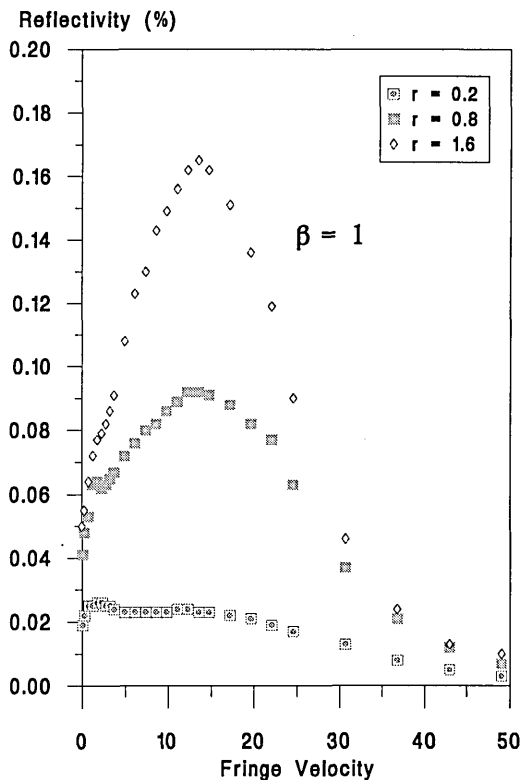


Figure 4. Phase conjugate reflectivity variation with fringe velocity for thick crystal.

The reflectivity exhibits maximum values when the interference pattern inside the crystal moves at an optimum velocity. As  $\beta$  increases towards unity and  $r$  is reduced, the optimum velocity jumps to a lower value. There is often an intermediate stage when two reflectivity maxima are found at separate fringe velocities. Figure 4. Shows the phase conjugate reflectivity of the thick crystal for a high pump ratio, the low velocity enhancement is only apparent at the lowest pump ratios, it is less noticeable because of the increased enhancement at higher pump ratios. The higher optimum velocity is predicted by coupled mode equations:[6] applied to dynamic holography in photorefractive crystals, this analysis is useful for small modulations when the differential equations of Kukhtarev et al: [7] may be applied. Similar fast and slow velocity effects in two-wave mixing diffraction processes have been observed and numerically analysed:[8].

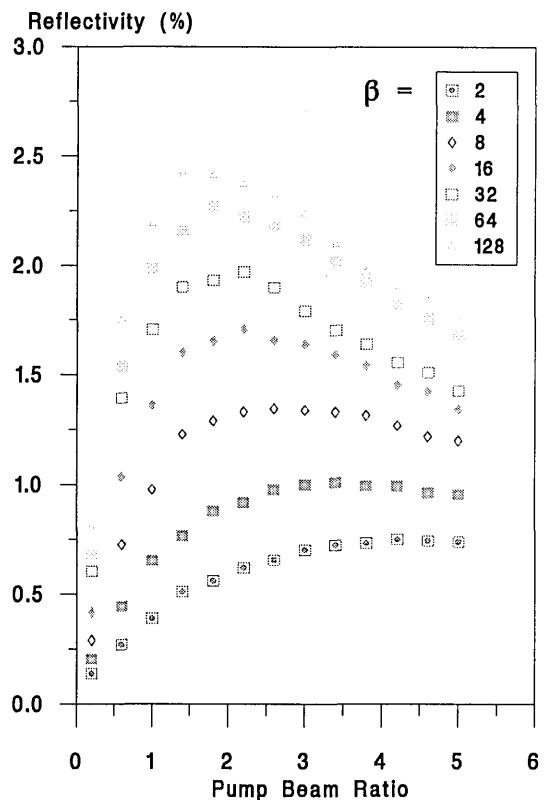


Figure 5. Variation of reflectivity with pump beam ratio.

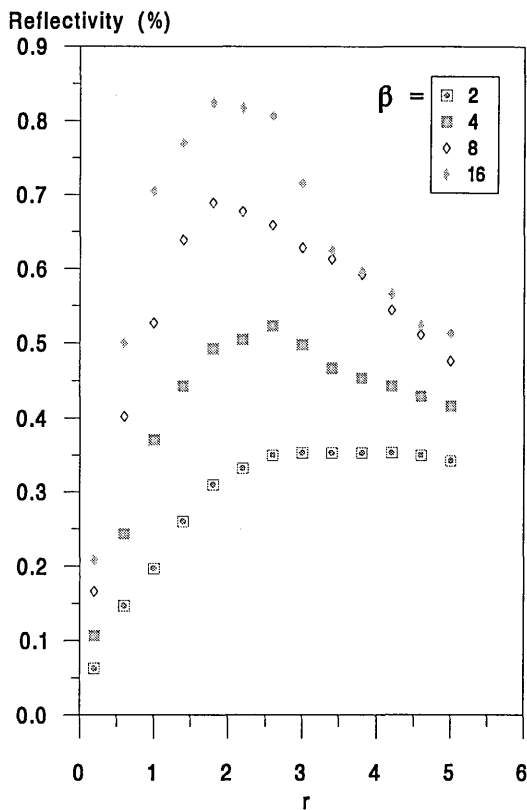


Figure 6. Variation of reflectivity with pump beam ratio for thick crystal.

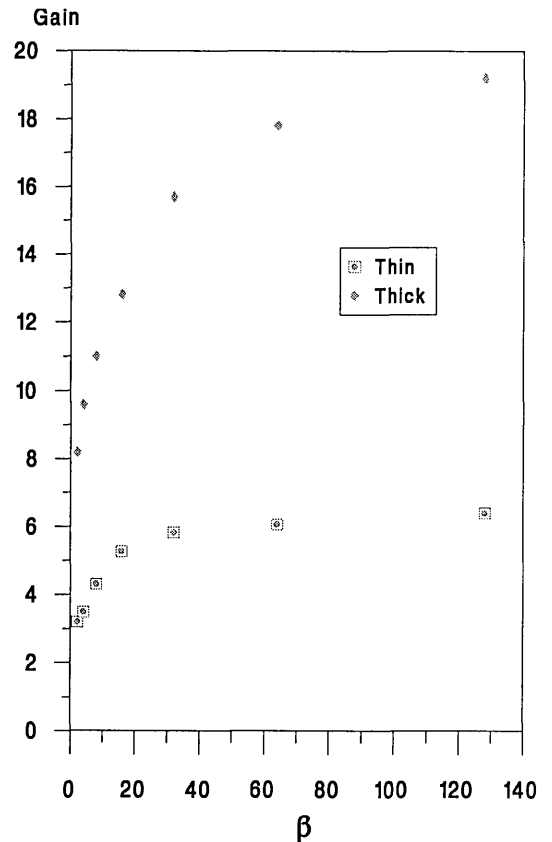


Figure 7. Reflectivity gain due to moving gratings.

The relationship between reflectivity,  $\beta$  and  $r$  is investigated more closely in Figures 5. and 6., each point was measured at the optimum fringe velocity. There is an optimum pump ratio which becomes more apparent and shifts to lower pump ratios as the signal ratio is increased. For stationary fringes the reflectivity maximum is obtained for  $r=1$ . Figure 7. shows how the gain (increase in reflectivity due to moving gratings) changes with pump ratio for the thin and thick crystals. As the signal ratio increases, the enhancement increases as well, as it increases further, the enhancement saturates. This phenomenon is qualitatively predicted by Au and Solymar's numerical results:[9].

1. Cronin-Golomb Mark, Fischer B, White J.O, Yariv A, IEEE J. Quantum Electron., **20**, 12, (Jan,1984).
2. Rajbenbach H, Huignard J.P, Refregier Ph, Opt. Lett., **9**, 558, (Dec,1984).
3. Wang Z.Q, Gillespie W.A, Cartwright C.M, App. Opt., **33**, 7627, (1994).
4. Brost George A, Photorefractive Materials, Effects and Devices, PRM '93, Kiev, (Aug,1993).
5. Toshiyuki Yoshikara, Iba J, Uesu Y, Hikita K, Iizuka H, Jpn. J. Appl. Phys., **31**, 3205, (Sep,1992).
6. Fischer Baruch, Cronin-Golomb M, White J.O, Yar iv A, Opt. Lett., **6**, 519, (Nov, 1981).
7. Kukhtarev N.V, Markov V.B, Odulov S.G, Soskin M.S, Vinetskii V.L, Ferroelectrics, **22**, 949, (1979).
8. Brost George B, Mat. Res. Soc. Symp. Proc., **261**, 197 (1992).
9. Au L.B, Solymar L, Opt. Lett., **8**, 660, (Aug, 1988).

## The Effects of Optical Bias on Moving Gratings in BSO at Large Fringe Modulation

C.M. Cartwright, W.A. Gillespie, Z.Q. Wang and N.J. Cook  
Department of Electronic and Electrical Engineering  
University of Abertay Dundee, Dundee, U.K.

### I. Introduction

It has previously been shown that holographic recording in BSO can be enhanced by the moving grating technique<sup>1</sup>. However, the nature of the dependence of the optimum fringe velocity on the fringe modulation limits its applications<sup>2-4</sup>. Practically, one can normally only use a fixed fringe velocity which would be suitable only for a certain limited range of fringe modulations. The difficulty occurs at fringe modulations close to unity where the optimum fringe velocity decreases by two orders of magnitude with respect to its value at smaller fringe modulations. There are two strategies to overcome this problem: 1. adjusting the recording beam ratios to avoid fringe modulations close to unity; 2. applying optical bias, i.e. additional uniform white-light illumination, to reduce the actual fringe modulations. We expect that while optical bias overcomes the difficulty of the sudden decrease in the optimum fringe velocity when the fringe modulation is close to unity, it will enhance the diffraction efficiency with a moving grating compared to that with a stationary grating.

### II. Experiments and Results

The experimental set-up is shown in Fig. 1, where W.L. is the white-light source, PBS is a polarisation beam splitter,  $\lambda/2$  is the half-wave plate, and D1 and D2 are the detectors. The recording conditions of the grating for the following measurements are:  $E_0 = 6.25$  kV/cm,  $I_0 = 25$  mW/cm<sup>2</sup> and  $\Lambda = 20$   $\mu$ m.

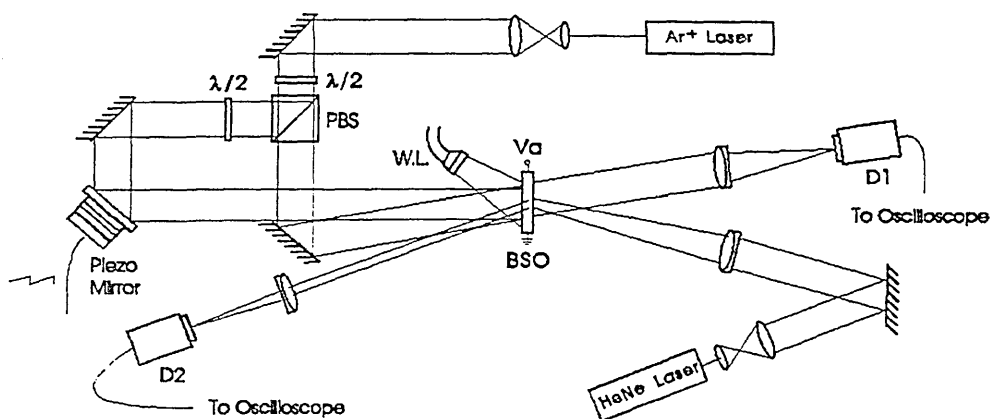


Fig. 1.

Fig. 2 presents the experimental results for the optimum fringe velocity versus the white-light intensity. We chose  $m = 0.9$  and  $m = 1$ , because the optimum fringe velocity at these modulations is much lower than that at smaller fringe modulations. We can see from Fig. 2 that for the  $m = 0.9$  curve the optimum fringe velocity jumps to a high value (459  $\mu$ m/s) when the white-light intensity increases to 40 % in relative units (relative to the photocurrent induced by the writing laser beams), and for the  $m = 1$  curve it jumps to a high value when the white-



light intensity increases to 56 % in relative units. This implies that by adopting a bias with intensity of 56 % in relative units, we are able to eliminate the sudden drop in the optimum fringe velocity.

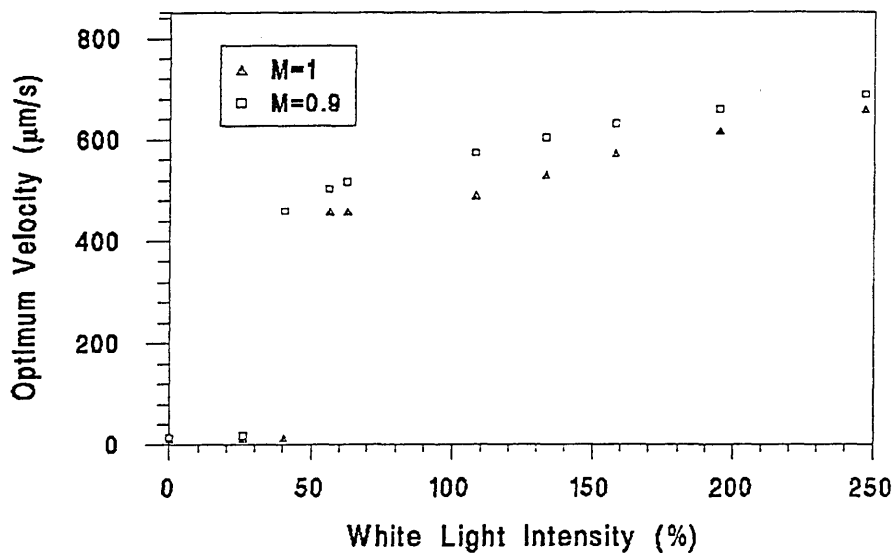


Fig. 2.

Fig. 3 presents the experimental results for the optimum fringe velocity versus the fringe modulation with ("With W.L." curve) and without ("No W.L." curve) white-light illumination. It can be seen that there is a sudden drop in the optimum fringe velocity at  $m \approx 0.9$  in the "No W.L." curve. The "With W.L." curve does not show this sudden drop, and therefore an average fringe velocity of  $440 \mu\text{m/s}$  in this case can be used to satisfactorily enhance the diffraction efficiency of all gratings with different modulations.

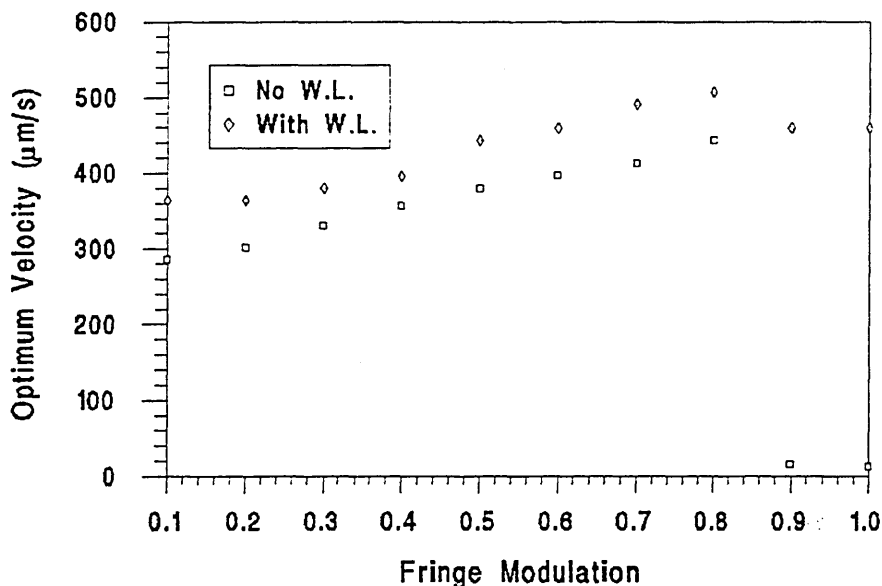


Fig. 5.3.

Fig. 4 presents the experimental results of the absolute diffraction efficiency versus white-light intensity. "Normal" denotes a stationary grating, while "M.G." denotes a moving grating. We can see that with a stationary grating, the diffraction efficiency drops monotonically and

rapidly as the white-light intensity increases. The situation is more complicated with a moving grating. In the lower optical bias range, as the white-light intensity increases the diffraction efficiency increases as well, until it reaches its peak value at a white-light intensity of 40 % in relative units. This is not expected by consideration of the optical bias influence on the fringe modulation. This phenomenon implies that with suitable optical bias and moving gratings the signal-to-noise ratio can be further improved. In the higher optical bias range, as the white-light intensity increases, the diffraction efficiency decreases monotonically. However the decrease is much slower than that with a stationary grating.

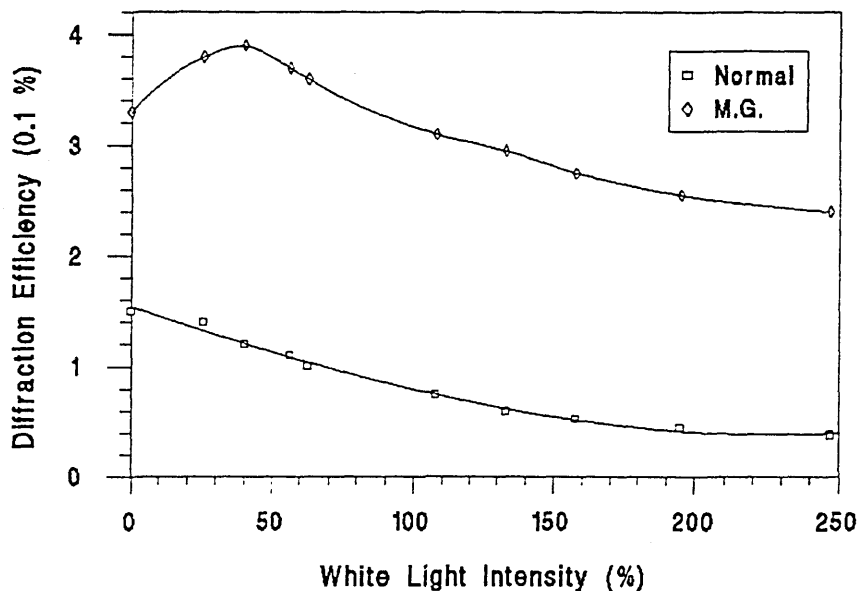


Fig. 4.

Fig. 5 presents the experimental results of the enhancement of the diffraction efficiency "G" using moving gratings with optical bias. G is defined as the ratio of the diffraction efficiency at the optimum fringe velocity to that with the stationary grating. The three curves correspond to the fringe modulations  $m = 0.8$ ,  $m = 0.6$ , and  $m = 0.4$ . It can be seen that as the white-light intensity increases, the enhancement of the diffraction efficiency increases as well. This can be explained by the nonlinearity of moving gratings at large fringe modulations<sup>1</sup>: the optical bias decreases the actual fringe modulation, and the smaller the fringe modulation is, the higher is the enhancement of the diffraction efficiency.

#### IV Conclusions

We have experimentally investigated the influence of optical bias on moving gratings at large fringe modulations. With a suitable optical bias, not only is the variation of the optimum fringe velocity improved, which is beneficial to the holographic reconstruction in the case of gratings with different fringe modulations, but also the absolute diffraction efficiency is further enhanced. This reveals a further insight into the fundamental nature of the grating formation in photorefractive materials. This also implies that with a moving grating a bright environment is harmless to dynamic holography, and the artificial "dark room" is not necessary. Optical bias increases the enhancement of the diffraction efficiency, which could be explained by the non-linear effect on the actual fringe modulations.

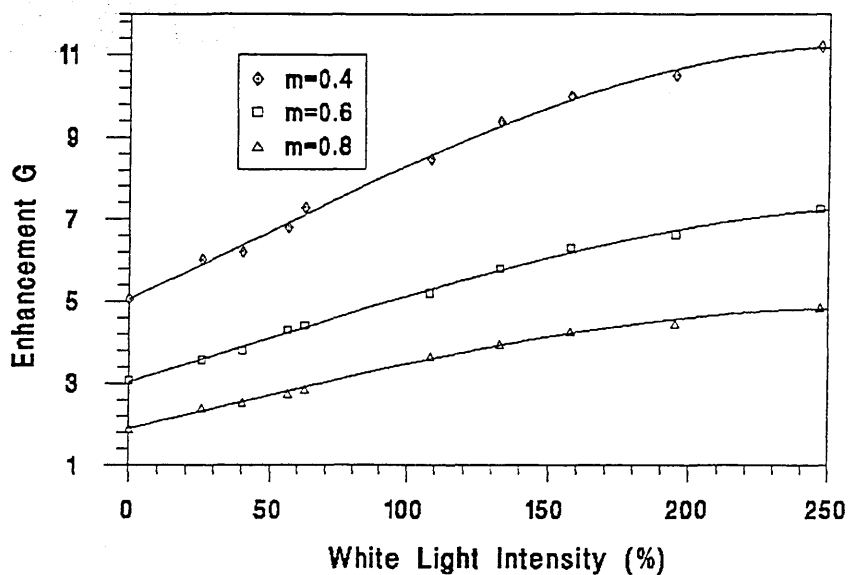


Fig. 5.

References:

1. Z.Q. Wang, W.A. Gillespie, and C.M. Cartwright, "Holographic-recording improvement in a bismuth silicon oxide crystal by the moving-grating technique". *Appl. Opt.*, **33** (1994) 7627-7633.
2. G. A. Brost, "Numerical analysis of the photorefractive response with moving gratings", presented at the Photorefractive Materials, Effects and Devices PRM93, Kiev, Ukraine, August 11-15, 1993.
3. L.B. Au and L. Solymar, "Space-charge field in photorefractive materials at large modulation", *Opt. Lett.* **13**, (1988) 660-662.
4. L.B. Au and L. Solymar, "Higher harmonic gratings in photorefractive materials at large modulation with moving fringes", *J. Opt. Soc. Am. A7*, (1990) 1554-1561.

## Optical Implementation of a Binary Joint Transform Correlator using Object Space Filters

C.M.Cartwright<sup>1</sup>, S.Vallmitjana<sup>2</sup>, A.Carnicer<sup>2</sup>, N.J.Cook<sup>1</sup>, I.Juvells<sup>2</sup> and W.A.Gillespie<sup>1</sup>

(1) University of Abertay, School of Engineering, Bell Street, Dundee DD1 1HG (UK).  
e-mail : c.m.cartwright@tay.ac.uk

(2) Universitat de Barcelona, Laboratori d'Optica, Departament de Fisica Aplicada i Electronica, Diagonal 647, E08028 Barcelona ( Spain )  
e-mail: santi@optica.fae.ub.es

### ABSTRACT

A Binary Joint Transform Correlator with spatial envelope removal is implemented in BSO with the aid of coded objects and filters in the input plane, resulting in a phase-only correlation.

### SUMMARY

#### 1. Introduction

The Joint Transform Correlator (JTC) is a popular choice for optical recognition tasks given its ease of alignment and suitability for hybrid-optical processing. However owing to the heavy d.c. content of the input it also produces relatively broad correlation profiles giving problems with discrimination and multi-target detection [1]. The Binary Joint Transform Correlator (BJTC) is one form of a non-linear JTC where the joint Fourier power spectrum is binarised according to some pre-determined threshold and can result in a correlator with improved characteristics such as light efficiency, correlation peak size and discrimination. Much effort has gone into investigating the selection of a suitable threshold and it has been shown that spatial envelope removal [2] can eliminate cross-correlation terms in the case of multiple targets although this involves recording and processing power spectra in a PC for each correlation performed.

We show in this paper that by suitable pre-processing of the object and filter presented to the input of a BSO based JTC, spatial envelope removal can be achieved and hence a BJTC implemented without any digital recording and processing of power spectra.

#### 2. Spatial Envelope Removal

The joint power spectrum at the Fourier plane of a JTC may be written as :

$$I(u, v) = |H_R(u, v)|^2 + |H(u, v)|^2 + 2|H_R(u, v)||H(u, v)| \times \cos(x_0 u + y_0 v + \varphi(u, v) - \varphi_R(u, v)) \quad (1)$$

where  $H_R(u,v)$  and  $H(u,v)$  are the Fourier transforms of the reference  $h_R(x,y)$  and the scene  $h(x,y)$  located at  $(x_0,y_0)$  respectively. In a BJTC  $I(u,v)$  is binarised and expressed as a Fourier expansion[3]. The d.c. terms are usually pre-recorded and subtracted from the joint power spectrum. In the Fourier expansion of  $I(u,v)$  the spatial envelope term :

$$|H_R(u,v)||H(u,v)|$$

can lead to cross-correlations in multi-target inputs but can be eliminated by a suitable choice of binarising threshold [3] or other methods [4]. We note however that if the amplitudes of  $H_R(u,v)$  and  $H(u,v)$  are unity the same result is obtained. This implies that the filter is the familiar phase-only filter (POF) and that the object must be pre-processed so as to contain only phase information at the Fourier plane of the JTC. In turn since these functions are to be displayed on a conventional spatial light modulator (SLM) some form of coding method is needed since in general functions of this kind will be real but contain both positive and negative values.

### 3. Object and filter coding

The technique used for coding the negative values of the filter and object is derived from the method of subtraction based on the decomposition of the function into two parts, positive and the negative, encoded in Ronchi gratings with the same frequency but with opposite phase[5]. This results in the subtraction of amplitudes in the Fourier plane.

A real two dimensional function  $h(x,y)$  may be expressed as

$$h(x,y) = h^+(x,y) - h^-(x,y), \tag{2}$$

where	$h^+(x,y) = h(x,y)$	when $h(x,y) > 0$
	$= 0$	when $h(x,y) < 0$
	$h^-(x,y) = -h(x,y)$	when $h(x,y) < 0$
	$= 0$	when $h(x,y) > 0$ .

Both  $h^+$  and  $h^-$  are positive functions and are called bipolar filters.

The transmission of a Ronchi grating may be represented by its Fourier series expansion

$$r^+(x,y) = 1 + \sum r_n \sin(2\pi n x / p), \tag{3}$$

where  $p$  is the spatial period. If the Ronchi grating is displaced  $p/2$  its transmission will be

$$r^-(x,y) = 1 - \sum r_n \sin(2\pi n x / p). \tag{4}$$

Note that  $r^+$  and  $r^-$  alternate between values of 0 and 1 along the x-axis and that they are complementary gratings.

Let us consider the following function

$$\begin{aligned} h_c(x,y) &= h^+(x,y) r^+(x,y) + h^-(x,y) r^-(x,y) \\ &= [h^+(x,y) + h^-(x,y)] + [h^+(x,y) - h^-(x,y)] \sum r_n \sin(2\pi nx/p) \end{aligned} \quad (5)$$

Its two dimensional Fourier transform is given by

$$\begin{aligned} H_c(u,v) &= [H^+(u,v)+H^-(u,v)] + [H^+(u,v)-H^-(u,v)] \otimes \sum r_n \delta(u-n/p) \\ &= [H^+(u,v)+H^-(u,v)] + H(u,v) \otimes \sum r_n \delta(u-n/p) \end{aligned} \quad (6)$$

Finally, by taking the Fourier transform of only one diffraction order, we shall obtain the desired function  $h(x,y)$ . Coding of a digital function is carried out by representing each sampled value using four pixels of a SLM. Both left pixels are switched on together when the original value is positive. Analogously, the right hand ones are switched on when the value is negative. The other two pixels remain zero. This technique is a simplification of a method for computer generated holograms[5].

#### 4. Results

We present in this abstract preliminary results of simulations and experiments which have been carried out to test the viability of this method. To begin with simulations of the BJTC have been performed which take into account the non-linear response of BSO with respect to the dependence of the diffraction efficiency on the fringe modulation. Figures 1 and 2 present simulation results comparing the performance of a BJTC with a conventional JTC implemented in both cases in BSO. We anticipate that the BJTC will have superior noise performance and discrimination.

In order to verify the coding method we have constructed a conventional JTC with BSO as the recording medium and coded the filter to produce a POF correlator. The scene used in the experiment consists of three different sized satellites with the Earth as a background as presented in Figure 3. The target is the largest satellite and its corresponding POF is coded in object space. The filter and scene are displayed on an Epson LCTV cell interfaced to a PC running in CGA mode to ensure correct pixel registration. The polariser and analyser orientation are such that the LCTV is operating in the amplitude-mostly configuration. The LCTV is illuminated with the 514nm output of a single mode Argon ion laser and the joint transform is formed at the plane of the BSO crystal at an average fringe spacing of 20  $\mu\text{m}$ ; a 6.25kV/cm field is applied to the crystal to facilitate the drift mechanism at these fringe spacings.

The expanded beam from a Helium Neon laser is incident from the other side of the crystal at the Bragg matching angle for the volume hologram ( at the above fringe spacing this condition is not too severe ) and reads the stored hologram; after a further Fourier transform the resulting correlation is captured by a CCD camera connected to a frame grabber.

The experimental correlation output corresponding to the POF is shown by the surface plot in Fig. 4. In order to quantify the results we have used two parameters. The signal to noise ratio (SNR) and the full width at half maximum (FWHM) defined as:

$$SNR = \frac{\text{peak value}}{\text{RMS value of pixels} < 50\% \text{ of peak height}} \quad (7)$$

$$FWHM = \frac{\text{number of pixels} > 50\% \text{ peak value}}{\text{total number of pixels}} \quad (8)$$

Values obtained were SNR=8.96 and FWHM=22

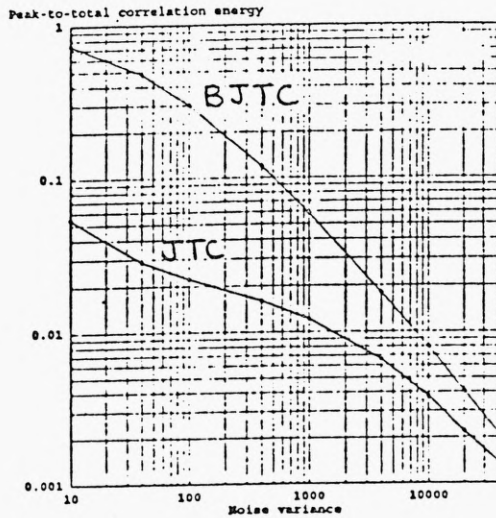


Fig 1 Comparison of JTC and BJTC efficiency

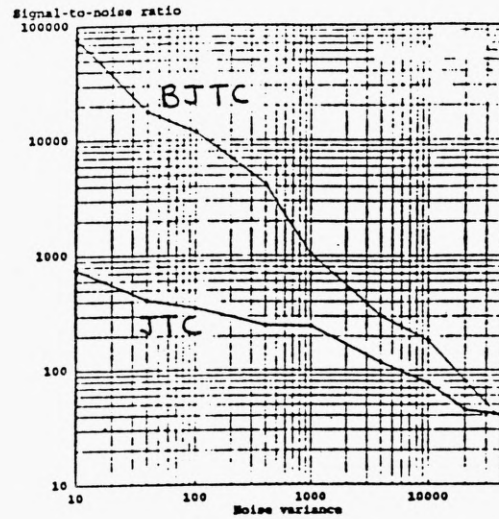


Fig 2 Comparison of noise performance

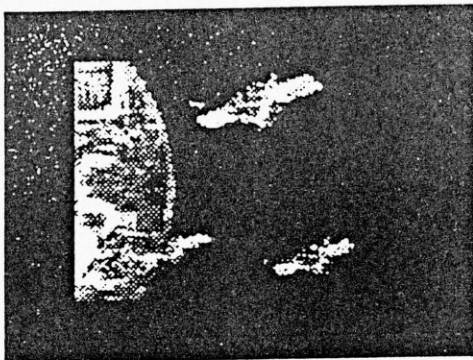


Fig 3 Scene displayed on SLM

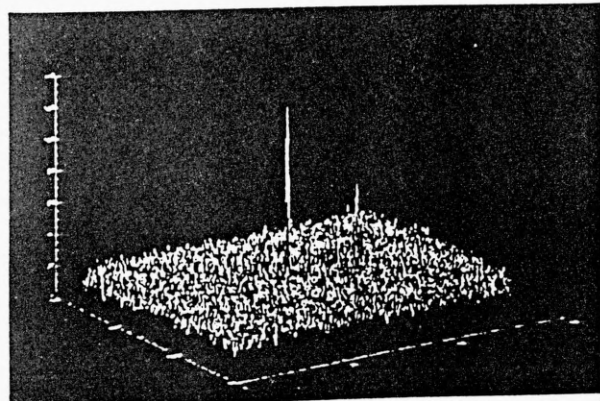


Fig 4 Correlation from JTC with POF

References

- [1] For a good overview of the non-linear JTC see :  
B.Javidi (Ed), *Real Time Optical Information Processing*, Acd. Press, Ch. 4
- [2] F.Cheng, F.T.S.Yu and D.A.Gregory, *App. Opt.*, **32**, 6521, (1993)
- [3] B.Javidi, J.Wang and Q.Ting, *App. Opt.*, **30**, 4234, (1991)
- [4] A.Carnicer, E.Martin-Badosa, I.Juvells and S.Vallmitjana, *Opt. Comm.*, **114**, 336, (1995)
- [5] C.B.Burckhardt, *App. Opt.*, **9**, 1949, (1970)

# Photorefractive Phase-only Joint Transform Correlator

A. Carnicer<sup>(1)</sup>, C. M. Cartwright<sup>(2)</sup>, N. J. Cook<sup>(2)</sup>, S. Vallmitjana<sup>(1)</sup>,  
W. A. Gillespie<sup>(2)</sup> and I. Juvells<sup>(1)</sup>

(1) Univ. de Barcelona, Laboratori d'Òptica, Dep. Física Aplicada i Electrònica.

Diagonal 647, E08028 Barcelona, E-mail: artur@athenea.fae.ub.es

(2) Abertay-Dundee Univ., School of Engineering, Bell Street, Dundee DD1 1HG (UK)

In this paper we implement a photorefractive joint transform correlator (PJTC) [1] which operates with a liquid cristal television (LCTV) the input and a BSO crystal in the Fourier plane. To enhance the detection capability of the correlator we use phase-only information in the input plane. In a PJTC, scene and reference (joint scene) are displayed on the input LCTV. The system is illuminated by a coherent plane wave and the joint power spectrum (JPS) is recorded in the focal plane of the Fourier lens by means of a video-camera (CCD). In a second stage, the JPS is displayed on the LCTV and the correlation is can be recorded by the CCD. The JPS is described by the following equation:

$$I(u, v) = |F_R(u, v)|^2 + |F_S(u, v)|^2 + 2|F_R(u, v)||F_S(u, v)| \cos(x_0u + y_0v + \phi_S(u, v) - \phi_R(u, v)) \quad (1)$$

where  $|F_R(u, v)|\exp(i\phi_R(u, v))$  and  $|F_S(u, v)|\exp(i\phi_S(u, v))$  are the Fourier transforms (FT) of the reference  $f_R(x, y)$  and the scene  $f(x, y)$  respectively. We assume that the scene is located at  $(x_0/2, y_0/2)$  and the reference is at  $(-x_0/2, -y_0/2)$ . The binary joint power spectrum  $I_b(u, v)$  (BJPS) is obtained by assigning the values +1 or -1 to  $I(u, v)$ , as below [2]:

$$I_b(u, v) = \begin{cases} 1 & \text{if } I(u, v) \geq I_T(u, v) \\ -1 & \text{if } I(u, v) < I_T(u, v) \end{cases} \quad (2)$$

where  $I_T(u, v)$  is a predetermined threshold function. By using a suitable threshold function, equation 1 becomes  $I_b(u, v) = \cos(x_0u + y_0v + \phi_S(u, v) - \phi_R(u, v)) + \dots$  and Fourier transforming this Equation the correlation can be written as:  $c(x, y) = \delta(x - x_0, y - y_0) + \delta(x + x_0, y + y_0)$

When two beams intersect inside a photorefractive crystal, an optically induced refractive-index grating is produced [3]. This grating is formed by the excitation of photo-electrons which migrate by diffusion and drift forming a local space-charge modulation which modifies the refractive index via the linear electro-optic effect. The intensity distribution incident on the crystal will be recorded as a sinusoidal variation in refractive index. The JPS may be analysed using a low power He-Ne beam which will diffract from the refractive index gratings with an efficiency  $\eta(u, v)$ . The Fourier component of the transmittance function that generates the first-order correlation signal is therefore,

$$\eta(u, v) \cos(x_0u + y_0v + \phi_S(u, v) - \phi_R(u, v)) = \frac{I_R(u, v)}{I_S(u, v)} \cos(x_0u + y_0v + \phi_S(u, v) - \phi_R(u, v)) \quad (3)$$

If  $|F_R(u, v)|^2 = |F_S(u, v)|^2$  for all  $(u, v)$ , then  $|F_R(u, v)|^2/|F_S(u, v)|^2 = 1$ . This can be achieved for all  $(u, v)$  in practical terms by setting  $|F_R(u, v)|^2 = |F_S(u, v)|^2 = 1$ , which is possible by coding the scene and reference as phase-only distributions. There are other advantages gained by using a photorefractive crystal as the JPS processor, rather than a CCD/LCTV setup, such as increased resolution; useful diffraction is possible with a grating spacing of  $5 \mu\text{m}$ , whereas the pitch of the CCD pixels is approx  $30 \mu\text{m}$ . Also the performance is not degraded by Fourier plane quantisation. The frame grabber used in these experiments has  $2^8$  quantisation levels. Lower quantisation values may be used when the low spatial frequency pixel values are nonlinearly compressed. A phase-only object-space distribution can be calculated as follows: Let  $F(u, v) = |F(u, v)|e^{i\phi(u, v)}$  be the Fourier transform of a



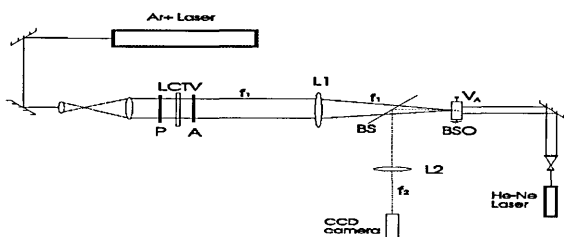


Figure 1:



Figure 2: joint scene

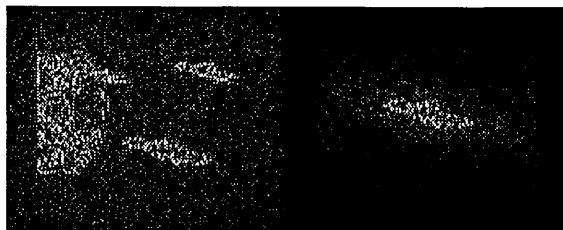


Figure 3: Phase-only joint scene

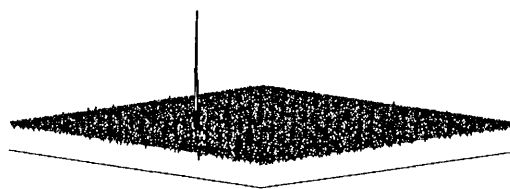


Figure 4: Optical detection of the bigger satellite

two-dimensional distribution  $f(x, y)$ . Let us define the phase-only version of  $f(x, y)$  in object space ( $f_{PO}(x, y)$ ) as  $f_{PO}(x, y) = FT^{-1}(FT(f(x, y))/|FT(f(x, y))|)$  where  $FT$  and  $FT^{-1}$  are the Fourier and inverse Fourier transform operators respectively.

The scene and target images are displayed side by side on the LCTV. The distance between the scene and target, combined with the choice of lens L1 gives a fringe spacing of  $20 \mu\text{m}$ , this ensures Bragg matching for objects throughout the scene. The different objects in the scene should not be so far apart that their intra-correlation signals coincide with the cross-correlation field. Images of  $768 \times 512$  pixels are generated by a frame grabber board and scaled to ensure correct registration of pixels on the LCTV. The LCTV is from an Epson VP-100PS projector, in this setup it has  $319 \times 200$  available pixels and a contrast ratio of 30:1. The polariser (P) and analyser (A) are aligned to give amplitude mostly modulation. The Fourier transform is formed at the BSO crystal by lens L1 (focal length 300mm), the zeroth order  $\text{Ar}^+$  laser power at the crystal is approx  $50 \mu\text{W}$ . A  $6.25 \text{kVcm}^{-1}$  (VA) field is applied to the crystal using silver painted electrodes to achieve drift-mode recording. The JPS grating is read using a low power He-Ne laser, this does not degrade the grating due to the spectral sensitivity of BSO. The first order diffraction (dotted line) is sampled using a 20% beam-splitter (BS), and the correlation output is formed by lens L2, then captured by a CCD camera linked to the same frame grabber. The experimental setup is shown in Figure 1. The scene used in the experiment is presented in Figure 2, while the phase only scene is shown in Figure 3. The filter and scene are displayed on an Epson LCTV cell interfaced to a PC running in CGA mode to ensure correct pixel registration. The polarizer and analyser orientation are such that the LCTV is operating in the amplitude-mostly configuration. The correlation obtained, detecting the satellite is shown in Figure 4.

## References

- [1] L. Pichon and J. P. Huignard, "Dynamic joint-Fourier- transform correlator by Bragg diffraction in photorefractive  $\text{Bi}_{12}\text{SiO}_{20}$  crystals", *Opt. Comm.* **36**, 277-280 (1981).
- [2] B. Javidi, "Nonlinear correlation joint transform correlation", *Appl. Opt.* **28**, 2358-2367 (1989).
- [3] T. J. Hall, R. Jaura, L. M. Connors and P. D. Foote, "The photorefractive effect. A review", *Prog. Quant. Electron.* **10**, 77 (1985).

This paper has been supported in part by the CICYT (*Comisi3n Interministerial de Ciencia y Tecnolog3a*), project n. TAP94-0303.